10-22-2015 12:00 AM

Reflectance and Emission Spectroscopy: Curve Fitting Methods with Application to Impact Glasses and the Varying Grain Size of Planetary Analogue Minerals

Michael A. Craig
The University of Western Ontario

Supervisor
Gordon R. Osinski
The University of Western Ontario Joint Supervisor
Roberta L. Flemming
The University of Western Ontario Joint Supervisor
Edward A. Cloutis
The University of Western Ontario

Graduate Program in Geology

A thesis submitted in partial fulfillment of the requirements for the degree in Doctor of Philosophy

REFLECTANCE AND EMISSION SPECTROSCOPY: CURVE FITTING METHODS WITH APPLICATION TO IMPACT GLASSES AND THE VARYING GRAIN SIZE OF PLANETARY ANALOGUE MINERALS

(Thesis format: Integrated Article)

by

Michael Andrew Craig

Graduate Program in Geology: Planetary Science

A thesis submitted in partial fulfillment
of the requirements for the degree of
Doctor of Philosophy

The School of Graduate and Postdoctoral Studies
The University of Western Ontario
London, Ontario, Canada

Abstract

Spectroscopy, i.e., the measurement of electromagnetic radiation as a function of wavelength, is arguably the technique responsible for the majority of what is collectively known about the composition of stars, the distances to galaxies, the age of the universe and so on. Spectroscopy is also the tool most used to discern the mineralogy of planetary bodies remotely. Measuring the speed at which a star is receding and its composition, or the composition of an interstellar cloud of gas are well understood uses of spectroscopy. When it comes to spectroscopies use to discern mineralogy, the scientific literature on the subject of the application of spectroscopy to the solid surfaces of asteroids and the nearby planets would lead one to conclude it too is as robust a measure as that of stellar composition or Doppler shift, although it is not.

A number of properties of the target under investigation, namely, mineralogy, grain size, packing (i.e., loose grains versus consolidated rock), phase angle and temperature strongly affect the reflectance and emission spectrum of the common minerals encountered when interrogating planetary surfaces. These effects can be profound and significantly complicate our ability to robustly identify mineralogy when the properties of the surface are not known.

The works herein address some of these issues, by firstly, providing a set of methods/functions and a set of guidelines for empirically curve fitting spectra in a robust and repeatable manner. Chapter 2 and its appendices were conceived in an effort to provide the spectroscopic community with a set of curve fitting tools, to be put freely in the hands of spectroscopists in the hopes that the community can see its way to providing fit metrics of spectra presented in the literature with transparency so the metrics can be widely understood and applied. Secondly, the methods presented in Chapter 2 were applied in Chapters 3 and 4 to the spectra of impact glasses and hydrothermal silicate evaporates to aid in their robust identification, and to the effects of significant grain size

variation on the most common planetary surficial analogue materials pyroxene, olivine and basalt.

Keywords

Spectroscopy, Curve Fitting, Impact Glasses, Grain Size, Spectral Analyses, Mars, Asteroids

Co-Authorship Statement

Chapter 2: Fitting the Curve in Excel®: Systematic Curve Fitting of Laboratory and Remotely Sensed Planetary Spectra

Coauthors are Michael A. Craig, Gordon R. Osinski, Edward A. Cloutis, Roberta L. Flemming, Matthew R. M. Izawa, Vishnu Reddy, Sherry K. Fieber-Beyer, Loredana Pompilio, Freek van der Meer, Jeffrey A. Berger, Michael S. Bramble, and Daniel M. Applin. Michael A. Craig wrote the manuscript and both appendices. Gordon R. Osinski, Edward A. Cloutis, and Roberta L. Flemming are Michael A. Craig's thesis supervisors, supervised the work and helped to evaluate and edit the manuscript and the appendices. Matthew R. M. Izawa assisted in the creating of several of the curve fitting functions in appendix 2A, evaluated the mathematics in appendix 2A and helped to evaluate and edit the manuscript and the appendices. Vishnu Reddy, Sherry K. Fieber-Beyer, Loredana Pompilio, and Freek van der Meer helped to evaluate and edit the manuscript and the appendices. Jeffrey A. Berger, Michael S. Bramble, and Daniel M. Applin, served as beta testers for appendix 2A, which shaped much of the instruction set in appendix 2B, and notes in appendix 2A written by Michael A. Craig. Jeffery A. Berger, Michael S. Bramble and Daniel M. Applin also helped to evaluate and edit the manuscript and appendices.

Chapter 3: Impact Glasses: Identifying and Differentiating Between Effusive Glasses, Glassy Impactites, Hydrothermal Deposits and the Milieu of Silicates on Mars using Reflectance and Emittance Spectroscopy

Coauthors are Michael A. Craig, Gordon R. Osinski, Edward A. Cloutis, Roberta L. Flemming, A. Deanne Rogers, Livio L. Tornebene, Matthew R. M. Izawa, Haley M. Sapers, Annemarie E. Pickersgill, and Cassandra L. Marion. Michael A. Craig prepared the samples, performed the analyses (all but IR emission), interpreted the data, and wrote

the manuscript, and the three appendices. Gordon R. Osinski, Edward A. Cloutis, and Roberta L. Flemming are Michael A. Craig's thesis supervisors, supervised the work and helped to evaluate and edit the manuscript and the appendices. A. Deanne Rogers collected IR emission spectra and it is expected she will help to evaluate and edit the manuscript and appendices at a later date. Livio L. Tornebene and Matthew R. M. Izawa have been available for many discussions and it is expected they will help evaluate and edit the manuscript at a later date. Haley M. Sapers, Annemarie E. Pickersgill, and Cassandra L. Marion have been available for many discussions and have contributed samples from their various theses work to the sample set. It is expected they will help to evaluate and edit the manuscript at a later date.

Chapter 4: The Effects of Grain Size (<10 μm to 4.75 mm) on the Reflectance Spectrum of Common Planetary Analogue Materials

Coauthors are Michael A. Craig, Gordon R. Osinski, Edward A. Cloutis, Roberta L. Flemming, Matthew R. M. Izawa, Vishnu Reddy, and Loredana Pompilio. Michael A. Craig prepared the samples, performed the analyses, interpreted the data, and wrote the manuscript and the appendix. Gordon R. Osinski, Edward A. Cloutis, and Roberta L. Flemming are Michael A. Craig's thesis supervisors, supervised the work and helped to evaluate and edit the manuscript and the appendix. Edward A. Cloutis wrote a draft of the literature review and also helped to conceive the study. Matthew R. M. Izawa has been available for many discussions and it is expected he will help to evaluate and edit the manuscript at a later date. Vishnu Reddy helped to conceive the study and it is expected he will help to evaluate and edit the manuscript at a later date. Loredana Pompilio is the creator of the Exponential Gaussian Optimization function (see Pompilio et al., 2009, Icarus 201, and Pompilio et al., 2010, Icarus 208) and it was intended EGO fits of the data would be included in the manuscript. EGO is presently inoperative, if that

should change in the near future, EGO fits will be added to the manuscript and appendix and it is expected she will help to evaluate the manuscript and appendix at a later date.

Acknowledgments

I would most like to thank my family and friends, past and present supervisors, classmates who have been there to support me… and, most notably, my wife Melissa.

'Twas noontide of summer,
And mid-time of night;
And stars, in their orbits,
Shone pale, thro' the light
Of the brighter, cold moon,
'Mid planets her slaves,
Herself in the Heavens,
Her beam on the waves.

I gazed awhile
On her cold smile;
Too cold- too cold for me-
There pass'd, as a shroud,
A fleecy cloud,
And I turned away to thee,
Proud Evening Star,
In thy glory afar,
And dearer thy beam shall be;
For joy to my heart
Is the proud part
Thou bearest in Heaven at night,
And more I admire
Thy distant fire,
Than that colder, lowly light.

Evening Star, by Edgar Allan Poe

Table of Contents

Abstract ii

Co-Authorship Statement iv

Acknowledgments vii

Table of Contents viii

List of Tables xii

List of Figures xiii

List of Appendices xxiii

Chapter 1 1

1 Introduction 1

1.1 References 10

Chapter 2 13

2 Fitting the curve in Excel®: Systematic curve fitting of laboratory and remotely sensed planetary spectra 13

2.1 Introduction 13

2.2 Curve Fitting Methodologies 16

2.3 Empirical Curve Fitting 21

2.3.1 Band Minima 24

2.3.2 The Continuum 28

2.3.3 Pin Points 33

2.3.4 Straight Line Apparent Continuum Removal 34

2.3.5 Band Centre 36

2.3.6 Band Depth 36

2.3.7 Band Area 37

2.4 Modelling 39

2.5 Further Parameterization and Manipulation of Spectra 43

2.6 Summary and Conclusions 44

2.7 Acknowledgements 45

2.8 References 47

Chapter 3 55

3 Impact Glasses: Identifying and Differentiating Between Effusive Glasses, Glassy Impactites, Hydrothermal Deposits and the Milieu of Silicates on Mars using Reflectance and Emittance Spectroscopy 55

3.1 Introduction 55

3.2 Experimental Procedure 56

3.3 Sample Descriptions and Definitions: Glass, Glassy and Amorphous 58

3.4 Spectral Features of Impactites 59

3.5 NIR versus IR and the Surface of Mars 60

3.6 Curve Fitting IR 65

3.7 Discussion 68

3.8 Conclusion 88

3.9 Acknowledgements 89

3.10 References 91

Chapter 4 101

4 The Effects of Grain Size (<10 μm to 4.75 mm) on the Reflectance Spectrum of Common Planetary Analogue Materials 101

4.1 Introduction 101

4.2 Previous Studies 102

4.2.1 Powders: Grain Size Effects 102

4.2.2 Slabs versus Powders 105
4.3 Experimental Procedure 107
4.4 Curve Fitting 109
4.5 Band Saturation and Scattering 110
4.6 Results 115
4.6.1 Pyroxene 115
4.6.2 Basalt 121
4.6.3 Olivine 125
4.7 Discussion 126
4.8 Conclusion 127
4.9 Acknowledgements 131
4.10 References 132
Chapter 5 137
5 Concluding Remarks 137
5.1 References 141
Appendices 146
6 Appendix 2B: Fitting the Curve, Workbook Instructions 146
6.1 Excel Short Cut Keys: 148
6.2 Keyboard Navigation (skip to page 11 if you are familiar with Excel) 149
6.2.1 Defined Name Ranges 154
6.2.2 Name Manager 159
6.3 Fitting the Curve: Example Walk-Through 161
6.4 The “Rules of the Road” 165

6.5 Adding Spectra to a Worksheet, and Inserting a Chart: 170

6.6 5. Picking portions of the spectrum to use for Pin Points: 182

6.7 Straight Line Apparent Continuum Calculation and Removal 193

6.8 Minima and Centre Fitting 199

6.9 Area Calculation and BAR 201

6.10 Derivatives, Curved Continua, Skew, Imposed and Real Continua, Gaussian Fit Optimization, Gaussian Modelling, Line Shapes, Smoothing and I/F 203

6.10.1 Derivatives 203

6.10.2 Curved Continua 205

6.10.3 Skew/Asymmetry 206

6.10.4 Blackbody Curves: Imposed and Real Continua 208

6.10.5 Gaussian Fitting and Gaussian Modelling (Fit Optimization and Curve Deconvolution) 211

6.10.6 Gaussian Fit Optimization using Solver and/or OpenSolver 213

6.10.7 Line Shapes 218

6.10.8 Smoothing 219

6.10.9 Imposed Continuum Removal, I/F (Intensity/Flux) and Thermal Excess 220

6.11 References 223

Curriculum Vitae 225

List of Tables

Table 4.1 119

List of Figures

Figure 1-1: A depiction of the polynomials used to derive absorption band minima, and the derivation of pin points for fitting of straight line apparent continua for later absorption band centring. 2

Figure 1-2: Infrared Emission Spectra within our window of interest for Mars. BAS101 is a Hawaiian basaltic glass, HMP99-064D is a pure quartz from the Haughton Crater, HNL60C is a pyroxenite impact glass from the Lonar Crater, MOL001 is a Moldavite Tektite, HMP00-263B is an impact glass from the Haughton Crater and RI-01 is an impact glass from the Ries Crater. These six sample are indicative of the changes in the fundamental stretching vibrational mode of Si-O which we can use to identify like assemblages on asteroids and other planets. 5

Figure 1-3: A depiction of the variation in the Band I absorption centre of a series of pyroxene grain size splits, which can be used, referencing other derived metrics (as depicted in Figure 1-4) to discern the grain size of a material under investigation. Solid squares denote the derived centres for each grain size separate. 8

Figure 1-4: Band I centre, of the grain size separates, versus the measured absolute reflectance value at the same point in the spectrum before the Band was centred and contrast stretched. Figure 1-4 is one of many empirical metric-versus-metric comparison can be used to discern grain size of a target under investigation, as well as assess our confidence level in a particular mineralogical identification. 9

Figure 2-1: The NIR spectrum of the pyroxene, solid black line, with black offset (+0.01) dashed lines depicting the 3rd order polynomials fits used to derive the straight line continuum pin points, grey offset (-0.01) dashed lines depicting the 3rd order polynomial fits used to derive band minima and black dotted lines depicting the straight line apparent continua that will be used to isolate the features of interest for band centring and area derivation. 22

Figure 2-2: Construction of the Combined Blackbody Curves (CBC) for a sample of pyroxene illustrating the removal of the continuum imposed on the sample spectrum by the reflectance instrument calibration/reflectance spectrum measurement process. 2-2A is the solar black body emission curve/reflectance blackbody curve at a temperature of 5770 K. 2-2B is the emission blackbody curve for the <45 μm powdered pyroxene sample at a temperature of 296.15 K (23 °C). 2-2C is the CBC which is removed via multiplication in panel 2-2D to illustrate the removal of the continuum imposed on the sample by the spectral measurement process. The black dashed line is the spectrum of a pyroxene depicting the normal output of a reflectance spectrometer where the pyroxene spectra is measured relative to a white reference standard, the solid black curve is the CBC for the sample and the thicker grey line is the real spectrum of the pyroxene with its imposed continuum removed. 28

Figure 2-3: The spectrum of pyroxene with Bands I and II isolated, but uncentred, based on the derived pin points presented in figure 1, with fit straight line apparent continua (solid black lines), and two oft used curved apparent continua, a 2nd order polynomial (dotted curve), and a natural cubic spline (the dashed curve). Any of the depicted straight or curved apparent continua could be used to further remove continuum from the spectrum, isolating the absorptions while centring them for derivation of area and simplification of band depth calculation. We advocate for the use of straight line apparent continuum removal in wavelength space as demonstrated. See Appendix A for further comparison of various straight and curved line continua apparent removal methods. 32

Figure 2-4: Straight line apparent continuum removed spectra of the two isolated bands of interest for asteroid 4 Vesta. The dotted spectrum has been straight line apparent continuum removed via division, i.e., centred, and the dashed line spectrum has been straight line apparent continuum removed via linear translation. The solid black spectrum is the unaltered (but offset) SMASS + SpeX spectra of Vesta. The heavy black lines which overlay the absorption minima for the centred dotted spectrum depict the

polynomials fit to derive the band centres. The spikes in the two continuum removed spectra within Band II, and the portions of the continuum removed spectra which are above unity are discussed, as is the fitting of data with gaps, in more detail in the Appendices. 35

Figure 2-5: Gaussian modelling of the pyroxene sample in eV space, with the imposed continuum removed in wavelength space such that the Gaussians used model the real absorptions responsible for the majority of the spectrum. Dotted lines depict the 6 Gaussians used, the thick grey spectrum is of the pyroxene sample with its imposed continuum removed, and the dashed black line residing within the thick grey spectrum is the summed Gaussian model. The quality of the fit is measured by the residual, where the better the fit, the less the residual varies about the 1.1 line (RMS 0.004). 41

Figure 3-1: NIR absolute reflectance spectra of a suite of glassy-impactites and other silicates we would expect to find in and around impact sites on Mars which would complicate the robust identification of glassy-impactites. The left and right panels share the same absolute reflectance scale and a separated into hydrated and "dry," respectively. 62

Figure 3-2: Right Width at Half Maximum (RWHM) of the ~ 8.8 to 10.5 μm asymmetric fundamental vibrational IR emission absorption of the silica versus the absorption minimum of that same absorption for our suite of glassy-impactites and examples available in the literature. In general, glassy-impactites form a band across the bottom with high-silica glassy-impactites and evaporites clustered at the bottom left. Volcanic, pyroclastic and the more canonical impact related glasses form an arc on the right side of the figure. 67

Figure 3-3: IR transmission and emission spectra and powder XRD patterns of 5 glass samples. BAS 101, a Hawaiian effusive basaltic glass, and glassy-impactites, CM09-DH1, SIL004, MOL001 and TEK001, which are a basaltic impact glass from the Mistastin Crater, pyroclastic Apache Tears, and Moldavite and Indochinite tektites

respectively. The powder XRD patterns on the right ascend in the same order as they run left-to-right in the two charts of spectra. 74

Figure 3-4: IR transmission and emission spectra BAS 101, a Hawaiian effusive basaltic glass, HMP99-064D which is pure detrital quartz from Haughton and glassy-impactites, HNL60C, MOL001, HMP00-263B and TEK001, which are a basaltic impact glass from the Lonar Crater (clearly more effusive in nature), a Moldavite tektite, a nearly pure glassy-impactite from Haughton (see Figure 3-3) and a glassy-impactite for Ries Crater which is partially devitrified and contains some phyllosilicates. 76

Figure 3-5: IR emission spectra in our window of interest for Mars. These are spectra of the same samples as in Figure 3-4 with the addition of diaplectic glass sample MM10-38. Spectra are smoothed using a 9-point boxcar function to ease separation of spectra by eye. 77

Figure 3-6: XRD Pattern and NMR spectra of Haughton glassy-impactite HMP00-263B. This is the glassiest Haughton sample and one can see how little the quartz is influencing the stretching fundamental vibration of Si-O-Si at 8.9 μm in Band I in the Figure in Sheet *11* of Appendix 3C. The influence of the minor amount of quartz in the sample can be seen by the crystalline peak, demarcated in blue in the XRD pattern and asymmetry of the PPM shift peak short-ward of its ~111.4 PPM centre. Based on Pseudo-Voigt modelling of the NMR peaks, the silica component of HMP00-263B is ~ 99.8% glass based on modelled peak area. 80

Figure 3-7: XRD pattern and NMR spectra of Haughton sample HMP00-264B. This sample is somewhat intermediate in the suite. One can clearly see the influence of this moderate volume of quartz in the IR emission spectrum in Sheet *12*, Appendix 3C, but even though it is quite apparent, and comprises ~11% of the silica content of the sample, the quartz' influence on the position of the glassy-impactites Band I minimum and RWHM value is negligible. If you would like to see an example of the spectrum of pure quartz, see sample HMP99-064D in Sheet *3*, Appendix 3C. Note: this sample contains a

marginal amount of crystalline oxide (likely iron and not potassium) and Morris et al., (2000), found that changes in iron oxidation state in glassy samples, has no discernable effect of their IR spectrum, and iron oxides are spectrally featureless in the Band I region in our IR emission spectra (see Christensen et al., 2000; Glotch et al., 2004). 81

Figure 3-8: XRD pattern and NMR spectra of sample MOL001 which is a Moldavite tektite. This sample is pure glass as evidenced by its XRD pattern and NMR spectrum. The IR emission spectrum of this sample is shown in Sheet *26*, Appendix 3C, and its Band I is sharpened as one would expect for a glassy-impactite, but not to the same extent as Band I of HMP00-263B or 00-264B. These differences arise as a result of the different formation environments of these samples; the Haughton samples are both clasts found within the melt breccia of Haughton crater and likely to have quenched from rapid pressure release in the crater floor while the Moldavite quenched very quickly in air under little to no constraining pressure. Sample MM10-38 (not shown here) is purely diaplectic glass at hand sample scale and its IR emission spectrum has very nearly the same RWHM as MOL001 but its Band I minimum position places it closer to the basaltic samples in composition which is in harmony with its plausible origin (see Stöffler et al., 2002). 82

Figure 3-9: RWHM versus Band I minimum for the suite of glassy-impactites and examples from the available IR emission spectra from the literature. Shaded areas represent two populations, red at the lower left being the high-silica glassy impactites and hydrothermal deposits with a sharper silica asymmetric stretching fundamental absorptions, and blue at the upper right with longer wavelength shallow and broad asymmetric stretching absorption more indicative of canonical glasses formation environments. The green arrow marks an area where we expect diaplectic samples will reside where they have not experienced a liquid phase transition and with increasing pressures, we expect both partially diaplectic samples, e.g., Ries RI-09-007, and fully diaplectic samples, e.g., Mistastin MM10-38, to travel in the direction the arrow points with an increase in maximum pressure experienced..... 84

Figure 4-1: An illustration of band saturation for Band II in pyroxene. As Mean Optical Path-Length (MOPL) increases and more inter- and intra-grain photon interactions occur (i.e., photon absorptions), band depths deepen, band widths widen and overall reflectance drops. The effect is illustrated in left panel, where with increasing absorption rates the absorption minimum falls well below zero in reflectance. The synthetic spectra on the right are more indicative of what one actual sees in the spectrum, though we do not see reflection reaching zero. Refection never reaches zero as long as the grains being imaged are larger than the wavelengths of light which are interrogating them, and in this instance, grains would have to be smaller than approximately 2 μm for optical interactions to occur and be a problem. Rather than zeroing, bands saturate and behave as is depicted in Figure 4-2. 111

Figure 4-2: NIR reflectance spectra of PYX023 in absolute (left) and straight line continuum removed reflectance (right). Left and right panels depict the effects of bad saturation on Bands I and II in pyroxene. The flattening of absorption bands with as a result of band saturation as grain sizes increases is readily apparent as is the "crashing" into zero which complicates band minimum and centre derivation (dotted-line spectra). After centring, the continuum removed spectra of Band II (right) illustrate the flattening of Band II in the larger grain size splits and the wandering centre measurements which accompany band saturation. While the effect of saturation appears most severe in Band II, in pyroxene it is more apparent in Band I, where it sets in at much smaller grain sizes than for Band II (see Appendix 4A, Sheet *A*). 112

Figure 4-3: Comparison of Absolute Reflectance value at the derived Band Centre before centring occurred and the Band Depth for the 33 grains size splits of PYX023. Band I is depicted left, Band II on the right. This relationship best demonstrates both enhanced scattering at smaller grain sizes and band saturation for larger grain sizes. In both panels, enhanced scattering increases albedo and decreases band depth which can be seen in the smaller grain sizes which break out from the cluster of samples at the bottommost right in each panel and climb toward the upper left. Band saturation is illustrated by the samples

dropping down to the lowest absolute reflectance values and clustering along a line of approximately 0.1% reflectance (which also illustrates the effect specular reflection has in ensuring reflectance never reaches zero). Both panels are also illustrative of the reasons for not relying on band depth and correlated area, and albedo/reflectance values for mineral identification as for a many different grains sizes, the measures are equivalent. In both of the panels we can surmise that the smallest grain sizes, those smaller than ~ 25 μm, scattering is dominating, and we may not be able to discern these grain sizes reliably using spectra with a multitude of empirical metrics (we could however suggest, grain size is small, and within a narrow range). We can also see band saturation, while apparent in all grain sizes larger than ~ 75 μm which are experiencing band saturation to some extent, only when they deviate leftward from the tight grouping of samples in the rightmost bottom corner, is saturation becoming enough of a concern, that we may no longer be able to reliably discern grain sizes larger than ~ 1 mm spectrally without further metrics, we could however, definitively state the grain size is between coarse sand and rock 114

Figure 4-4: NIR absolute reflectance spectra of the first 7 of the dry sieved splits of pyroxene sample PYX023 depicted with a full reflectance scale at left, and an expanded scale in the panel at the right. Evident in both Bands I and II are the general trends in reflectance spectra when going from a small to a large grain size. The <20 μm split is high in albedo (in both the Figure and for the set of 33 splits), with muted (i.e., low depth) absorption features (the centred Band I depth in the <20 μm split is the shallowest centred Band I depth in the 33 split set), as grain size increases albedo drops and band depth increases until it reaches a maximum (the maximum centred band depths for both Band I and II occur in the 150-180 μm split), then centred band depth shallows in lock step with decreasing albedo. 116

Figure 4-5: NIR absolute reflectance spectra of the last 6 of the dry sieved splits of pyroxene sample PYX023 and the rock spectrum depicted with a full reflectance scale in the left panel and, with a significantly expanded scale in the right panel. The clustering

of spectra close to zero reflectance due to band saturation is evident at left, as is the marginally higher albedo and slight red-sloped deviation of the rock spectrum from the rest of the set. Evident in the right panel, is the blue-slope of the largest of the grain size splits (for a progression through all sizes see Appendix 4A). 116

Figure 4-6: Band I Centre versus BAR plot for the 33 split series for pyroxene sample PYX023. This is the most efficacious of the empirical metric comparisons despite the scatter in some of the larger grain size splits in the upper left quadrant of the chart. Band saturation first appears in the between ~ 150 and 180 µm where the deviation of the Band I centre falls outside of the spectral resolution bounds of the ASDI spectrometer. The metrics were produced using centred bands where pin points where fixed inside the points of band extinction for all the samples in the set so scatter in the Band I Centre and BAR are the result of specular reflection and band saturation. Specular reflection in the smallest grain size splits effects band depth and area but across all of the samples investigated in this study it has little to no effect on centre values..... 118

Figure 4-7: Band I Centre versus Band II Centre and Band I Centre versus BAR plots for the 5 size series of pyroxene PYX023. These two plots appear to make it clear that there is a definitive and easily exploitable relationship between grain size, band centres and band areas. Unfortunately if one references Figure 4-5 (or others in the Appendix 4A) the relationships are not quite as clear. Band saturation produces significant scatter about the larger grains sizes, though these relationships may be more indicative of naturally occurring grain size distributions which will rarely be sorted with the specificity of the 33 split series..... 120

Figure 4-8: Linear trendline Band I Centre versus Band II Centre and Band I versus BAR plots of the two grain size series of pyroxene PYX023. These two empirical relationships are the most exploitable for the determination of grains size and degree of band saturation as depicted in Figure 4-6 and 4-7. In the left panel, grain size increases from top left to bottom right, and in the right panel, from bottom left to top right. Band centres follow

reasonably consistent trends from smallest to largest grain size, while depth and area follow a low-to-high-to-low trend which complicates the use of either metric. Area versus area and depth versus depth comparisons are not of use (see Appendix 4A) and as BAR is an established metric that is widely used to determine asteroid mineralogy, BAR is the metric recommended. 120

Figure 4-9: NIR absolute reflectance spectra of the first 7 of the dry sieved splits of basalt sample SA-51 depicted with a full reflectance scale in the left panel and an expanded scale in the right panel. The absorption feature centred at approximately 1 μm, due to crystal field transitions related to iron in the pyroxene and olivine crystals in the basalt is the absorption feature of interest. Throughout both of the basalt grain size sets, despite the appearance of band saturation with increasing grain size, the band centre remains relatively constant. 121

Figure 4-10: NIR absolute reflectance spectra of the last 6 of the dry sieved splits of Basalt sample SA-51 and the rock spectrum depicted with a full reflectance scale in the left panel and, with a significantly expanded scale in the right panel. The clustering of spectra close to zero reflectance due to band saturation is evident in the left panel, as is the marginally higher albedo and significantly blue-sloped deviation of the rock spectrum from the rest of the set. Evident in the right panel is the marginally blue-slope of the largest of the grain size splits which contrasts with the slightly red-slope of the smallest grain sizes in Figure 4-9 (for a progression through all sizes see Appendix 4A). 122

Figure 4-11: Band I Centre versus Band I Area for the 33 grain size series of basalt sample SA-51. While there is no positive correlation, this pattern fits with what can generally be said about the changes of the correlated metrics of band depth and area with increasing grain size, band depth and/or area is lowest in the smallest grain size splits were specular reflection is most active, depth/area increase to a maximum at some point at an intermediate size, in this instance in the 25-38 μm split, and generally falls off again

as grain size increases. The largest grain sizes evidence band depths/areas equal to or lower than the depth/area of the smallest grain size splits. 123

Figure 4-12: NIR absolute reflectance (left) and straight line continuum removed spectra (right) of olivine sample OLV003. In the largest of the grains size splits, 500-1000 µm, band saturation is apparent in both the absolute reflectance spectra and the centred spectra but it is not exerting a large enough influence to affect the empirical measures of the ~ 1 µm absorption. Muting of the absorptions short-ward in wavelength of the ~ 0.8 µm reflectance maximum can be seen and can be attributed to specular reflection but the muting of the ~ 1 µm absorption of interest is also not effective enough to exert and influence that would complicate the sample identification as olivine using empirical measures. 124

Figure 4-13: Correlation of Band Depth and Area for the ~ 1 µm absorption triplet of olivine sample OLV003. The left panel is a comparison of the empirical measures and the right panel is a linear trendline fit through the data. While this is not an extremely positive correlation it does fit with the general spectral alteration expected with increasing grain size. More interesting, as the sensitivity of olivine to spectral alteration with grain size is driven largely by its iron content, a relationship akin to the one depicted may be of use to discern iron content with a modicum of accuracy. Given a set of similarly derived empirical metrics, another olivine of differing composition is likely to plot on a line of differing slope. 125

List of Appendices

Appendices……146

6 Appendix 2B: Fitting the Curve, Workbook Instructions……...…..…146

Excel® Appendices (attached to the electronic version of this thesis)

Appendix 2A: Fitting the Curve

Appendix 3A: Impact Glass XRD and NMR Data

Appendix 3B: Impact Glasses NIR Spectra and Curve Fitting

Appendix 3C: Impact Glasses IR Spectra and Curve Fitting

Appendix 4A: Grain Size Spectra and Curve Fitting

Chapter 1

1 Introduction

Reflectance spectroscopy is the most powerful tool we possess to assess mineralogy remotely, and although spectroscopy is an established technique, identification of mineralogy in both the reflective ultraviolet through near-infrared (UV-Vis-NIR) and emissive infrared (IR) regimes, are largely stuck in the realm of probability. Remotely-obtained spectral signatures that claim definitive identification of mineralogy are often hubris.

The UV-Vis-NIR range of the spectrum (~ 0.3 to 2.5 μm in wavelength as defined by common detectors) is where spectral absorption features are the result of nuclear interactions, outer electron shell (crystal field) transitions or overtones and harmonics of vibrational modes that occur in the IR. In the UV-Vis-NIR range, reflectance spectra suffer from alteration due to grain size, packing, temperature and phase angles which changes the characteristics of shape, and position of the spectral absorptions we use to identify mineralogy. While spectral alteration due to these effects is not always significant, for the most part, the UV-Vis-NIR spectra can experience enough spectral alteration that identification of the mineralogy often cannot be definitive.

The fact that most mineralogical identifications are mired in the realm of probability does not result from any endemic weaknesses in spectral acquisition techniques, post-processing practices or instrumental issues; it results from a lack of laboratory studies that fully quantify the spectral alterations caused by changes in grain size, temperature, phase angle and packing, and the lack of shared tools (or free tools) to assess the changes in the spectra of minerals. Classically researchers have taken results from limited studies addressing each issue separately, using a limited range of minerals, or a limited set of grains sizes for example, and extrapolated those results to account for changes in all other minerals. This practice is simply unsatisfactory.

To aid in moving mineralogical identification from probability to definitive identification, we (as no one truly works alone in graduate school) have aimed to provide simple, repeatable, and freely available tools with each particular research project to provide members of the community, especially students and new researchers, with the mechanisms to define alteration effects, or simply to provide measures of spectra, we can all reliably use.

In the first study, Chapter 2, we produced a manuscript that outlines what we believe are a set of reasonable and robust guidelines for curve fitting UV-Vis-NIR or IR spectra (or any curve) which employ methods that are easy to understand, fully documented, and easy to visualize. The manuscript is a guide as is Appendix 2B, to the curve fitting math, and functions contained in Appendix 2A, which is a large Microsoft Excel workbook containing all of the functions necessary to empirically curve fit and model spectra, and a series of functions for working with spectra in general, i.e., interpolating, measuring skew, smoothing, calculating derivatives, automated Gaussian fitting, and so on.

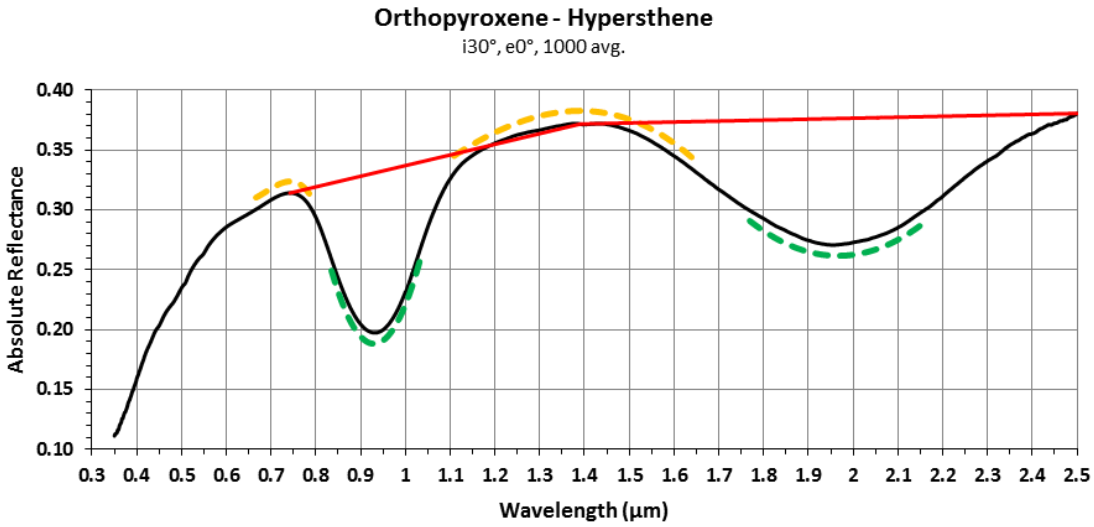

Figure 1-1: A depiction of the polynomials used to derive absorption band minima, and the derivation of pin points for fitting of straight line apparent continua for later absorption band centring.

We have done this because methods employed when curve fitting and modelling spectra can be confusing and difficult to comprehend. Students and researchers who are new to field are unlikely to find adequate documentation in the scientific literature or in the software packages available for curve fitting (or sources are closed and proprietary so one does not know how the fitting is being performed). The problematic lack of documentation in the literature also extends to dissemination of derived metrics when curve fitting has been performed. Often, derived metrics from some form of curve fitting are reported, such as band centres, but any discussion of exactly how the metrics were derived is not included. Our aim with Chapter 2 is to remove the issue. We are presenting methods to curve fit spectral data of various types using functions written to be used in, or to exploit the built-in functions within, Microsoft Excel® software, free of macros, which operate in a cut-and-paste fashion. We espouse empirical methods as our favoured techniques, but have provided methods and procedures for all of the common curve fitting methods currently employed in the planetary and terrestrial spectroscopic communities (i.e., Gaussian fitting akin to MGM, function which interpolate, and so on). All of the metrics one can derive from spectra, and the mathematics to do so, are documented in the workbook (Appendix 2A) and are open to scrutiny, which ameliorates many of the unknowns encountered when using black box commercial software.

We also believe that we have provided a framework, not only for curve fitting, but also a framework for the sharing of data (i.e., sharing spectral data in spreadsheet form). The vast majority of manuscripts, as well as providing little reference to methods for derivation of curve fit metrics, also do not provide any of the spectral data. The theme which runs thought Chapter 2, and its appendices is sharing. We are sharing all of the methods for curve fitting the group of coauthors could think of, and we would hope others in the community share it forward. We also are sharing the raw data and ideally, the curve fitting maths, for Chapters 3 and 4, and intend to do so going forward. The coauthors of Chapters 2 are a group of spectroscopists with various experience, who specialize in different areas, and going forward the idea is, we have all committed to share our data and methods as freely as we suggest for those who read and apply the methods provided in Chapter 2.

Modelling spectra, as in making a model of an existing spectrum to derive metrics are discussed and methods to do so are covered also covered in Chapter 2. Not included are Hapke Modelling/Scattering theory (Hapke, 1981, 1984, 1986, 2002, 2008; Hapke and Wells, 1981), Mie-Conel, Kubelka-Munk, and other equally applicable radiative transfer models, as these sorts of models are used to model spectra of materials to simulate their spectra. While applicable to Chapters 3 and 4, the radiative transfer models produced to date cannot adequately model the complex interactions which happen in geologic materials such that spectra produced by radiative transfer modelling will at best be close, but not a match, for the real spectra of minerals. The inadequacy of radiative transfer modelling is best covered by Moersch and Christensen, 1995, who found that even with monomineralic samples, no single model could adequately reproduce the real spectrum for a single mineralogy and at any grain size. Hapke scattering as modified by Lucy (1998) is included within the discussion section of Chapter 4 where it applies to the change in absorption coefficient with varying grain size in pyroxene, where in the confines of a monomineralic sample, in the reflectance regime only, Hapke modelling as modified by Lucy is efficacious, though does not fully model the changes seen in the reflectance spectrum of orthopyroxene with changing grain size.

Chapter 3 is a study of UV-Vis-NIR and IR spectral features of impact glass. To our knowledge, the study contains the largest set of naturally-occurring terrestrial impact glasses thus far assembled. It is also the first study to apply empirical curve fitting methods to IR emission spectra in the hopes of more robustly identifying impact and volcanic/pyroclastic glasses, and hydrothermal evaporate silicates on the surface of asteroids and Mars.

Hypervelocity impacts are ubiquitous on Mars and asteroids, and inherent in the impact process is the production of ejecta, melts, breccias, and glasses, and when impacts are large enough, hydrothermal systems. Impact craters, their melt products and induced hydrothermal systems could be among the youngest and most exploitable habitats for life on Mars (e.g., Izawa et al., 2010; Osinski et al., 2013; Sapers et al., 2015). A fruitful approach to continuing the search for evidence of life on Mars is to focus on habitats and

microhabitats associated with impact craters, specifically in the glasses and hydrothermal deposits produced by hypervelocity impacts as they are plausibly the youngest and perhaps the richest sites on Mars within which primitive life may have thrived, or plausibly began, and hold potential to preserve evidence thereof (Schultz et al., 2014).

The spectra of impact glasses can, and do, exhibit a number of unique spectral features which are related to the extreme pressures and fast quench rates these materials experience (e.g., Velde and Couty, 1987; Williams and Jeanloz, 1988; Williams and Jeanloz, 1989; Williams et al., 1993; Agarwal and Tomozawa, 1997). Impact deposits a huge amount of energy into a target in an instant and produced unique impactites (e.g., diaplectic glasses) and a variety of melt products giving evidence of various levels of shock. We are most interested in the ability to differentiate between shock and melt-produced silicate glasses, volcanic and pyroclastic effusive silicate glasses and hydrothermal evaporate silicates, and differentiating between these materials and the basaltic/palagonitic background rocks and dust of Mars. High levels of shock and high confining pressures (i.e., melts produced under pressure and quickly quenched via rapid depressurization), produce a number of spectral features we can exploit to robustly identify these materials when we also have contextual geomorphologic evidence.

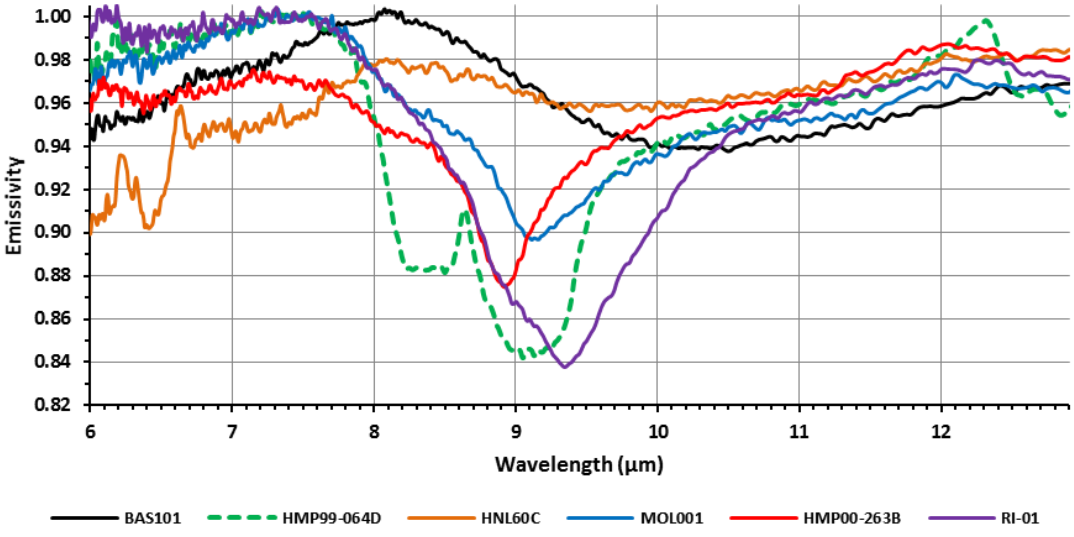

Figure 1-2: Infrared Emission Spectra within our window of interest for Mars. BAS101 is a Hawaiian basaltic glass, HMP99-064D is a pure quartz from the Haughton Crater,

HNL60C is a pyroxenite impact glass from the Lonar Crater, MOL001 is a Moldavite Tektite, HMP00-263B is an impact glass from the Haughton Crater and RI-01 is an impact glass from the Ries Crater. These six sample are indicative of the changes in the fundamental stretching vibrational mode of Si-O which we can use to identify like assemblages on asteroids and other planets.

Firstly, with application of compressive stress, the networks of silica tetrahedra in glasses exhibit changes in short-range ordering (i.e., polymerization, or, ordering about specific bridging oxygen bond angles), then with increasing pressure silica tetrahedra distort and new, high-order coordination environments are a created (e.g., Williams et al., 1993; Closman and Williams, 1995). In-situ high-pressure diamond anvil cell experiments using IR spectroscopy (e.g., Williams and Jeanloz, 1988; Koike and Tomozawa, 2007) have demonstrated changes in the IR spectra of silicates which are indicative of both changes in short-range order and the creation of higher-order Si coordination environments, but for remote sensing, and the IR emission spectra we can collect now, only the order changes produce spectral changes which we can apply.

The UV-Vis-NIR spectra of impactites also differ from that of their non-impact related brethren, but unfortunately, NIR spectra of impactites are of little use for differentiating between glasses, evaporates, or the background rocks of Mars or asteroids. UV-Vis-NIR spectra, simply are too similar to one another and do not vary in albedo or slope in any systematic way.

IR spectra are useful, and have been exploited in attempts to identify mineralogy, and impactites on Mars. Ramsey and Christensen (1998) showed linear unmixing, or curve deconvolution/curve matching to be a viable technique in the IR, to a first approximation, and a number of researchers have exploited it in an attempt to suggest mineralogy on Mars. Their collective works have resulted in disagreement (e.g., Bandfield 2000; McSween et al., 2003; Rogers and Christensen, 2007; Cannon and Mustard, 2015). This arises as using a set of silicates to unmix an assemblage of silicates will result in the answer being silicates, but different researchers, using the same set of silicates to unmix the same Martian spectra, and different sets of silicates in their models, to unmix the

same Martian spectra, have come to different conclusions (see McSween et al., 2003, and references therein). In light of this, we explored the use of an empirical set of metrics derived from IR emission spectra and we have found that, with robust geomorphological context (e.g. careful study of HiRISE images), we can be robust in our mineralogical identifications using IR emission spectra.

In Chapter 4, we are exploring the effects of grain size on the spectra of pyroxene, olivine and basaltic rocks. These are the most common analogues for the surface mineralogy of asteroids and the basaltic surface of the neighboring rocky planets. UV-Vis-NIR reflectance spectroscopy is the most powerful tool we have to explore the mineralogy of these bodies, and grain size, second to mineralogy, is the target property that most affects the albedo, absorption feature depth/area and absorption wavelength positions of reflectance spectra. To our knowledge, this is the first study of grains size affects in these materials to address the changes associated with grains between the grain size of course sand, ~ 1 mm in diameter, and rock. For this study, 33 finely confined grain size fractions from <10 μm through 4.75 mm were produced of an orthopyroxene and a basalt. 5 size fractions from <45 to 1000 μm were produced of olivine and the same pyroxene and basalt.

Grain size, in small size fractions below ~ 1mm has been thoroughly studied and the enhanced scattering, which most alters spectra at small grain size, and band saturation which most alter the spectra of materials with large grain sizes are well understood phenomena (.e.g., Pieters, 1983; Hiroi and Pieters, 1994; Lucey, 1998). Not well understood is, at what grain sizes do these optical phenomena make mineralogical identification, and identification of grain size when observing remote objects, unreliable?

Our results follow pre-established general patterns where with decreasing grain size albedo increases and band depth decreases (e.g., Adams and Filice, 1967; Pieters, 1983). When grain size is progressively increased from small to large, albedo will be first brighten, then decrease with increasing grain size before essentially flat lining when band saturation is dominating and reflectance sits very near zero (note, it does not actually reach zero). Band depth will initially be shallow with progressively increasing grain size

from the smallest fractions, than it will deepen to a maximum in intermediate grains sizes before decreasing again with further grain size increase. At points both among the smallest grains sizes, and amount the largest, the effects of enhanced scatter and band saturation will be so deleterious we can no longer robustly identify the minerals or assess their grain size. Excepting the study of Mustard and Hays (1997), which explored the spectra of samples in 5 µm size intervals from 5 to 25 µm, ours is the first study to use such a tightly-confined range of grain size fractions and to demonstrate at what grain sizes empirical measures break down.

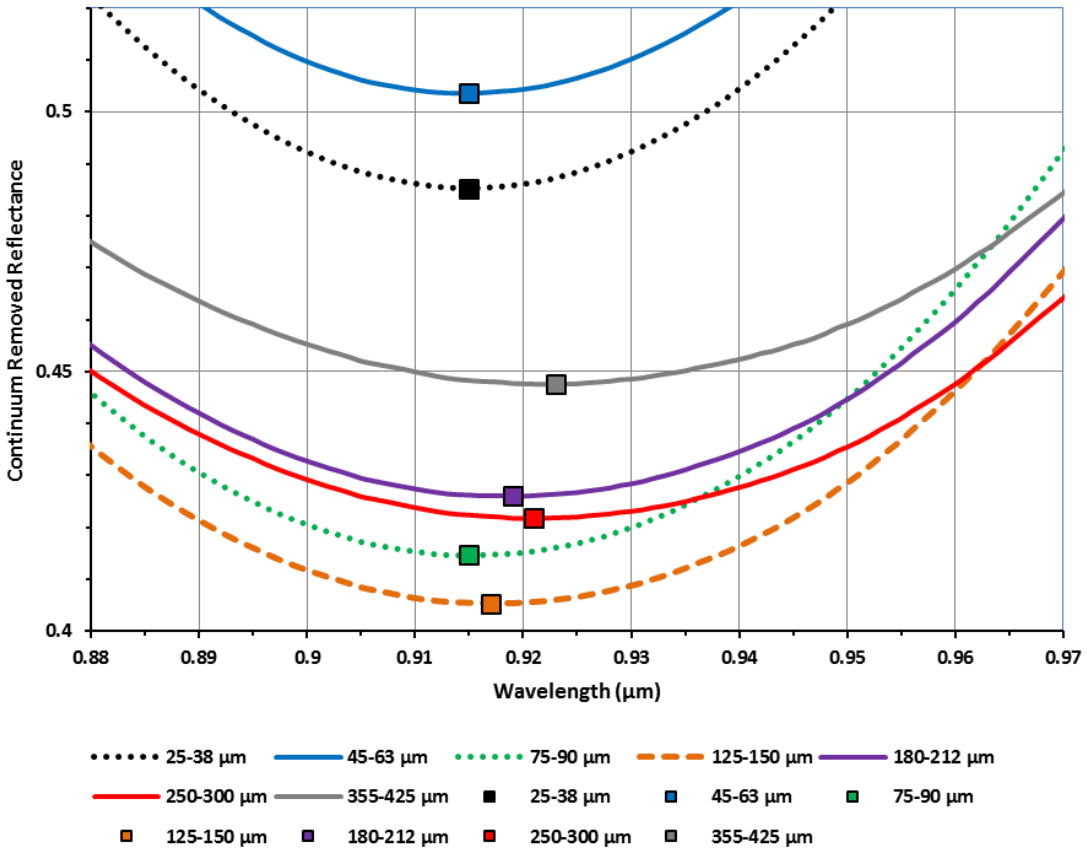

Figure 1-3: A depiction of the variation in the Band I absorption centre of a series of pyroxene grain size splits, which can be used, referencing other derived metrics (as depicted in Figure 1-4) to discern the grain size of a material under investigation. Solid

squares denote the derived centres for each grain size separate.

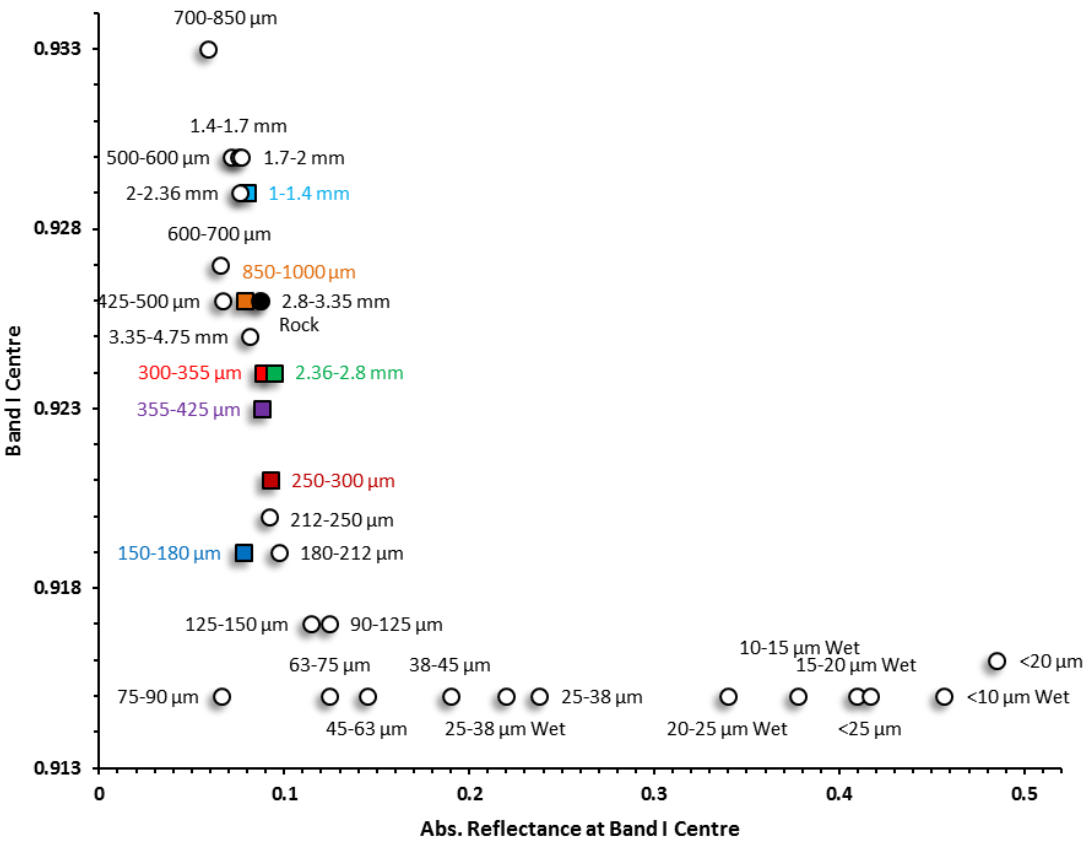

Figure 1-4: Band I centre, of the grain size separates, versus the measured absolute reflectance value at the same point in the spectrum before the Band was centred and contrast stretched. Figure 1-4 is one of many empirical metric-versus-metric comparison can be used to discern grain size of a target under investigation, as well as assess our confidence level in a particular mineralogical identification.

1.1 References

Adams, J.B., Filice, A.L., 1967. Spectral reflectance 0.4 to 2.0 microns of silicate rock powders. Journal of Geophysical Research 72, 5705-5715.

Agarwal, A., and Tomozawa, M., 1997. Correlation of silica glass properties with infrared spectra. Journal of Non-Crystalline Solids 209, 166-174.

Bandfield J.L., Hamilton V.E., and Christensen P.R., 2000. A global view of Martian surface compositions from MGS-TES. Science 287, 1626-1630.

Cannon, K.M., and Mustard, J.F., 2015. Preserved glass-rich impactites on Mars. Geology G36953.1.

Closmann, C., and Williams, Q., 1995. In-situ spectroscopic investigations of high-pressure hydrated (Mg,Fe)SiO3 glasses: OH vibrations as a probe of glass structure. American Mineralogist 80, 201-212.

Hiroi, T., and Pieters, C.M., 1994. Estimation of grains sizes and mixing ratios of fine powder mixtures of common geologic materials. Journal of Geophysical Research 99, No. E5, 10867-10879.

Hapke, B., 1981. Bidirectional reflectance spectroscopy: 1. Theory. Journal of Geophysical Research 86, No. B4, 3039-3054.

Hapke, B. and Wells, E., 1981. Bidirectional reflectance spectroscopy: 2. Experiments and observations. Journal of Geophysical Research 86, No. B4, 3055-3060.

Hapke, B., 1984. Bidirectional reflectance spectroscopy: 3. Correction for macroscopic roughness. Icarus 59, 41-59.

Hapke, B., 1986. Bidirectional Reflectance Spectroscopy: 4. The extinction coefficient and the opposition effect. Icarus 67, 264-280.

Hapke, B., 2002. Bidirectional reflectance spectroscopy: 5. The coherent backscatter opposition effect and anisotropic scattering. Icarus 157, 523-534.

Hapke, B., 2008. Bidirectional reflectance spectroscopy: 6. Effects of porosity. Icarus 195, 918-926.

Izawa, M.R.M., Banerjee, N.R., Flemming, R.L., Bridge, N.J., and Schultz, C., 2010. Basaltic glass as a habitat for microbial life: Implications for astrobiology and planetary exploration. Planetary and Space Science, 58, 583-591.

Koike, A., and Tomozawa, M., 2007. IR investigation of density changes of silica glass and soda-lime silicate glass caused by microhardness indentation. Journal of Non-Crystalline Solids 353, 2318-2327.

Lucey, P.G., 1998. Model near-infrared optical constants of olivine and pyroxene as a function of iron content. Journal of Geophysical Research 103, No. E1, 1703-1713.

McSween, H.Y. Jr., Grove, T.L., and Wyatt, M.B., 2003. Constraints on the composition and petrogenesis of the Martian crust. Journal of Geophysical Research 108, No. E12, 9-1-19.

Moersch, J. E., and Christensen, P. R., 1995. Thermal emission from particle surfaces: A comparison of scattering models with measured spectra. Journal of Geophysical Research 100, No. E4, 7465-7477.

Mustard, J.F., Hays, J.E., 1997. Effects of hyperfine particles on reflectance spectra from 0.3 to 25 μm. Icarus 125, 145-163.

Osinski, G.R., Tornabene, L.L., Banerjee, N.R., Cockell, C.S., Flemming, R., Izawa, M.R.M., McCutcheon, J., Parnell, J., Preston, L.J., Pickersgill, A.E., Pontefract, A., Sapers, H.M., and, Southam, G.,2013. Impact-generated hydrothermal systems on Earth and Mars. Icarus 244, 347-363.

Pieters, C.M., 1983. Strength of mineral absorption features in the transmitted component of near-infrared reflected light: First results from RELAB. Journal of Geophysical Research 88, 9534-9544.

Ramsey, M. S., and Christensen, P.R., 1998. Mineral abundance determination: Quantitative deconvolution of thermal emission spectra. Journal of Geophysical Research 103, No. B1, 577-596.

Rogers, A.D., and Christensen, P.R., 2007. Surface mineralogy of the Martian low-albedo regions from MGS-TES data: Implications for upper crustal evolution and surface alteration. Journal of Geophysical Research 112, E01003.

Sapers, H.M., Osinski, G.R., Buitenhuis, E., Banerjee, N.R., Flemming, R.L., Hainge, J., and Bain, S., 2015. Impact-generated hydrothermal activity beyond the Ries crater rim. LPSCXLVI, abstract #2917.

Schultz, P.H., Harris, R.S., Clemett, S.J., Thomas-Keptra, K.L., and Zarte, N., 2014. Preserved flora and organics in impact melt breccias. Geology 42, 515-518.

Velde, B., and Couty, R., 1987. High-pressure infrared spectra of silica glass and quartz. Journal of Non-Crystalline Solids 94, 238-250.

Williams, Q., and Jeanloz, R., 1988. Spectroscopic evidence for pressure-induced coordination changes in silicate glasses and melts. Science 239, No. 4842, 902-905.

Williams, Q., and Jeanloz, R., 1989. Static Amorphization of Anorthite at 300K and comparison with diaplectic glass. Letters to Nature 388, 413-415.

Williams, Q., Hemley, R.J., Kruger, M.B., and Jeanloz, R., 1993. High-pressure infrared spectra of α-quartz, coesite, Stishovite and silica glass. Journal of Geophysical Research 98, No. B12, 22157-22170.

Chapter 2

2 Fitting the curve in Excel®: Systematic curve fitting of laboratory and remotely sensed planetary spectra

2.1 Introduction

Spectroscopy is the principal – and sometimes the only – technique that can provide information regarding the compositional and mineralogical make up of planetary bodies. Notable examples include the linkage between the ordinary chondrites and the S-type asteroids cemented by the Itokawa – Hayabusa encounter and verified by sample return (Binzel et al., 2001; Abe et al., 2006; Abell et al., 2007; Nakamura et al., 2011); the link between the Howardite-Eucrite-Diogenite (HED) meteorites and asteroid 4-Vesta (McCord et al., 1970; Gaffey et al., 1982; Gaffey, 1983, 1997), confirmation of which was provided by the Vesta-Dawn encounter (McSween et al., 2013); and the soon to fly OSIRIS-REx sample return mission which is expected to confirm the link between the carbonaceous meteorites and the missions target, B-type asteroid Bennu [1999 RQ36] (Clark et al., 2011; Hergenrother et al., 2013). Given the robustness of the connection between observational asteroid spectra and their analogous meteorites confirmed thus far, it is also rather likely that the proposed linkages such as those suggested for the Chelyabinsk meteorite and Baptistina asteroid family by Reddy et al. (2014), the mesosiderites and the Maria asteroid family suggested by Fieber-Beyer et al. (2011), and the relationship between 6 Hebe and the H-type ordinary chondrites suggested by Gaffey and Gilbert (1998), are similarly as robust. We use spectroscopy to remotely probe a wide variety of solar system bodies that we cannot visit, primarily using reflectance spectroscopy in the ultraviolet through near-infrared wavelengths and emission spectroscopy in the mid through far-infrared. To discern mineralogy using spectroscopy we attempt to match the unknown with known spectra from spectral libraries or diagnostic spectral features and to do this we must curve fit the collected spectra.

Despite all of the obvious successes, and a raft of literature on the subject, there is what can be best described as a communication problem within the planetary science spectroscopic community. The primary metrics one needs to derive and communicate are the positions of the maxima/minima/centres for absorption bands and secondarily the band areas/Band-Area-Ratios (BAR) and band depths which are often included in manuscripts, but often presented with no reference to the measurement methods or the constraints on the curve fits used to derive them. If the measurement methods are mentioned, for those new to the field, it can be confusing what is meant when an author refers to the application of straight-line or curved-line continua, a method of apparent continuum removal or the centring of absorption bands. Often causing further confusion is the use of the word modelling to describe a number of analytical methods which meet a broad definition of the word “modelling,” though most often, mathematical functions ("curves") are being fit to spectra where functions are not representative of the physical processes responsible for the absorptions, as in reflectance, or apparent continuum removed reflectance spectra. While these methods are technically modelling, the fitting of curves, e.g., curve deconvolution using Gaussians to raw or apparent continuum removed reflectance spectra, cannot model the physical processes which are responsible for the creation of spectral absorptions in energy space and should aptly be referred to as Gaussian fitting rather than modelling.

When attempting to describe an object with spectral data, researchers should define the curve fitting algorithms and the fitting parameters used, and the constraints and uncertainties of the fits. We need to ensure that useful data is being disseminated and derived metrics are mathematically defined for repeatability and validation.

Metrics should be derived from spectra via a process of measurement of absorption band positions, i.e., minima, maxima and centres, as well as absorptions depths and when applicable, areas, skew, and so on, using a standardized methodology for curve fitting that is entirely transparent and fully repeatable. In this work we have assembled as many of the spectral analysis and deconvolution functions we could envisage that would be useful, and those that could be useful for furthering understanding and interpretation of,

and extraction of information from, spectral data, as a set of what should be universally applicable functions with suggestions for implementation to curve fit spectra.

The included supplementary materials in Appendices 2A and 2B provide a basic guide to robust and reliable methods for empirical curve fitting that, first, demonstrate functions in a manner that is comprehensible to those who may be new to spectroscopy and may be having difficulty visualizing what is meant by continua, centres and the like, as well as demonstrating the mathematics used to produce curve fits in a simplified format. Secondly, we believe the examples in the appendices are good illustrations of the necessity for the dissemination of more completely defined parameterized data to the community.

The concept of curve fitting spectra (also often referred to as spectral deconvolution) is not new, and continues to evolve (e.g., Doetsch, 1928; Lonn, 1932; Kaper, 1966; Clark and Roush, 1984; Sunshine et al., 1988; van der Meer, 2004; Clenet et al., 2011; Parente et al., 2013). Curve fitting is a necessity as all measured spectroscopic data are a series of data points employing x and y coordinates for localization in wavelength or energy space. One has to remember that, while the actual waveform is analog, and spectra are often visually represented by a solid line, collected spectra are not lines or curves, rather, they are a collection of discrete points which subsample the analog waveform. As such, we fit curves representative of the actual waveform through the measured discrete points, along which any number of corresponding x and y points can be interpolated to either calculate a wavelength or wavenumber value for the absorption band minimum/maximum/centre, or discern which measured point in the existing data is closest to what would be the perfectly resolved interpolated minimum/maximum/centre.

The fitting of mathematical functions to a spectrum is a method that allows the derivation of a set of metrics that are used to describe properties of a spectrum and which can be used to decipher the mineralogy or mineral assemblage responsible for the features of a particular spectrum. This system needs to be transparent, repeatable, and ideally easy to implement and understand, such that the derivation of the reported metrics is eminently clear. Spectra obtained from planetary surfaces do not have the set of constrained

variables that prepared laboratory samples have. In the laboratory, grain size, packing (and to an extent porosity), temperature, phase angle (i.e., viewing geometry) and signal-to-noise-ratio can be controlled, and mineral mixtures can be precisely constrained or understood. In addition, given the ever present complications caused by processes operating on planetary surfaces (such as space weathering), several of the metrics that might allow one to curve match one spectrum with another such as slope, band depth and albedo can differ significantly between planetary surfaces and laboratory spectra for even small differences in mineral or mixture composition (e.g., Gaffey, 2010). The most important metrics are arguably the band minima/maxima and the centre as they are the most sensitive to mineralogy and the least sensitive to the spectral effects of grain size, packing, temperature and the poorly constrained effects of space weathering one must deal with for atmosphere-less bodies (Gaffey, 2008).

2.2 Curve Fitting Methodologies

This work is focused on the curve fitting of ultraviolet through near-infrared reflectance spectra of minerals, asteroids and planetary surfaces for the purpose of interpreting remote-sensing spectra of planetary bodies – though many of the methodological points are equally applicable to any other spectrum or curve one might want to fit or model.

In order to successfully curve-fit spectra of solid minerals, a certain amount of a priori knowledge is required of spectroscopy, mineralogy, and the basics of curve fitting mathematics. In order to understand how to effectively curve fit spectra it is important to understand the drivers for spectroscopic absorptions and be familiar with the lexicon. One also needs to understand the limitations of the mathematics involved.

Researchers use varying combinations of techniques to derive qualitative or quantitative information from spectra, e.g., curve matching, curve deconvolution, and empirical curve fitting. Each technique has strengths and weaknesses, and an understanding of the application of one or more techniques requires precise knowledge of the spectroscopic lexicon and the metrics the various techniques provide.

To understand the majority of the spectroscopic absorptions occurring in ultraviolet through infrared reflectance spectra of planetary and asteroidal solid surfaces, one operates from the hypothesis that all absorptions occur at a specific central maximum or minimum in energy space, the probability of absorption of a photon, which translates into the shape of an absorption feature (or band) will follow a normal symmetric distribution in energy space about its centre, and the 'wings' on either side of the absorption extend to infinity. If a band does not conform, i.e., it is not symmetric, the asymmetry must be due to another contributing absorption, either from the same material or another constituent in the assemblage, such as a series of partially or fully overlapping absorptions which appear as though they are one asymmetric absorption, a continuum that superimposes an asymmetry on a symmetric absorption, or the absorption band may be optically saturated, which can make an absorption appear to be flattening across its minimum or otherwise affect the apparent symmetry of a band.

Curve matching is a catch-all term for a number of practices where one is attempting to compare one spectrum with another, mostly visually. The most common application uses a technique where one employs a library of sample spectra, taken from laboratory data of usually pristine, monomineralic, prepared (i.e., powdered, sieved, washed, etc.) samples which are combined mathematically in a linear fashion (often called spectral deconvolution, linear deconvolution and/or quantitative deconvolution, not to be confused with curve deconvolution), e.g., a0.5 + b0.25 + c0.25 = x, to produce a facsimile spectrum which closely matches the entire spectrum of an unknown sample. The facsimile spectrum is overlain atop the observed spectrum of an unknown sample or surface, and modified by either varying amounts of individual contributors, e.g., a0.25 + b0.5 + c0.25 = x, and or adding or subtracting more contributors, e.g., a0.25 + b0.25 + c0.15 + d0.1 + e0.05 +f0.05 + g0.05 + h0.05 + i0.03 + j0.02 = x, until an acceptable match with the observed spectrum is produced which appears analogous to the person performing the curve matching or until some threshold residual for the facsimile versus observed spectrum is met (e.g., McSween et al., 2003, and references therein). As a first pass, the technique can be illustrative if one has very little context for the spectrum under investigation but it requires a spectral library and algorithms (e.g., Ramsey and

Christensen, 1998) to produce and fit the deconvolved spectrum/facsimile to some residual or human input to suggest or rule out contributors, but it does not capture the fact that spectra of mineral assemblages rarely, if ever, mix linearly (Singer, 1981; Clark, 1999; Kraft et al., 2003; Berger et al., 2015). As a technique it also may ignore other factors that can contribute to altering a particular mineral, or an assemblage of mineral spectra, such as, grain size, porosity, texture or roughness, grain packing, temperature, phase angle, atmosphere, adsorbed species, spatial resolution, spectral resolution, distance, the probable effects of space weathering, and so on. This is problematic as libraries of spectra that explore alteration of spectra by factors like phase angle and grain size do not exist in any quantity. Curve matching can also refer to searching data bases of spectra for samples with absorptions/curves/slopes that are similar to a sample's or simply plotting multiple spectra on the same chart to compare one spectrum with another and noting plausible similarities or suggesting similarities with vertical lines to draw the eye. No matter the methodology, as a set of techniques to constrain actual mineralogy, curve matching often fails to provide robust quantitative information (e.g., Gaffey, 2008, 2010). This simple technique can be useful for initially constraining possible spectral contributions, which can then optimize subsequent more rigorous approaches.

Curve deconvolution/Gaussian fit optimization is a quantitative approach based on the mathematics of spectral absorptions using Gaussian fitting for solid material spectra. It correctly operates under the supposition that the majority of absorptions are symmetric in energy space, and any band asymmetries are contributions from an adjacent absorption(s). Importantly, this technique can fail to converge or provide realistic results if some initial constraints are not placed on the fitting algorithms, i.e., approximate starting centre wavelengths, and the number of absorptions to use for a particular fit. It may also fail if more than a single monomineralic sample spectrum is fed into the deconvolution algorithm and initial parameterization does not take this into account, though researchers are presently working on methodologies to remove the need for initial fixed parameter sets (e.g., Makarewicz et al., 2009, Clenet et al., 2011; Buz and Ehlmann, 2014). The most widely used and freely available deconvolution software package used in planetary science is the Modified Gaussian Model (MGM) suite of scripts for

MATLAB™ produced by Sunshine et al. (1988, 1989, 1990, 2004) and Sunshine and Pieters (1993). If applied correctly, curve deconvolution (more aptly called Gaussian fit optimization) provides a quantitative approach, but 'correct' application requires the spectrum under investigation to be reasonably well known to constrain the initial starting parameters, e.g., one must constrain an MGM analyses by directing MGM to optimize the fit of two Gaussians for the first and one Gaussian for the second of the two large near-infrared absorptions present in pyroxene. In Sunshine et al. (1989) and Sunshine and Pieters (1998), the authors address the problems that arise with a set of unconstrained variables, noting that the number of absorptions and wavelengths for the band centres of those absorptions must be in the initial parameter set, and should they not be provided because the sample mineralogy is unknown, there are simply too many unconstrained variables and any curve deconvolution/Gaussian fit optimization techniques will not produce nonunique solutions. Curve deconvolution as a technique has real merit and may be the best technique for reliably identifying a shoulder on an absorption (i.e., a smaller absorption band visible on the wing of a larger absorption band).

It should also be noted that Gallie et al. (2008) found that for the purposes of fitting, Gaussians in wavenumber, i.e., energy space, and those in wavelength space are numerically equivalent. So, if one is attempting to fit a series of Gaussians, it matters little whether one is working in energy space or wavelength space, though there will always be an issue of repeatability as automated fit optimization as performed by MGM and the methods demonstrated in the appendices are exceedingly unlikely to produce the same grouping of Gaussians twice, producing unrepeatable fits (see Appendix 2A). One also has to be aware that while MGM has the word "Model" in its name, it is not in normal practice modelling absorptions, as the standard procedure is to remove straight line apparent continua in an energy space converted reflectance spectrum which has already had its imposed continuum removed.

An alternative to curve deconvolution is empirical curve fitting, the technique used and advocated for herein. In this method, spectra are curve fit systematically using polynomials fit about the minima or centres of absorptions to derive said metrics, and

then the fit minima/centres can be compared with similar curve fits performed using laboratory spectra of calibrated standards and calibrated mixtures. The methodology uses a simple set of rules for curve fitting where one does not need to worry about unconstrained/over-constrained/under-constrained variables, fit residuals or the intricacies of the application of Gaussian fit optimization/curve deconvolution. In its simplest application, such as when fitting hydrated phyllosilicates hydration features for comparison with Martian remote sensing spectra, after converting Martian intensity-over-flux measures (I/F) to reflectance spectra as per Bakker et al. (2014), the user would do no more than fit absorption minima/maxima and provide those numbers with their manuscript as per the examples in Appendix 2A. Ideally, full fits, including spectra would be included as supplementary material with any published manuscript so no questions arise later about what was done when the spectra were curve fit.

For decades, a number of researchers and research groups have advocated for this methodology (e.g., Kaper, 1966; Gaffey, 1976, 2010; Clark, 1980, 1981, 1999; Farr et al., 1980; McCord et al., 1981; Singer, 1981; Clark and Roush, 1984; Cloutis et al., 1986; Cloutis and Gaffey 1991; Gaffey et al., 1993, 2002; Gaffey and Gilbert 1998; Gaffey and McCord 1978, 1979; Clark et al., 2003; van der Meer, 2004; Storm et al., 2007; Burbine et al., 2009; van Ruitenbeek et al., 2014), largely because it is easy to apply and reproduce when the fitting procedure is defined. Researchers often use proprietary routines that perform very similar or identical functions to those we have provided herein, and/or the SPECtrum Processing Routine software (SPECPR). For the purposes of empirically fitting spectra, we are interested in applying and performing operations that are identical to the straight line apparent continuum removal of SPECPR and Tetracorder, and the polynomial fitting functions of SPECPR (Clark, 1980, 1993; Clark et al., 2003, Livo and Clark, 2014; software available from the USGS). SPECPR and Tetracorder are freely available as are instruction manuals, but the software can be extremely cumbersome to use.

2.3 Empirical Curve Fitting

Empirical curve fitting relies on a series of calculations used to derive a set of metrics from a spectrum that can be used for characterization and comparison (e.g., Singer, 1981; Clark and Roush, 1984; Cloutis and Gaffey, 1986). As noted, when deriving these metrics, a priori knowledge of the physical processes that produce spectroscopic absorptions is ideal, but not a requisite. A central guiding principle is that all absorptions are distributed about a specific central point in energy space and that the absorption feature, or band, will follow a Gaussian distribution of energies around that centre (in solids), and the 'wings' on either side of the absorption go 'to infinity' – that is, they extend with ever decreasing intensity to higher and lower energy levels than the band centre. If a band does not conform, i.e., it is not symmetric, the asymmetry must be due to another contributing absorption, either from the same material, another constituent in the assemblage under investigation, or a continuum that superimposes asymmetry on a symmetric absorption, or band saturation (Clark and Roush, 1984; Lucey and Clark, 1985.) The symmetry of an absorption as a central tenet applies to spectra in energy space but not to spectra in wavelength where the majority of the metrics we are attempting to derive originate, so when empirically curve fitting we can somewhat ignore the drivers for the absorptions we are fitting.

In order to derive some meaning from a single band, or set of bands, some knowledge of the possible structures contributing to the absorption is required but we are not attempting to account for everything producing the spectrum when deriving metrics empirically. For instance, if one were trying to derive a set of metrics from the laboratory spectrum of the pyroxene sample shown in Figures 2-1 thru 2-4, knowing that pyroxene has absorptions due to different electronic interactions with Fe2+ in the M1 and M2 octahedral sites, producing the absorption feature referred to as Band I, that is a combination of two absorptions at ~1 and 1.15 μm while Band II at ~ 2 μm is a singular feature, is

advantageous, but not a requisite (Cloutis et al., 1986; Burns, 1993; Klima et al., 2007, 2011).

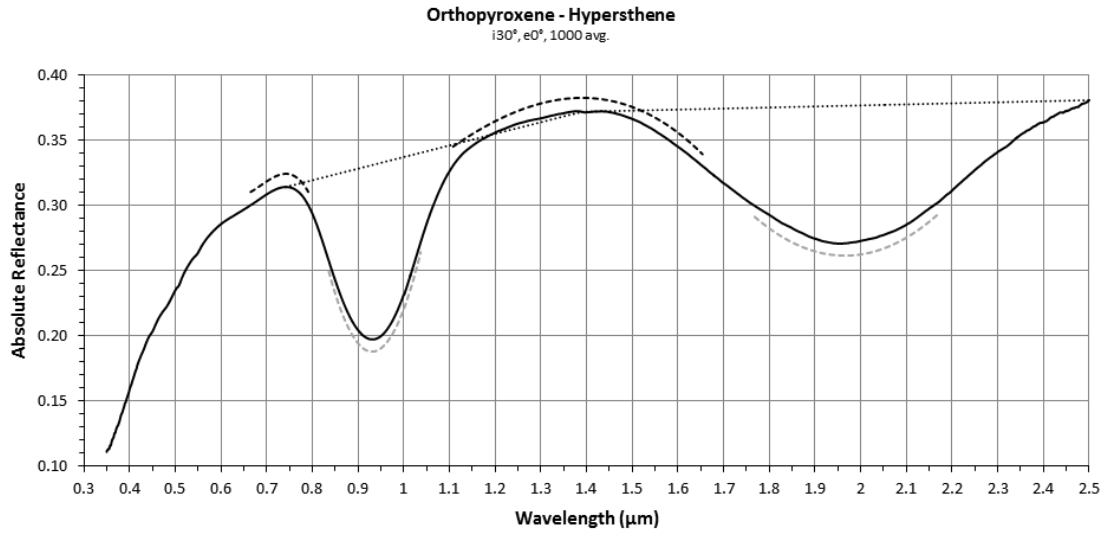

Figure 2-1: The NIR spectrum of the pyroxene, solid black line, with black offset (+0.01) dashed lines depicting the 3rd order polynomials fits used to derive the straight line continuum pin points, grey offset (-0.01) dashed lines depicting the 3rd order polynomial fits used to derive band minima and black dotted lines depicting the straight line apparent continua that will be used to isolate the features of interest for band centring and area derivation.

Given the limitations of the curve fitting techniques described herein (or any other techniques, see Appendix 2A and 2B), how one would logically go about deriving absorption band minima, centres, depths and areas would be driven by the directives for application and limitations of the method/technique, a priori knowledge of the causes and number of absorption features and how a set of derived metrics would compare with those gathered from pre-existing research. For example, while the second contributing absorption of Band I in the pyroxene example spectrum is obvious, its exact position and contribution to the shape and area of Band I is not as important as understanding that it should be included in centring, depth and area determination. This is because the directive in empirical curve fitting is to include its contribution by fitting straight line

apparent continua to the point of band extinction (the point of maximum reflectance between two adjacent absorption band minima), therefore it is included in the metrics one is producing now just as it has been in metrics produced in the past by other researchers employing the same techniques.

Despite methodological differences, from all spectra one can derive the main metrics of an absorption band or feature, i.e., the minimum, band centre, band depth and band area; and other less critical metrics such as measures of asymmetry, i.e., skew, kurtosis; measures of width, i.e., full width at half maximum (FWHM), and area, that should have universally applicable definitions, but often do not. Below, we provide definitions of the most important terms.

Band Minima: Denotes the wavelength or energy of the position of lowest reflectance over a specified wavelength interval, derived from a spectrum that has not had its imposed continuum removed. There should always be a definition of the procedure for measuring the band minimum which includes a description of any modifications made to the spectra before the minima are measured, e.g., breaks in the spectra at the detector junctions that may have been removed by application of a particular function, the reflectance spectra was fit as delivered by the spectrometer, the spectrum was offset or normalized, etcetera.

Band Centre: Denotes the wavelength position of lowest reflectance over a specified interval after some kind of continuum removal for a band has been performed; e.g., apparent continuum removal by division, i.e., y divided by the straight or curved line apparent continuum value for the same x value.

Band Depth: Is defined in a number of ways, but it is always the depth of an absorption at the derived wavelength minimum or centre value relative to a defined point above that value. Most often, band depth is the length of a vertical line expressed in percent reflectance, which extends downward tangentially from 100% reflectance or unity, to the derived centre or minima (e.g., Clark and Roush, 1984; Clark, 1999). Band depth is

normally expressed in percent reflectance, even in cases where bands have been contrast stretched by imposed continuum removal and the centring process of further apparent continuum removal.

Band Area: Is a measure of the area of a band which can be derived in a number of different, but complementary, methods, and expressed as a dimensionless value which will always require some definition based on the function(s) used for area derivation (see Appendices 2A and 2B). Band area should ideally be a measure of the area of the absorption bound by some form of continuum removal which has isolated the absorption, and not the area of a Gaussian or other curve used for fitting or modelling. If the band areas calculated and shared in a manuscript are based on the areas of a number of fit Gaussians, the definitions provided in the text for band areas must include a description of the derivation of the fit curves which specifically notes how the full area was calculated.

All of the possible derived metrics are of potential importance, but we consider band minima the requisite principal metric and the focus of the methodology we are espousing. We would suggest band centre, depth and area follow in importance and form a set of four primary metrics that should be referred to when discussing spectra, and those for which the methodologies for derivation should be robust, absolutely reproducible, easy to understand and completely transparent (i.e., not buried in the 'black box' of proprietary, complex, or expensive software).

2.3.1 Band Minima

The minimum wavelength position for any absorption or band minima is the most universally applicable metric as it is measured from existing spectra unaltered by removal of an imposed or apparent continuum. We advocate for the use of 3rd order polynomial functions to derive the band minima of the spectral absorptions of interest because it is optimally suited for a symmetric curve and will not over-fit the data. Figure 2-1 is an example of a laboratory spectrum and, as such, it has an extremely high spectral

resolution and high signal-to-noise ratio, so if one picked the lowest recorded reflectance value within this absorption, it may well be the actual minima. However, if the spectrum is of low spectral resolution, such as many observational data for solar system bodies, the real minimum value may well fall between two measured values. In order to compare the high resolution data with the low resolution data in a tenable manner, we curve fit systematically using the same methodology for both sets of spectra such that our comparisons are as robust as possible. The minima and/or centre can then be reported in two different manners, either as the actual measured minimum reflectance value or the minimum reflectance that the fit polynomial subtends. Though we advocate for the exclusive use of the nearest actual measured value, if it is to be called a minima or centre, one needs to be sure when citing previous work, whether the minima or centre reported is for an actual measured value nearest the theoretical fit minimum, or if it is an interpolated value.

The use of a polynomial and the order of the polynomial used are exceedingly important. A polynomial is used as it is a simple function and given a fixed set of coefficients, will always return a single solution. When discussing modelling (see Appendix 2A and 2B) one encounters statistical measures of goodness of fit, fit quality, or measures of fit error. Fitting a polynomial is not modelling as we would define it, and we would suggest that it is not necessary to aim for a specific measure of fit quality. Rather, when curve fitting a spectrum in a repeatable, robust and transparent manner using a function that has a single solution with no free variables, the problem of fit quality is ameliorated when the polynomial function and full fit are reported and/or the requisite spectrum and listing of nodes are included so it can be reproduced. If one strays from the caveats regarding asymmetries about the minimum/maximum or centre wavelength noted in the appendices, they may run into a problem, but as long as the process remains transparent, another researcher can revisit the fits.

We would suggest, even for the highest resolution laboratory data, cubic or 3rd order polynomials should be used exclusively. Other orders of polynomials have been supplied in the appendices for other purposes, but their use should be limited to rare

circumstances.

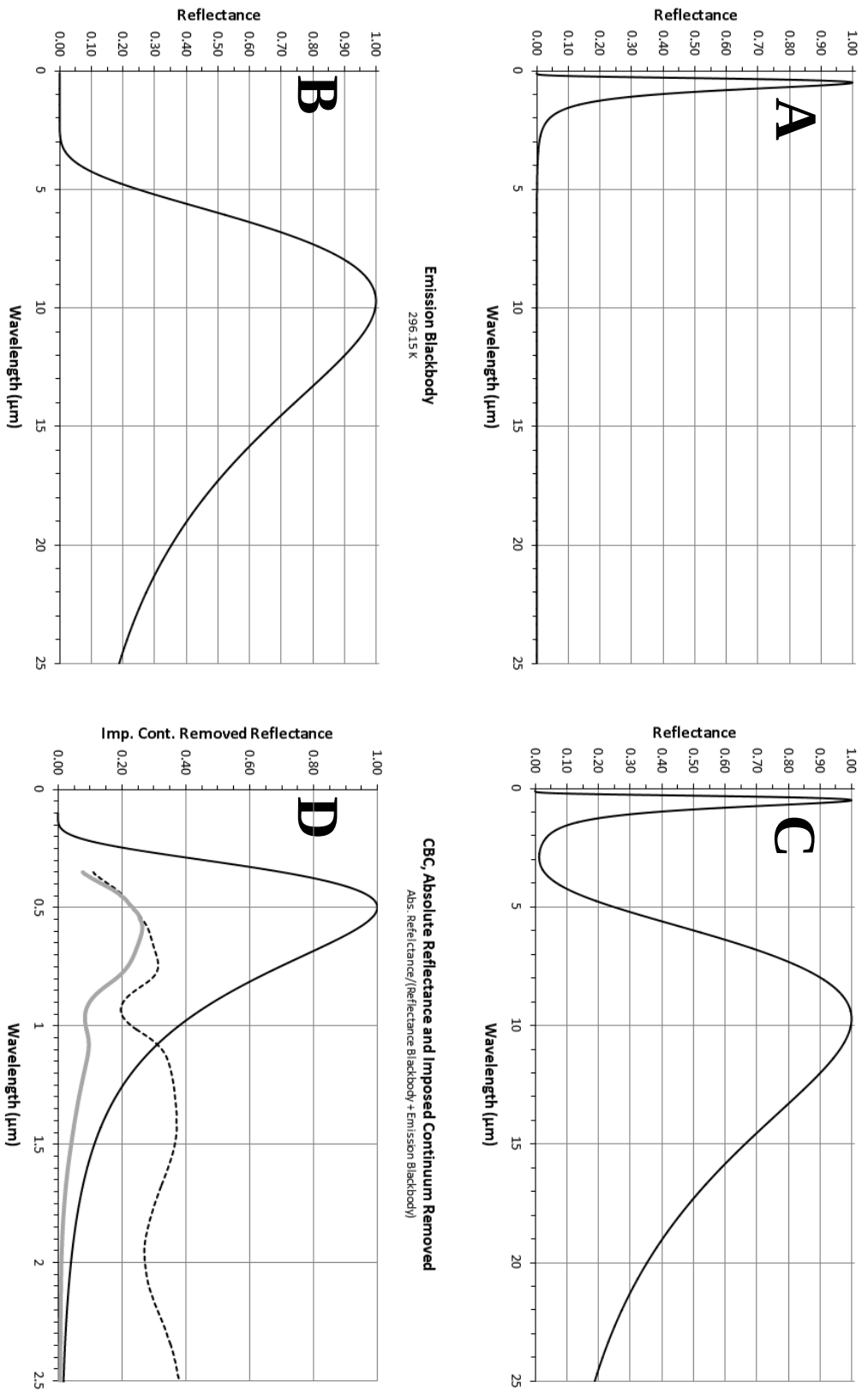
Reflectance Blackbody
5770 K
A
Reflectance
Wavelength (µm)
Emission Blackbody
296.15 K
B
Reflectance
Wavelength (µm)
CBC
Reflectance Blackbody + Emission Blackbody
C
Reflectance
Wavelength (µm)
CBC, Absolute Reflectance and Imposed Continuum Removed
Abs. Reflectance/(Reflectance Blackbody + Emission Blackbody)
D
Imp. Cont. Removed Reflectance
Wavelength (µm)

Figure 2-2: Construction of the Combined Blackbody Curves (CBC) for a sample of pyroxene illustrating the removal of the continuum imposed on the sample spectrum by the reflectance instrument calibration/reflectance spectrum measurement process. 2-2A is the solar black body emission curve/reflectance blackbody curve at a temperature of 5770 K. 2-2B is the emission blackbody curve for the <45 µm powdered pyroxene sample at a temperature of 296.15 K (23 °C). 2-2C is the CBC which is removed via multiplication in panel 2-2D to illustrate the removal of the continuum imposed on the sample by the spectral measurement process. The black dashed line is the spectrum of a pyroxene depicting the normal output of a reflectance spectrometer where the pyroxene spectra is measured relative to a white reference standard, the solid black curve is the CBC for the sample and the thicker grey line is the real spectrum of the pyroxene with its imposed continuum removed.

A 3rd order polynomial is the best compromise for the typical spectral resolutions returned by the remote and telescopic platforms characteristic of planetary science and will return consistent results across a multitude of datasets of varying resolution. Higher order polynomials have their purposes, but will 'follow the line' to too great an extent when spectra is of low resolution or noisy. It should also be noted that a 3rd order polynomial is a simple function, whose use should be limited to concave or convex portions of a curve and not both, as a curve that both rises and falls across the number of points fed into a fit of a 3rd order polynomial will skew the centre or minima values and the inflection points calculated will fall between the desired, and arguably correct values. If one wants to chart all of the inflection points in a spectrum as a first pass prior to deciding what to fit, the use of derivatives or higher order polynomials may be appropriate (see Appendices 2A and 2B).

2.3.2 The Continuum

To derive the other primary metrics, excepting minima, one must be familiar with the concept of the continuum and how it might be applied to a spectrum. The continuum and

removal of the apparent or imposed continuum by various curves or straight lines can be difficult to comprehend. However, continuum removal has two purposes: to remove some effect imposed by the measurement/calibration process used when collecting a spectrum (imposed continuum removal); or to isolate a portion of the spectrum (apparent continuum removal).

The continuum can be thought of as a combination of curves, chiefly, the emission curves of the light source and sample, and the continuum of absorptions caused by crystal field absorptions, charge transfers, vibrational modes, overtones of vibrational modes, wings of absorption bands, optical effects, wavelength dependent scattering, and so on (see Morris et al., 1982; Clark and Roush, 1984). In normal practice, as part of the calibration of the reflectance instrument, a large portion of the continuum, which is represented by the combined reflectance and emission Blackbody Curves (CBC) of the light source and the sample, will be removed by division. As this type of continuum removal is imposed on the reflectance spectrum by the normal calibration procedures for a reflectance instrument, we refer to it as imposed continuum removal, and when we refer to spectra as reflectance spectra, imposed continuum removal is implied.

To begin, one has to understand the measurement and white referencing processes used by a particular spectrometer to collect a spectrum. For a spectrometer collecting ultraviolet thru near-infrared reflectance spectra for example, the spectra will be collected relative to a white reference reflectance standard, normally halon or Spectralon® (see Ruff et al., 1997 for an infrared emission example). A spectrometer has an inherent response function (a curve or a series of curves) due to the response functions of the individual detector(s) used, the light source will also have an inherent emission curve, and so will the sample. The process of measuring relative to a standard, such as Spectralon®, creates a translation curve that will remove both the instrument's detector response function(s) and the CBC by translating the combined curves to unity, or 100% reflectance, relative to the measured unity value as defined by the white reference standard. A consequence of the process of measuring reflectance spectra in this manner

is that all reflectance spectra output by the instrument will be imposed continuum removed.

Figure 2-2 illustrates the two components of the CBC (2-2A and 2-2B), their combination into a single curve to facilitate the removal of the continuum imposed by the measurement process (2-2C) the reflectance or imposed continuum removed spectra, and the spectrum with its imposed continuum re-applied (2-2D). This applies to reflectance spectra collected in the laboratory as well as remotely sensed reflectance spectra. Often asteroid spectra, for example, are referred to as I/F or Intensity-over-Flux spectra, and they undergo the same process where the continuum of the light source, i.e., its emission curve, or Flux is removed by dividing the returned signal, Intensity, by Flux. I/F spectra are collected in the same manner as laboratory spectra with two significant exceptions. The majority of asteroid spectra are collected by Earth-based telescopes, and a portion of the instrument calibration procedure involves accounting for or removal of the absorptions by Earth's atmosphere. Unlike laboratory spectra, a CBC is not used, rather the only the reflectance emission, or solar curve in Figure 2-2A is used to create the imposed continuum removed spectra of 2-2D, and this has implications that are discussed further in the appendices.

Using the CBC illustrated in 2-2C to remove the imposed continuum, imposed on the sample spectrum by the spectral measurement process, one arrives at the true measured spectrum of the sample relative to that sample's real continuum, e.g., the thick grey spectrum in 2-2D.

The reapplication of the imposed continuum removed via the reflectance instrument calibration/reflectance measurement process using the CBC in this manner, provided the CBC used is the same shape as the CBC initially applied to the spectrum and it is removed in the same multiplicative or additive manner, can recover the true band centres of absorptions by removing the apparent skew imparted on said absorptions by the reflectance instrument calibration/reflectance measurement procedure (see Clark and Roush, 1984; Clark, 1999; and the examples in Appendix 2A). If any modelling of spectral absorptions is to be performed, it must be completed with a spectrum where

removal of the continuum imposed by the spectral measurement process has been performed.

To derive any metric other than the band minima from reflectance spectra one must somehow deal with the remaining continuum, and further remove a portion of the apparent continuum to isolate a particular spectral absorption. When an absorption band is thus isolated, properties such as the band centre, band depth (relative to the apparent continuum) and band area can be calculated, subject to whatever constraints are imposed by the choice of apparent continuum removal method. One could choose not to remove any portion of the continuum, as is done specifically for the derivation of band minima, and still calculate a band depth. However, outside of modelling absorption features (which is further discussed in the Appendices), there are reasons for removing a portion of the apparent continuum: for isolation for defining an area, centring to remove a modicum of asymmetry, adding contrast for ease of centre wavelength determination and to facilitate broad comparison with spectra where similar apparent continuum removal has been performed (e.g., Clark et al., 2003).

One can remove apparent continua in a number of ways and we are advocating for straight line apparent continuum removal, i.e., fitting of a straight line from the points of band extinction short- and long-ward of the absorption band of interest (dotted straight lines in Figure 2-1, solid straight lines in Figure 2-3). This is the simplest method

mathematically and is repeatable.

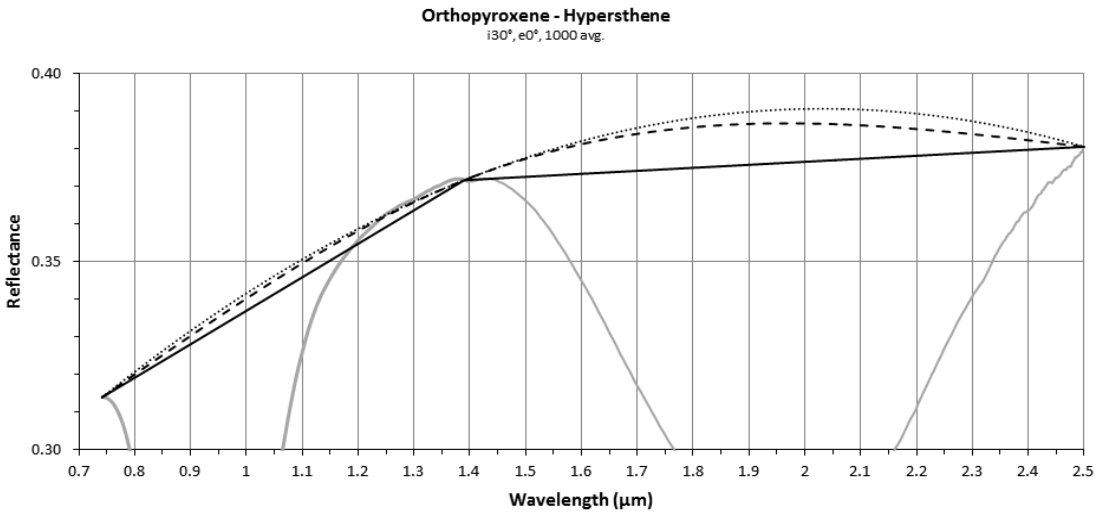

Figure 2-3: The spectrum of pyroxene with Bands I and II isolated, but uncentred, based on the derived pin points presented in figure 1, with fit straight line apparent continua (solid black lines), and two oft used curved apparent continua, a 2nd order polynomial (dotted curve), and a natural cubic spline (the dashed curve). Any of the depicted straight or curved apparent continua could be used to further remove continuum from the spectrum, isolating the absorptions while centring them for derivation of area and simplification of band depth calculation. We advocate for the use of straight line apparent continuum removal in wavelength space as demonstrated. See Appendix A for further comparison of various straight and curved line continua apparent removal methods.

The fitting of an apparent continuum would ideally be based on sound scientific justification for the use of a particular apparent continuum removal technique and only in rare instances will straight lines or the commonly used curves such as natural cubic splines or low order moving average polynomials approximate the shape of the blackbody curves (Figure 2-3). We believe the soundest scientific argument for a favoured line shape for apparent continuum removal would be a comparison of that lines shape with the shape of the blackbody curve across the wavelength range in question. Only in very rare instances will any of the commonly use apparent continuum removal

line shapes approximate the line shape of the local blackbody curve, and rarely will using a cubic spline or low order moving average polynomial produce a different centre than a straight line. No compelling arguments have been advanced for fitting a curve in place of a straight line for apparent continuum removal. Further, the fitting of curved lines to facilitate apparent continuum removal adds significant and often unnecessary complexity to the calculation and production of continuum removed spectra. As such, we suggest the simplest and most easily repeatable option is the straight line apparent continuum removal in wavelength space method we advocate (see the curved continua comparison in Appendix 2A and discussion in Appendix 2B) which also allows for the widest comparison with previous studies performed where straight line apparent continuum removal was applied.

2.3.3 Pin Points

Picking the points to which the straight line continuum is pinned depends most on the goal one hopes to achieve or the method chosen, e.g., while fitting the example pyroxene spectrum, we have used 3rd order polynomials to derive the inflection points/extinction points/pin points for the areas of absorption features in the wavelength regions of interest (see Figure 2-1), though there are other methods for deriving pin points, or simply picking them. One common procedure is to use the tangent points associated with straight line continuum fit. For example, if one were working with a set of spectra, for instance, a set of silica samples as in Rice et al. (2013), or Milliken and Mustard (2005), or a set of pyroxene samples of varying grains sizes, as in Craig et al. (2008), or a set of spectra of mixtures of pyroxene and olivine, as in Cloutis et al. (1986), one might decide on a fixed set of pin points which always remain inside of the extinction points between adjacent bands for an entire set of samples and ignore the changes in extinction/pin point values from sample to sample. It may sometimes be preferable to perform the centring in the same manner as previously fit data. When the pin points are known, or the methods used are known, such as using fixed pin points at 0.7 and 2.4 μm, and using a derived pin point for the point of extinction between Bands I and II as was done in Cloutis et al.

(1986), deriving pin points using second order polynomials and using a fixed 2.5 μm pin point if an extinction between 2 and 2.5 μm was not obvious as in Storm et al. (2007), or using the two peaks on either side of the absorption, defined in an unknown manner, with a fixed 2.5 μm pin point as in Dunn et al. (2010) and (2013), those methodologies may be preferred.

For the sake of consistency across data sets we would suggest that deriving the continuum pin points using 3rd order polynomial fitting should be standard practice, unless the pin points cannot be calculated, and must be picked. When fitting pin points, one should adhere to the same set of simple constraints suggested for deriving band minima and centre polynomial fits, and similarly for the fitting of minima or centres.

The derivation of pin points can be problematic when there is no obvious point of band extinction, i.e., no obvious region of convexity to fit with a polynomial function. In our pyroxene example, we have chosen to pin the long wavelength end of the straight line continuum between 1.39 and 2.5 μm to the measured reflectance value at 2.5 μm. This just happens to be common practice when fitting near-infrared spectra for asteroid analog materials measured in the laboratory due to detector limitations and telescopic asteroid spectra which also commonly end at or about 2.5 μm due to atmospheric water vapour issues (e.g., Cloutis et al., 1986; Storm et al., 2007; Dunn et al., 2010, 2013). In this instance, it is a fortunate coincidence, but there are no existing selection rules for creating a pin point if an obvious extinction point does not exist. What is most important, as with all other curve fitting, is that one share the pin points and the methods of derivation or the position of the point used if it was chosen instead of calculated and if appropriate, the reasoning for the choice.

2.3.4 Straight Line Apparent Continuum Removal

With pin points derived or chosen, the straight line segments for apparent continuum removal are produced, which are most often referred to as straight line continua, and the straight line apparent continuum is mathematically removed so band depth for the

continuum removed band, band centres and band areas can be calculated. The straight line continuum can be removed by dividing it out, i.e., sampley ÷ continuumy for the same x, which centres the absorption, and/or it could also be removed by linear translation, i.e., (1 – continuumy) + sampley for a given x. The method of linear translation to unity is useful for visualization and for calculation of area without the contrast stretching that occurs when centring absorptions via division.

Both methods are illustrated in Figure 2-4, where the black spectrum is the SMASS + SpeX (Rayner et al., 2003), scaled spectrum of Vesta, the dotted line spectrum is Bands I and II centred and the dashed line spectrum is Band I and II translated linearly to unity.

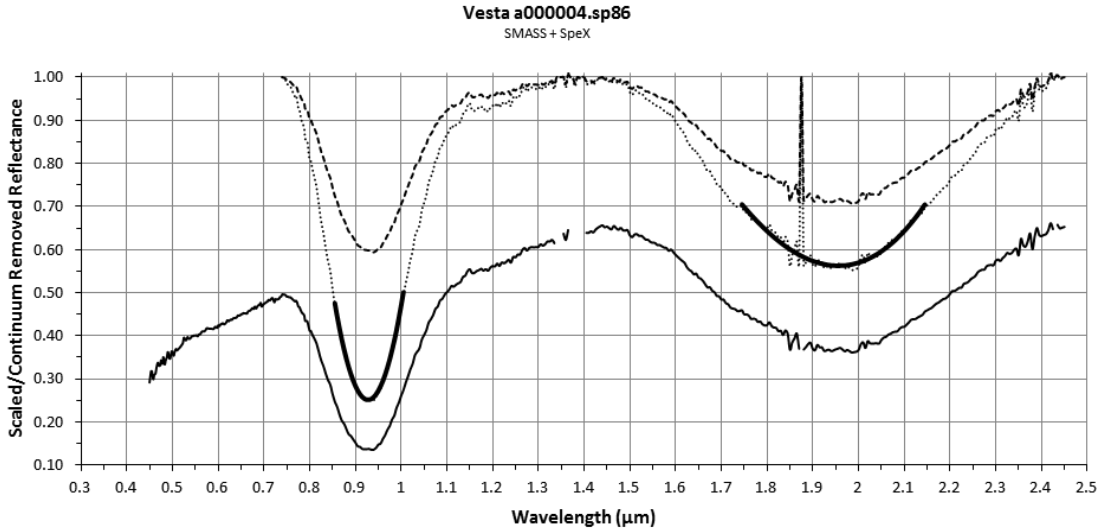

Figure 2-4: Straight line apparent continuum removed spectra of the two isolated bands of interest for asteroid 4 Vesta. The dotted spectrum has been straight line apparent continuum removed via division, i.e., centred, and the dashed line spectrum has been straight line apparent continuum removed via linear translation. The solid black spectrum is the unaltered (but offset) SMASS + SpeX spectra of Vesta. The heavy black lines which overlay the absorption minima for the centred dotted spectrum depict the polynomials fit to derive the band centres. The spikes in the two continuum removed spectra within Band II, and the portions of the continuum removed spectra which are above unity are discussed, as is the fitting of data with gaps, in more detail in the Appendices.

2.3.5 Band Centre

Band centres are fit in the same manner as band minima, using 3rd order polynomials, but fit to spectra where the band has been centred. It is important that centres only be reported when an apparent continuum has been removed by division and the spectra have experienced the contrast stretch that is applied by this method of apparent continuum removal. It must also have been performed on spectra where the continuum imposed by the reflectance (or, where the reflectance blackbody curve, as we have defined it, has been removed) measurement process is still intact before the straight or curved line apparent continuum was removed to isolate the absorption in question. It may be tempting to use the term band centre to denote any measure of a minimum on a band that has had the continuum altered in some way or a portion removed as in infrared emission spectra, but, given the ubiquity of its use for near-infrared reflectance spectra, the term band centre should be reserved for near-infrared use.

The band centre value is derived by fitting a 3rd order polynomial function to a subsection of the centred spectrum (solid black fits in Figure 2-4). Best practice is to pick a portion of the centred spectrum which is reasonably symmetric, visually, about the minimum value with approximately the same number of points either side of the approximate centre. One can stray marginally from an area of symmetry around the approximate centre value, but with significant skew, visually favouring the left or right wing of an absorption or significant asymmetry inherent in the data, the derived centre value will be inappropriate (see Appendices 2A and 2B for further examples and explanation).

2.3.6 Band Depth

Band depth can be calculated in a number of different manners depending on the spectrum under investigation. Regardless, band depth is always the depth to the

minimum or centre along a straight line, which intersects the band minima (though not necessarily a fit minima), or centre, tangent to a fit straight line continuum, unity, or following from some other defined position in the parameterized spectrum. Unlike centres, band depth has no standardized meaning and this requires that it be defined in each instance (see Rice et al., 2013, for a thoroughly documented example of the methods suggested by Clark and Roush, 1984).

2.3.7 Band Area

One can calculate the area of a band using one of the three methods we have provided: using chords, the trapezoid rule or integration of regression, or some other method. What matters in the calculation of area is not the method so much as consistent application of one method across the spectra being fit or a method that is consistent with the spectra to which they will be compared. Using all three methods will result in different measured values for area (which can be made to reflect real numbers) that when ratioed will return very nearly the same result (see Appendix 2A for a comparison). When representing Band Area Ratio (BAR), it is of utmost importance that BAR be calculated using area measures derived from bands centred by dividing out of straight line apparent continua. When centring a band, one is dividing out the apparent continuum which can be described as linearly moving the numerically highest pin point reflectance value to unity, while swinging the rest of the values up such that the straight line apparent continuum becomes a straight horizontal line at unity. This results in a contrast stretch, i.e., the depth of the band increases, and the degree to which it deepens is governed by the degree to which the straight line continuum has swung to achieve unity.

Referencing the straight dotted lines in Figure 2-1, the straight line apparent continuum running from 0.742 to 1.39 µm has significantly more positive slope than the straight line running from 1.39 to 2.5 µm. When centring both bands, the contrast stretch factors (a number calculated by ratioing the depth of the centre of the centred band to the depth of that same wavelength value for the same band translated linearly to unity) are 3.02 and

2.66 for Bands I and II respectively. This means that the bands have not been stretched by the same factor when centering, and the BAR is inherently altered as a result, e.g., the BAR of the centred bands is 1.93, while the BAR for the uncentred bands is 2.20, so, if one were plotting the band area ratios on the S Asteroid subtype plot of Cloutis and Gaffey (Gaffey, 1993), not recognizing the difference could lead to significant misinterpretation. The issue is readily apparent graphically in the centred and uncentred band comparison in Figure 2-4.

The spectrum of 4 Vesta, Figure 2-4, illustrates another set of problems that are commonly encountered when dealing with remotely obtained spectra, which are rarely encountered in laboratory spectra: noise and missing data. Noisy data are the primary reason for using a 3rd order polynomial for fitting, as 3rd order polynomial fits are generally insensitive to the high-frequency noise encountered in spectral data sets (for modelling another choice may be appropriate), but the noise can present another problem. When fitting the curves for the apparent continuum pin points, the noise may affect the positioning and may result in portions of the continuum removed spectrum exceeding a value of 1, or unity. In these instances, the calculations for area we have devised will subtract the calculated areal values which surpass unity, or 100% reflectance. This may also occur in high resolution, relatively noise free spectra, where centred reflectance values may exceed unity after apparent continuum removal. In these instances, the calculations for area treat the values exceeding unity in a manner defined by the chosen areal calculation method (see Appendix 2A for illustrative examples).

When dealing with missing data, which is also illustrated in Figure 2-4, it is up to the person performing the fitting what sort of gap size is tolerable, and how the data gap may be treated. When data gaps are small, i.e., on the order of a few nanometres, for the purposes of fitting, we have provided polynomial fitting routines that can fit data with these small gaps and unique functions for centred and linear translation apparent continuum removal. When removing the apparent continuum for gapped data, the functions replace all missing y values with 1’s to provide a visual reminder that one will have to use a function specific to gapped data when calculating band areas. Like the

polynomials specific to gaps, idealized functions have been created to ignore the data gaps for the three areal measurement methods provided (see Appendices). We suggest that ignoring the gaps for area calculation is the mathematically soundest method when data gaps are small and fully removing gaps and allowing the trapezoidal area function to in-fill them in a linear manner is most efficacious when gaps are minor. However, for instances where gaps are quite large one may be better served by in-filling missing data points using polynomial interpolation. Functions for doing so are provided in the appendices but suggesting any sort of framework for their use is exceedingly difficult; deciding when and how to interpolate missing data points should be made on a case by case basis. In the example provided in Figure 2-4, regarding the SMASS + SpeX spectrum of Vesta, the BAR which results from areas calculated using the trapezoidal area with gapped values being 1 (which results in no areal values being reported for gaps, and gap adjacent areas) is 1.39, versus BAR values of 1.41 calculated using trapezoid functions for the same spectrum where gaps were in-filled using polynomial and/or linear interpolation functions. If one plots these on the Cloutis/Gaffey S-Asteroid plot of Gaffey (1993), or the modified plot of Dunn et al. (2013), it could be argued that the effect in this instance is negligible, but the matter is debatable, as in cases where a sample's Band I centre versus BAR might have it subtend an S asteroid subtype boundary, what was a negligible difference in BAR value may now prove quite significant. What matters is not necessarily how it was done, but that the methods are disseminated such that cross comparisons with other data sets, or comparisons by other researchers, are valid.

2.4 Modelling

Modelling spectra deserves particular attention as it is an oft misunderstood term which can lead to confusion; we propose that the term "modelling," in the context of spectral absorptions, be restricted to a narrow definition. We would suggest that any model must be modelling the real physical processes responsible for the creation of an absorption.

We suggest this constriction on the bounds of the use of the word ‘model’ as the standard procedure with ultraviolet through far-infrared spectra, after the derivation of band minima, would be to isolate an absorption by removing a straight line apparent continuum for further derivation of spectral parameters. This is normally performed on a reflectance spectrum that has its imposed continuum resulting from the measurement process intact, which means that the spectrum one is attempting to model has absorption shapes skewed by the reflectance instrument calibration procedure, and then those same absorptions are skewed further via removal of more of the continuum in a rather arbitrary fashion. Procedurally, this is acceptable, when both the researcher and the intended audience understand that the process of measurement has removed the reflectance continuum and the absorption in question has been centred as per standard practice and definition.

Where many seem to go awry is in assuming that any fitting of a spectrum where any portion of the continuum has been twice altered is in some way modelling of the spectrum. As noted earlier, any altering of the spectrum, by application of an imposed continuum through measurement processes or via removal of straight or curved line apparent continua either by division or translation will alter the spectrum such that the positions and shapes of absorptions have no basis in physical reality, meaning that no

actual modelling, as we define it, can occur.

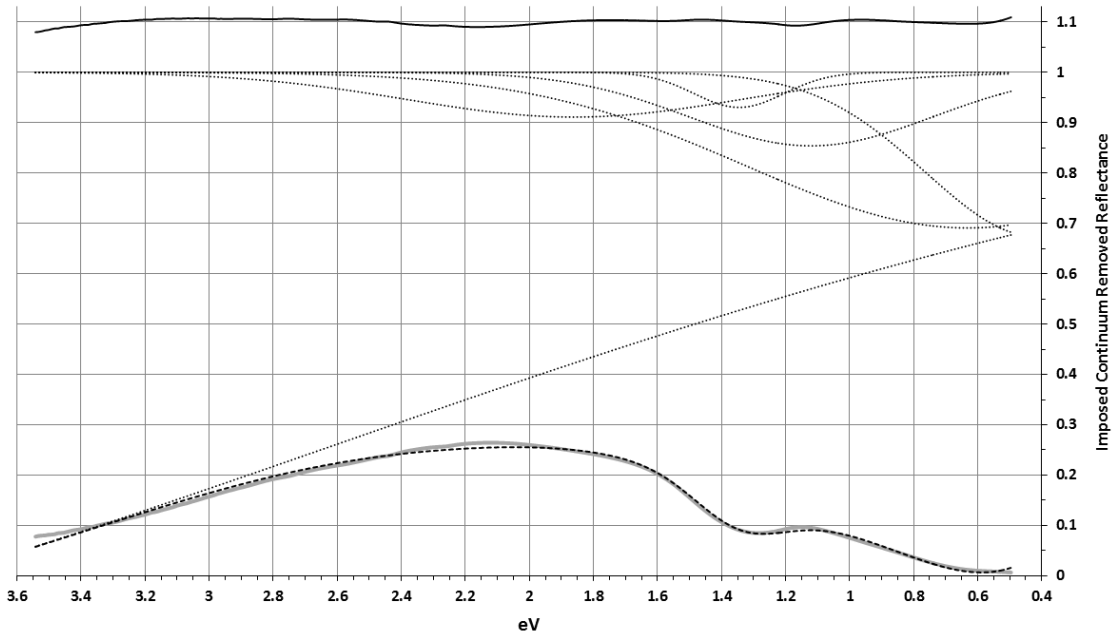

Figure 2-5: Gaussian modelling of the pyroxene sample in eV space, with the imposed continuum removed in wavelength space such that the Gaussians used model the real absorptions responsible for the majority of the spectrum. Dotted lines depict the 6 Gaussians used, the thick grey spectrum is of the pyroxene sample with its imposed continuum removed, and the dashed black line residing within the thick grey spectrum is the summed Gaussian model. The quality of the fit is measured by the residual, where the better the fit, the less the residual varies about the 1.1 line (RMS 0.004).

The pyroxene spectrum of Figure 2-5 is an example of modelling of the real spectrum, with its imposed continuum in wavelength space removed (as seen in Figure 2-2D), modelled in energy space using summed Gaussians, where they are modelling the physical absorptions creating the spectrum and are as representative as they can be of the full spectrum, given that the Gaussians used are there purely to model crystal field transition and are ignoring other processes influencing the spectrum. For this example 6 Gaussians are used, although only three Gaussian centre positions are of importance for the pyroxene spectrum, i.e., those centred at 0.92, 1.105 and 1.965 μm (1.345, 1.121 and 0.632 eV). Three of the Gaussians used model the spectral features due to Fe2+ in the

M1 and M2 coordination sites in the pyroxene and the other three serve as placeholders for a number of absorptions, and important to note, while only three Gaussian centres are of importance, the 6 modelled absorptions, and an additional 7 which would be required to thoroughly model this portion of the pyroxene samples spectrum, exert influence on the absorptions which were modelled. This model was produced via a combination of hand and automated fit optimization, and the residual is offset plus 0.1 above unity for clarity. One can see a representation of the quality of the model via the general lack of deviation about 1.1 of the residual line (RMS 0.004). This qualifies as modelling, by our definition, as it is based in the fundamental physics that one would use to derive the idealized energy values for the crystal field transitions and overtones responsible for the combination absorptions which produce the large features of interest in the spectrum.

The model is illustrative of two significant points: 1) while the fit residual is low, we have not adequately modelled all 13 of the absorptions that are required at a minimum in this wavelength range to thoroughly model the spectrum (two of which will be placeholders for absorptions we cannot see, but are quite powerful, on either end of the spectral range). As such, we cannot be fully confident that the Gaussian centres, depths and FWHM are accurate models of reality, despite the low residual and fact that we have chosen the Gaussian centre positions at points that are reasonable representations of reality, as they are based on the energy centres of real modelled and measured absorptions with sound physical explanations (e.g., Rossman, 1980; Burns, 1993); and, 2) despite using Gaussians whose centres are based on the physics of absorptions in pyroxene, a low residual model can be produced with Gaussians centred at disparate locations which have no associated physical process and still produce an equally low residual. The fine dotted lines in Figure 2-5 are the individual Gaussians used and minor changes in one modelled absorption can largely be compensated for by a minor change in another, such that one could easily shift centre positions, FWHM values and scaling values of the Gaussians to produce a low residual model but those values would not be physically meaningful. Akin to MGM, where some set of reasonably fixed starting parameters are required, this sort of brute force modelling requires a set of starting values that are based on the physics of the absorptions to be valid and valuable.

Further problems with the modelling exist because the removal of the continuum imposed by the reflectance measurement process is not absolutely correct, given that the applied solar emission curve/reflectance continuum may not adequately replicate the combined effect of the light source and instrument correction curves applied to the spectrum being measured and the emission continuum may not reflect the sample temperature adequately (as the interacting volume of the sample under measurement may be heated above the ambient room temperature by the light source), such that we may not know the exact values for the necessary curves with absolute certainty.

In general one should approach modelling of any spectra with caution as, even with monomineralic samples where the effects of grain size, packing, porosity, temperature and so on are known and may be quantifiable individually, we cannot yet adequately constrain the effects each, in combination, is having on a particular sample's spectrum.

When solid samples of known mineralogy are being modeled, we will always have issues when modelling that are difficult to overcome which arise from known complications such as minute errors in the curves we are using for imposed continuum removal and re-application, not being able to adequately account for wavelength dependent scattering, optical effects, overtones, combination bands, hot bands, Fermi resonances, etc., and, extra contributors in samples from adsorbed species, site substitutions, inclusions and so on.

When samples are mixed assemblages of minerals of different grains sizes in the laboratory, mixed assemblages with different packing densities, grain sizes, and so on, or natural rocks, issues simply compound and physically meaningful spectral modelling may well be impossible.

2.5 Further Parameterization and Manipulation of Spectra

Beyond methods for the derivation of the four principal empirical curve fitting metrics, i.e., band minima, centre, depth, and area, we have included several other metrics,

methods for their derivation, and illustrative examples of common functions performed on spectra that deserve further explanation and/or those that are almost universally harmful and benefit from graphical explanations. Chief among these are a variety of conversions, interpolation methods, measures of skew, curved continuum removal, spectral convolution, automated and manual curve deconvolution/Gaussian fit optimization methods and modelling comparisons, further derivation of the line shapes for Lorentzian and Pseudo-Voigt curves and an exploration of smoothing functions, all of which can be found in the appendices.

2.6 Summary and Conclusions

This work presents fitting routines written for Microsoft Excel® that allow one to empirically curve fit spectra using polynomial fits of raw, or straight line apparent continuum removed spectra to mathematically and repeatably define band minima or centres with linear least squares, best-fit polynomials, in a robust and transparent cut-and-paste manner. The included functions do not rely on macros or any other add-ins to Excel that can malfunction if the included workbook or workbooks derived from it are shared across Excel platforms.

We advocate for the use of 3rd order polynomials almost exclusively for the derivation of band minima and centres, as a cubic polynomial has been found through extensive experimentation to be most efficacious across data sets of varying spectral resolution and signal-to-noise ratios. We suggest that straight line apparent continuum removal in wavelength space be the exclusive method for centring as-measured, ultraviolet through near-infrared absorption bands, and that the term's common definition change to reflect both this, and the exclusion of the use of curved continua for band centring. We hope that the confusion that arises when the terms fitting and modelling are used interchangeably can be ameliorated by respecting the definitions we adopt herein, where modelling is only used to denote spectra modelled in energy space with real continua intact/imposed continua removed. We also expect that, following a thorough review of

the material included in the appendices, it will be abundantly clear why fully parameterized fits of spectra need to be included in or alongside published manuscripts if the planetary science community is to gain from the publication of manuscripts including and/or referencing spectra. One will find on review, that most studies which perform empirical curve fitting or curve deconvolution do not include enough data about the curve fitting or deconvolution, or parameterization thereof, to allow one to repeat the fitting for the spectra referenced within them.

In an ideal world, we would hope that all researchers would always be on the same page regarding the use of one universally applicable succinct curve fitting methodology, where either the curve fits themselves are always shared or the methods are absolutely transparent and all of the requisite nodes are included so the fitting is repeatable. For those well-versed in the collection and application of spectroscopic data, the rationale for curve fitting is abundantly clear, but how to curve fit is often times not. We suggest this needs to change with the application of a consistent, robust, repeatable and transparent methodology, where spectra with included fits are shared openly, or spectra with complete sets of nodes/parameters/fit statistics are included in any and all manuscripts that reference a fit metric, such that the fit metrics can be referenced in perpetuity without questions regarding their validity. Or, spectra should always be included so each researcher could then later apply their favoured curve fitting methodology to every spectrum to which their research might refer. The former suggestion is significantly less time consuming and easier to achieve.

2.7 Acknowledgements

MAC gratefully acknowledges funding from the Natural Sciences and Engineering Research Council of Canada (NSERC), the NSERC Collaborative Research and Training Experience Program-Technologies and Techniques for Earth and Space Exploration, and the Ontario Graduate Scholarship Program that contributed to this work. The HOSERLab at the University of Winnipeg, where a portion of the presented spectra were

collected, was established with funding provided by the Canadian Foundation for Innovation, the Manitoba Research Innovations Fund and the Canadian Space Agency. A portion of the data utilized in this publication and its appendices was obtained from, and made available by The MIT-UH-IRTF Joint Campaign for NEO Reconnaissance. The IRTF is operated by the University of Hawai'i under cooperative agreement no. NCC 5-538 with the National Aeronautics and Space Administration, Office of Space Science, Planetary Astronomy Program. The MIT component of this work is supported by NASA grant 09-NEOO009-001, and by the National Science Foundation under grants Nos. 0506716 and 0907766.

2.8 References

Abe, M., Takagi, Y., Kitazato, K., Abe, S., Hiroi, T., Vilas, F., Clark, B.E., Abell, P.A., Lederer, S.M., Jarvis, K.S., Nimura, T., Uede, Y., and Fujiwara, A., 2006. Asteroid Itokawa from the Hayabusa spacecraft. Science 312, 1334-1338.

Abell, P.A., Vilas, F., Jarvos, K.S., Gaffey, M.J., and Kelley, M.S., 2007. Mineralogical composition of (25143) Itokawa 1998 SF36 from visible and near-infrared reflectance spectroscopy: Evidence for partial melting. Meteoritics & Planetary Science 42, Nr. 12, 2165-2177.

Adams, J.B., 1974. Visible and near-infrared reflectance spectra of pyroxenes as applied to remote sensing of solid objects in the solar system. Journal of Geophysical Research 79, No. 32, 4829-4836.

Bakker, W.H., F.J.A., van Ruitenbeek, H.M.A., van der Werff, T.E., Zegers, J.H.P., Oosthoek, S.H., Marsh, and F.D., van der Meer, 2014. Processing OMEGA/Mars Express hyperspectral imagery from radiance-at-sensor to surface reflectance. Planetary and Space Science 90, 1-9.

Binzel, R.P., Rivkin, A.S., Bus, S.J., Sunshine, J.M. and Burbine, T.H., 2001. MUSES-C target asteroid (25143) 1998 SF36: A reddened ordinary chondrite. Meteoritics & Planetary Science 36, 1167-1172.

Berger, J.A., King, P.L., Green, A., Craig, M.A., Spilde, M.N., Wright, S.P., Kunkel, T.S., and Lee, R.J., 2015. Effect of halite coatings on thermal infrared spectra. Journal of Geophysical Research: Solid Earth, 120, 2162-2178.

Burbine, T.H., Buchanan, P.C., Dolkar, T., and Binzel, R.P., 2009. Pyroxene mineralogies on near-Earth vestoids. Meteoritics & Planetary Science 44, Nr 9, 1331-1341.

Burns, R.G., 1993. Mineralogical applications of crystal field theory. Cambridge University Press, Cambridge, 551.

Buz, J., and Ehlmann, B. L., 2014. Effects of grain size on the reflectance spectroscopy of olivine in the vis-nir and the derivation of olivine composition using modified Gaussian model. LPSC XLV, abstract #2810.

Clark, R.N., 1980. A large-scale interactive one-dimensional array processing system. Publications of the Astronomical Society of the Pacific 92, 221-224.

Clark, R.N., 1981. Water frost and ice: The near-infrared spectral reflectance 0.65 – 2.5 μm. Journal of Geophysical Research 86, No. B4, 3087-3096.

Clark, R.N., 1993. SPECtrum Processing Routines user's manual version 3 (program SPECPR): U.S. Geological Survey, Open-File Report 93-595.

Clark, R.N., 1999. Spectroscopy of rocks and minerals and principles of spectroscopy. In, Manual of Remote Sensing, edited by A. N. Renz, pp. 3-58, John Wiley, New York.

Clark, R.N., and Roush, T.L., 1984. Reflectance spectroscopy: Quantitative analysis techniques for remote sensing applications. Journal of Geophysical Research 89, No. B7, 6329-6340.

Clark, R.N., Swayze, G.A., Livo, K.E., Kokaly, R.F., Sutley, S.J., Dalton, J.B., McDougal R.R., and Gent, C.A., 2003. Imaging spectroscopy: Earth and planetary remote sensing with the USGS Tetracorder and expert systems. Journal of Geophysical Research 108, No. E12, 5-1-5-44.

Clark, B.E., Binzel, R.P., Howell, E.S., Cloutis, E.A., Ockert-Bell, M., Christensen, P., Barucci, MA., DeMeo, F., Lauretta, D.S., Connolly, H. Jr., Soderberg, A., Hergenrother, C., Lim. L., Emery, J., and Mueller, M., 2011. Asteroid (101955) 1999 RQ36: Spectroscopy from 0.4 to 2.4 μm and meteorite analogs. Icarus 216, 462-475.

Clenet, H., Pinet, P., Daydou, Y., Heuripeau, F., Rosemberg, C., Baratoux, D., and Chevrel, S., 2011. A new systematic approach using the modified Gaussian model: Insight for the characterization of chemical composition of olivines, pyroxenes and olivine-pyroxene mixtures. Icarus 213, 404-422.

Cloutis, E.A., Gaffey, M.J., Jackowski, T.L., and K.L. Reed, 1986. Calibrations of phase abundance, composition, and particle size distribution for olivine-orthopyroxene mixtures from reflectance spectra. Journal of Geophysical Research 91, No. B11, 11641-11653.

Cloutis, E.A., and Gaffey, M.J., 1991. Pyroxene spectroscopy revisited: Spectral-compositional correlations and relationships to geothermometry. Journal of Geophysical Research 96, No. E5, 22809-22826.

Craig, M.A., Cloutis, E.A., Reddy, V., Bailey, D.T., and Gaffey, M.J., 2008. The effects of grain size, <10μm – 4.75mm, on the reflectance spectrum of planetary analogs from 0.35-2.5μm. LPSCXXXIX, abstract #2082.

Doestsch, G. Von, 1928. The elimination of the Doppler effect in spectroscopic fine structure and exact determination of the components, Zeitschrift fur Physik 49, 705-730.

Dunn, T.L., McCoy, T.J., Sunshine, J.M., and McSween. H.Y. Jr., 2010. A coordinated spectral, mineralogical, and compositional study of ordinary chondrites. Icarus 208, 789-797.

Dunn, T.L., Burbine, T.H., Bottke, W.F., Jr., and Clark, J.P., 2013. Mineralogies and source regions for the near-Earth asteroids. Icarus 222, 273-282.

Farr, T.G., Bates, B.A., Ralph, R.L., and Adams, J.B., 1980. Effects of overlapping optical absorption bands of pyroxene and glass on the reflectance spectra of lunar soils. Proceedings of the Lunar and Planetary Science Conference XI, 719-729.

Fieber-Beyer, S.K., Gaffey, M.J., Kelley, M.S., Reddy, V., Reynolds, C.M., and Hicks, T., 2011. The Maria asteroid family: Genetic relationships and a plausible source of the mesosiderites near the 3:1 Kirkwood gap. Icarus 213, 524-537.

Gaffey, M.J., 1976. Spectral Reflectance Characteristics of the Meteorite Classes. Journal of Geophysical Research 81, No. 5, 905-920.

Gaffey, M. J., 1983. The asteroid (4) Vesta: Rotational spectral variations, surface material heterogeneity, and implications for the origin of the basaltic achondrites. LPSCXIV, abstract #1118.

Gaffey, M.J., 1993. Mineralogical variations within the S-type asteroid class. Icarus 106, 573-602.

Gaffey, M. J., 1997. Surface lithologic heterogeneity of asteroid 4 Vesta. Icarus 127, 130-157.

Gaffey, M.J., 2003. Observational and data reduction techniques to optimize mineralogical characterizations of asteroid surface materials. LPSC XXXIV, abstract #1602.

Gaffey, M.J., 2005. The critical importance of data reduction calibrations in the interpretability of S-type asteroid spectra. LPSCXXXVI, abstract #1916.

Gaffey, M.J., 2008. Interpreting asteroid spectra – avoiding the three “great mistakes”. Asteroids, Comets, Meteors Conference, abstract #8162.

Gaffey, M.J., 2010. Space weathering and the interpretation of asteroid reflectance spectra, Icarus 209, 564-574.

Gaffey, M.J., King, T.V.V., Hawke, B.R., and Cintala, M.J., 1982. Asteroid spectral variations: Implications for composition and surface processes. LPSCXIII, abstract #1128.

Gaffey, M.J., and Gilbert, S.L., 1998. Asteroid 6 Hebe: The probable parent body of the H-type ordinary chondrites and the IIE iron meteorites. Meteoritics & Planetary Science 33, 1281-1295.

Gaffey, M.J., Cloutis, E.A., Kelley, M.S., Reed, K.L., 2002. Mineralogy of Asteroids. In Bottke, W.F. Jr, Cellino, A., Paolicchi, P., and Binzel, R.P. (Eds.), Asteroids III. University of Arizona Press, Tucson, 183-204.

Gallie, E.A., D.A., Lyder, B., Rivard, and E.A., Cloutis, 2008. Technical Note: Equivalence of modified Gaussian model (MGM) in wavenumber and Gaussian in wavelength for deconvolution of hyperspectral reflectance spectra. International Journal of Remote Sensing 29, No. 14, 4089-4096.

Hergenrother, C.W., Nolan, M.C., Binzel, R.P., Cloutis, E.A., Barucci, MA., Michel, P., Scheeres, D.J., Drouet d'Aubigny, C., Lazzaro, D., Pinilla-Alonso, N., Campins, H., Licandro, J., Clark, B.E., Rizk, B., Beshore, E.C., and Lauretta, D.S., 2013. Lightcurve, color and phase function photometry of the OSIRIS-Rex target asteroid (101955) Bennu. Icarus 226, 663-670.

Kaper, H.G., Smites, D.W., Schwarz, U., Takakubo, K., and van Woerden, H., 1966. Computer analysis of ordered distributions into Gaussian components. Bulletin of the Astronomical Institute of the Netherlands 18, 465-487.

Klima, R.L., Pieters, C.M., and Dyar, M.D., 2007. Spectroscopy of synthetic Mg-Fe pyroxenes I: Spin-allowed and spin-forbidden crystal field bands in the visible and near-infrared. Meteoritics & Planetary Science 42, Nr. 2, 235-253.

Klima, R.L., Dyar, M.D., and Pieters, C.M., 2011. Near-infrared spectra of clinopyroxenes: Effects of calcium content and crystal structure. Meteoritics & Planetary Science 46, No. 3, 379-395.

Kraft, M.D., Michalski, J.R., and Sharp, T.G., 2003. Effects of pure silica coatings on thermal emission spectra of basaltic rocks: Considerations for Martian surface mineralogy. Geophysical Research Letters 30, No. 24, 2288.

Livo, K.E., and Clark, R.N., 2014. The Tetracorder user guide-version 4.4: U.S. Geological Survey, Open-File Report 2013-1300.

Lucey, P.G., and Clark, R.N., 1985. Spectral properties of water ice and contaminants. In Ices in the solar system, edited by J. Klinger et al., pp. 155-168, D. Reidel Publishing Company, France.

Lonn, E. Von, 1932. Proof of the Uniqueness of the Decomposition of an Intensity Curve into its Components. Zeitschrift fur Physik 75, 348-349.

Makarewicz, H.D., Parente, M., Bishop, J.L. 2009. Deconvolution of VNIR spectra using Modified Gaussian Modeling (MGM) with automatic parameter initialization (API) applied to CRISM. IEEE Whispers, Article 5289046.

McCord T.B., Adams J.B. and Johnson T.V. 1970. Asteroid Vesta: spectral reflectivity and compositional implications. Science 168, 1445-1447.

McCord, T.B., Clark, R.N., Hawke, B.R., McFadden, L.A., Owensby, P.D., Pieters, C.M., and Adams, J.B., 1981. Moon: Near-infrared spectral reflectance, a first good look. Journal of Geophysical Research 86, No. B11, 10883-10892.

McSween, H.Y. Jr., Grove, T.L., and Wyatt, M.B., 2003. Constraints on the composition and petrogenesis of the Martian crust. Journal of Geophysical Research 108, No. E12, 5135.

McSween, H.Y. Jr., Binzel, R.P., De Sanctis, M.C., Ammannito, E., Prettyman, T.H., Beck, A.W., Reddy, V., Le Corre, L., Gaffey, M.J., McCord, T.B., Raymond, C.A., Russell, C.T., and the Dawn Science Team, 2013. Dawn; the Vesta-HED connection; and the geologic context for eucrites, diogenites and howardites. Meteoritics & Planetary Science 48, Nr. 11, 2090-2104.

Milliken, R.E., and Mustard, J.F., 2005. Quantifying absolute water content of minerals using near-infrared reflectance spectroscopy. Journal of Geophysical Research 110, E12001, 25.

Morris, R.V., Neely, S.C., and Mendell, W.W., 1982. Application of Kubelka-Munk theory of diffuse reflectance to geologic problems: The role of scattering. Geophysical Research Letters 9, No. 2, 113-116.

Nakamura, T., Noguchi, T., Tanaka, M., Zolensky, M.E., Kimura, M., Tsuchiyama, A., Nakato, A., Ogami, T., Ishida, H., Uesugi, M., Yada, T., Shirai, K., Fujimura, A.,

Okazaki, R., Sandford, S.A., Ishibashi, Y., Abe, M., Okada, T., Ueno, M., Mukai, T., Yoshikawa, M., and Kawaguchi, J., 2011. Itokawa dust particles: a direct link between S-type asteroids and ordinary chondrites. Science 333, 1113-1116.

Parente, M., Makarewicz, H.D., and Bishop, J.L., 2011. Decomposition of mineral absorption bands using nonlinear least squares curve fitting: Application to Martian meteorites and CRISM data. Planetary and Space Science 59, 423-442.

Ramsey, M.S. and Christensen, P.R., 1998. Mineral abundance determination: Quantitative deconvolution of thermal emission spectra. Journal of Geophysical Research 103, No. B1, 577-596.

Rayner, J.T., Toomey, D.W., Onaka, P.M., Denault, A.J., Stahlberger, W.E., Vacca, W.D., Cushing, M.C., and Wang, S., 2003. SpeX: A medium-resolution 08-5.5 micron spectrograph and imager for the NASA infrared telescope facility. Publications of the Astronomical Society of the Pacific 115, 362-382.

Reddy, V., Sanchez, J.A., Bottke, W.F., Cloutis, E.A., Izawa, M.R.M., O'Brien, D.P., Mann, P., Cuddy, M., Le Corre, L., Gaffey, M.J., and Fujihara, G., 2014. Chelyabinsk meteorite explains unusual spectral properties of Baptistina asteroid family. Icarus 237, 116-130.

Rice, M.S., Cloutis, E.A., Bell III, J.F., Bish, D.L., Horgan, B.H., Mertzman, S.A., Craig, M.A., Renaut, R.W., Gautason, B., and Mountain, B., 2013. Reflectance spectra diversity of silica-rich materials: Sensitivity to environment and implications for detection on Mars. Icarus 223, 499-533.

Rossman, G.R., 1980. Pyroxene spectroscopy. In: Pyroxene. Reviews in Mineralogy No. 7. Mineralogical Society of America, Washington, DC, 93-115.

Ruff, S.W., Christensen, P.R., Barbera, P.W., and Anderson, D.L., 1997. Quantitative thermal emission spectroscopy of minerals: A laboratory technique for measurement and calibration. Journal of Geophysical Research 102, No. B7, 14889-14913.

Singer, R.B., 1981. Near-infrared spectral reflectance of mineral mixtures: Systematic combinations of pyroxenes, olivine, and iron oxides. Journal of Geophysical Research 86, No. B9, 7967-7982.

Storm, S., Bus, S.J., and Binzel, R.P., 2007. Olivine-pyroxene distribution of S-type asteroids in the main belt. Bulletin of the American Astronomical Society 39, 448.

Sunshine, J.M., Pieters, C.M., and S. F. Pratt, S.F., 1988. Gaussian Analysis of Pyroxene Reflectance Spectra. LPSC XIX, Abstract #1151.

Sunshine, J.M., Pieters, C.M., and Pratt, S.F., 1989. Mathematical deconvolution of mineral absorption bands. LPSCXX, abstract #1087.

Sunshine, J.M., Pieters, C.M., and Pratt, S.F., 1990. Deconvolution of mineral absorption bands: An improved approach. Journal of Geophysical Research 95, No. B5, 6955-6966.

Sunshine, J. M., and Pieters, C.M., 1993. Estimating modal abundances from the spectra of natural laboratory pyroxene mixtures using the modified Gaussian model. Journal of Geophysical Research 98, No. E5, 9075-9087.

Sunshine, J.M., and Pieters, C.M., 1998. Determining the composition of olivine from reflectance spectroscopy. Journal of Geophysical Research 103, No. E6, 13675-13688.

van der Meer, F.D., 2004. Analysis of spectral absorption features in hyperspectral imagery. International Journal of Applied Earth Observation and Geoinformation 5, 55-6.

van Ruitenbeek, F.J.A., W.H., Bakker, H.M.A, van der Werff, T.E., Zegers, J.H.P., Oosthoek, Z.A., Omer, S.H., Marsh, and F.D., van der Meer, 2014. Mapping the wavelength position of deepest absorption features to explore mineral diversity in hyperspectral images. Planetary and Space Science 101, 108-117.

Chapter 3

3 Impact Glasses: Identifying and Differentiating Between Effusive Glasses, Glassy Impactites, Hydrothermal Deposits and the Milieu of Silicates on Mars using Reflectance and Emittance Spectroscopy

3.1 Introduction

Hypervelocity impact is a pervasive process on planetary bodies with a solid planetary surface and may be the dominant geologic process on airless bodies and the rocky planets other than Earth over geological time. The impact cratering process deposits huge amounts of energy at a focused point on the surface of a planetary body, and in a geological instant. This results in changes to the target rocks, ranging from solid-state shock metamorphic effects, such as shatter cones and planar deformation features (French and Koeberl, 2010), to the complete melting of individual minerals and whole rocks (Osinski et al., 2012). This produces a class of rocks known as impactites (Grieve and Therriault, 2013). The heat deposited by an impact event is also capable of generating a hydrothermal system that may subsequently alter these primary-impact-generated lithologies (Osinski et al., 2013).

Recently, it has been shown that impact glasses have a particular penchant for preserving extinct and extant biological content and provide an easily metastable source of energy for primitive life to exploit (Schultz and Mustard, 2004; Schultz et al., 2014; Sapers et al.,2015). While certain shock metamorphic products are of geological interest, and may be unique spectrally (e.g., diaplectic glass; Williams and Jeanloz, 1989), the glasses and glassy-impactites generated by impact and hydrothermal sites created by the impact are important astrobiologically due to the potential of these sites to harbour and preserve life (Izawa et al., 2010; Sapers et al., 2015).

Identifying an impact crater on Earth is relatively simple if projectile remnants are found around a crater. As the size of a crater and erosion increases, one has to rely on

diagnostic shock-metamorphic criteria to confirm an impact (French and Koeberl, 2010). Identifying impactites and more localized sites that may contain impact derived melt and/or glasses is not a trivial task on Earth and is even harder on other planetary bodies. Without in-situ analyses, identifying impact glasses is not without difficulty. One of the common instruments used for planetary exploration is the spectrometer and the goal of this work was to determine if silica-rich glassy-impactites have a unique spectral signature. We have assembled a suite of impact glasses from four terrestrial craters and characterize spectral features that may evidence an impact origin and that mimic those that have been identified experimentally as being produced by the high pressures, high temperatures and the quick quenching times these glasses experience in the distinct formation environment of a hypervelocity impact. The ability to robustly identify glassy-impactites from amongst a suite of silicates including hydrothermal deposits, effusive and pyroclastic volcanic, shocked and unshocked impactites, weathering soils and dust, still, has been somewhat elusive. Various researchers have attempted to discern the volume and nature of glasses on Mars (e.g., Bandfield 2000; McSween et al., 2003; Rogers and Christensen, 2007; Cannon and Mustard, 2015), but not without disagreement. Disagreement seems to have arisen from the methods employed, i.e., linear curve deconvolution, and the region of the spectrum employed, i.e., near-infrared reflectance or infrared emission.

To help develop more robust spectroscopy-based methods and analytical techniques to identify impactites on Mars and asteroids, we have assembled a large suite of naturally occurring impact glasses and compared their near-infrared reflectance and infrared emission spectra to search for empirical relationships that can be used to robustly identify glassy-impactite samples for the first time when robust geologic context is employed.

3.2 Experimental Procedure

A suite of glassy-impactites samples (described in Table 1, Appendix 3C) were crushed and dry sieved by hand to produce <45 μm powdered splits that were characterized by

Near-Infrared (NIR) reflectance and Fourier Transform Infrared (FTIR) emission spectroscopy.

NIR spectra were collected at the University of Winnipeg Planetary Spectroscopy Facility (PSF) using and Analogue Spectral Devices Inc. (ASDI) Field Spec Pro reflectance spectrometer. Spectra were collected, at incidence=30°, emission=0°, from 0.35 to 2.5 µm, relative to Spectralon® and corrected for minor irregularities in the spectrum of Spectralon between 2 and 2.5 µm. Wavelength calibration was performed via the periodic measurement of a holmium oxide wavelength standard. 1000 dark current, white reference and sample spectra were collected and averaged to increase the signal-to-noise ratio. Illumination was provided by a PSF built 50 watt collimated Quartz-Tungsten-Halogen light source. The FOV was ~ 5 mm as was the diameter of the spot illuminated by the collimated light source. The ASDI spectrometer uses a unique fibre-optic assembly with a random distribution of fibres at the pickup end that split internally to feed the three individual detectors. This arrangement can result in small reflectance offsets at the detector junctions at 1 and 1.83 µm and is the reason the FOV is listed as approximate. These offsets are corrected by normalizing the 0.35 to 1.0 and 1.83 to 2.5 µm ranges to the central detectors thermally stabilized 1.0 to 1.83 µm wavelength range. Spectra were collected and are presented in absolute reflectance.

Infrared (IR) emission spectroscopy was performed at Stony Brook University Earth and Planetary Remote Sensing lab/Vibrational Spectroscopy Laboratory. Emissivity spectra from 4000-225 cm-1 were collected using a Nicolet 6700 FTIR which has been modified to collect emissivity spectra using methods and apparatus similar to those detailed in Ruff et al., (1997). Spectra were collected at 80°C using the one temperature method of Ruff et al., (1997), using pellets produced by compacting the <45 µm powders in a 7.5 ton press.

The sample splits were prepared and NIR spectra were collected followed by powder X-Ray Diffraction (XRD) analyses. Aliquots of those samples were then prepared for FTIR emissivity analyses, while aliquots of a selected subset of the sample suite were prepared for X-Ray Fluorescence (XRF) and 29Si Nuclear Magnetic Resonance (NMR) analyses.

XRD was performed in the Powder X-Ray Diffraction and Micro X-Ray Diffraction Laboratory at the University of Western Ontario in the Department of Earth Sciences. XRF analyses and NMR spectroscopy were performed at the Laboratory for Geochemical Analysis and the J.B. Stothers NMR Facility, respectively, within the University of Western Ontario departments of Earth Sciences and Chemistry.

3.3 Sample Descriptions and Definitions: Glass, Glassy and Amorphous

Impact glass, as in purely amorphous material produced by hypervelocity impact events, is likely to be exceedingly rare at the hand-sample and outcrop scale that we can image with the highest resolution spectrometers currently interrogating the surface of Mars. Typically, impact glasses in terrestrial craters are restricted to isolated cm-sized clasts and particles in breccias and cm- to dm-sized quenched margins of larger melt bodies (Osinski et al., 2012). Our suite of glassy impactites and terrestrial impact glasses includes seven glasses (Table 1); IMP001, TEK001, the two DAK samples, 07044 and 07054, which are samples of Darwin Glass; an Indochinite tektite, two samples of Dakhleh glass; HMP00-263B from the Haughton Impact Structure which in hand sample looks like sandstone, but of low density; sample MM10-38 which is a hand sample from the Mistastin impact structure which is entirely diaplectic glass and one non-impact related pure glass sample, BAS101, which is an effusive basaltic glass sample from the Kilauea caldera. The majority in our samples and likely the majority on any of glass bearing impactites on any planetary surface will fall into the category we term glassy. Glassy refers to a sample where there is a mixture of glass and crystalline components, be they clasts from pre-impact target rock, quench crystallites or products of devitrification. The samples we refer to as glass are pure glasses, i.e., with no crystalline phases present in XRD patterns, or, where applicable, no crystalline component in their NMR spectra as well. The glasses we have defined here as pure, be they effusive, pyroclastic or impact generated meet this definition as defined by their XRD patterns and are homogenous on the macroscopic scale. All of the other samples within the sample suite, which were

collected and/or prepared by the authors, fall into the glassy category. Glassy refers to samples which may well be nearly 100% glass in content but have crystalline features as denoted by sharp peaks in their XRD patterns. Several samples were analysed by 29Si NMR and for those we can be definitive regarding glass versus crystalline content. Given how few 29Si NMR spectra we were able to obtain due to the ever-present complications of heterogeneity in natural samples and the paramagnetics within them, i.e., iron, it is difficult to derive the absolute amounts of glass and crystalline components in each sample. It should be noted that the samples in this suite are the glassiest we could find after sifting through hundreds of glassy-impactite samples and these represent the high end of the scale in terms of glass content. For the purposes of the discussion herein, we will refer to all of the samples as glassy-impactites.

Amorphous, as used herein, refers to glasses or the glass components of glassy samples and the structurally amorphous vitreous silica as observed by NIR and XRD (±NMR), rather than optically amorphous components. Our, and most glass samples, and the glass components of our glassy-impactite samples are structurally amorphous to some degree, i.e., they largely lack the long range structural order that gives rise to crystals. This contrasts with optically amorphous, i.e., samples where the grain size is smaller than the wavelengths of light interrogating the samples surface such that emitted light is almost completely specular such, as microscopically fine-grained clays which are both optically and X-ray amorphous as seen in Ries sample RI-01 and the surficial palagonitic dust coatings of Mars (Bell et al., 1993; Roush and Bell, 1995; Morris et al., 2003; and discussion below).

3.4 Spectral Features of Impactites

Following the determination of the glassiness of samples via NIR reflectance spectral measurements, we also investigated the plausibility of impact glasses containing spectral features unique to impactites imparted by the high pressures and accelerated quenching times that glassy impactite samples may well experience (see Velde and Couty, 1987;

Williams and Jeanloz, 1988; Williams and Jeanloz, 1989; Williams et al., 1993; and Agarwal and Tomozawa, 1997). A subset of the full sample suite was subjected to a third experimental procedure where aliquots of the <45 μm grain size splits were mixed with KBr to produce pellets for infrared transmission measurements.

We pursued this additional avenue of investigation because in-situ (i.e., in press, in diamond anvil cells) experimental results and models produced by several different researchers have suggested that, in addition to short range order increasing (i.e., the bonding environments becoming more alike) in the silica networks of glasses and producing sharper absorptions as can be seen in emission spectra, impactites can also exhibit new spectral features which arise from impact-created species having higher Si coordination numbers (Williams and Jeanloz, 1988; Williams and Jeanloz, 1989; Williams et al., 1993; Closman and Williams, 1995). We have found evidence for both of these effects occurring and being preserved in glassy impactites, although they are unlikely to be detectable in remotely-sensed spectra. The sharpened absorption features (i.e., narrower FWHM values) can be present in other silicate phases unrelated to impact, and new spectral features which arise from higher coordination sites within the glasses can only be seen spectrally in laboratory a transmission spectrum, which precludes the use of these laboratory spectra for comparison with emission spectra which can be remotely obtained. Though this course of investigation led to the exclusion of the use of laboratory transmission spectra, it led us to conclude that we needed to do more than simply investigate the spectra of glassy samples, but also the applicability of both NIR reflectance and IR emission spectra with regards to the usefulness of each wavelength region for making robust identifications of glassy impactites, non-impact glasses, and related silicate phases on the surface of Mars.

3.5 NIR versus IR and the Surface of Mars

No matter the type of spectra, reflectance or emission, geomorphology should be a driver for robust identification of surface materials. In both wavelength regimes, spectra alone,

especially the spectra of silicates, cannot robustly characterize the composition of a mixture of silicates outside of the laboratory. The surface of a body such as Mars will normally be a complex mixture of materials produced by chemical and physical weathering, and are mixtures of cohesive rock(s), and powdered materials of unknown grain sizes and packing densities. They are also likely to be optically complex (i.e., bare surfaces, coated surfaces, surfaces with significant phase variation within the imaged scene, significant shadowing, and so on) the combination of which precludes robust spectral interpretations. Imagery can help to resolve some of this complexity.

To attempt to reduce this complexity, we investigated which of the two wavelength regimes separately, or in combination, might lead to robust identification of glass/glassy and/or other high-silica phases that may be our best chance for finding the youngest plausible habitats for life on Mars, or those sites which may have exhumed or encapsulated evidence of Martian life (Izawa et al., 2010; Osinski et al., 2013; Schultz, 2014; Sapers et al., 2015).

Ideally NIR reflectance spectra would be preferred as the current CRISM instrument is of the highest spatial and spectral resolution compared to the thermal emission spectrometers such as TES and THEMIS. Unfortunately we have concluded NIR reflectance spectra is the least robust. The spectra of our glassy sample suite are depicted

in Figure 3-1.

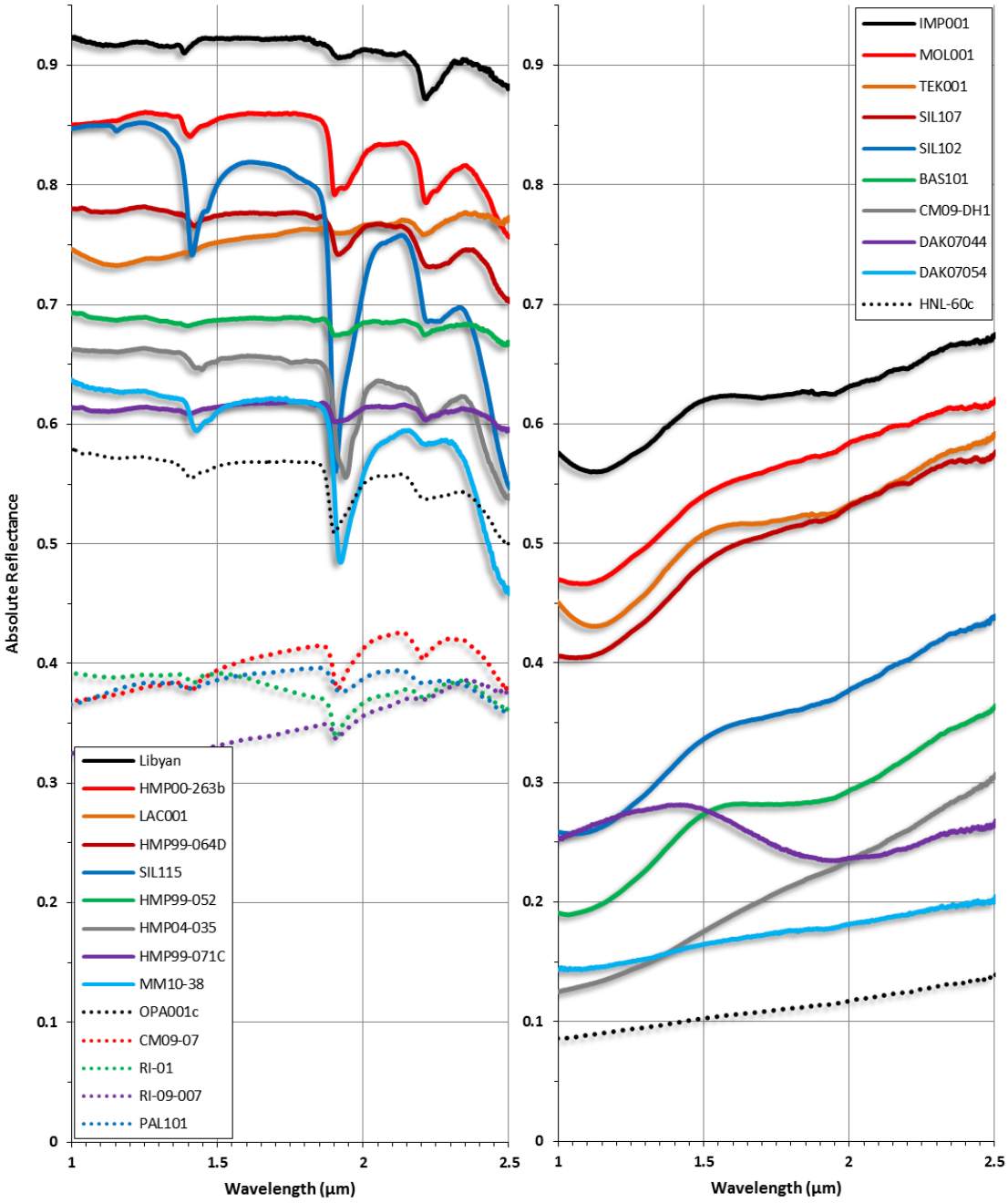

Figure 3-1: NIR absolute reflectance spectra of a suite of glassy-impactites and other silicates we would expect to find in and around impact sites on Mars which would complicate the robust identification of glassy-impactites. The left and right panels share the same absolute reflectance scale and a separated into hydrated and "dry," respectively.

We have restricted the wavelength window shown to that used by Cannon and Mustard, (2015) to compare our results to theirs concerning the efficacy of using NIR reflectance spectra to identify glassy-impactites. Panels A and B in Figure 3-1 are split into hydrated (A) and "dry" (B) suites, and include a subset of the full suite of glassy-impactites as well as the spectra of other silica-rich samples we might expect to be present in impact craters where we would be searching for glassy impactites and hydrothermal deposits, and the likely to be ubiquitous weathering product, palagonite (Morris et al., 2003). The two panels share the same absolute reflectance scale and are illustrative of reasons that suggest that NIR reflectance spectra are inappropriate to use to identify glass, glassy- or silica-rich impactites or impact related hydrothermal deposits among the suite of silicates that may be present in Martian impact craters:

There is no discernable trend within the spectral data set with regard to absolute reflectance. Silica content ranges from ~50-100% and this has no relationship to the sample albedo (see Appendix 3B). This is not unexpected, as accessory opaque materials can darken spectra without introducing additional absorption features (e.g., Britt and Pieters, 1994; Lucey and Riner, 2011).

I. Similarly, there is no discernable relationship between albedo and glass content. Pure glasses are both the darkest and the brightest samples (see Appendix 3B). Again, opaque phases, or small amounts of iron can substantially darken reflectance spectra of glasses (Craig et al., 2014).

II. There is no discernable trend with regard to the amount of crystalline content in each sample. High-silica crystalline minerals such as quartz and its high pressure polymorphs have no discernible spectral absorption features in the NIR. The samples with crystalline content that have NIR spectral features may be generally darker than those without, but they are intermingled with pure glass sample which span a wide range of albedos (see Appendices 3B and 3C).

III. Those samples with absorption features not associated with hydration (which are at ~1.4, 1.9, 2.2 and 2.7 μm in 1A) are related to very minor amounts of bound iron in crystallites and are not reliable indicators of glassiness as they could be masked by the crystal field absorptions in adjacent and intermingled crystalline materials (recall: these samples are the glassiest of glassy-impactites).

IV. Hydration features would appear to be of use but they are not, as shown by Closman and Williams, (1995); Navarra et al., (2009); Rice et al., (2013); and Smith et al., (2013), because with surface exposure on Mars the features of adsorbed water are likely to disappear and/or shift to longer wavelengths (as a result of dehydration and freezing, respectively), and the features associated with Si-OH vibrational modes become nondescript (i.e., they preferentially hydrogen bond, Si-OH-HO-Si and Si-OH-O, and no longer reference the underlying structure to which the Si atom is connected), despite becoming better resolved, such that hydration features in silicates become unreliable for identifying silicates of any origin.

V. With dehydration, we will not be able to discern the difference between hydrothermal silica deposits, glass- and glassy-impactites, and glassy acid weathering rinds in the NIR within the wavelength range shown by Cannon and Mustard, (2015), and throughout the full UV-thru-NIR wavelength range as shown in Horgan and Bell, (2012) and Craig et al., (2014).

VI. Spectral slope is not useful to discern between samples, as with dehydration, the slopes of the hydrated samples will either become indistinguishable from the spectrally dark dehydrated sample with shallow slopes which will darken the spectrum of any materials they are intimately mixed with (see the four least hydrated and darkest of the hydrated samples in 1A and dehydrated samples in Cloutis et al, 2008; Rice et al., 2013), or they will flatten and be very bright featureless spectra which will brighten other samples with which they are intimately mixed, both of which will occur in a highly non-linear manner (e.g., Clark, 1999).

VII. Pyroxene, olivine and glass spectra at grains sizes larger than those shown (i.e., >45 μm) and of cohesive rock are going to be saturated in the wavelength range from ~1 to 2.5 μm (Craig et al., 2007, 2008; and Appendix 3B). If one takes the saturated dark spectrum and scales it, adding spectral contrast, given the nature of band saturation (e.g., Clark and Roush, 1984; Lucey and Clark, 1985; Clark, 1999 and references therein) and the shape of the real continuum (see Chapter 2) when scaled, the saturating range from ~ 1 to 2.5 μm will be contrast stretched by the scaling of the spectrum and manufacture an absorption that mimics that of a crystallite bearing, shallowly sloped glass basaltic glass, where no absorption feature actually exists.

VIII. The featureless shallow slope of the dehydrated glassy impactites is essentially spectrally identical to the NIR spectrum of the vast majority of the palagonitic surface of Mars (Morris et al., 2003).

IX. Intimate mixtures of minerals do not mix linearly in the NIR (see Singer 1981; Clark and Roush, 1984; Clark, 1999; Kraft et al., 2003; and Berger et al., 2015), and we cannot apply a linear intimate mixing model to NIR reflectance spectra of intimate mixtures likely to be present on the surface of Mars.

Contrasting with NIR reflectance spectra, IR emission spectra are significantly more useful. While we are still not be able to be absolutely definitive about hydrothermal deposits, glass- and glassy-impactites, glassy weathering rinds and other silicates in intimate and areal mixtures, because of the poor spatial resolution of our presently available emission data sets, IR emission spectra can point us in a direction, with context, that NIR cannot.

3.6 Curve Fitting IR

Ramsey and Christensen, (1998), established that to a first approximation, linear mixing and unmixing (spectral deconvolution) of infrared spectra to discern spectral contributors in intimate mixtures is a viable technique. Linear unmixing has been used to describe the

surficial mineralogy of the majority of the surface of Mars, but not without disagreement (see Bandfield et al., 2000; Bandfield, 2002; Hamilton et al., 2001; McSween, et al., 2003, Rogers, 2007; Roger et al, 2007; Ruff et al., 2007; Wyatt et al., 2001; Wyatt and McSween, 2007). We would suggest the mineralogical uncertainties stem from two sources: 1) The spatial resolution of the TES data sets results in a lack of specificity, as each spectrum covers a wide swath of ground representing intimate and areal mixtures of multiple materials on a large scale; and 2) The process of deconvolution involves the use of a data set of laboratory spectra which is under-constrained (i.e., to few spectra, and/or spectra without enough mineralogical variety), the deconvolution algorithms in early modeling returned an answer even when none made sense (i.e., given a large enough data set of spectra almost anything can be modelled by spectra which have no physical relationship with the spectrum being modelled, e.g., sulphates can adequately model silicates), and when modelling silicates with silicates, the deconvolved fit returned will be of silicates, but it is unlikely to be the same set of silicates twice (e.g., McSween et al. 2013, and references therein). These limitations have been recognized and discussed in most previous studies.

Rather than perform linear deconvolution we have taken another approach based on the empirical curve fitting methods described in Chapter 2. To our knowledge this is the first implementation of empirical curve fitting methods applied to IR emission spectra.

Laboratory IR emission spectra where split into two wavelength regions based on the CO2 windows of the Martian atmosphere, spanning ~6 to 12.9 and 17.8 to 25 μm (Smith et al., 2000). Thusly isolated, the band minima were derived using 3rd order polynomials, band depths were calculated from unity to the depth of the derived minima, areas were calculated using a chord-based method based on Lagrange-Polynomials to interpolate new data points between existing measured spectral data points, which were fit to spectral ranges ± 1 μm of the derived band minimum. Full Width at Half Maximum (FWHM), Right Width at Half Maximum (RWHM) and Left Width at Half Maximum (LWHM) were calculated based on the nearest real measured spectral value to the

derived half-maximum depth point (See Appendix 3C for spectra and curve fitting, and see Chapter 2 for procedures)

The results of fitting our sample suite as well as selected spectra from Bandfield et al., (2000); Michalski et al., (2003), Minitti and Hamilton, (2010); and Wyatt et al., (2001) are presented in Figure 3-2. We chose the relationship between the measured minimum of the ~8.8 to 10.3 µm stretching fundamental of Si-O-Si (see Agarwal and Tomozawa, 1997; Efimov and Pogareva, 2006) and the derived RWHM of the same absorption, which we have called Band I, as the empirical relationship most useful for robustly identifying silicate type based on IR emission spectra (Further 2-dimensional empirical relationships are explored in Appendix 3C).

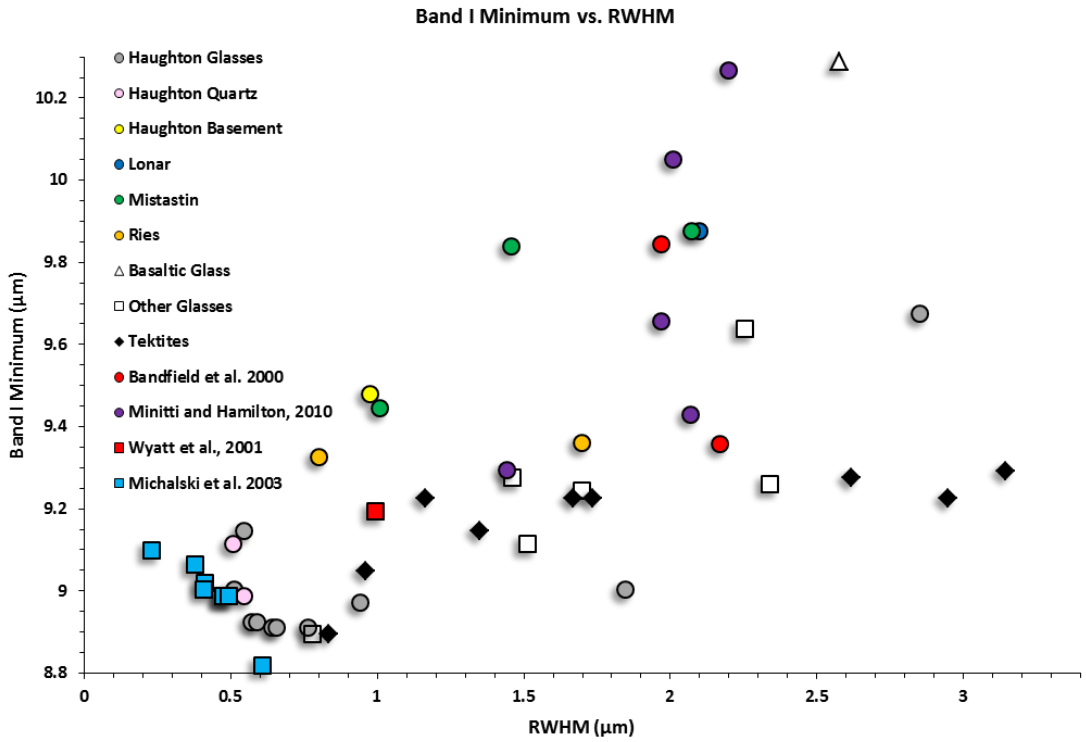

Figure 3-2: Right Width at Half Maximum (RWHM) of the ~ 8.8 to 10.5 µm asymmetric fundamental vibrational IR emission absorption of the silica versus the absorption minimum of that same absorption for our suite of glassy-impactites and examples available in the literature. In general, glassy-impactites form a band across the bottom

with high-silica glassy-impactites and evaporites clustered at the bottom left. Volcanic, pyroclastic and the more canonical impact related glasses form an arc on the right side of the figure.

3.7 Discussion

Thorough exploration of the IR emission spectra of glasses presents unique opportunities, as IR spectra can, and do evidence, the degree of ordering in the glasses. The FWHM values of spectral absorptions are a measure of the width of the Si-O-Si stretching vibration absorption centred at ~ 9.25 μm and the clearest indicator of a preferential Si-O-Si bond angle within amorphous glasses (Velde and Couty, 1987; Hazen et al., 1989). In-situ experiments have clearly demonstrated that silica glasses exposed to high pressures and varying temperatures evidence different preferential bond angle arrangements (Velde and Couty, 1987; Williams and Jeanloz, 1988; Hazen et al., 1989; Farnan et al., 1992; Williams et al., 1993; Closman and Williams, 1995; Agarwal and Tomozawa, 1997; Koike and Tomozawa, 2007; Inamura et al., 2007; Reibstein et al, 2011). Glasses probed under high pressure in-situ experiments have new absorption features that arise from the development of higher order silica coordination environments (e.g., Velde and Couty, 1987, Williams et al., 1993). While these new absorption features disappear in glasses that cannot be quenched quickly enough such that the glasses relax, herein we report the first evidence for the preservation of higher order Si-O coordination environments in impactites.

The structure of silica glasses and amorphous solids is a field of study unto itself with a myriad of manuscripts and several journals dedicated to their study. Interrogating the wealth of information contained in the vastness of the field is beyond the scope of this work; what is of interest is how pressure, temperature and quench rate affect the amorphous mid- thru high-silica glasses found in impact sites terrestrially and on Mars. The majority of the references, reference pure, synthetic silica glasses, with emphasis on low to high-pressure experiment and modelling discussing melts within the Earth and not

siliceous impact glasses. Several of the samples are "pure" silica glasses, as in, all of the silica content within the samples appears to be amorphous to the best of our ability to discern this using near-infrared (NIR) reflectance, IR emission spectra, powder XRD and ^{29}Si NMR, and these pure glasses are likely to be rather rare in nature. Glass by definition is structurally amorphous (but not necessarily optically amorphous), although locally SiO_4 tetrahedra are locally ordered (i.e., bond lengths and angles maintain a tetrahedral arrangement), they are disordered on intermediate-range scales (i.e., Si-O-Si linkages are not regular periodic environments) which leads to the disruption of the long-range symmetry inherent in crystalline silicates (Farnan et al., 1992). As a consequence, we can still "see" the IR spectral fundamental absorptions in silicate glasses and assess the changes which occur in their infrared spectra that have been subjected to an increase in fictive temperature, and high-pressures.

Most interesting are the changes in the position, shape and relative intensity of the Si-O-Si stretching fundamental absorption band, which we refer to as Band I, and the occurrence of new absorption features which arise as pressure increases and new silica species of 5- and 6-fold coordination are created (Williams and Jeanloz, 1988; Closman and Williams, 1995; Agarwal and Tomozawa, 1997; Martonak et al., 2006). For example, with an increase in applied pressure, the Si-O-Si bond angle in silica glasses decreases, which results in a decrease in the wavenumber (increase in wavelength) band minimum position of the ~ 8.5 to 10.5 μm Band I absorption. Increases in applied pressure also result in decreases in viscosity, compressibility and diffusion coefficient, with increases in density, refractive index, coefficient of thermal expansion, etch rate and hardness (Agarwal and Tomozawa, 1997). The shift of the Band I minimum with the application of increasingly higher pressure spans a large range in pure silica samples and given the contamination in natural samples from other crystalline silica phases, especially the basaltic glasses, band shift cannot simply use this indicator to suggest what pressure was ultimately applied (though it is a favoured empirical metric). Whether or not spectral features which arise from exposure to high-pressure are retained metastably at ambient pressure is also a concern as researchers have found that not all of the spectrally

characterizable features of a high-pressure excursion may be quenchable (e.g. Closman and Williams, 1995; Inamura et al., 2007).

The question of the retention of a spectral feature indicative of high-pressure revolves around how quickly the pressure and temperature change in the system, as pressure, temperature and volume are intimately linked. Experiments i*n-situ* using diamond anvil cells require time to cool and/or decompress, which means in these experiments, samples which are quenched pass through the pressure-temperature points of phase transition slowly, giving the glasses time to relax, which may remove spectral features which arose from the creation of ^{5}Si and ^{6}Si coordination environments, as is seen in models (e.g., Rustad et al., 1992; Martonak et al., 2006) and *in-situ* experiments using various techniques to assess order change and densification of glasses (e.g., Velde and Couty, 1987; Williams and Jeanloz, 1988; Williams et al., 1993; Closman et al., 1995; Inamura et al., 2007; Koike and Tomozawa, 2007; Reibstein et al., 2011). Change in the dimensions of the unit cell of the silica tetrahedron itself are relatively minor to modelled pressures of 70 GPa and measured experimentally to 47 GPa (Rustad et al., 1992; Williams et al., 1993). The densification and order changes, which occur in glasses and can be seen spectrally, occur not because the silica tetrahedron is being compressed, but rather because the network is being modified. With increasing pressure, tetrahedra rearrange themselves and their short- to intermediate-range order is modified (i.e., the bridging oxygen bond angle closes), then as pressure increases further, the interpolyhedral repulsion produced by the short oxygen-oxygen distance of the silica tetrahedra results in a distortion of the tetrahedron itself, where two of the four O-Si-O bond angles open which is followed by the creation of a fifth silicon-oxygen bond between closely approaching silicon and oxygen neighbors (Williams et al., 1993). This produces the range of 4- and 6-fold coordination environments which have been evidenced spectrally (e.g., Williams and Jeanloz, 1988; Williams et al., 1993; Closman and Williams, 1995; Agarwal and Tomozawa, 1997), and modelled (e.g., Rustad et al., 1992; Martonak et al., 2006). The same effect of order change with increasing pressure and fictive temperature has been noted using *in-situ* Single X-Ray Scattering, Synchrotron Small Angle X-Ray Scattering, and XRD experiments referencing the first

sharp diffraction peak (e.g., Hazen et al., 1989; Inamura et al., 2007; Reibstein et al., 2011), and post quench NMR (e.g., Farnan et al., 1992)

Both fictive temperature and pressure/compression affect the IR spectra of glasses (as do composition, grain size, and so on). Fictive temperature is defined as "the temperature at which the glass would find itself in equilibrium if suddenly brought to that temperature from its given state" by Tool, (1946). In other words, fictive temperature is the maximum temperature which a glass experiences, if it is allowed to experience it for enough time to equilibrate. Fictive temperature affects the position of the IR fundamentals of glasses, but over ranges as large as 500°C, the resulting shift in minimum position is a maximum of 3 nanometres. i.e., too negligible to be a consideration (Agarwal and Tomozawa, 1997; Koike and Tomozawa, 2007). Pressure change however will affect an absorption's wavelength, depth and width. Increasing pressure will shift the band minima wavelengths by firstly splitting them to create a triplet, followed by larger shifts to longer wavelengths of up to 0.13 to 0.15 μm from 0 to 4 GPa (Velde and Couty, 1997; Williams and Jeanloz, 1993; Williams et al., 1993, Agarwal and Tomozawa, 1997; Koike and Tomozawa, 2007). Further increases in pressure thru 30 GPa result in marginally larger shifts in band minima with significant decreases in band depths and broadening of bands; Band I disappears over ~ 30 GPa (Williams et al, 1993; Closman and Williams, 1995). Closman and Williams, (1995), also note, akin to the low temperature spectra of Navarra et al., (2009), that hydroxyl groups bonded to silica favour H-bonding as pressure rises and their band centres shift quite significantly between ~4 and ~4.5 μm with pressure increase through approximately 0 to 30 GPa and eventually disappear, but these absorptions are outside the working wavelength range of the Mars Global Surveyor Thermal emission spectrometer whose data set we wish to exploit with our glassy-impactite emission spectra (Christensen et al., 2001).

In general, most researchers agree that the following is occurring in the IR spectra of glasses, α-quartz, cristobalite, tridymite, coesite, stishovite, and a modelled post-stishovite stage noted by Martonak et al., (2006): with increasing pressure, the

fundamental vibrational absorptions of silica glasses, and the high-pressure polymorphs of quartz first split, to form three absorptions, then shift to higher wavelengths (lower wavenumbers) concurrently with a loss of depth and resolvability. At lower pressures, below ~ 10 GPa, the changes are the result of compaction of the silicate network and change in the short-range ordering due to closing of the bridging oxygen bond angles between adjacent tetrahedra. Above ~ 10 GPa, the silica tetrahedra are distorting and ^{5}Si and ^{6}Si domains are forming. The higher coordination environments give rise to new spectral features that coexist with those of the silica tetrahedra between ~ 11.7 and 13 μm (Williams and Jeanloz, 1988). The spectral features which appear in the glasses are caused by quartz-, coesite- and stishovite-like domains in the glass, but it is important to note that they are still amorphous materials, and new spectral absorptions which appear are not the result of long-range ordering due to the appearance of crystalline phases (Williams et al., 1993). The transitions which occur and produce compaction leading to band shift and higher-order domain creation do not occur along a continuum, but rather, abruptly with several steps and significant changes in enthalpy associated with each (Rustad et al. 1992; Martonak et al., 2006). The same is true in reverse, much like the quartz, coesite, stishovite transitions, the rate at which the transitions are crossed in both pressure and temperature drives the quenchability of densified glasses and the 5- and 6-fold coordination environments within them. In most *in-situ* experiments the cool down and/or pressure release is too slow and, for example, in the experiments performed by Closman and Williams, (1995) the spectral features noted in samples *in-situ* above 30 GPa were not quenchable, as they reverted on decompression. Depending on apparatus, speed, and ultimate pressure reached, this is not always true as the samples in the experiments of Closman and Williams, (1995) which were quenched from pressure not exceeding 30 GPa retained many of their high-pressure IR absorptions and, Inamura et al., (2007) and Reibstein et al., (2011), working at pressure bellow ~ 7.4 GPa quenched samples which retained mid- and long-range order increase and densification of 20%, respectively. One should expect that given the remarkable speed with which pressure and temperatures can change in hypervelocity impacts on compression and decompression,

glassy impactites are likely to evidence the same sorts of spectral IR absorption features and changes researchers are creating in the laboratory.

Given the evidence presented it behooved us to search for these spectral features. Published IR spectra of glasses subject to high-pressures show where the shifts in band minima are significant, but the absorptions which arise due the creation of higher-order coordination environments are rather muted (see Velde and Couty, 1987; Williams and Jeanloz, 1988; Williams et al., 1993; Closman and Williams, 1995). Given the nature of these absorptions, we supposed the spectral absorption splitting and weak absorption of ^{5}Si and ^{6}Si environments were unlikely to be resolved in IR emission spectra, but might be discernable in contrast optimized transmission spectra; a supposition which held. We collected IR transmission/absorbance spectra of the same <45 μm grain size splits as the NIR spectra, mixed with KBr to produce pellets for collection of transmission spectra. Transmission spectra were collected using the Bruker Vertex 70 FTIR, from 5000 to 400 cm^{-1} using the Stirling cooled internal MCT detector at a resolution of 2 cm^{-1} in a dry, purged nitrogen atmosphere. Normally, sample and KBr would be mixed in fixed ratios. Given the weakness of the spectral features we were looking for and the expected significant loss of absorption depth, a new experimental procedure was devised. Sample powders and KBr were mixed and pressed into pellets, spectra were collected, then new pellets were produced and spectra were again collected until changing the ratio of sample powder to KBr up or down no longer affected the overall contrast ratio of the collected spectrum. This was performed to capture each sample spectrum with the absolute maximum spectral contrast ratio possible so we could best resolve the absorptions of interest. This method of spectral collection did result in success, and we were able to resolve the features of interest as depicted in Figure 3-3. The laboratory transmission/absorbance spectra will not be useful when searching for glasses and glassy-impactites remotely on Mars.

In the upper chart of Figure 3-3, one can see the well-resolved splitting of the 9.145 μm asymmetric stretching Band I of MOL001, a purely glass, Moldavite tektite. The spectral absorption at ~ 12.5 μm and the loss of band depth at 9.145 and ~ 21.5 μm are clear

(recall this is the maximum achievable spectral contrast ratio). Ideally from this we could infer the sample had experienced pressures above 27 GPa, but not significantly higher as Band I is still quite resolvable. If we applied the same criteria to sample BAS101 however, one might be inclined to think this effusive basaltic glass sample had experienced a similar high pressure excursion, as its Band I minimum is shifted, and its Band I and ~ 21.5 µm absorption depths are muted, though it has not experienced pressures above ambient while quenching in air; this is the first issue that arises when attempting to discern volcanic/pyroclastic versus impact origin for glassy samples.

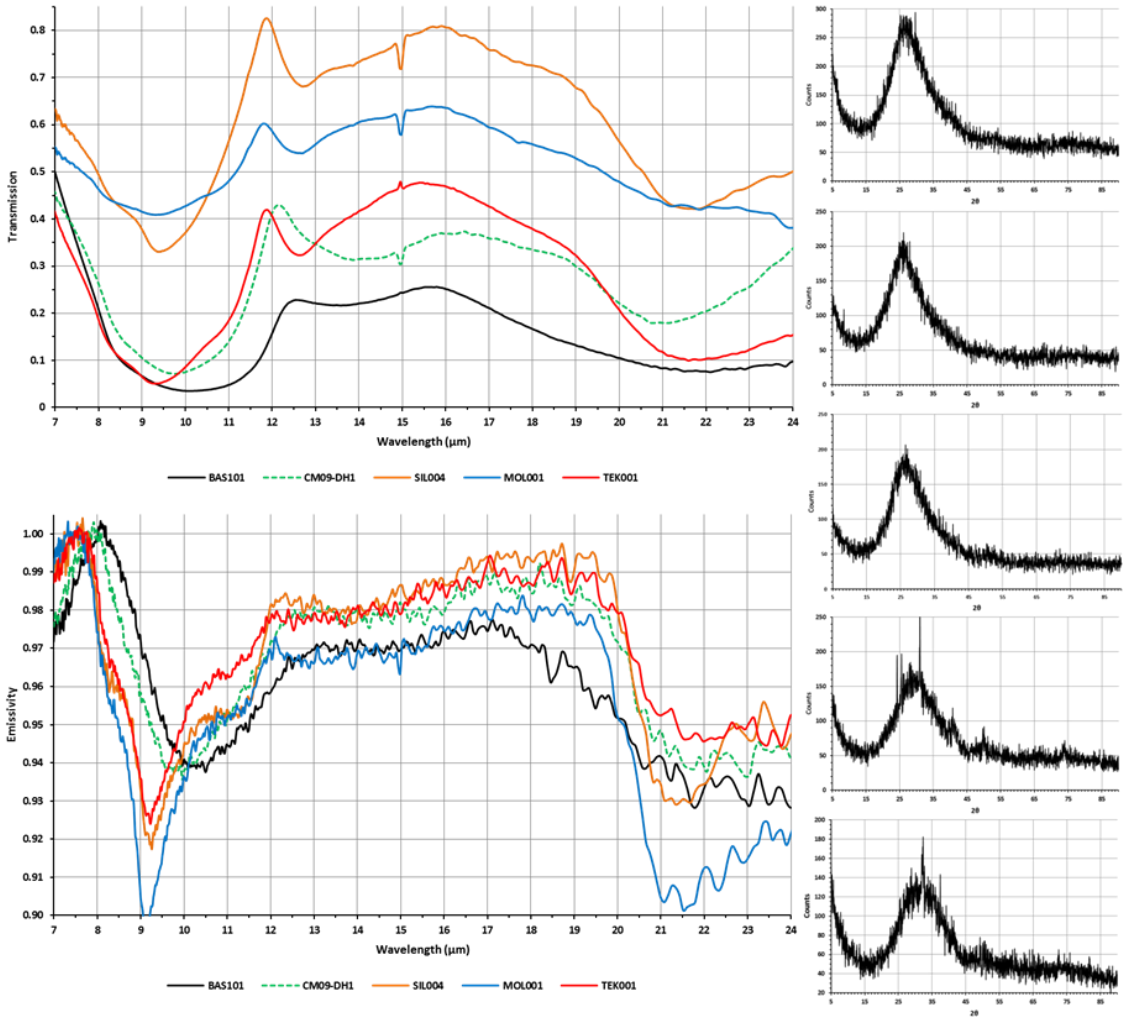

Figure 3-3: IR transmission and emission spectra and powder XRD patterns of 5 glass samples. BAS 101, a Hawaiian effusive basaltic glass, and glassy-impactites, CM09-

DH1, SIL004, MOL001 and TEK001, which are a basaltic impact glass from the Mistastin Crater, pyroclastic Apache Tears, and Moldavite and Indochinite tektites respectively. The powder XRD patterns on the right ascend in the same order as they run

left-to-right in the two charts of spectra.

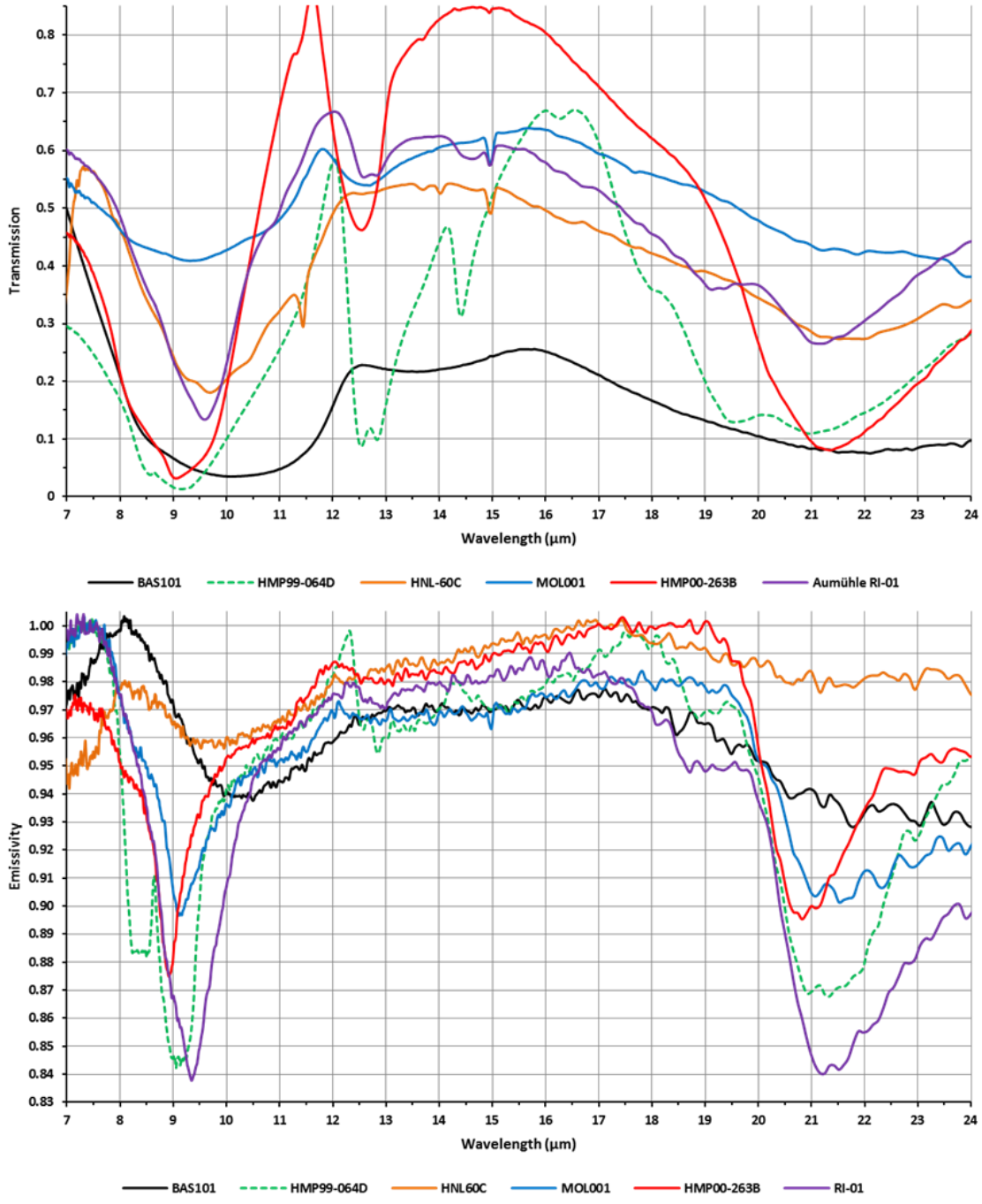

Figure 3-4: IR transmission and emission spectra BAS 101, a Hawaiian effusive basaltic glass, HMP99-064D which is pure detrital quartz from Haughton and glassy-impactites, HNL60C, MOL001, HMP00-263B and TEK001, which are a basaltic impact glass from

the Lonar Crater (clearly more effusive in nature), a Moldavite tektite, a nearly pure glassy-impactite from Haughton (see Figure 3-3) and a glassy-impactite for Ries Crater which is partially devitrified and contains some phyllosilicates.

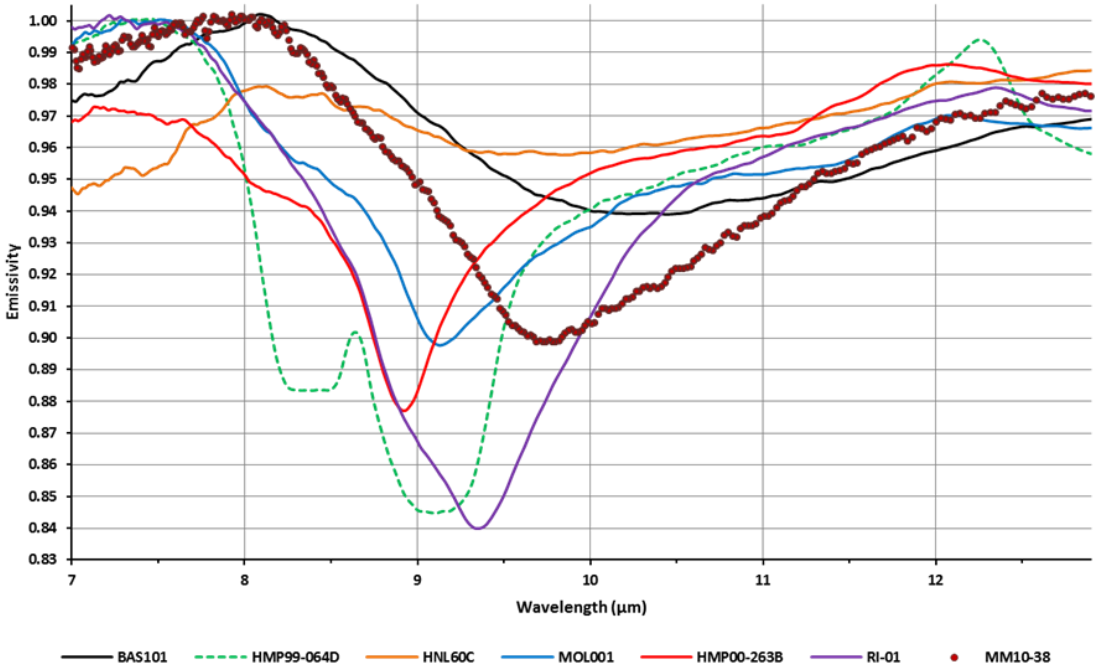

Figure 3-5: IR emission spectra in our window of interest for Mars. These are spectra of the same samples as in Figure 3-4 with the addition of diaplectic glass sample MM10-38. Spectra are smoothed using a 9-point boxcar function to ease separation of spectra by eye.

The second problem arises when we look at the emission IR spectra in the lower chart of Figure 3-3. Here we can very clearly see the different between an effusive glass, BAS101, and an impact glass, MOL001. MOL001 clearly demonstrates the sharpened asymmetric stretching fundamental, Band I, but it is not muted as it is in transmission spectra, nor is its ~ 21.5 µm bending fundamental absorption (relative to crystalline phases and/or un-densified glass, see Figure 3-4), and the secondary absorptions associated with ^{5}Si and ^{6}Si are now a muted shoulder at approximately 11 µm which is difficult to resolve empirically.

In emission spectra the evidence for an increase in ordering remains apparent, but the evidence for excursions to extremely high pressures is more elusive. If we did not know that BAS101 was an effusive volcanic glass and HNL-60C (depicted in Figure 3-4) was a basaltic impact glass from Lonar, we may mistake both samples for glassy-impactites when only one is impact related in origin, where both are canonical basaltic glasses, and their muted broad IR absorptions in both IR transmission and emission spectra are the result of pyroxene crystallites in the glass and not impact-related compression features. The third issue which arises when working with IR emission and transmission spectra are absorptions associated with detrital or recrystallized crystalline phases. We have found pure glass, and very nearly pure glass samples (as depicted in Figure 3-3) to be exceedingly rare in terrestrial impact sites and volcanic/pyroclastic glasses (also see Osinski, 2003; Wright et al., 2011). In Figure 3-4 we have included the spectra of glassy-impactites which contain crystalline phases: minor amounts of crystalline pyroxene in BAS101, with more present in HNL-60C, pure detrital quartz HMP99-064D, approximately 0.02% crystalline quartz by volume in HMP00-263B and minor phyllosilicates in sample RI-01. Referencing the upper chart of Figure 3-4, and concentrating on the transmission spectra, in both of the pyroxene-bearing samples (the basaltic glasses from Hawaii and Lonar Crater), the presence of nearly undetectable pyroxene in BAS101 and marginally more (but still on the order on less than 1%) in HNL-60C, has a clear effect on their spectrum. It results in mimicry of the features one expects in very highly compressed impact glasses. In Sample MOL001, the Moldavite tektite, we know there is no discernible crystalline content (via XRD or ^{29}Si NMR) but if we did not, the absorption at approximately 12.5 μm could be interpreted as a minor amount of quartz. In sample HMP00-263B we know the amount of quartz is minute, but the effect it has on the spectrum appears to be rather significant. In sample RI-01 spectrum there are clearly resolvable quartz and clay spectral features. Contrasted with the emission spectra in the lower chart of Figure 3-4, much of what might lead one to identify crystalline phases in these samples disappears. Only the crystalline quartz, HMP99-064D has a spectrum that is clearly something other than glass. The two basaltic glasses appear as though they are highly compressed, though they are not, RI-01 appears

glassy, but may have excess depth (though without broad comparison with phyllosilicate and non-phyllosilicate bearing samples we cannot be certain) and a spectral feature we might attribute to quartz at ~ 19 µm, we may not, as spectra originally collected in cm^{-1} are becoming exceedingly poor in wavelength resolution (see the example in Appendix 3C, Sheet *Spectra*). When focused purely on emission spectra, as it can be applied when attempting to interpret mineralogy for Mars and other planetary surfaces, and using the ~ 9 µm spectral absorption alone as our source of empirical metrics, one can see in Figure 3-5 that the individually resolvable features which where resolvable in the hyper-contrast transmission spectra are no longer of use. All that remains of their presence in the emission spectrum are weakly contributing shoulders that contribute to the RWHM measures, but whose minima/centres cannot be fit empirically.

Given the lack of resolvability of fine and/or weakly contributing (i.e., not of significant band depth) spectral absorptions in IR emission spectra that might arise from higher order coordination environments, we have found searching for these features in IR emission spectra to be of no use. We also find the spectral resolution beyond 17.8 µm to be inadequate for characterizing these features. Finally, through comparison of combinations of all the empirical metrics we derived, we have found concentrating in Band I alone to be most efficacious.

The following three Figures (3-6, 3-7 and 3-8) are XRD patterns and NMR spectra of three samples: HMP00-263B is the glassiest of the Haughton impact crater samples but contains minor trace quartz as seen by XRD (Figure 3-6). This amount is too small to be seen by NMR, which is an inherently insensitive technique; HMP00-264B (Figure 3-7) also contains quartz but significantly more than 263B. One can see the influence of amount of quartz but we cannot simply add the two values for silica, quartz and an amorphous component in 263B as we can in 264B. For example, in sample 264B the sharp peak centred at ~ 107 ppm indicative of silica in quartz has a modelled unitless area value of ~ 2,200,000,000 while the broad peak centred at ~ 111 ppm indicative of amorphous silica has a unitless area value of ~ 280,000,000, the total silica content by area is ~ 2,480,000,000, which calculates out to volumetric total silica content of

approximately 11% crystalline, 89% glass. Ideally we would then apply this relationship to other samples to derive glass content, but this will be the focus of future work using the handful of samples successfully analysed via ^{29}Si NMR. For sample HMP00-264B, we have a reasonable handle on total silica content, and Rietveld quality XRD data to measure peak counts, from which we could then calculate the total volume of the other crystalline content, but for the purposes of this manuscript; the spectra of these three examples clearly demonstrate how little the crystalline content is influencing the infrared (IR) emission spectra of interest. Also included (Figure 3-8) are the XRD pattern and ^{29}Si NMR spectrum of the purely glass sample MOL001, a Moldavite tektite which retains some of the short-range ordering imparted by quench; and falls on Figure 3-2 (and Figure 3-9) between the canonical more effusive glasses of the right side of Figure 3-9 (and Figure 3-2) and the glassy-impactites from the Haughton, Ries and Mistastin craters.

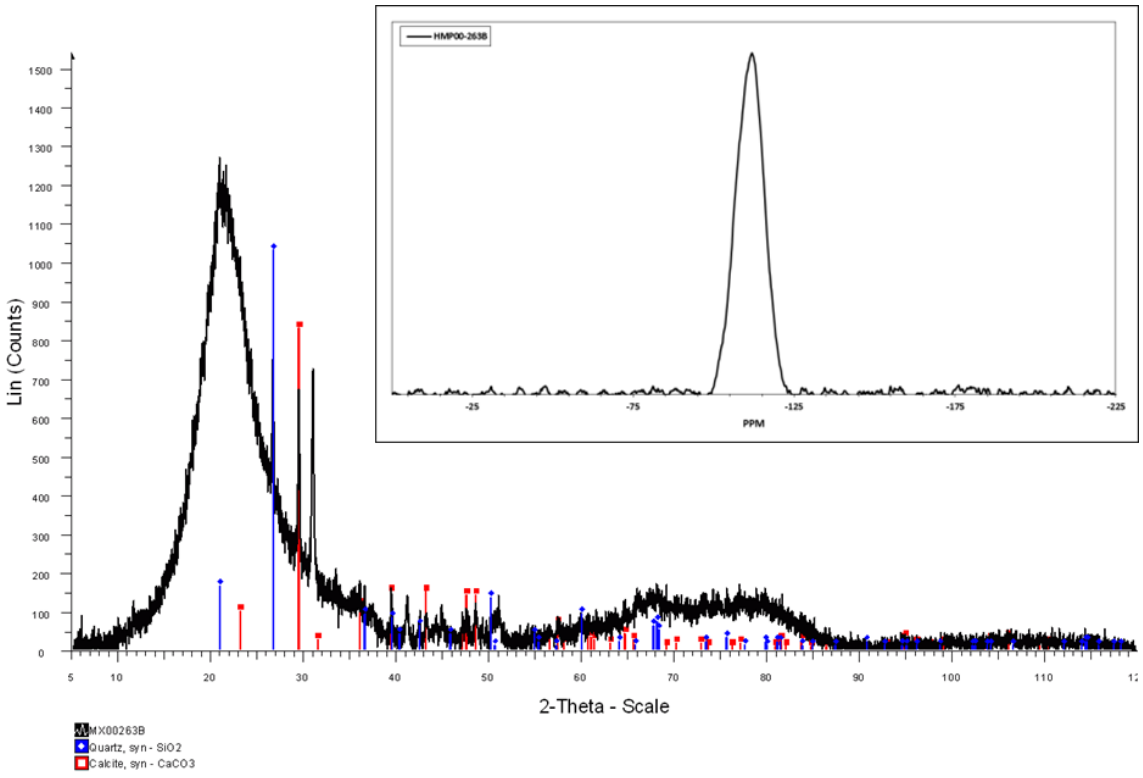

Figure 3-6: XRD Pattern and NMR spectra of Haughton glassy-impactite HMP00-263B. This is the glassiest Haughton sample and one can see how little the quartz is influencing

the stretching fundamental vibration of Si-O-Si at 8.9 µm in Band I in the Figure in Sheet *11* of Appendix 3C. The influence of the minor amount of quartz in the sample can be seen by the crystalline peak, demarcated in blue in the XRD pattern and asymmetry of the PPM shift peak short-ward of its ~111.4 PPM centre. Based on Pseudo-Voigt modelling of the NMR peaks, the silica component of HMP00-263B is ~ 99.8% glass based on modelled peak area.

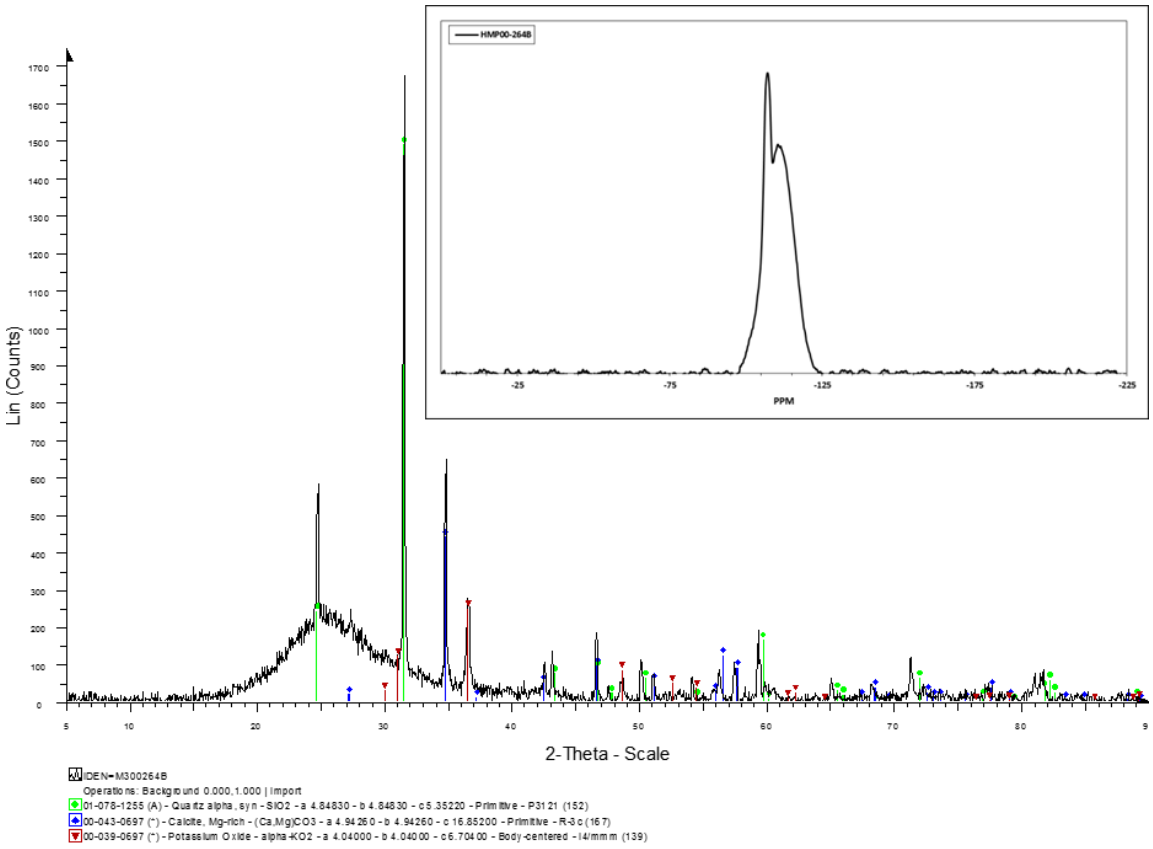

Figure 3-7: XRD pattern and NMR spectra of Haughton sample HMP00-264B. This sample is somewhat intermediate in the suite. One can clearly see the influence of this moderate volume of quartz in the IR emission spectrum in Sheet *12*, Appendix 3C, but even though it is quite apparent, and comprises ~11% of the silica content of the sample, the quartz' influence on the position of the glassy-impactites Band I minimum and RWHM value is negligible. If you would like to see an example of the spectrum of pure quartz, see sample HMP99-064D in Sheet *3*, Appendix 3C. Note: this sample contains a

marginal amount of crystalline oxide (likely iron and not potassium) and Morris et al., (2000), found that changes in iron oxidation state in glassy samples, has no discernable effect of their IR spectrum, and iron oxides are spectrally featureless in the Band I region in our IR emission spectra (see Christensen et al., 2000; Glotch et al., 2004).

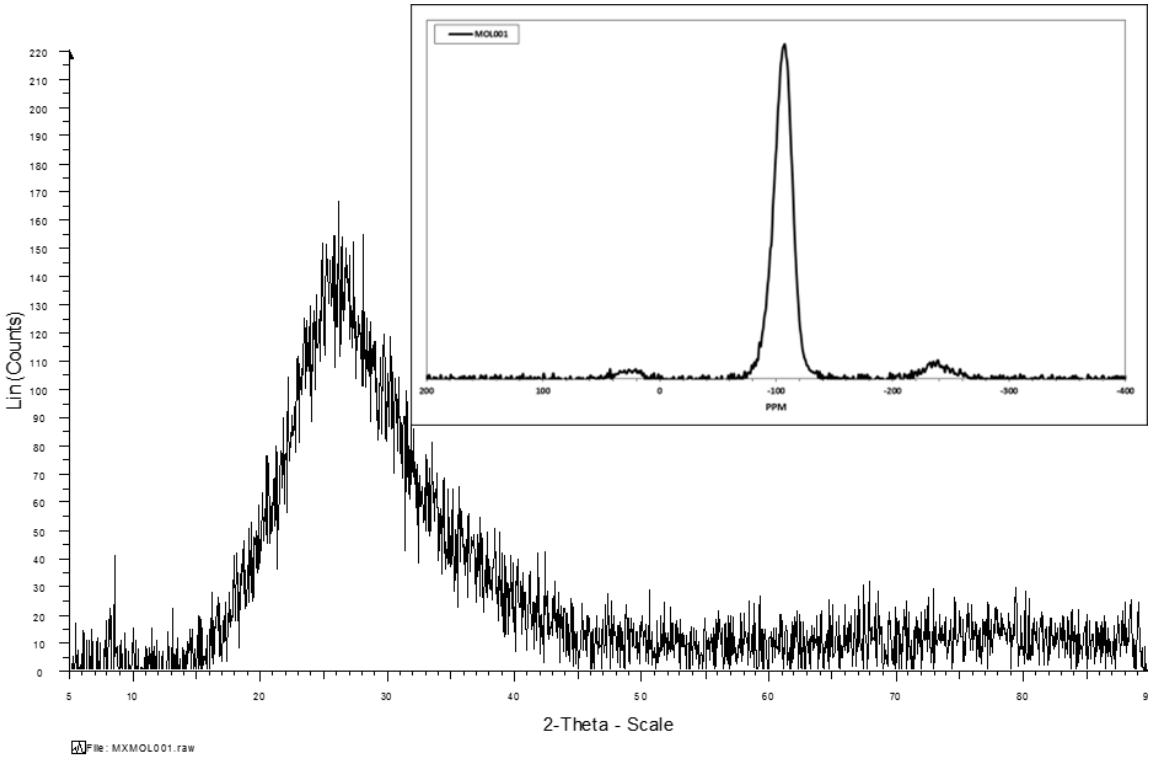

Figure 3-8: XRD pattern and NMR spectra of sample MOL001 which is a Moldavite tektite. This sample is pure glass as evidenced by its XRD pattern and NMR spectrum. The IR emission spectrum of this sample is shown in Sheet *26*, Appendix 3C, and its Band I is sharpened as one would expect for a glassy-impactite, but not to the same extent as Band I of HMP00-263B or 00-264B. These differences arise as a result of the different formation environments of these samples; the Haughton samples are both clasts found within the melt breccia of Haughton crater and likely to have quenched from rapid pressure release in the crater floor while the Moldavite quenched very quickly in air under little to no constraining pressure. Sample MM10-38 (not shown here) is purely

diaplectic glass at hand sample scale and its IR emission spectrum has very nearly the same RWHM as MOL001 but its Band I minimum position places it closer to the basaltic samples in composition which is in harmony with its plausible origin (see Stöffler et al., 2002).

Hyper velocity impacts are exceedingly complex events that have greatly affected the surface of Mars. Though impact craters are geomorphologically quite complex we can make broad generalizations about where we might find glassy-impactites, their lithology, their composition and the generalized spectrum for each locale. On Mars we can generally expect the majority of impactites to favour a basaltic starting composition, and in small simple craters, where no central uplift has formed (i.e., no significant excavation from depth), we would expect glassy-impactites to reflect their low-silica (relative to our suite of glassy-impactites) composition and fall largely within the blue shaded population of effusive volcanic, pyroclastic glasses and glassy-impactites which formed without constraining or high-pressure excursion. In our sample suite, we have four basaltic samples, one from Hawaii, an effusive basaltic glass, a second from Lonar crater, also effusive, and two glassy-impactites from Ries crater. Both of the canonical, effusive basaltic glass samples fall within the shaded blue region of Figure 3-9. One should not expect this to always be the case for basaltic glassy-impactites however. Samples from Ries and the like samples from Lonar, studied by Wright et al., (2011), are basaltic glassy-impactites whose IR emission spectra strongly resemble those of the samples transitioning between the blue and red populations of Figure 3-9 with a significantly sharpened Band I absorption. Basaltic glass samples from classes 5A and 5B (those with the highest supposed pressure exposure) of Wright et al., (2011) ,would fall approximately between the two populations of Figure 3-9 near the green arrow as do the

Ries, two of the Mistastin samples and HMP04-035 which is a sample of shock-melted granitic basement rock from Haughton.

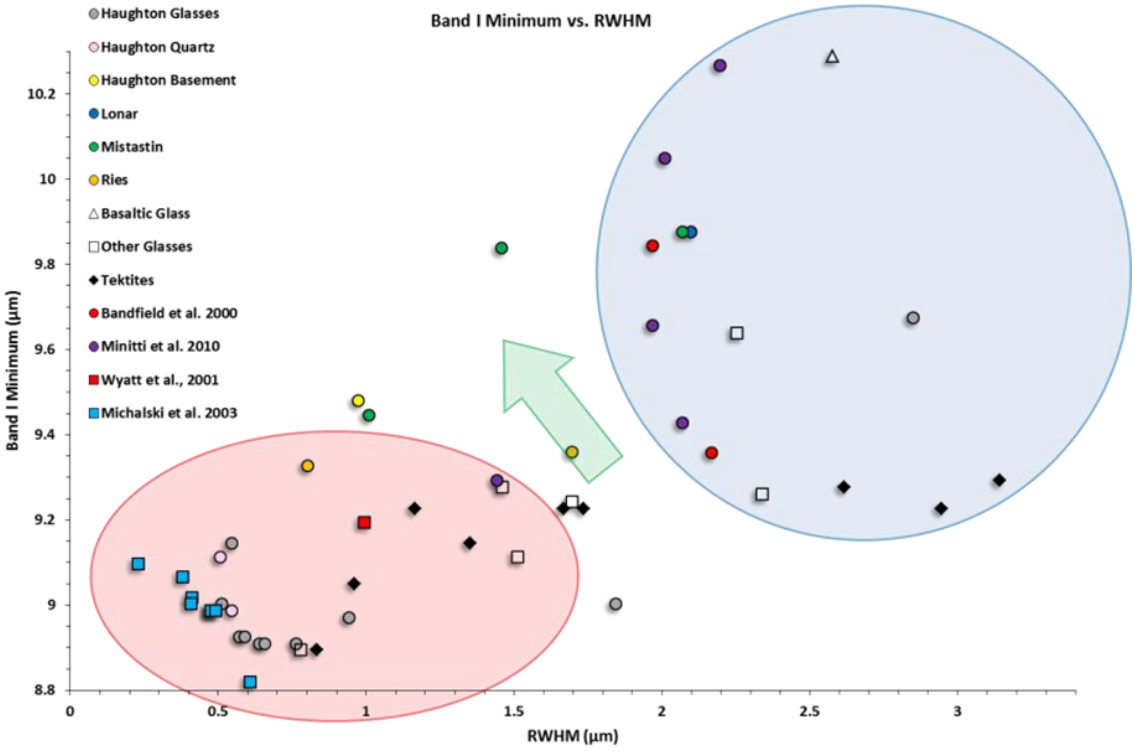

Figure 3-9: RWHM versus Band I minimum for the suite of glassy-impactites and examples from the available IR emission spectra from the literature. Shaded areas represent two populations, red at the lower left being the high-silica glassy impactites and hydrothermal deposits with a sharper silica asymmetric stretching fundamental absorptions, and blue at the upper right with longer wavelength shallow and broad asymmetric stretching absorption more indicative of canonical glasses formation environments. The green arrow marks an area where we expect diaplectic samples will reside where they have not experienced a liquid phase transition and with increasing pressures, we expect both partially diaplectic samples, e.g., Ries RI-09-007, and fully diaplectic samples, e.g., Mistastin MM10-38, to travel in the direction the arrow points with an increase in maximum pressure experienced.

The Wright et al., (2011) 5A and 5B basaltic glassy-impactites from Lonar, we suggest, represent two formation mechanisms, but one locale. We would suggest from the spectral evidence that they were formed below ground in high-pressure areas and were exhumed where Wright et al. (2001) 5A and our RI-09-007 Ries samples sit near the border between diaplectization and melting, while samples 5B from Wright et al., (2011), RI-01 from Ries, HMP04-035 from Haughton and CM09-07 from Mistastin are samples which completely melted but quenched while under a high confining pressure (a photograph of Ries sample RI-01 can be seen in Tornebene et al., 2013, Figure 2d; Ries sample RI-09-007 is very similar to Ries sample Aumühle 2005 shown in 2e.). Sample HNL-60C from our sample suite is an example of a canonical effusive basaltic glass, and although it is related to an impact, its formation environment would be more akin to glasses formed on the quench surfaces of melt sheets and ponds where reasonably fast quenching occurs under low pressures.

Osinski, (2003) suggested four sites within and around craters where impact melts products, or glasses, could be found. 1) crystalline melt sheets or melt ponds; 2) glassy clasts within melt-bearing breccias or suevites; 3) dikes injected in the crater floors or walls; and 4) ejecta. The suggestion was that all of the glassy lithologies formed via shock melting of the target rocks beneath the impact point and were exhumed. We would add that we would expect glassy-impactites to also form at the contacts between melt ponds and the rocks they abut. Glassy-impactites will run the gamut from air-quenched, i.e., no confining pressure, to diaplectic glasses formed without a liquid melt stage. The suite of glasses found within the Ries fall back breccias span the range from low-pressure air-quenched tektite-like bombs though full melts and diaplectic glasses (Osinski, 2003). We should expect that all of the types of glassy impactite can be found anywhere and everywhere within and outside a crater in the distal ejecta. We can expect to find any glass morphology anywhere. On a scale that is likely to be evidenced in TES spectra, we can expect high-pressure, sharp-featured glasses to be present in central uplifts and fall-back breccias as large clasts, and effusive melt-like glasses to be at the margins of melt ponds and within breccias.

High-silica evaporates (e.g., opal), with very sharp and low wavelength Band I minima (see Figure 3-9) we might find in any parts of the crater, though likely to be concentrated to the exterior of an extant melt sheet/melt breccias, on the margins of these deposits, among the faults of the crater rim, and plausibly outside the crater rim (Osinski, et al., 2005; Sapers et al., 2013), where we would not expect to find physically large samples of high-pressure melt or diaplectic glasses. On Mars, within the crater, other than in a central uplift, we would rarely expect to see crystalline silicates, such as quartz, which we might mistake for hydrothermal deposits, though spectral evidence exists for the exhumation of quartz in some central uplifts (Christensen et al., 2005). The empirical metrics we have used, were envisioned to be of use to data mine TES spectra and we would expect spectra which fall in the lower, leftmost corner of the chart would be interrogated individually, as would the surficial geomorphology to discern whether or not the spectrum may be of exhumed indigenous quartzite, opal-like evaporates of high-silica glassy impactites.

Thus, if the samples were available for study in the laboratory, we could use these new spectral features to identify glasses as definitively of impact origin. Unfortunately, the newly created spectral features of interest in impact glasses cannot be found in emission spectra (as they are too weak) and fall outside of the range of the Martian CO2 windows (Smith et al., 2000).

As the search for definitive spectral features of impact in glasses has not proved fruitful with respect to the identification of these features on Mars we are left with the stretching and bending fundamentals of silica in tetrahedral coordination in the glassy-impactites centred at ~9.25 and ~21.5 μm and what empirical measures we can derive from them. From our data we have found the comparison of the band minimum of the ~ 9.25 μm stretching fundamental, or Band I, and the RWHM of the same feature to be most efficacious empirical relationship to discern the origin of glassy impactites. RWHM is used rather than FWHM for comparison in Figure 3-2, as it somewhat ameliorates the effects of detrital quartz that is present in many of the Haughton samples. While there is spectral evidence for exhumation of quartz in impact craters of Mars (Christensen et al.,

2005), when looking specifically for glasses and hydrothermal silica-rich deposits, removing much of the unlikely influence of crystalline quartz from the IR emission spectra produces a more exploitable relationship than FWHM versus the Band I minima (see Appendix 3C).

Referencing Figure 3-2, there are general trends we can exploit to make our identification of glassy-impactites and silica-rich deposits more robust. Silica content increases right-to-left and top-to-bottom. Short-range order in the glassy-impactites and silica-rich samples increases right-to-left, and top-to-bottom. Silica-rich evaporates (e.g., opal) and glassy-impactites cluster in a band across the bottom of the figure while the canonical glasses with broad shallow IR absorptions more akin to well-studied and understood effusive volcanic glasses form an arced pattern largely separating themselves from the band of glassy-impactites and silica-rich hydrothermal samples which dominate the bottom, leftmost portion of the figure. Samples with higher potassium contents (i.e., Sample HMP04-35 which is of the K-rich basement rock from Haughton and the K-rich glass of Wyatt et al., 2001), which is known to be a network modifier which strongly influences the degree of ordering in glasses also, fall in the bottom, leftmost portion of the figure. Lastly, the Mistastin sample, MM10-38, which is entirely diaplectic glass, finds itself alone, separated from the two glassy-impactite and silica-rich populations, above the cluster of glassy-impactites and left of the arc of canonical glasses. Some scatter is introduced to the plot by minor amounts of phyllosilicate and carbonate in a few of the Ries and Mistastin samples which pushes those few samples upward and rightward on the figure and these sorts of spectral contaminants should also be expected in Martian glassy-impactites.

If one were to plot TES spectra using the same empirical relationships, we would expect the identification of glassy-impactites and/or silica-rich hydrothermal deposits would be significantly more robust than they are at present. Geomorphology is a first step, supported by spectral data, as searching for these sites is highly important. Recognizing impact-generated, glassy-bearing sites in our existing data sets will allow us to place the

next round of Martian explorers on locales of potentially high astrobiological significance.

Interrogating these locales should be a high priority as recent evidence suggests that not only are impact sites likely the youngest sites on Mars to have fostered life, they are also the sites where life may have originated and sites which provide abundant and easily exploitable energy and food sources (e.g., Izawa et al., 2010; Osinski et al., 2013, Sapers et al., 2015). Impact craters have undoubtedly been hosts for surficial liquid water forming lakes and rivers as well as being hosts for post impact hydrothermal networks which span a number of locales both inside and outside the crater rim (Osinski et al., 2013). Hypervelocity impacts produce glassy-impactites which, whether in-situ with liquid water, or without, provide attractive habitats consisting of amorphous material of extreme physical and chemical heterogeneity which require less energy for microbial metabolism that can support greater metabolic diversity and has implications both for the development and evolution of Martian life forms.

Glassy-impactites possess characteristics which make them ideal locales for the development of life and the long-term preservation of life (Cannon and Mustard, 2015; Sapers et al., 2015). The general friability of glassy impactites and their resistance to physical and chemical weathering may be questionable, but given the dry surface conditions that have persisted on the Martian surface for what appears to be billions of years, and the apparent stability of the Martian northern circumpolar dune fields, which arguably experienced significant perennial physical and chemical weathering but persist despite consisting of glassy-pyroclastics (Horgan and Bell III, 2012), we would suggest glassy-impactites on the surface of Mars are stable enough to withstand millions, to billions of years of surficial exposure and weathering.

3.8 Conclusion

Glassy impactites possess attributes which make them ideal habitats for the development of microbial life and have the potential to preserve evidence thereof long-term (e.g.,

Izawa et al., 2010, Schultz et al., 2014, Sapers, 2015). Interrogating these locales should be a high priority, and to that end, we investigated NIR reflectance and IR emission spectra of terrestrial impactites and hydrothermal evaporates to develop more robust spectroscopy-based methods and analytical techniques to aid in the identification of various impact related silicate assemblages on asteroids, and on Mars. Our findings suggest NIR reflectance spectra are ill suited for differentiating between glasses, glassy impactites evaporate silicates (e.g. opals), and silicates such as palagonite which is the major component of Martian dust.

IR emission spectra are much more useful. Concentrating on empirical relationships among the fundamental vibrational IR absorptions in the spectrum of impact-related silicate assemblages we can progress significantly toward robust identification of glasses and glassy impactites from orbit. With equally robust geomorphological context, we can be definitive.

3.9 Acknowledgements

We would like to acknowledge J. L. Bandfield, M. B. Wyatt, J. R. Michalski, M. E. Minitti and their coauthors for providing the emission spectra made available via the ASU Spectral Library available at speclib.asu.edu, Matt Willins and Johnathan Altenbeck for assistance with NMR data collection and peak modelling, respectively, as well as Richard Grieve, Horton Newsom and Neil Banerjee for providing select samples and the students of the Stony Brook University Earth and Planetary Remote Sensing lab/Vibrational Spectroscopy Laboratory who collected the emission spectra. This work was funded in part by grants from the Natural Sciences and Engineering Research Council of Canada (NSERC), the Natural Sciences and Engineering Research Council of Canada's Collaborative Research and Training Experience Program – Technologies and Techniques for Earth and Space Exploration, and the Ontario Graduate Scholarship Program.

3.10 References

Agarwal, A., Davis, K.M., and Tomozawa, M., 1995. A simple IR spectroscopic method for determining fictive temperature of silica glasses. Journal of Non-Crystalline Solids 185, 191-198.

Agarwal, A., and Tomozawa, M., 1997. Correlation of silica glass properties with infrared spectra. Journal of Non-Crystalline Solids 209, 166-174.

Bandfield J.L., Hamilton V.E., and Christensen P.R., 2000. A global view of Martian surface compositions from MGS-TES. Science 287, 1626-1630.

Bandfield, J.L., 2002. Global mineral distribution on Mars, Journal of Geophysical Research 107, No. E46, 5042.

Bell III, J.F., Morris, R.V., and Adams, J.B., 1993. Thermally altered palagonitic tephra: A spectral process analog to the soil and dust of Mars. Journal of Geophysical Research 98, No. E2, 3373-3385.

Berger, J.A., King, P.L., Green, A., Craig, M.A., Spilde, M.N., Wright, S.P., Kunkel, T.S., and Lee, R.J., 2015. Effect of halite coatings on thermal infrared spectra. Journal of Geophysical Research: Solid Earth, 120, 2162-2178.

Britt, D.T., and Pieters, C.M., 1994. Darkening in black and gas-rich ordinary chondrites: The spectral effects of opaque morphology and distribution. Geochimica et Cosmochimica Acta 58, No. 18, 3905-3919.

Cannon, K.M., and Mustard, J.F., 2015. Preserved glass-rich impactites on Mars. Geology G36953.1.

Christensen, P.R., Bandfield, J.L., Hamilton, V.E., Howard, D.A., Lane, M.D., Piatek, J.L., Ruff, S.W., and Stefanov, W.L., 2000. A thermal emission spectral library of rock forming minerals. Journal of Geophysical Research 105, No. E4, 9735-9739.

Christensen, P.R., Bandfield, J.L., Clark, R.N., Edgett, K.S., Hamilton, V.E., Hoefen, T., Kieffer, H.H., Kuzmin, R.O., Lane, M.D., Malin, M.C., Morris, R.V., Pearl, J.C., Pearson, R., Roush, T.L., Ruff, S.W., and Smith, M.D., 2000. Detection of crystalline hematite mineralization on Mars by the thermal emission spectrometer: Evidence for near-surface water. Journal of geophysical Research 105, No. E4, 9623-9642.

Christensen et al., 2001. Mars Global Surveyor Thermal Emission Spectrometer experiment: Investigation description and surface science results. Journal of Geophysical Research 109, No. E10, 23823-23871.

Christensen, P.R., McSween H.Y. Jr., Bandfield, J.L., Ruff, S.W., Rogers, A.D., Hamilton, V.E., Gorelick, N., Wyatt, M.B., Jakosky, B.M., Kieffer, H.H., Malin, M.C., and Moersch, J.E., 2005. Evidence for magmatic evolution and diversity on Mars from infrared observations. Nature 436, 504-509.

Clark, R.N., and Roush, T.L., 1984. Reflectance spectroscopy: Quantitative analysis techniques for remote sensing applications. Journal of Geophysical Research 89, No. B7, 6329-6340.

Clark, R.N., 1999. Spectroscopy of rocks and minerals and principles of spectroscopy. In, Manual of Remote Sensing, edited by A. N. Renz, pp. 3-58, John Wiley, New York, 1999.

Closmann, C., and Williams, Q., 1995. In-situ spectroscopic investigations of high-pressure hydrated (Mg,Fe)SiO3 glasses: OH vibrations as a probe of glass structure. American Mineralogist 80, 201-212.

Cloutis, E.A., Craig, M.A., Kruzelecky, R.V., Jamroz, W.R., Scott, A., Hawthorne, F.C., and Mertzman, S.A., 2008. Spectral reflectance properties of minerals exposed to simulated Mars surface conditions. Icarus 195, 140-168.

Craig, M.A., Cloutis, E.A., and Bailey, D.T., 2007. The effects of grain size, <45-1000 μm, on the reflectance spectrum of planetary analogs from 0.35-2.5 μm. LPSCXXXVIII, abstract #1356.

Craig, M.A., Cloutis, E.A., Reddy, V., Bailey, D.T., and Gaffey, M.J., 2008. The effects of grain size, <10 μm – 4.75 mm, on the reflectance spectrum of planetary analogs from 0.35-2.5 μm. LPSCXXXIX, abstract #2082.

Craig, M.A., Osinski, G.R., Flemming, R.L., and Cloutis, E.A., 2011. Spectral identification of impact glasses via NIR reflectance spectroscopy. LPSCXLII, abstract #2411.

Craig, M.A., Flemming, R.L., Osinski, G.R., Cloutis, E.A., Izawa, M.R.M., Sapers, H. M., and Marion C.L., 2013. XRD patterns of glassy impactites: Amorphous curve fitting and composition determination with implications for Mars. LPSC XLIV, abstract #2319.

Craig. M. A., Osinski, G.R., Flemming, R.L., Cloutis, E.A., Horgan, B., Tornebene, L.L., Izawa, M.R.M., Sapers. H.M., Marion, C.L., Applin, D.M., Mann, P., and Stromberg, J., 2014. Near-infrared spectra of glassy impactites from terrestrial impact structures. LSPCXLV, abstract #2417.

Craig, M.A., Osinski, G.R., Cloutis, E.A., Flemming, R.L., Izawa, M.R.M., Reddy, V., Fieber-Beyer, S.K., Pompilio, L., van der Meer, F., Berger, J.A., Bramble, M.S., and Applin, D.M., 2015. Fitting the curve in Excel: Systematic curve fitting of laboratory and remotely sensed planetary spectra. Chapter 1, this text.

Efimov, A.M., and Pogareva, V.G., 2006. IR absorption spectra of vitreous silica and silicate glasses: The nature of bands in the 1300 to 5000 cm-1 region. Chemical geology 229, 198-217.

Farnan, I., Grandinetti, P.J., Baltisberger, J.H., Stebbins, J.F., Werner, U., Eastman, M.A., and Pines, A., 1992. Quantification of the disorder in network-modified silicate glasses. Nature 358, 31-35.

French, B.M., Koeberl, C., 2010. The convincing identification of terrestrial meteorite impact structures: What works, what doesn't, and why. Earth-Science Reviews 98, 123–170.

Glotch, T.D., Morris, R.V., Christensen, P.R., and Sharp, T.G., 2004. Effect of precursor mineralogy on thermal infrared emission spectra of hematite: Application to Martian hematite mineralization. Journal of Geophysical Research 109, E07003.

Grieve, R.A.F., Therriault, A.M., 2012. Impactites: Their characteristics and spatial distribution, in: Osinski, G.R., Pierazzo, E. (Eds.), Impact Cratering: Processes and Products. Wiley-Blackwell, Oxford, United Kingdom (GBR), pp. 90–105.

Hazen, R.M., Finger, L.W., Hemley, R.J., and Mao, H.K., 1989. High-pressure crystal chemistry and amorphization of α-quartz. Solid Sate Communications 72, No. 5, 507-511.

Inamura, Y., Katayama, Y., and Utsumi, W., 2007. Transformation in intermediate-range structure of vitreous silica under high pressure and temperature. Journal of Physics: Condensed Matter 19, 415104.

Johnson, J.R., Christensen, P.R., and Lucey, P.G., 2002. Dust coatings on basaltic rocks and implications for thermal infrared spectroscopy. Journal of Geophysical Research 107, No. E6, 5035.

Hamilton, V.E., Wyatt, M.B., McSween, H. Y. Jr., and Christensen, P.R., 2001. Analysis of terrestrial and Martian volcanic compositions using thermal emission spectroscopy: 2. Application to Martian surface spectra from the Mars Global Surveyor Thermal Emission Spectrometer. Journal of Geophysical Research: Planets 106, No. E7, 14733-14746.

Hazen, R.M., Finger, L.W., Hemley, R.J., and Mao, H.K., 1989. High-pressure crystal chemistry and Amorphization of α-quartz. Solid Sate Communications 72, No. 5, 507-511.

Horgan, B., and Bell III, J.F., 2012. Widespread weathered glass on the surface of Mars. Geology, 40, No. 5, 391-394.

Inamura, Y., Katayama, Y., and Utsumi, W., 2007. Transformation in intermediate-range structure of vitreous silica under high pressure and temperature. Journal of Physics: Condensed Matter 19, 415104.

Izawa, M.R.M., Banerjee, N.R., Flemming, R.L., Bridge, N.J., and Schultz, C., 2010. Basaltic glass as a habitat for microbial life: Implications for astrobiology and planetary exploration. Planetary and Space Science, 58, 583-591.

Koeppen, W.C., and Hamilton, V.E., 2005. Discrimination of glass and phyllosilicate minerals in thermal infrared data. Journal of Geophysical Research 110, E08006.

Koike, A., and Tomozawa, M., 2007. IR investigation of density changes of silica glass and soda-lime silicate glass caused by microhardness indentation. Journal of Non-Crystalline Solids 353, 2318-2327.

Kraft, M.D., Michalski, J.R., and Sharp, T.G., 2003. Effects of pure silica coatings on thermal emission spectra of basaltic rocks: Considerations for Martian surface mineralogy, Geophysical Research Letters, 30, No. 24, 2288.

Lucey, P.G., and Clark, R.N., 1985. Spectral properties of water ice and contaminants. In Ices in the solar system, edited by J. Klinger et al., pp. 155-168, D. Reidel Publishing Company, France.

Lucey, P.G., and Riner, M.S., 2011. The optical effects of small iron particles that darken but do not redden: Evidence of intense space weathering on Mercury. Icarus 212, 451-462.

Krolikowski, S., Brungs, S. and Wondraczek, L., 2009. Relaxation of Libyan Desert Glass: Evidence for Negative Viscosity-Pressure Dependence on Silica. Journal of Non-Crystalline Solids 355, 1666-1668.

Martonak, R., Donadio, D., Oganov, A.R., and Parrinello, M, 2006. Crystal structure transformation in SiO2 from classical and ab initio metadynamics. Nature Materials 5, 623-626.

McSween, H.Y. Jr., Grove, T.L., and Wyatt, M.B., 2003. Constraints on the composition and petrogenesis of the Martian crust. Journal of Geophysical Research 108, No. E12, 9-1-19.

Michalski, J.R., Kraft, M.D., Diedrich, T., Sharp, T.G., and Christensen, P.R., 2003. Thermal emission spectroscopy of the silica polymorphs and considerations for remote sensing on Mars. Geophysical Research Letters 30, No. 19, 2008.

Minitti, M.E., and Hamilton, V.E., 2010. A search for basaltic-to-intermediate glasses on Mars: Assessing the Martian crustal mineralogy. Icarus 210, 135-149.

Morris, R.V., Le, L., Lane, M.D., Golden, D.C., Shelfer, T.D., Lofgren, G.E., and Christensen, P.R., 2000. Multidisciplinary study of synthetic Mars global average soil glass. LPSC XXXI, abstract #1611.

Morris, R.V., Graff, T.G., Mertzman, S. A., Lane, M.D., and Christensen, P.R.., 2003. Palagonitic (not andesitic) Mars: Evidence from thermal emission and VNIR spectra of palagonitic alteration rinds on basaltic rocks. Sixth International Conference on Mars, abstract #3211.

Navarra, G., Vella, E., Grandi, S., Leone, M. and Boscaino, R., 2009. Temperature effects on the IR absorption bands of hydroxyl and deuteroxyl groups in silica glass. Journal of Non-Crystalline Solids 355, 1028-1033.

Osinski, G.R., 2003. Impact glass in fallout suevites from the Ries impact structure, Germany: An analytical SEM study. Meteoritics and Planetary Science 38, Nr. 11, 1641-1667.

Osinski, G.R., Lee, P., Parnell, J., Spray, J.G., and Baron, M., 2005. A case study of impact-induced hydrothermal activity: The Haughton impact structure, Devon Island, Canadian high arctic. Meteoritics and Planetary Science 40, Nr. 12, 1859-1877.

Osinski, G.R., Grieve, R.A.F., Marion, C.L., Chanou, A., 2012. Impact melting, in: Osinski, G.R., Pierazzo, E. (Eds.), Impact Cratering: Processes and Products. Wiley-Blackwell, Chichester, pp. 125–145.

Osinski, G.R., Tornabene, L.L., Banerjee, N.R., Cockell, C.S., Flemming, R., Izawa, M.R.M., McCutcheon, J., Parnell, J., Preston, L.J., Pickersgill, A.E., Pontefract, A., Sapers, H.M., and, Southam, G.,2013. Impact-generated hydrothermal systems on Earth and Mars. Icarus 244, 347-363.

Ramsey, M. S., and Christensen, P.R., 1998. Mineral abundance determination: Quantitative deconvolution of thermal emission spectra. Journal of Geophysical Research 103, No. B1, 577-596.

Reibstein, S., Wondraczek, L., de Ligny, D., Krolokowski, S., and Sirotkin, S., 2011. Structural heterogeneity and pressure-relaxation in compressed borosilicate glasses by in situ small angle x-ray scattering. The Journal of Chemical Physics 134, 204502.

Rice, M.S., Cloutis, E.A., Bell III, J.F., Bish, D.L., Horgan, B.H., Mertzman, S.A., Craig, M.A., Renaut, R.W., Gautason, B., and Mountain, B., 2013. Reflectance spectra diversity of silica-rich materials: Sensitivity to environment and implications for detection on Mars. Icarus 223, 499-533.

Rogers, A.D., and Christensen, P.R., 2007. Surface mineralogy of the Martian low-albedo regions from MGS-TES data: Implications for upper crustal evolution and surface alteration. Journal of Geophysical Research 112, E01003.

Rogers, A.D., Bandfield, J.L., and Christensen, P.R., 2007. Global spectral classification on Martian low-albedo regions with Mars Global Surveyor thermal emission spectrometer. Journal of Geophysical Research 112, E02004.

Rogers, A.D., 2011. Crustal compositions exposed by impact craters in the Tyrrhena Terra region of Mars: Considerations for Noachian environments. Earth and Planetary Science Letters 301, 353-364.

Roush, T.L., and Bell III, J.F., 1995. Thermal emission measurements 2000-400 cm-1 (5-25 μm) of Hawaiian palagonitic soils and their implications for Mars. Journal of geophysical Research 100, No. E3, 5309-5317.

Ruff, S.W., Christensen, P.R., Barbera, P.W., and Anderson, D.L., 1997. Quantitative thermal emission spectroscopy of minerals: A laboratory technique for measurement and calibration. Journal of Geophysical Research 102, No. B7, 14889-14913.

Ruff, S.W., and Christensen, P.R., 2007. Basaltic andesite, altered basalt, and a TES-based search for smectite clay minerals on Mars. Geophysical Research Letters 34, L10204.

Rustad, J.R., Yuen, D.A., and Spera, F.J., 1992. Coordination variability and the structural components of silica glass under high pressures. Chemical Geology 96, 421-437.

Sapers, H.M., Osinski, G.R., Buitenhuis, E., Banerjee, N.R., Flemming, R.L., Hainge, J., and Bain, S., 2015. Impact-generated hydrothermal activity beyond the Ries crater rim. LPSCXLVI, abstract #2917.

Schultz, P.H., and Mustard, J.F., 2004. Impact melts and glasses on Mars. Journal of Geophysical Research 109, E01001.

Schultz, P.H., Harris, R.S., Clemett, S.J., Thomas-Keptra, K.L., and Zarte, N., 2014. Preserved flora and organics in impact melt breccias. Geology 42, 515-518.

Singer, R.B., 1981. Near-infrared spectral reflectance of mineral mixtures: Systematic combinations of pyroxenes, olivine, and iron oxides. Journal of Geophysical Research 86, No. B9, 7967-7982.

Skok, J.R., Mustard, J.F., Tornabene, L.L., Pan, C., Rogers, D., and Murchie, S.L., 2012. A spectroscopic analysis of Martian crater central peaks: Formation of the ancient crust. Journal of Geophysical Research 117, E00J18.

Smith, M.D., Bandfield, J.L., and Christensen, P.R., 2000. Separation of atmospheric and surface spectral features in Mars Global Surveyor thermal emission spectrometer (TES) spectra. Journal of Geophysical Research 105, No. E4, 9589-9607.

Smith, M.R., Bandfield, J.L., Cloutis, E.A., and Rice M.S., 2013. Hydrated silica on Mars: Combined analysis with near-infrared and thermal-infrared spectroscopy. Icarus 223, 2, 633-648.

Stöffler, D., Artemieva, N.A., and Pierazzo, E., 2002. Modeling the Ries-Steinheim impact event and the formation of the moldavite strewn field. Meteoritics and Planetary Science 37, 1893-1907.

Tool, A.Q., 1946. Viscosity and the extraordinary heat effects in glass. Journal of the American Ceramic Society, 29, 240-253.

Tornebene, L.L., Osinski, G.R., McEwen, A.S., Wray, J.J., Craig, M.A., Sapers, H.M., and Christensen, P.R., 2013. An impact origin for hydrated silicates on Mars: A synthesis. Journal of Geophysical Research 118, 994-1012.

Velde, B., and Couty, R., 1987. High-pressure infrared spectra of silica glass and quartz. Journal of Non-Crystalline Solids 94, 238-250.

Williams, Q., and Jeanloz, R., 1988. Spectroscopic evidence for pressure-induced coordination changes in silicate glasses and melts. Science 239, No. 4842, 902-905.

Williams, Q., and Jeanloz, R., 1989. Static Amorphization of Anorthite at 300K and comparison with diaplectic glass. Letters to Nature 388, 413-415.

Williams, Q., Hemley, R.J., Kruger, M.B., and Jeanloz, R., 1993. High-pressure infrared spectra of α-quartz, coesite, Stishovite and silica glass. Journal of Geophysical Research 98, No. B12, 22157-22170.

Wright, S.P., Christensen, P.R., and Sharp, T.G., 2011. Laboratory thermal emission spectroscopy of shocked basalt from Lonar Crater, India, and implications for Mars orbital and sample data. Journal of Geophysical Research 116, E09006.

Wyatt, M.B., Hamilton, V.E., McSween, H.Y. Jr., Christensen, P.R., and Taylor, L.A., 2001. Analysis of terrestrial and Martian volcanic compositions using thermal emission spectroscopy: 1. Determination of mineralogy, chemistry, and classification strategies. Journal of Geophysical Research 106, E7, 14711-14732.

Wyatt, M.B., and McSween, H.Y. Jr., 2002. Spectral evidence for weathered basalt as an alternative to andesite in the northern lowlands of Mars. Letters to Nature 417.

Chapter 4

4 The Effects of Grain Size (<10 μm to 4.75 mm) on the Reflectance Spectrum of Common Planetary Analogue Materials

4.1 Introduction

Near-infrared (NIR) reflectance spectroscopy is one of the most powerful techniques for identifying mineralogy on planetary surfaces and it is well understood that a variety of factors associated with target lithology exert an influence on NIR reflectance spectra. Mineralogy, grain size, grain packing, phase angle and temperature are arguably the target properties which most effect NIR reflectance spectroscopy and a number of previous studies have addressed the effects of coarse sand size and smaller grain sizes on the NIR reflectance spectra of minerals that are thought to represent the major mineral constituents of asteroids, and the basaltic surfaces of the neighboring planets (e.g., Adams and Filice, 1967; Hunt and Salisbury, 1970; Pieters, 1983; Mustard and Pieters, 1989; Mustard and Hays, 1997; Lucey et al., 1998; Hinrichs and Lucey, 2002; Pompilio et al., 2009; Pompilio et al., 2010; Beck et al., 2012; Sanchez et al., 2012).

Thematically, studies have focused on the common minerals pyroxene and, olivine and basaltic rocks, and studied the effects of fine powders, as small as ~ 5 μm through coarse sand of ~ 1 mm (e.g., King and Pieters, 1981; Mustard and Hays, 1997), as well as slabs meant to be representative of rocks (e.g., Yon and Pieters, 1988; Harloff and Arnold, 2001).

Collectively, past studies have found that at small grain sizes, surface scatter (i.e., reflection of rain surface) dominate, so that absorption bands become shallower and albedo rises with decreasing grain size. With increasing grain size, volume scattering (absorption within a grain) becomes more important, so that absorption bands become deeper and albedo decreases. At some grain size, essentially all photons of particular

wavelengths that are not surface scattered, are absorbed within grains, leading to absorption band saturation. To our knowledge, this is the first study to investigate the effects of grain size on biconical Vis-NIR reflectance spectra that includes a continuous and finely-divided grain size series that also covers size gap between coarse sand and rocky surfaces. We spectrally characterized, 33 finely demarcated grain sizes fractions from <10 μm to 4.75 mm.

4.2 Previous Studies

Variations in grain size are known to affect reflectance spectra of mafic materials in a number of ways, and many studies have examined these effects in varying levels of detail.

One of the first studies of these effects was by Adams and Filice, (1967). They found that for basalts, overall reflectance was relatively constant for average grain size <~45-90 μm. For average grain sizes <~45-90 μm up to ~ 1300 μm albedo increased. The behavior of the R/B (0.7/0.4 μm) ratio versus visible region albedo varied significantly for different Basalt samples (from ~ 1-2.2 for fine-grained highly vesicular unweathered basalt and ~1.05-1.20 for highly-weathered basalt). However, their data suggest that this relationship breaks down for some mafic igneous rocks for particles sizes in the few tens of μm range. They also emphasized that spectral changes with grain size were wavelength dependent. Their study was one of the first to quantify albedo-reflectance-grain size relationships.

4.2.1 Powders: Grain Size Effects

Hunt and Salisbury, (1970), examined reflectance spectra of a number of anhydrous silicates, including olivines, plagioclase feldspars, and pyroxenes. Grain sizes that were spectrally characterized included <5, <74, 74-250, and 250-1200 μm. Low-Fe olivine, which has a very weak 1 μm band, showed a progressive decrease in overall reflectance

with increasing grain size. A more Fe-rich olivine (Fa~13), which has a stronger 1 μm band, also showed decreasing overall reflectance with increasing grain size, while the two largest grain sizes had similar overall reflectance; 1 μm band depth increased with increasing particle size. Pyroxenes showed similar spectral behavior to olivine: overall reflectance decreases with increasing particle size, while band depth increases with increasing grain size for all but the 250-1200 μm size fraction. Plagioclase feldspars, which are essentially free of absorption bands, show very similar reflectance for the two smallest grain size fractions (<5 and <74 μm), while the larger grain sizes have lower overall reflectance and a deeper 1.25 μm region absorption band for the Fe-bearing samples.

King and Pieters, (1981), examined reflectance spectra of plagioclase, enstatite and ilmenite in four grain size splits, <30, 30-45, 45-108 and 150-250 μm, and noted that grain size has significant effect on absorption strength (i.e., band depth), unexpectedly, moreso than mixing very low albedo ilmenite with enstatite. Morris et al., (1982) went on to use these same enstatite samples and noted the effects of band flattening, identified the mismatch between fitting data with Gaussians and the flattening absorption features associated with larger grain sizes, and measured the effects of wavelength dependent scattering.

Pieters, (1983), documented how in these same samples again, that decreasing particle size was correlated with decreasing band depth and higher overall reflectance for enstatite, labradorite, and ilmenite. She attributed the decrease in absorption band depth with decreasing particle size in enstatite to a decrease in the mean optical path length (MOPL) of the transmitted component, and noted that a minor decrease in overall reflectance occurred in the smallest fraction.

Mustard and Hays, (1997), conducted a detailed study of particle size effects on reflectance spectra of olivine and quartz from 0.3 to 25 μm. They used well-constrained particle size fractions (5 μm intervals from 0 to 25 μm). The focus of their study was on infrared spectral features, however, their reflectance spectra showed that overall

reflectance increases and 1 μm region absorption band depth decreased with decreasing grain size, continuing trends known for larger particles (e.g., Cloutis et al., 1986).

Harloff and Arnold, (2001), examined reflectance spectra of basalt and pyroxene as a function of grain size, powders versus slabs, and slab surface roughness. They found that for powders, maximum reflectance decreases with increasing powder size, with the rate of decrease most pronounced for the finest particle sizes. For powdered samples, spectral slope measured via the slope of a straight line from the onset of Band I, to the offset of Band II (i.e., from the extinction points, or reflectance maxima short-ward of Band I and long-ward in wavelength of Band II) was found to increase with increasing grain size to some maximum value, and then to decline with further increases in average grain size. For their M1 diopside sample, the reddest slope (i.e., reflectance increasing with increasing wavelength) was found for an average grain size of ~175 μm. For their G1 basalt sample, the reddest slope was found for an average grain size of ~60 μm. The finest grain size sample (<25 μm) and samples coarser than ~150 μm had blue spectral slopes (i.e., reflectance decreasing with increasing wavelength). In terms of band depths, their M3 augite sample showed band depths near 1 and 2 μm increasing with increasing grain size to ~100 μm average grain size, followed by either a slight additional increase (2 μm band) or a slight decrease (1 μm band) with further increases in particle size. A similar behavior was seen for the G1 basalt sample, with the turnover occurring near 200 μm grain size.

Duffard et al., (2005), examined how changes in grain size for four eucrite meteorites and one diogenite meteorite affected various absorption band parameters. They found that band area ratios (i.e., ratio of the area of the absorption band in the 2 μm region to the absorption band area in the 1 μm region) increased with increasing grain size, reaching a maximum near a mean grain size of ~100 μm. Band depths were also seen to increase to a maximum value near an average grain size of ~50 μm, and to decrease thereafter. Band centers were found to be relatively constant for the diogenite, but increased slightly for eucrites (by ~10-15 nm) with increasing grain size.

Pompilio et al., (2009), examined reflectance spectra of orthopyroxene for a variety of grain sizes (<45, 45-90, 90-250, 250-500, and 500-1000 μm) both neat and mixed with barium sulfate. They found that band saturation occurs at smaller grain sizes for more Fe-rich pyroxenes, while overall reflectance decreases with increasing grain size. The pyroxene + barium sulfate mixtures were used to demonstrate that band saturation is a function of pyroxene grain size and iron content, and that the presence of a spectrally neutral phase does not affect band saturation.

4.2.2 Slabs versus Powders

Yon and Pieters, (1988), examined reflectance spectra of basalt slabs as a function of surface roughness. This study was undertaken in response to the fact that basalt slab spectra are commonly blue-sloped, as compared to generally red-sloped spectra for particulate samples. They determined that single Fresnel reflections (reflections which occur at a discrete interface between two media with differing refractive indices, e.g., at the air-slab interface) dominate the reflected intensity for slabs, thereby accounting for the shallowness of absorption bands in basalt slab spectra relative to powdered samples. This behavior was seen in other studies where slab and powder spectra are compared (e.g., Anbazhagan and Arivazhagan, 2009).

Harloff and Arnold, (2001), in their study of slab versus powder spectra noted that band depths were nearly always lower in slab versus powder spectra for pyroxenes and basalts. They also noted that spectral slopes and maximum reflectance showed a high degree of overlap between pyroxene and basalt powders and slabs. For roughened slabs, with progressively rougher surfaces, the following trends were observed: spectral slope initially increased and then decreased (for M1 diopside and G3 basalt), maximum reflectance decreased and reached a steady state (for M2 enstatite and G3 basalt), and band depth increased to a constant value or decreased slightly for the roughest surface (for M1 diopside and G3 basalt). Their spectral measurements were made with a symmetrical biconical reflectance geometry.

Poulet and Erard, (2004), found that reflectance spectra of basalt samples could not be well-modeled using the Shkuratov scattering theory (Shkuratov et al., 1999), largely because the opaque minerals in basalts can be smaller than the wavelength of incident light, and this is not accounted for well in Shkuratov scattering theory.

Carli and Sgavetti, (2011), examined the effects of texture and composition on reflectance spectra of a variety of basalts. The slab spectra were uniformly blue-sloped while the powdered (<250 μm) samples showed generally neutral or red-sloped behavior. They found that the spectra became increasingly darker and blue sloped with increasing average particle size. They also determined that blue-sloped spectral behavior was characteristic of slabs, due to welded mineral particles resulting in less internal and external surface reflections, and that this was enhanced by the presence of opaques. Carli, (2009), found that band centers in the rock spectra were consistent with their expected positions.

In summary, previous studies have found, that at progressively smaller grain sizes, surface scatter increasingly dominates, so that absorption bands become shallower while albedo increases, and with progressively larger grain sizes, volume scattering increasingly dominates and bands become deeper, while albedo decreases. Between the finest (<5 μm) and the largest, ~ (1 mm) grain size fractions studied to date, albedo is brightest among the smallest sizes but does not follow a systematic trend where the smallest is brightest, and then albedo falls off with increasing size (e.g., Pieters, 1983). As grain size progresses from small to large, albedo generally decreases from smallest to largest grain size, band depths are shallow at the smallest grain sizes, deepen to reach a point of maximum depth in intermediate grain sizes (where this occurs depends on the mineral, its overall albedo and the volume of the absorbing species in the mineral, e.g., iron in olivine and pyroxene), and then shallow with increasing size where generally band depth decrease and albedo decrease correlate. Spectral slope has been shown to trend blue, or increase, with increasing grain size progression from small to large, reach a maximum, and then redden with further grain size increase (e.g., Harloff and Arnold, 2001; Carli and Sgavetti, 2011). In slabs, spectral slopes have been found to generally be

bluer than their powdered counterparts, band depths are shallower and albedos have been lower than the largest grain sizes studied, between ~ 1 and 1.3 mm.

4.3 Experimental Procedure

Three samples were included in this study: (1) a crystalline enstatite, PYX023, from Mount St. Helena, Lake County CA, USA; (2) a fine-grained basalt, SA-51, from the margin of a Columbia River dike in Wallowa County, OR, USA; and (3) olivine crystals, OLV003, from San Carlos County, AZ, USA. Two suites, encompassing 38 grain size separates were produced from the enstatite and basalt. The samples were crushed and dry sieved by hand or dry sieved and then wet sieved in alcohol to produce a large series of grain size splits. Hand samples were initially crushed and sieved by crushing a small amount, then hand brushed through a series of sieves from the largest to the smallest to produce a series in the following grain size splits: <20, <25, 25-38, 38-45, 45-63, 63-75, 75-90, 90-125, 125-150, 150-180, 180-212, 212-250, 250-300, 300-355, 355-425, 425-500, 500-600, 600-700, 700-850, 850-1000 µm, 1-1.4, 1.4-1.7, 1.7-2, 2-2.36, 2.36-2.8, 2.8-3.35, 3.35-4.75 mm. From the same rocks, a second series of grain size splits at <45, 45-90, 90-250, 250-500 and 500-1000 µm were also produced in the same manner. A large volume of <45 µm powder was crushed and dry sieved, and from that split, <10, 10-15, 15-10, 20-25, and 25-38 µm wet sieved grain size sets were produced. In addition, more restricted suite of the crystalline olivine, OLV003, has been included and a 5 split set was produced in the same manner with grain sizes of <45, 45-90, 90-250, 250-500 and 500-1000 µm (see Table 4.1 for compositions). Hand sample of PYX023 and SA-51 were retained and spectra were collected of the natural face, and a cut rock face roughened with 220 grit corundum sandpaper, respectively.

Samples were loaded into aluminium sample cups by lightly tamping the powders or grains into the sample wells and drawing the edge of a clean glass microscope slide across the surface of the sample cup to produce a flat matte surface.

Biconical absolute reflectance spectra were collected at the University of Winnipeg Planetary Spectrometer Facility (PSF) using an Analogue Spectral Devices Inc. (ASDI) FieldSpec Pro HR field portable near-infrared spectrophotometer (Cloutis et al., 2006). Spectra were collected at incidence=30°, emission=0°, from 0.35 to 2.5 μm, relative to Spectralon® and corrected for irregularities in Spectralon's® reflectance from 2 to 2.5 μm. Wavelength calibration was monitored via periodic measurement of a holmium oxide wavelength standard. 1000 spectra of the reflectance standard (or white standard), sample and dark current were averaged to increase the signal-to noise ratio for each individual spectrum and sets of individual spectra were averaged together to ameliorate the effects of non-equidimensional grains by collecting a spectrum of the sample (each of 1000 averaged spectra), removing the sample from the PSF-built goniometer, rotating the sample a fixed amount and collecting another spectrum. For the 33 split sets, for the sizes <10 wet sieved through the 125-150 μm, the sample cup was rotated once 90° and two spectra were averaged, for the 150-180 through 850-1000 μm splits the samples cups were rotated 90° twice, and for the 1.1-1.4 through 3.35-4.75 mm spits the samples were rotated randomly four times as were the two rock samples. For the five grain size series, the <45, 45-90 and 90-250 μm splits were rotated 90° once and 250-500 and 500-100 μm were rotated 90° three times. The ASDI spectrometer was set to collect spectra continuously, and to prevent heating of the sample by the collimated beam of the PSF built Quartz-Tungsten-Halogen light source, for each sample rotation, the samples were kept out of the beam of incident light to avoid adding uncalibrated for thermal excess while collecting a spectrum.

The spectral resolution of the ASDI varies between 2 and 7 nanometers depending on where one is in the wavelength range of its three internal detectors which cover wavelength ranges from 0.3 to 1, 1 to 1.83 and 1.82 to 2.5 μm, respectively. Spectra are then sampled internally and converted via a proprietary ASDI weighted cubic spline function and output at an interpolated resolution of 1 nanometre.

The ASDI instrument using a fibre-optic pickup end and FOV of the spectrometer and the light source was approximately 5 mm. The FOV is listed as approximate as the fibre-

optic bundle of the ASDI spectrometer splits internally to feed the three detectors and has a random distribution of fibres at the pick-up end. As a result the FOV of each detector is not the same and this sometimes results in small offsets in the spectra at the detector junctions. The offsets are corrected by normalizing the 0.3 to 1 μm and 1.83 to 2.5 μm detectors to the range covered by the SWIR I detector which is thermal stabilized by a Stirling cooler.

4.4 Curve Fitting

To derive comparable metrics, straight line continua were divided out of the spectra using pin points at fixed wavelength positions (i.e., at points inside of the reflectance maximum between adjacent absorption features). This methodology was followed so that band centres, areas and depths could be compared within each sample set without the complication of variable continuum end points which would affect the derived empirical metrics. Curve fitting was performed using the methods discussed an illustrated in Chapter 2 and its appendices. Band centres were derived via fitting of 3rd order polynomials. For Band I in all sample spectra, the range over which the polynomials were fit for band centre derivation were initially set to 0.05 μm to either side of the lowest measured reflectance value the continuum removed region. For Band II in both pyroxene sets, the centres were derived by beginning with a fixed 0.05 μm interval on either side of the measured minimum, and then the fit interval was adjusted based on the degree of influence exerted by the ~ 1.9 μm adsorbed water absorption.

An absorption feature due to water is apparent in all of the sample spectra near 1.9 μm, but is only relevant to the empirical measures of Band II in the pyroxene grain size sets, and, care was taken, in the empirical measure of centre for each spectrum individually, to avoid including the water absorption feature as much as was possible in measures of centre. For measures of band depth, the adsorbed waters influence is negligible but it is included in every measure of area. The effect is visible, and is likely responsible for some of the scatter in the measures of band area, although band saturation is the dominant

perturbing effect on all of the empirical metrics. For a listing of metrics, pin points and nodes (see Tables in Sheets *A*, *B*, *C*, *D* and *E* in Appendix 4A).

4.5 Band Saturation and Scattering

Surface scattering and volumetric scattering, or band saturation, effect all empirically derived measures of spectra. Surface scattering is less prominent an effect on the spectra of pyroxene, olivine and basaltic rocks because it is most conspicuous at shorter wavelengths, and smaller grain sizes. Given the position of the Band I absorption features in pyroxene, olivine and basalts (in basalt, Band I is a combination absorptions from both pyroxene and olivine) it follows that surface scattering significantly brightens the albedo of these features but has little effect on the measure of their centres. Small grain size has essentially no effect on the centre of Band II in pyroxene, although it does affect band depth and area, indicating as it should, that surface scattering is less at play in the 2 μm region, but present in grain sizes smaller than ~25 μm.

Bands are saturating with increasing grain size because mean optical path length (MOPL) increases as grain size increase (Pieters, 1983). As grains grow in size, there are more opportunities for photon absorption as increasing MOPL increases the likelihood of intra-grain photon interactions; it also becomes more likely with increasing grain size that a photon emerging from one grain will encounter another and enter it in an inter-grain interaction before leaving the sample proper. Larger grains have a higher volume:surface ratio, therefore photons are more likely to penetrate a grain (and be absorbed) rather than reflect off its surface.

Band saturation is also wavelength dependent, and the degree to which it affects a reflectance spectrum is determined by intra-grain scattering, inter-grain scattering (both, functions of grain size), and by the absorption coefficient of the material with which the photons are interacting (Morris et al. 1982, Morris and Mendel, 1982, Clark and Roush, 1984, Lucey and Clark, 1985). For example, in ice, given the difference in absorption coefficients at different wavelengths, 25% of incident light at 3.075 μm, will be absorbed

with 1 µm or penetration (Irvine et al., 1968), while at 1.04 µm a path length of 4.1 cm in required for the same 25% absorption (Lucey and Clark, 1985). This is driven by the composition and absorbing species in the materials, in the case of ice it is the H_2O molecule and for the spectra of pyroxene, olivine and basalt, ferrous iron. Where absorption coefficients are highest, in Bands I and II for orthopyroxene and Band I for olivine and basalt, absorption will be most efficient and band saturation most evident (e.g., Hiroi and Pieters, 1994; Lucey, 1998).

Band saturation is the phenomenon most responsible for the change seen in the spectra as grain size increases (Morris et al. 1982, Morris and Mendel, 1982, Clark and Roush, 1984, Lucey and Clark, 1985). In general, when going from smaller to larger grain sizes, band depth will initially be shallow and spectra will have a high albedo (a result of enhanced scattering), then as grain size increases, absorption band depth will increase reaching a maximum before decreasing again with further increases in grain size while overall brightness continually decreases (Hunt and Salisbury, 1970; Pieters, 1983). This trend is seen for our pyroxene: the spectrum of powdered pyroxene is brightest (highest in albedo as measured by a linear trendline fit to the full spectrum) at <25 µm grain size and falls off in brightness as average grain size increases until approximately 425 µm, where brightness levels off close to zero, its greatest Band I and II depths are at the 180-212 µm size and decrease with increasing grain size. Band saturation is illustrated in Figures 4-1 and 4-2.

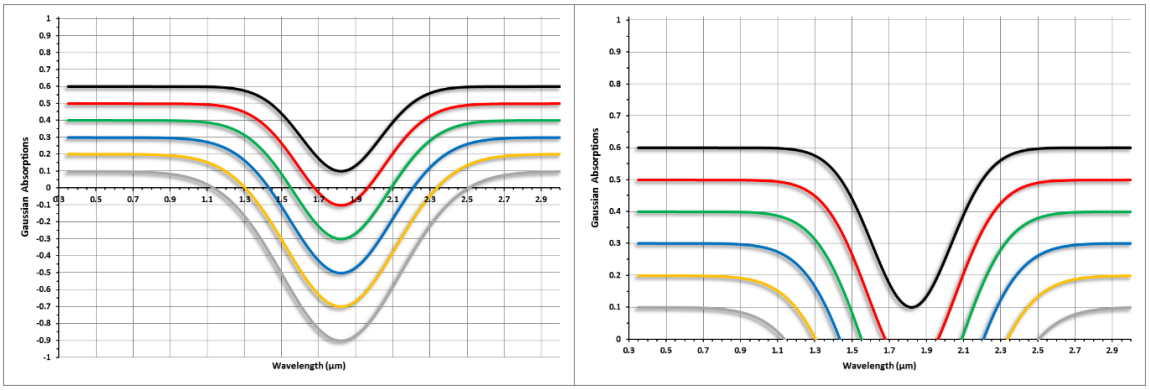

Figure 4-1: An illustration of band saturation for Band II in pyroxene. As Mean Optical Path-Length (MOPL) increases and more inter- and intra-grain photon interactions occur

(i.e., photon absorptions), band depths deepen, band widths widen and overall reflectance drops. The effect is illustrated in left panel, where with increasing absorption rates the absorption minimum falls well below zero in reflectance. The synthetic spectra on the right are more indicative of what one actual sees in the spectrum, though we do not see reflection reaching zero. Refection never reaches zero as long as the grains being imaged are larger than the wavelengths of light which are interrogating them, and in this instance, grains would have to be smaller than approximately 2 µm for optical interactions to occur and be a problem. Rather than zeroing, bands saturate and behave as is depicted in Figure 4-2.

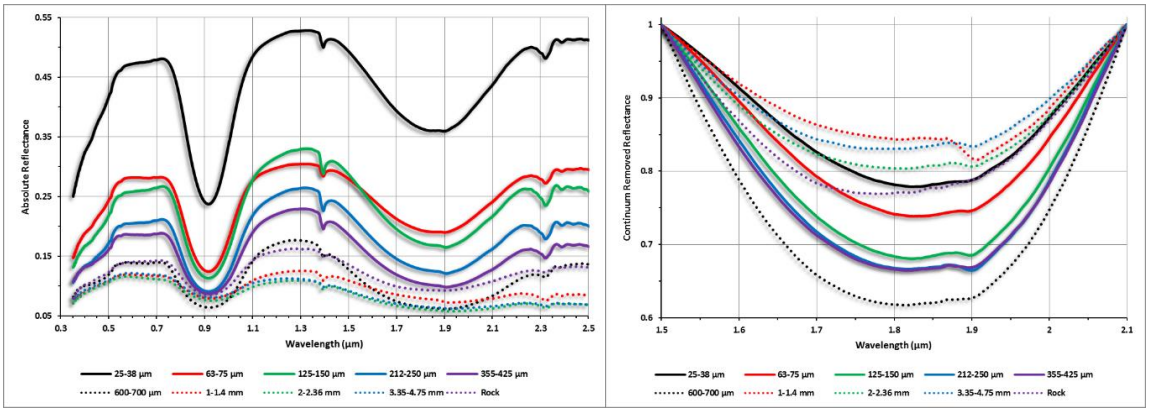

Figure 4-2: NIR reflectance spectra of PYX023 in absolute (left) and straight line continuum removed reflectance (right). Left and right panels depict the effects of bad saturation on Bands I and II in pyroxene. The flattening of absorption bands with as a result of band saturation as grain sizes increases is readily apparent as is the "crashing" into zero which complicates band minimum and centre derivation (dotted-line spectra). After centring, the continuum removed spectra of Band II (right) illustrate the flattening of Band II in the larger grain size splits and the wandering centre measurements which accompany band saturation. While the effect of saturation appears most severe in Band II, in pyroxene it is more apparent in Band I, where it sets in at much smaller grain sizes than for Band II (see Appendix 4A, Sheet *A*).

While band saturation is essentially, reflectance going to zero as a result of increasing intra-and inter-grain photon absorption, reflectance will not actually go to zero because there is always some component of incident light that will be specularly reflected as long

as the grain size being investigated is larger than the wavelength of incident light (Clark and Lucey, 1984; Lucey and Clark, 1985). For example, the smallest grain size studied herein is ~ 10 µm which is significantly larger than the wavelengths of light interrogating the sample which range from 0.3 to 2.5 µm. For reflection to go to zero, the sample under investigation would have to be a black body, or perfect absorber and emitter, which is only theoretically attainable.

Modelling of the absorption coefficients of orthopyroxene by Lucey, (1998) would suggest band saturation would be most prevalent for Band I, and slightly less so for Band II. In the 33 fraction series of pyroxene PYX023, band saturation begins to flatten Band I at a grains size of ~ 75 µm as absolute reflectance drops to, and remains consistently between 0.05 and 0.1% reflectance as grain size increases. Band depths cluster between values of 0.45 and 0.7 from grains size splits from 75 µm through ~ 1000 µm before dropping off to a value of 0.19 in the 2.8-3.35 mm fraction. Both the 3.35-4.75 mm fraction and the rock spectrum have greater band depths as both deviate from the grains size fractions with bluer slopes and marginally higher albedos which is consistent with previous studies where rocks have behaved somewhat differently than powders (e.g., Yon and Pieters, 1998).

Scattering of light by the smallest grain size fractions of pyroxene dominates Band I below approximately 25 µm and significantly reduces band depth, and correspondingly area. Band I centre is however, unaffected by enhanced scattering, and only begins to shift progressively to longer wavelengths with the onset of bands saturation at ~ 75 µm. Measures of Band II centre are largely unaffected by band saturation until grain size of ~ 500 µm whereafter it decreases in wavelength until ~ 1.4 mm where with further increase in grain size, Band II centre becomes unreliable. The effects of enhanced scattering and band saturation are best illustrated by comparisons of Band Depth and the absolute reflectance values of derived band centres before centring has occurred and is depicted in Figure 4-3.

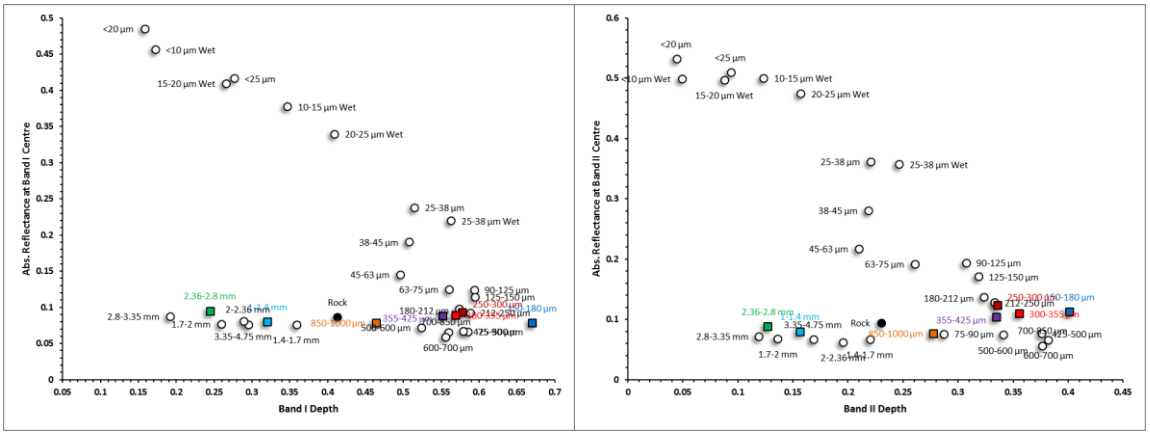

Figure 4-3: Comparison of Absolute Reflectance value at the derived Band Centre before centring occurred and the Band Depth for the 33 grains size splits of PYX023. Band I is depicted left, Band II on the right. This relationship best demonstrates both enhanced scattering at smaller grain sizes and band saturation for larger grain sizes. In both panels, enhanced scattering increases albedo and decreases band depth which can be seen in the smaller grain sizes which break out from the cluster of samples at the bottommost right in each panel and climb toward the upper left. Band saturation is illustrated by the samples dropping down to the lowest absolute reflectance values and clustering along a line of approximately 0.1% reflectance (which also illustrates the effect specular reflection has in ensuring reflectance never reaches zero). Both panels are also illustrative of the reasons for not relying on band depth and correlated area, and albedo/reflectance values for mineral identification as for a many different grains sizes, the measures are equivalent. In both of the panels we can surmise that the smallest grain sizes, those smaller than ~ 25 µm, scattering is dominating, and we may not be able to discern these grain sizes reliably using spectra with a multitude of empirical metrics (we could however suggest, grain size is small, and within a narrow range). We can also see band saturation, while apparent in all grain sizes larger than ~ 75 µm which are experiencing band saturation to some extent, only when they deviate leftward from the tight grouping of samples in the rightmost bottom corner, is saturation becoming enough of a concern, that we may no longer be able to reliably discern grain sizes larger than ~ 1 mm

spectrally without further metrics, we could however, definitively state the grain size is between coarse sand and rock

4.6 Results

The results are presented in the following 10 Figures, Appendix 4A, and subsections addressing each mineral or mineral assemblage individually.

4.6.1 Pyroxene

Sample PYX023 is a low-calcium orthopyroxene, enstatite (see Table 4.1). Low calcium pyroxenes such is PYX023 typically have two spectral absorption centred at approximately 1 and 2 μm caused by crystal field absorptions related to ferrous iron in the M1 an M2 sites I (Burns, 1993; Klima et al., 2011).

PYX023 is a mixture of coarsely crystalline grains in a matrix of fine grains and minor olivine. The sample fractions were prepared from isolated orthorhombic dipyramidal crystals of the pyroxene removed from the matrix by gentle crushing with an alumina motar and pestle. As the larger grain sizes were often large pieces of rectangular crystals extra care was taken when loading sample cups to ensure an even distribution of grain faces.

Spectra and empirical metric comparisons are shown in Figures 4-4 through 4-8.

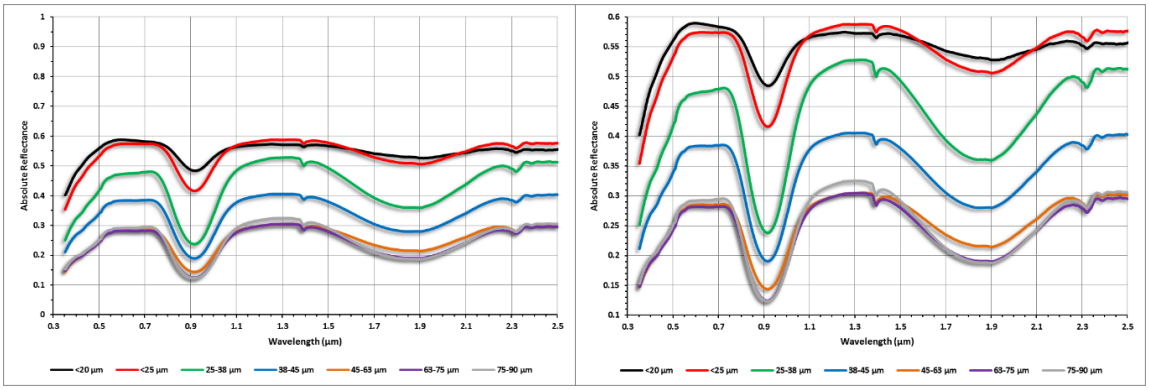

Figure 4-4: NIR absolute reflectance spectra of the first 7 of the dry sieved splits of pyroxene sample PYX023 depicted with a full reflectance scale at left, and an expanded scale in the panel at the right. Evident in both Bands I and II are the general trends in reflectance spectra when going from a small to a large grain size. The <20 µm split is high in albedo (in both the Figure and for the set of 33 splits), with muted (i.e., low depth) absorption features (the centred Band I depth in the <20 µm split is the shallowest centred Band I depth in the 33 split set), as grain size increases albedo drops and band depth increases until it reaches a maximum (the maximum centred band depths for both Band I and II occur in the 150-180 µm split), then centred band depth shallows in lock step with decreasing albedo.

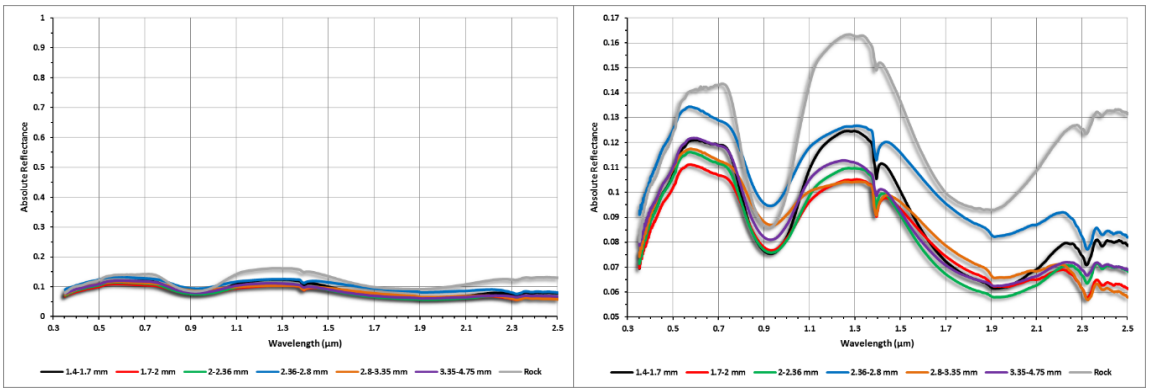

Figure 4-5: NIR absolute reflectance spectra of the last 6 of the dry sieved splits of pyroxene sample PYX023 and the rock spectrum depicted with a full reflectance scale in the left panel and, with a significantly expanded scale in the right panel. The clustering

of spectra close to zero reflectance due to band saturation is evident at left, as is the marginally higher albedo and slight red-sloped deviation of the rock spectrum from the rest of the set. Evident in the right panel, is the blue-slope of the largest of the grain size splits (for a progression through all sizes see Appendix 4A).

Albedo as represented by a linear trendline fit to the full spectrum ranges from ~0.54 to 0.1. Albedo declines consistently from < 10 µm to ~ 425 µm where it holds at ~0.1 from ~425 µm through to the spectrum of rock. Band centres for Band I, centred between 0.915 and 0.933 µm, is consistently within a few nanometres from <10 µm through ~180 µm then rise to a maximum of 0.933 µm at 700 nm, after which band centre falls slowly to approximately 0.925 µm for the spectrum of rock. Referencing Band II, band centre is consistently ~1.8 µm from <10 µm through ~500 µm in size where band saturation is evidenced as a wander, first shorter in wavelength from ~1.81 to ~1.79 µm with progressively larger grains sizes through ~ 1.7 mm, then unpredictably with increasing grain size. Band depths and band areas for both Bands I and II follow remarkably similar patterns with shallow varying depths from <10 µm to ~25 µm, and ~1.4 mm through rock, with little variance from ~25 µm through 1000 µm.

Band saturation is most apparent in the Band I centre and in a plot of Band I centre versus Band Area Ratio (BAR) which is the ratio of the Band II Area/Band I Area. In Figure 4-6, smaller grains sizes cluster along a centre value of 0.915 µm with BAR values generally increase from ~ 0.55 to 0.90. With increasing grain size, both Band I centre and BAR values increase with a somewhat positive correlation. There is scatter, but Band I centre versus BAR is the most useful empirical metric determination of grain size. The most useful single measure of band saturation is the Band I centre, where with grain sizes above ~ 150 µm, versus depth comparisons are not of use (see Appendix 4A) and as BAR is an established metric that is widely used to determine asteroid mineralogy, BAR is the

metric recommended.

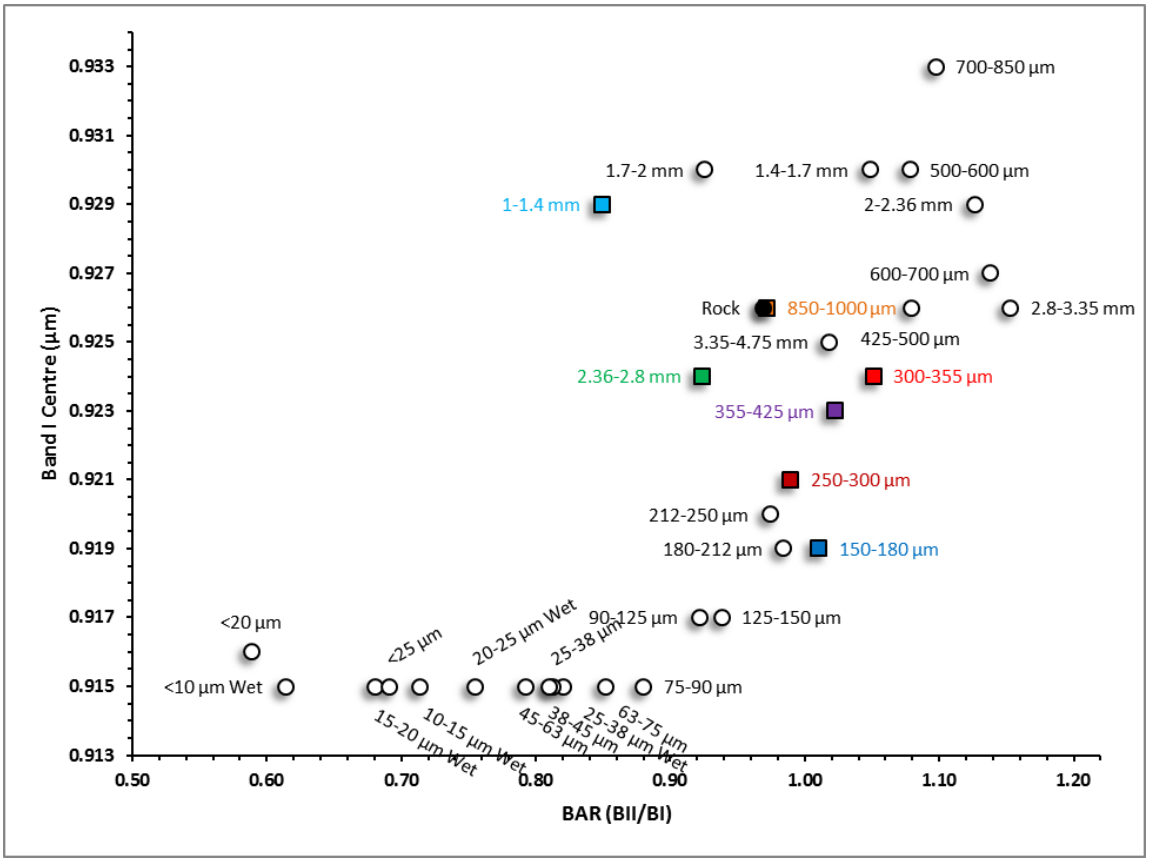

Figure 4-6: Band I Centre versus BAR plot for the 33 split series for pyroxene sample PYX023. This is the most efficacious of the empirical metric comparisons despite the scatter in some of the larger grain size splits in the upper left quadrant of the chart. Band saturation first appears in the between ~ 150 and 180 µm where the deviation of the Band I centre falls outside of the spectral resolution bounds of the ASDI spectrometer. The metrics were produced using centred bands where pin points where fixed inside the points of band extinction for all the samples in the set so scatter in the Band I Centre and BAR are the result of specular reflection and band saturation. Specular reflection in the smallest grain size splits effects band depth and area but across all of the samples investigated in this study it has little to no effect on centre values.

Table 4.1

Phase Sample # Grain Sizes Rock Type Location	Enstatite PYX023 <10 µm thru 4.75 mm (32 splits) + Rock Crystalline Pyroxene Mirabel Springs, Mount St. Helena, Lake County California	Basalt SA-51 <10 µm thru 4.75 mm (32 splits) + Rock Fine grained basalt, from the margin of a dike Roza Member of the Columbia River Basalt group, Wallowa County Oregon, Elk Mountain Quadrangle, 4N/45E/34ENW		Olivine OLV003 <45, 45-90, 90-250, 250-500, 500-1000 µm Crystalline Olivine San Carlos County Arizona	
	wt %	wt %.[4]		wt %	
SiO_2	56.86	51.49		40.64	
Al_2O_3	0.76	13.27		0.11	
FeO	6.36[1]	14.23[3]		9.25[1]	
Fe_2O_3	0.83[1]	--		0.59[1]	
MgO	34.04	4.47		49.13	
CaO	0.65	8.54		0.07	
Na_2O	0.00	2.55		0.08	
TiO_2	0.01	3.122		0.00	
Cr_2O_3	0.45	--		0.01	
V_2O_5	tr.	--		0.00	
CoO	0.03	--		0.04	
NiO	0.08	--		0.33	
MnO	0.17	0.221		0.09	
ZrO_2*	0.00	--		--	
Zn0*	--	--		0.00	
K_2O	--	1.44		0.00	
P_2O_5	--	0.672		0.00	
Total	100.00			100.15	
Atomic Ratios					
Mg	89.3			90.4	
Fe^{2+}	9.4			9.6	
Ca	1.3				
Number of Ions on the Basis of 6 Oxygens[5]		***ppm***		***6 Oxygens[5]***	***ppm***
Si	1.965	Ni	9	0.994	3350
Al	0.031	Cr	29	tr.	412
Al	--	Sc	40		
V	tr.	V	415	--	2
Ti	tr.	Ba	529	--	
Zr	--	Rb	45		
Cr	0.012	Sr	305	tr.	29
Fe^{3+}	0.022	Zr	185	0.011	22
Fe^{2+}	0.184	Y	44	0.190	
Mg	1.753	Nb	18.3	1.793	
Ca	0.025	Ga	22	0.002	
Co	0.001	Cu	29	0.001	
Ni	0.002	Zn	134	0.006	
Mn	0.004	Pb	7	0.002	
Na	--	La	31		
Zn	--	Ce	35	--	
Total	4.000	Th	4		
M2 cations[2]	0.999	Co			155

1. FeO determined by wet chemistry at the University of Alberta; Fe2O3 is determined as the difference between total Fe and FeO.
2. Sum of cations that preferentially occupy the M2 site in clinopyroxenes (Cr + Ca + Mn + Na + Zn)
3. Total Fe expressed as FeO.
4. Analyses from Atkinson (1989)
5. Analysis by Electron Microprobe at the University of Calgary

tr. = trace (<0.01 wt. %)

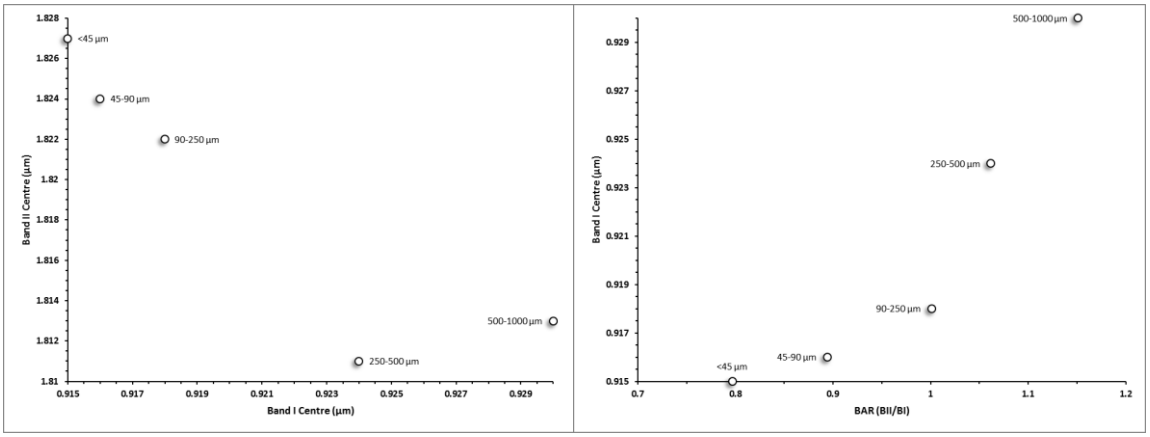

Figure 4-7: Band I Centre versus Band II Centre and Band I Centre versus BAR plots for the 5 size series of pyroxene PYX023. These two plots appear to make it clear that there is a definitive and easily exploitable relationship between grain size, band centres and band areas. Unfortunately if one references Figure 4-5 (or others in the Appendix 4A) the relationships are not quite as clear. Band saturation produces significant scatter about the larger grains sizes, though these relationships may be more indicative of naturally occurring grain size distributions which will rarely be sorted with the specificity of the 33 split series.

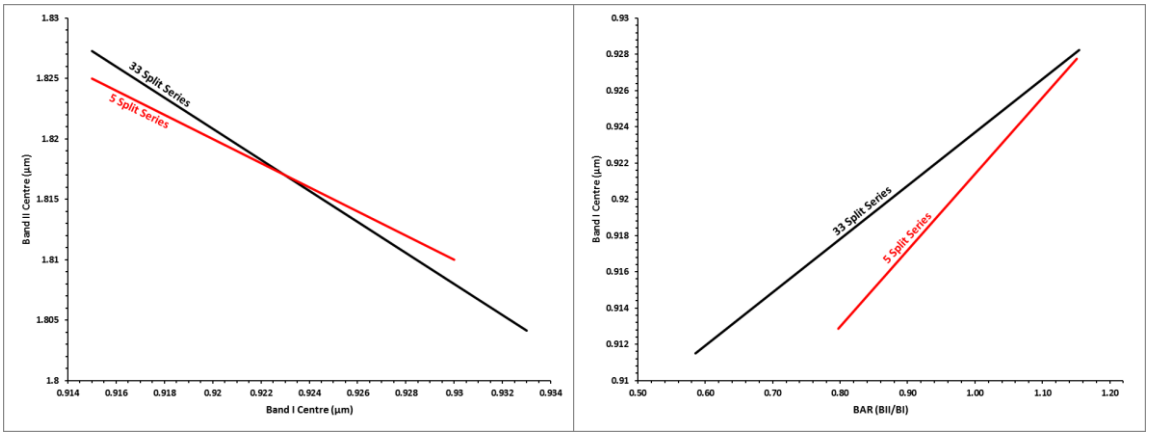

Figure 4-8: Linear trendline Band I Centre versus Band II Centre and Band I versus BAR plots of the two grain size series of pyroxene PYX023. These two empirical relationships are the most exploitable for the determination of grains size and degree of

band saturation as depicted in Figure 4-6 and 4-7. In the left panel, grain size increases from top left to bottom right, and in the right panel, from bottom left to top right. Band centres follow reasonably consistent trends from smallest to largest grain size, while depth and area follow a low-to-high-to-low trend which complicates the use of either metric. Area versus area and depth versus depth comparisons are not of use (see Appendix 4A) and as BAR is an established metric that is widely used to determine asteroid mineralogy, BAR is the metric recommended.

4.6.2 Basalt

The macroscopic sample of SA-51, an aphanitic basalt with minor vesiculation, consisted of a series of chunks, chips and offcuts from thin section preparation of fine grained basalt with composition noted in Table 4.1. The large volume of prepared sample had no obvious signs of surficial weathering.

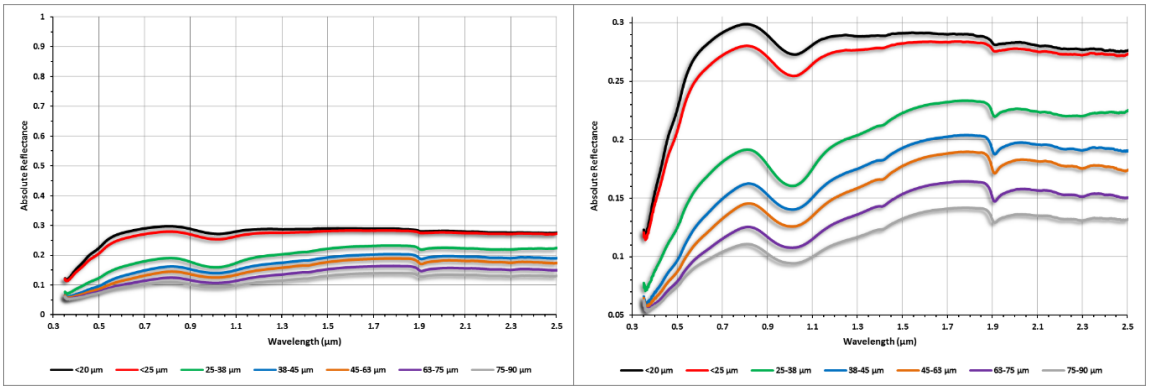

Figure 4-9: NIR absolute reflectance spectra of the first 7 of the dry sieved splits of basalt sample SA-51 depicted with a full reflectance scale in the left panel and an expanded scale in the right panel. The absorption feature centred at approximately 1 µm, due to crystal field transitions related to iron in the pyroxene and olivine crystals in the basalt is the absorption feature of interest. Throughout both of the basalt grain size sets, despite the appearance of band saturation with increasing grain size, the band centre remains relatively constant.

Unlike PYX023, the basalt sample has only one spectral absorption of note centred at approximately 1 µm due to ferrous iron present in the pyroxene and olivine within the sample. The other spectral absorptions seen in Figure 4-9 and 4-10 are at ~ 1.4, 1.9 and 2.1 through 2.5 µm are probably the result of water in the sample, possibly metal-OH absorptions and a weak 2 µm region, high calcium, pyroxene absorption band.

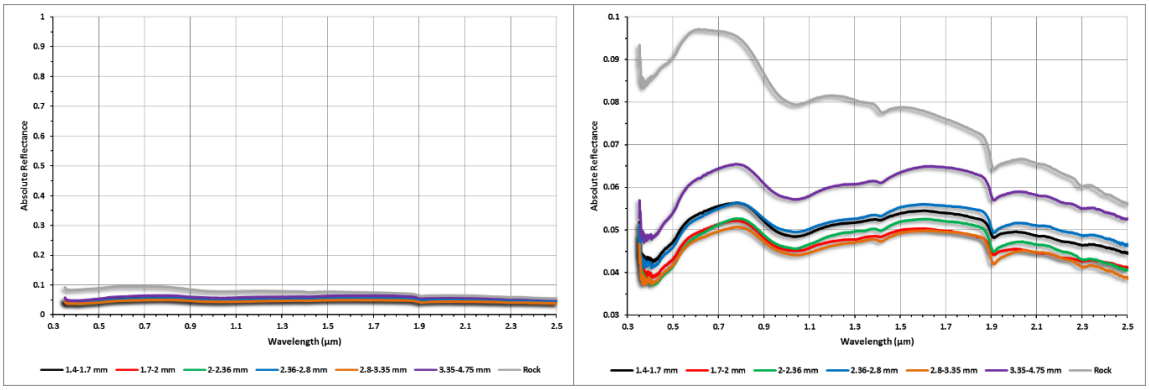

Figure 4-10: NIR absolute reflectance spectra of the last 6 of the dry sieved splits of Basalt sample SA-51 and the rock spectrum depicted with a full reflectance scale in the left panel and, with a significantly expanded scale in the right panel. The clustering of spectra close to zero reflectance due to band saturation is evident in the left panel, as is the marginally higher albedo and significantly blue-sloped deviation of the rock spectrum from the rest of the set. Evident in the right panel is the marginally blue-slope of the largest of the grain size splits which contrasts with the slightly red-slope of the smallest grain sizes in Figure 4-9 (for a progression through all sizes see Appendix 4A).

With only one crystal field absorption we cannot compare empirical metrics from two absorptions and have compared the metrics of the one absorption band to one another for both the 33 and 5 fraction series. Individually, band depth and area, as they are correlated measures, correlate with one another, as was the case in pyroxene. Depth and area follow the same general trend where decreasing grain size results in increased albedo and decreased band depth in the smallest grain size splits, while in band saturation, albedo and band depth both decrease. Albedo, as expressed by a linear trendline fit through the full wavelength range, follows a general decreasing trend from the smallest

grain sizes to ~ 180 µm where it levels off at ~ 0.1 and remains so through to rock. Band depth is remarkably constant across both the 33 and 5 size sets, and only shows evidence of a very slow drop off from the smallest grain sizes to a minimum value of 0.989 µm in the 1.4-1.7 mm split which appears to be an anomalous result. If the derived centre for the 1.4-1.7 mm split is removed from the set, the variance from the smallest to the largest value is only 13 nanometres. The derived empirical metrics for Band I (see Appendix 4A, Sheet *B*) do not have correlation as is depicted in Figure 4-11. However, the relationship between empirical metrics does agree with the general trends related to grain size for most all mineral separates.

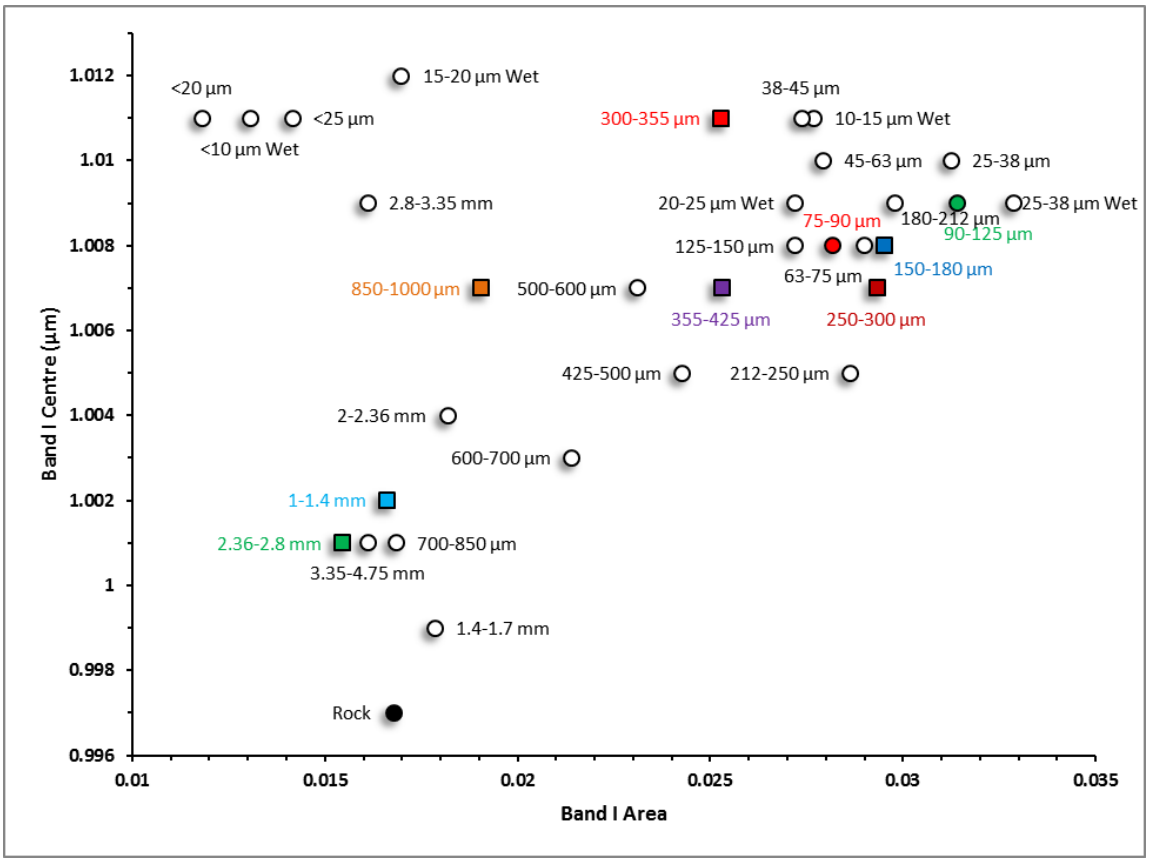

Figure 4-11: Band I Centre versus Band I Area for the 33 grain size series of basalt sample SA-51. While there is no positive correlation, this pattern fits with what can generally be said about the changes of the correlated metrics of band depth and area with increasing grain size, band depth and/or area is lowest in the smallest grain size splits were specular reflection is most active, depth/area increase to a maximum at some point

at an intermediate size, in this instance in the 25-38 µm split, and generally falls off again as grain size increases. The largest grain sizes evidence band depths/areas equal to or lower than the depth/area of the smallest grain size splits.

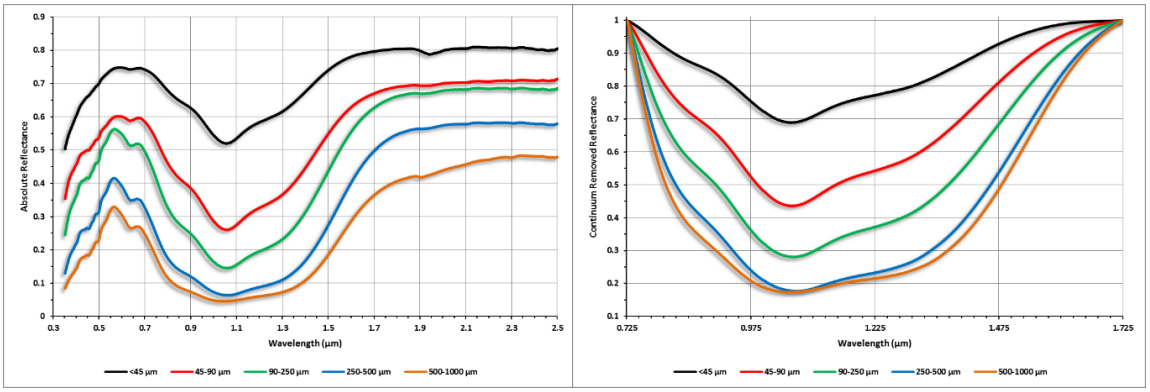

Figure 4-12: NIR absolute reflectance (left) and straight line continuum removed spectra (right) of olivine sample OLV003. In the largest of the grains size splits, 500-1000 µm, band saturation is apparent in both the absolute reflectance spectra and the centred spectra but it is not exerting a large enough influence to affect the empirical measures of the ~ 1 µm absorption. Muting of the absorptions short-ward in wavelength of the ~ 0.8 µm reflectance maximum can be seen and can be attributed to specular reflection but the muting of the ~ 1 µm absorption of interest is also not effective enough to exert and

influence that would complicate the sample identification as olivine using empirical measures.

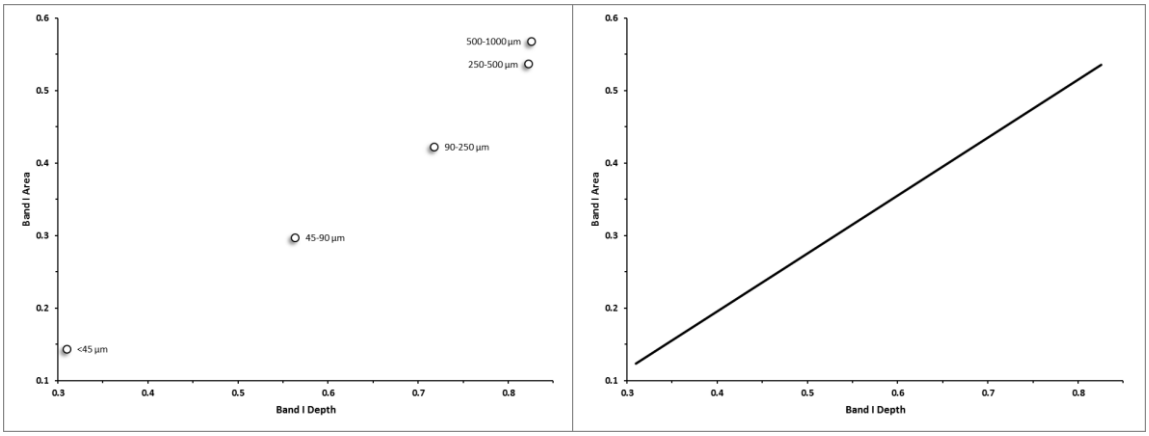

Figure 4-13: Correlation of Band Depth and Area for the ~ 1 µm absorption triplet of olivine sample OLV003. The left panel is a comparison of the empirical measures and the right panel is a linear trendline fit through the data. While this is not an extremely positive correlation it does fit with the general spectral alteration expected with increasing grain size. More interesting, as the sensitivity of olivine to spectral alteration with grain size is driven largely by its iron content, a relationship akin to the one depicted may be of use to discern iron content with a modicum of accuracy. Given a set of similarly derived empirical metrics, another olivine of differing composition is likely to plot on a line of differing slope.

4.6.3 Olivine

The olivine sample, OLV003, $Fa_{76}Fo_{24}$, consisted of loose relatively pristine olivine crystals (see Table 4.1). Like basalt, the olivine sample has only one significant absorption, a characteristic triplet, with a central absorption centred at ~ 1.06 µm due to ferrous iron in the M2 site and side bands at ~ 0.85 and 1.25 µm which are attributed to iron in the M1 site (Burns, 1993). The two side bands are shoulders on the larger and deeper ~1.06 µm absorption. There is no empirical method for fitting shoulders, but shoulder positions and depths can be modelled.

The individual empirical metrics for the 5 size series of OLV003 all appear to be of use, though band area and depth form the only exploitable comparison. Band centres subtend a range of only 13 nanometres with no systematic pattern of variation. Spectra are shown in Figure 4-12. In the spectra of the olivine sample we see the muting of absorption features short-ward of ~ 0.7 μm that can be attributed to enhanced surface scatter in the smallest grain size fraction, and a decrease in the band depths of the absorptions in the triplet with no loss of the ability to resolve each absorption or a shift in band centre. In the 500-1000 μm size fraction, flattening of the ~1.05 μm absorption and a loss of the resolvability of the triplet is readily apparent, but is not yet severe enough for a measure of centre to deviate. The band saturation is affecting the depth of the absorption triplet but for an olivine sample with low ferrous iron content and bright albedo, grain size would have to be larger to exert an effect large enough for band depth and area to deviate from the trendline for the empirical metric comparison shown in Figure 4-13.

4.7 Discussion

To our knowledge, this is the first study to investigate the effects of grain sizes larger than ~ 1.3 mm and to thoroughly investigate the effects of the onset of band saturation as it relates to our ability to derive spectral metrics. It is generally thought that planetary surfaces, such as asteroids and the majority of the surface of Mars are dominated by fine submicron dust, although from thermal inertia and infrared studies, and HiRISE imagery, relatively dust free and rocky surfaces are exposed on Mars and soil samples analysed with the Phoenix lander's Robotic Arm Camera (22 μm pixel^{-1}) and Optical Microscope (4 μm pixel^{-1}) show there to be a significant population of 20-100 μm grains on the surface (e.g., Mellon et al., 2000; Putzig and Mellon, 2007; Goetz et al., 2010; Michalski and Niles, 2010). The Hayabusa-Itokawa asteroid encounter clearly demonstrated a surface with particle sizes ranging from boulders to gravels which were responsible for significant differences in albedo (Abe et al., 2006), while the sample return portion of the mission returned a suite of particles typically less than 50 μm in diameter dominated by

those smaller than 10 μm (Nakamura et al., 2011), which confirmed earlier grains size estimates made by Hiroi et al., (1995), using ground based telescopic reflectance spectra.

Grain size may significantly complicate identification of composition. When grains are small, surface scattering dominates, reducing band depth. When grain sizes are large and absorption bands saturate, band depth is also reduced, compromising empirical measures of band depth, centre or minimum, and area. Each of the empirical metrics: band centre, depth, area and a measure of albedo, either fixed, or as a measure of the entire spectrum, has a relationship to both small grain size surface scatter and large grain size band saturation that is exploitable. In general, in reference to the two large grain size sets, band centres hold steady across a wide set of small through mid-grain sizes and vary with larger sizes when band saturation is an issue, while band depths hold steady through the middle range of sizes and vary at both extremes in the size range, and band areas follow the trend of band depths. Overall albedos as measured by linear trendline, fall steadily as grain size runs from small to mid-way through each set where albedos level out as measured reflectance sits very close to zero.

4.8 Conclusion

Band saturation and enhanced scattering effect grain size splits in different size ranges, but have essentially the same effect; both are decreasing band depth (and correlated band area), and altering albedo. The effects of both are most obvious in the relationship between band depth and the absolute reflectance value, at the derived centre, before the band was centred, as depicted in Figure 4-3. Enhanced scattering is responsible for the spread of the smallest grain size fractions of pyroxene, <10 to ~ 90 μm, in Band I and <10 to 180 μm in Band II (Figure 4-3, Panels A and B, respectively). At ~ 90 and ~ 180 μm in Bands I and II, respectively, enhanced scattering is no longer a factor and band saturation begins to take over. From these two size fractions, with increasing grain size, although the bands are beginning to saturate, the effect is not strong enough to yet affect depth. From fraction sizes ~ 90 and ~ 180 μm in Bands I and II, respectively, the

absolute reflectance minimum has essentially flat-lined at ~ 0.1% (recall, while more photons are being absorbed as grain size, and the effects of band saturation are increasing, reflectance will not go to zero as there is always a specular component to reflectance if the grain sizes being interrogated are larger than the wavelength of light; see Figures 4-1 and 4-2). Band saturation is increasing with further increase in grain size, although, from ~ 180 µm through ~ 1000 µm, band depth in both Bands I and II stabilizes and remains rather fixed. At and above a grain size of ~ 1 mm in pyroxene, band saturation is strong enough an effect that band depth deviates from its zone of stabilization, i.e., in grain sizes from ~ 90 to 850 µm in Band I and ~ 180 to ~ 850 µm in Band II, and progressively approaches zero with increasing grain size. The spectra of hand sample does not to saturate as significantly as the grain size fractions larger than ~ 1 mm, and it blues, which is likely and effect Fresnel reflection at the air-rock interface as noted by Yon and Pieters, (1988), and/or the brightening of hand sample spectra as a result of welded mineral particles noted by Carli and Sgavetti, (2011).

The effects of enhanced scattering and band saturation, and where they occur in the grain size suite of the orthopyroxene sample are clearly demonstrated in Figure 4-3, and the results correlate with the empirical relationships of Band I versus Band II centre and Band I centre versus BAR that we, and previous studies would suggest are the empirical relationships best suited to define mineralogy and grain size in orthopyroxenes (e.g., Cloutis et al., 1986; Cloutis and Gaffey, 1991). In Figure 4-6 and others in Appendix 4A, one can see the same patterns in the measures of band centre and BAR, which shift at corresponding grain size values. Band I centre, when compared with BAR is relatively fixed at ~ 0.915 µm with increasing grain size until a size of ~ 90 µm is reached. From ~ 90 µm, with increasing grain size, Band I centre and progressively increases with increasing grain size until ~ 800 µm, where it begins to slowly decrease with further increases in grain size. Band II centre decreases very gradually from ~ 1.825 to ~1.810 µm, with progressively increasing grain size from the smallest fraction, < 10 µmm through ~ 1 mm, whereafter, with increasing grain size it wanders as band saturation has nearly wiped out the ~ 2 µm absorption feature and the centre can no longer be reliably measured. Referencing Figures 4-3 and 4-6, this pattern can be seen in both. In Figure 4-

3 the grain size fractions of orthopyroxene from which we can reliably derive mineralogy, and a reasonably accurate measure of grain size, are clustered in the bottommost right corner, and in Figure 4-6 they are the same grouping of grain sizes which very nearly subtend a line from mid-bottom to rightmost top. From grain size split 75-90 µm, through 700-850 µm, with increasing grains size, each larger fraction, with minor scatter, steps progressively up a line connecting the 75-90 and 700-850 µm fractions. At grain sizes larger than ~ 850 µm, with increasing grain size, the Band I versus BAR points for each fraction scatter back down the line.

From these results, we can conclude, enhanced scattering in orthopyroxene complicates the determination of mineralogy and grain size below ~ 75 µm, and band saturation complicates determination of mineralogy and grain size above ~ 850 µm. Grain sizes between ~ 75 µm and 850 µm, mineralogy and grain size can be robustly identified. At grain sizes both smaller and larger we can still be confident in mineralogy, but best served by binning grain sizes into two categories, those smaller than 75 µm and those larger than ~ 850 µm. To be confident in our measures when specificity is afforded between grain sizes of ~ 75 and ~ 850 µm, and in the binned grain size grouping at the small and large extremes of grain size, the empirical measures of band centre, depth, area (for BAR calculation) and reflectance at band centre before centering (or band minimum) are required. If band minimum or reflectance at the band centre, before the band is centered, were not available (e.g., as in reflectance spectra for an asteroid), centre vs. centre and Band I vs. BAR relationships, and individual metrics are exploitable for mineralogical identification, but confidence in the assessment of grain size would be lost, and the grain size groupings should be changed to ~ 90 µm, and larger than ~ 300 µm. Other empirical measures such as R/B versus albedo, of Adams and Filice (1967) and slope from Band I onset to Band II offset of Harloff and Arnold 2001 (or as calculated in Appendix 4A, from the fixed pin point on the short-wavelength side of Band I to the fixed point on the long-wavelength side of Band II) are useful, as are other empirical metrics, although no others appear to be able to discern grain size to the level of specificity, or will provide as much confidence in mineralogical identification as centre vs. centre, centre vs. BAR, and depth vs. reflectance minimum.

In basalt, much the same can be said for relationships between the empirically metrics derived from only the ~ 1 µm absorption feature, although we cannot be as confident as in pyroxene when assessing grain size spectrally. For basalt the most utilizable empirical relationship is Band I centre versus area (or depth). As depicted in Figure 4-11, with increasing grain size, grain size fractions from <10 through ~ 38 µm cross the top of the figure from left to right, with further increasing grain size, they cluster in the topmost right corner until a grain size of ~ 300 µm is reached, whereafter, with further grain size increase, the points spread both leftward, and downward. Enhanced scattering is evident in the grain size fractions < ~ 38 µm, and band saturation is evident in grain size fractions larger than ~ 300 µm. The basalt sample has the highest ferrous iron content of the three samples, which equates to the highest absorption coefficient at ~ 1 µm among the three, and the lowest band depths of the three. As a result, rather than a cluster in the bottom, rightmost corner of a depth vs. reflectance minimum plot (see Appendix 4A), the minimum reflectance value is reached at a grain size of ~180 µm, and band depths tail off to approach zero thereafter. For the basalt, robust identification of mineralogy via spectra is likely from the smallest grain size through the largest as there is very little spread in the band centre which would be relied on most to make that determination. Grain size could not be assessed confidently with specificity. It would be best with basalt to bin the grain size into ranges of <38, 38-300, 300-600, and 600 µm to 4.75 mm/rock. No relationship among metrics was found that would significantly better spectral based assessment of grains size; a high absorption coefficient and degree of band saturation which we surmise is actively suppressing absorption features in all of the grain sizes of basalt studied.

Olivine, in the 5 fraction set studied herein, has consistent band centres, depths, and areas, and the only change of note with increasing grain size is a decrease in albedo. In the absolute and continuum removed spectra depicted in Figure 4-12, enhanced scattering is evidenced in the <45 µm grain size fraction as muting of spectral absorption short-ward of ~ 0.55 µm, and band saturation appears to be flattening the absorption triplet in the 500-1000 µm fraction. These effects are however, not significant enough to affect the empirical metrics normally employed, i.e., band centre, depth, and area. Figure 4-13 would appear to be a positive, exploitable correlation, although, the comparison is of

depth and area, which are always correlated. The spread along the trendline in Figure 4-13 can be used, but with little more specificity than to say, grain size is small, medium or large. Mineralogical identification of olivine in all grain sizes from <45 through 1000 μm will be robust.

Of the three common planetary analogue materials, the two minerals pyroxene and olivine, and the basaltic sample, which is in essence, a slightly more calcium rich combination of the two, only the orthopyroxene has empirical relationships that can be utilized to robustly identify mineralogy, and grain size, with specificity very nearly approaching the finely-demarcated grain size fractions.

4.9 Acknowledgements

MAC gratefully acknowledges Loni Stewart, Kaitlyn McCormack and Lindsay Kaletzke for their assistance with sample preparation. Funding from the Natural Sciences and Engineering Research Council of Canada (NSERC), the NSERC Collaborative Research and Training Experience Program-Technologies and Techniques for Earth and Space Exploration, and the Ontario Graduate Scholarship Program that contributed to this work. The HOSERLab at the University of Winnipeg, where the NIR spectra presented herein were collected was established with funding provided by the Canadian Foundation for Innovation, the Manitoba Research Innovations Fund and the Canadian Space Agency.

4.10 References

Abe, M., Takagi, Y., Kitazato, K., Abe, S., Hiroi, T., Vilas, F., Clark, B.E., Abell, P.A., Lederer, S.M., Jarvis, K.S., Nimura, T., Uede, Y., and Fujiwara, A., 2006. Asteroid Itokawa from the Hayabusa spacecraft. Science 312, 1334-1338.

Adams, J.B., Filice, A.L., 1967. Spectral reflectance 0.4 to 2.0 microns of silicate rock powders. Journal of Geophysical Research 72, 5705-5715.

Adams, J.B., 1974. Visible and near-infrared reflectance spectra of pyroxenes as applied to remote sensing of solid objects in the solar system. Journal of Geophysical Research 79, No. 32, 4829-4836.

Anbazhagan, S., Arivazhagan, S., 2009. Reflectance spectra of analog basalts; implications for remote sensing of lunar geology. Planetary and Space Science 57, 1346-1358.

Beck, P., Pommerol, A., Thomas, N., Schmitt, B., Moynier, F., and Barrat, J.-A., 2012. Photometry of meteorites. Icarus 218, 364-377.

Burns, R.G., 1993. Mineralogical applications of crystal field theory. Cambridge University Press, Cambridge, 551.

Carli, C., 2009. Spectral analyses in the VNIR region of igneous rocks: Surface composition characterization of terrestrial planets. Plinius 35, 83-890.

Carli, C., Sgavetti, M., 2011. Spectral characteristics of rocks: Effects of composition and texture and implications for the interpretation of planet surface compositions. Icarus 211,

Clark, R.N., and Lucey, P.G., 1984. Spectral properties of ice-particulate mixtures and implications for remote sensing 1. Intimate mixtures. Journal of Geophysical Research 89, No. B7, 6341-6348.

Clark, R.N., and Roush, T.L., 1984. Reflectance spectroscopy: Quantitative analysis techniques for remote sensing applications. Journal of Geophysical Research 89, No. B7, 6329-6340.

Cloutis, E.A., Gaffey, M.J., Jackowski, T.L., and K.L. Reed, 1986. Calibrations of phase abundance, composition, and particle size distribution for olivine-orthopyroxene mixtures from reflectance spectra. Journal of Geophysical Research 91, No. B11, 11641-11653.

Cloutis, E.A., and Gaffey, M.J., 1991. Pyroxene spectroscopy revisited: Spectral-compositional correlations and relationships to geothermometry. Journal of Geophysical Research 96, No. E5, 22809-22826.

Cloutis, E.A., Craig, M.A., Kaletzke, L., McCormack, K., and Stewart, L., 2006. HOSERLab: A new planetary spectroscopy facility. Lunar and Planetary Science Conference XXXVII, abstract #2121.

Duffard, R., Lazzaro, D., De León, J., 2005. Revisiting spectral parameters of silicate-bearing meteorites. Meteor. Plant. Sci. 40, 445-459.

Gaffey, M.J., 2008. Interpreting asteroid spectra – avoiding the three “great mistakes”. Asteroids, Comets, Meteors Conference, abstract #8162.

Goetz, W., Pike, W.T., Hviid, S.F., Madsen, M.B., Morris, R.V., Hecht, M.H. and others, 2010. Microscopy analysis of soils at the Phoenix landing site, Mars: Classification of soil particles and description of their optical and magnetic properties. Journal of Geophysical Research 115, E00E22.

Harloff, J., Arnold, G., 2001. Near-infrared reflectance spectroscopy of bulk analog materials for planetary crust. Planetary and Space Science 49, 191-211.

Hunt, G.R., Salisbury, J.W., 1970. Visible and near-infrared spectra of minerals and rocks: I Silicate minerals. Modern Geology 1, 283-300.

Irvine, W.M., and Pollack, J.B., 1968. Infrared optical properties of water and ice spheres. Icarus 8, 324-360.

King, T.V.V., and Pieters, C.M., 1981. Particulate mineral mixtures: The relation of albedo and apparent absorption band strength. Lunar and Planetary Science Conference XII, 547-549.

Hinrichs, J.L., and Lucey, P.G., 2002. Temperature-dependent near-infrared spectral properties of minerals, meteorites, and lunar soil. Icarus 155, 169-180.

Hiroi, T., and Pieters, C.M., 1994. Estimation of grains sizes and mixing ratios of fine powder mixtures of common geologic materials. Journal of Geophysical Research 99, No. E5, 10867-10879.

Hiroi, T, Binzel, R.P., Sunshine, J.M., Pieters, C.M., and Takeda, H., 1995. Grain sizes and mineral compositions of surface regoliths of Vesta-like asteroids. Icarus 115, 374-386.

Klima, R.L., Dyar, M.D., and Pieters, C.M., 2011. Near-infrared spectra of clinopyroxenes: Effects of calcium content and crystal structure. Meteoritics & Planetary Science 46, No. 3, 379-395.

Lucey, P.G., and Clark, R.N., 1985. Spectral properties of water ice and contaminants. In Ices in the solar system, edited by J. Klinger et al., pp. 155-168, D. Reidel Publishing Company, France.

Lucey, P.G., 1998. Model near-infrared optical constants of olivine and pyroxene as a function of iron content. Journal of Geophysical Research 103, No. E1, 1703-1713.

Lucey, P.G., Keil, K., and Whitely, R., 1998. The influence of temperature on the spectra of the A-asteroids and implications for their silicate chemistry

Mellon, M.T., Jakosky, B.M., Kieffer, H.H., and Christensen, P.R., 2000. High-resolution thermal inertia mapping from the Mars Global Surveyor thermal emission spectrometer. Icarus 148, 437-455.

Michalski, J.R., and Niles, P.B., 2010. Deep crustal carbonate rocks exposed by meteor impact on Mars. Nature Geoscience 3, No. 11, 751-755.

Morris, R.V., Neely, S.C., and Mendell, W.W., 1982. Application of Kubelka-Munk theory of diffuse reflectance to geologic problems: The role of scattering. Geophysical Research Letters 9, No. 2, 113-116.

Mustard, J.F., and Pieters, C.M., 1989. Photometric phase functions of common geologic minerals and applications to quantitative analysis of mineral mixture reflectance spectra. Journal of Geophysical Research 94, No. B10, 13619-13634.

Mustard, J.F., Hays, J.E., 1997. Effects of hyperfine particles on reflectance spectra from 0.3 to 25 μm. Icarus 125, 145-163.

Nakamura, T., Noguchi, T., Tanaka, M., Zolensky, M.E., Kimura, M., Tsuchiyama, A., Nakato, A., Ogami, T., Ishida, H., Uesugi, M., Yada, T., Shirai, K., Fujimura, A., Okazaki, R., Sandford, S.A., Ishibashi, Y., Abe, M., Okada, T., Ueno, M., Mukai, T., Yoshikawa, M., and Kawaguchi, J., 2011. Itokawa dust particles: a direct link between S-type asteroids and ordinary chondrites. Science 333, 1113-1116.

Pieters, C.M., 1983. Strength of mineral absorption features in the transmitted component of near-infrared reflected light: First results from RELAB. Journal of Geophysical Research 88, 9534-9544.

Pompilio, L., Pedrazzi, G., Sgavetti, M., Cloutis, E.A., Craig, M.A., Roush, T.L., 2009. Exponential Gaussian approach for spectral modeling: The EGO algorithm 1. Band saturation. Icarus 201, 781-794.

Pompilio, L., Pedrazzi, G., Cloutis, E.A., Craig, M.A., Roush, T.L., 2010. Exponential Gaussian approach for spectral modeling: The EGO algorithm II. Band asymmetry. Icarus 208, 811-823.

Poulet, F., Erard, S., 2004. Nonlinear spectral mixing: Quantitative analysis of laboratory mineral mixtures. Journal of Geophysical Research 109, E02009, doi: 10.1029/2003JE002179, 2004.

Putzig, N.E., and Mellon, M.T., 2007. Apparent thermal inertia and the surface heterogeneity of Mars. Icarus 191, 68-94.

Sanchez, J.A., Reddy, V., Nathues, A., Cloutis, E.A., Mann, P., and Hiesinger, H., 2012. Phase reddening on near-Earth asteroids: Implications for mineralogical analysis, space weathering and taxonomic classification. Icarus 220, 36-50.

Shkuratov, Y.G., Starukhina, L., Hoffmann, H., Arnold, G., 1999. A model of spectral albedo of particulate surfaces: Implications for optical properties of the Moon. Icarus 137, 235-246.

Yon, S.A., Pieters, C.M., 1988. Interactions of light with rough dielectric surfaces: Spectral reflectance and polarimetric properties. Proceedings of the Lunar and Planetary Science Conference 18, 581-592.

Chapter 5

5 Concluding Remarks

Authoring research papers, and working to finish a Ph.D. project at times, can feel like an inordinate amount of effort to add another drop to an ocean. The goal of any scientific Ph.D. thesis is to create original research, and I trust we have managed just that in a number of areas.

Each of the studies detailed in the preceding thesis contributes original research to the spectroscopic community with a single theme that ties all three together. We have been working to bring some transparency to the spectroscopic research community by sharing as much of the methodology, and data, as is possible. We have created a set of tools, and are freely sharing them with everyone. The best one can hope for is to have a positive impact and the collective works of this thesis have already done so. Two of the coauthors of Chapter 2 who participated in the creation the Excel curve fitting workbook have gone on to graduate school with the focus of their work being spectroscopy. Each, with a set of tools that will let them excel (pun intended). We hope they pay it forward and continue to practice what we are espousing herein, that they continue to share the tools they may create, and hold to the edict to share their raw data in future publications.

The focus of Chapter 2 is curve fitting, as written and structured, with emphasis on the fitting of reflectance spectra. The methods are logical, robust and most importantly, repeatable. We champion empirical metrics, i.e., those derived from the curve fitting of absorption features in existing data, which can be repeated in perpetuity without error. Referring to polynomial fitting of band minima and centres, if one fits a polynomial of the same order, between the same nodes, using the same data they will always get the same answer. This is the single most important element in empirical fitting; if a measurement or derived metric is not repeatable it is useless. This is a part of the message we would like those who make use of the curve fitting workbook take home. The other, we will all be better served if we share.

There are is no new math in Chapter 2 (although there are new applications in each of Chapters 2, 3 and 4). The concept of curve fitting is not new, and has been evolving for some time (e.g. Doetsch, 1928; Lonn, 1932; Kaper, 1966; Gaffey, 1976, 2010; Clark, 1980, 1981, 1999; Farr et al., 1980; McCord et al., 1981; Singer, 1981; Cloutis et al., 1986; Sunshine et al., 1988; Cloutis and Gaffey 1991; Gaffey et al., 1993, 2002; Gaffey and Gilbert 1998; Gaffey and McCord 1978, 1979; Clark et al., 2003; van der Meer, 2004; Storm et al., 2007; Burbine et al., 2009; Clenet et al., 2011; Parente et al., 2013; van Ruitenbeek et al., 2014). Each of these researchers and, in many instances, multiple members of research groups have moved the field forward. Although, the only software programs to come from these collective works, that are publically accessible and useable, with documentation, are SpecPR and Tetracorder, both created by Roger Clark (Clark, 1980, 1993; Clark et al., 2003; Livo and Clark, 2014). Both are freely available, although difficult for the uninitiated to use.

Fitting with polynomials, straight line continuum removal, modelling with Gaussians, and the like, have existed for decades (e.g., Clark and Roush, 1984; Sunshine et al., 1988). New in Chapter 2 is accessibility. To illustrate, before The Excel curve fitting workbook was created, only two of the coauthors of Chapter 2 had the ability to perform straight line continuum removal of spectra and derive band centres using polynomials. To do so they had access to a proprietary version of quite old and highly modified software, with no ability to share it. Only two of the authors used the Modified Gaussian Model (MGM), but had not used it for publication, as neither could defend it against arguments put forward by reviewers that is was black box software and should not be used before Parente et al., (2013) published a paper which described the mathematics underlying MGM. With the publication of Chapter 2 (currently under review), the authors and anyone else who wants to make use of the functions in the Excel workbook will have free access to do so, no need to hide methods, no need to buy software (which graduate students can rarely fund on their own) and no need to justify the methods later. The mathematics are plainly laid out, and there is nothing hidden in a macro, or anything in anyway proprietary. What the workbook does not do is make it easy, as, unlike the commercial software packages, using the functions in the workbook are rather time

consuming. The benefit is that, once spectra are fit, the data, the fits, and the metrics derived, can be preserved indefinitely.

The impact glasses referenced in Chapter 3 are the largest set of spectrally characterized impactites noted in the literature. The majority of past research into the spectral characteristics of Martian and asteroidal impactites have utilized synthesized samples (e.g., Bandfield 2000, Wyatt et al. 2001, Minitti and Hamilton, 2010; Cannon and Mustard, 2015), as representative of impactites. It is also the first reporting of spectral features created by 5Si and 6Si coordination environments preserved in silicate glasses outside of in-situ experiments within diamond anvil cells (e.g., Williams and Jeanloz, 1988; Closman and Williams, 1995). In addition, Chapter 3 contains two new applications of curve fitting: (1) where Lagrange based polynomial interpolation is used to add resolution to data for the purposes area derivation via chords in a method that could be applied in an automated system like that created by van Ruitenbeek et al., (2014) with application to Martian hyperspectral imagery; and (2) the application of empirical curve fitting to IR emission spectra.

IR emission spectra have been classically unmixed, via linear unmixing or spectral deconvolution. It is an effective technique, but not without issues as it relies on libraries of spectra to deconvolve emission spectra which has led to interpretations of Martian mineralogy that are somewhat contradictory (e.g., Bandfield et al., 2000; Bandfield, 2002; Hamilton et al., 2001; McSween, et al., 2003, Rogers, 2007; Roger et al, 2007; Ruff et al., 2007; Wyatt et al., 2001; Wyatt and McSween, 2002). We believe we have come up with a unique solution by studying the spectra of naturally occurring impactites and using empirical relationships to assess mineralogy. We already know that, TES spectra of the central uplifts of a number of craters on Mars exhibit spectral features suggestive of exhumed impact glasses with absorption features akin to those in our study (per. comm., A. D. Rogers), and in the follow-on study, the spectra from Chapter 3 will be used to robustly identify said assemblages.

The Chapter 4 grain size study marks a few firsts: (1) it is the first study to assess the effects grains of diameter ~ 1 to 4.75 mm, are having on the reflectance spectra of the

common analogue minerals for asteroid and Martian surface mineralogy; (2) it is the first study of its kind to assess the effectiveness of empirical curve fitting to derive both grain size and consider when empirical relationships break down, and identification of mineralogy may fail; and (3) it is the first study to assess the effects of grain size in 33 finely-demarcated gain size fractions for pyroxene and basalt. Via comparison of a multitude of empirical metrics for the two minerals and one rock type studied in Chapter 3, we can confirm the general finding that, with grain size progressively increasing from small to large, albedo will be first brighten, then decrease with increasing grain size. Band depths will begin at their shallowest, deepen to a maximum, and then decrease with increasing grain size. Band centre measurements, at both extremes in grain size, are unreliable, but if we compare each and every metric we can derive, it is only at the very extremes, below ~ 25 μm and above ~ 2 mm, where we well have difficulty making robust assessments of mineralogy and grain size remotely.

All in all, not bad for a few years work!

5.1 References

Bandfield J.L., Hamilton V.E., and Christensen P.R., 2000. A global view of Martian surface compositions from MGS-TES. Science 287, 1626-1630.

Bandfield, J.L., 2002. Global mineral distribution on Mars, Journal of Geophysical Research 107, No. E46, 5042.

Burbine, T.H., Buchanan, P.C., Dolkar, T., and Binzel, R.P., 2009. Pyroxene mineralogies on near-Earth vestoids. Meteoritics & Planetary Science 44, Nr 9, 1331-1341.

Cannon, K.M., and Mustard, J.F., 2015. Preserved glass-rich impactites on Mars. Geology G36953.1.

Clark, R.N., 1980. A large-scale interactive one-dimensional array processing system. Publications of the Astronomical Society of the Pacific 92, 221-224.

Clark, R.N., 1981. Water frost and ice: The near-infrared spectral reflectance 0.65 – 2.5 μm. Journal of Geophysical Research 86, No. B4, 3087-3096.

Clark, R.N., 1993. SPECtrum Processing Routines user's manual version 3 (program SPECPR): U.S. Geological Survey, Open-File Report 93-595.

Clark, R.N., 1999. Spectroscopy of rocks and minerals and principles of spectroscopy. In, Manual of Remote Sensing, edited by A. N. Renz, pp. 3-58, John Wiley, New York.

Clark, R.N., and Roush, T.L., 1984. Reflectance spectroscopy: Quantitative analysis techniques for remote sensing applications. Journal of Geophysical Research 89, No. B7, 6329-6340.

Clark, R.N., Swayze, G.A., Livo, K.E., Kokaly, R.F., Sutley, S.J., Dalton, J.B., McDougal R.R., and Gent, C.A., 2003. Imaging spectroscopy: Earth and planetary remote sensing with the USGS Tetracorder and expert systems. Journal of Geophysical Research 108, No. E12, 5-1-5-44.

Clenet, H., Pinet, P., Daydou, Y., Heuripeau, F., Rosemberg, C., Baratoux, D., and Chevrel, S., 2011. A new systematic approach using the modified Gaussian model: Insight for the characterization of chemical composition of olivines, pyroxenes and olivine-pyroxene mixtures. Icarus 213, 404-422.

Closmann, C., and Williams, Q., 1995. In-situ spectroscopic investigations of high-pressure hydrated (Mg,Fe)SiO3 glasses: OH vibrations as a probe of glass structure. American Mineralogist 80, 201-212.

Cloutis, E.A., and Gaffey, M.J., 1991. Pyroxene spectroscopy revisited: Spectral-compositional correlations and relationships to geothermometry. Journal of Geophysical Research 96, No. E5, 22809-22826.

Doestsch, G. Von, 1928. The elimination of the Doppler effect in spectroscopic fine structure and exact determination of the components, Zeitschrift fur Physik 49, 705-730.

Farr, T.G., Bates, B.A., Ralph, R.L., and Adams, J.B., 1980. Effects of overlapping optical absorption bands of pyroxene and glass on the reflectance spectra of lunar soils. Proceedings of the Lunar and Planetary Science Conference XI, 719-729.

Gaffey, M.J., 1976. Spectral Reflectance Characteristics of the Meteorite Classes. Journal of Geophysical Research 81, No. 5, 905-920.

Gaffey, M.J., 2010. Space weathering and the interpretation of asteroid reflectance spectra, Icarus 209, 564-574.

Gaffey. M.J., and McCord, T.B., 1978. Asteroid surface materials: Mineralogical characterization form reflectance spectra. Space Science Reviews 21, 555-628.

Gaffey, M.J., King, T.V.V., Hawke, B.R., and Cintala, M.J., 1982. Asteroid spectral variations: Implications for composition and surface processes. LPSCXIII, abstract #1128.

Gaffey, M.J., and Gilbert, S.L., 1998. Asteroid 6 Hebe: The probable parent body of the H-type ordinary chondrites and the IIE iron meteorites. Meteoritics & Planetary Science 33, 1281-1295.

Gaffey, M.J., Cloutis, E.A., Kelley, M.S., Reed, K.L., 2002. Mineralogy of Asteroids. In Bottke, W.F. Jr, Cellino, A., Paolicchi, P., and Binzel, R.P. (Eds.), Asteroids III. University of Arizona Press, Tucson, 183-204.

Hamilton, V.E., Wyatt, M.B., McSween, H. Y. Jr., and Christensen, P.R., 2001. Analysis of terrestrial and Martian volcanic compositions using thermal emission spectroscopy: 2. Application to Martian surface spectra from the Mars Global Surveyor Thermal Emission Spectrometer. Journal of Geophysical Research: Planets 106, No. E7, 14733-14746.

Kaper, H.G., Smites, D.W., Schwarz, U., Takakubo, K., and van Woerden, H., 1966. Computer analysis of ordered distributions into Gaussian components. Bulletin of the Astronomical Institute of the Netherlands 18, 465-487.

Livo, K.E., and Clark, R.N., 2014. The Tetracorder user guide-version 4.4: U.S. Geological Survey, Open-File Report 2013-1300.

Lonn, E. Von, 1932. Proof of the Uniqueness of the Decomposition of an Intensity Curve into its Components. Zeitschrift fur Physik 75, 348-349.

McCord, T.B., Clark, R.N., Hawke, B.R., McFadden, L.A., Owensby, P.D., Pieters, C.M., and Adams, J.B., 1981. Moon: Near-infrared spectral reflectance, a first good look. Journal of Geophysical Research 86, No. B11, 10883-10892.

McSween, H.Y. Jr., Grove, T.L., and Wyatt, M.B., 2003. Constraints on the composition and petrogenesis of the Martian crust. Journal of Geophysical Research 108, No. E12, 9-1-19.

Minitti, M.E., and Hamilton, V.E., 2010. A search for basaltic-to-intermediate glasses on Mars: Assessing the Martian crustal mineralogy. Icarus 210, 135-149.

Parente, M., Makarewicz, H.D., and Bishop, J.L., 2011. Decomposition of mineral absorption bands using nonlinear least squares curve fitting: Application to Martian meteorites and CRISM data. Planetary and Space Science 59, 423-442.

Rogers, A.D., and Christensen, P.R., 2007. Surface mineralogy of the Martian low-albedo regions from MGS-TES data: Implications for upper crustal evolution and surface alteration. Journal of Geophysical Research 112, E01003.

Rogers, A.D., Bandfield, J.L., and Christensen, P.R., 2007. Global spectral classification on Martian low-albedo regions with Mars Global Surveyor thermal emission spectrometer. Journal of Geophysical Research 112, E02004.

Ruff, S.W., and Christensen, P.R., 2007. Basaltic andesite, altered basalt, and a TES-based search for smectite clay minerals on Mars. Geophysical Research Letters 34, L10204.

Singer, R.B., 1981. Near-infrared spectral reflectance of mineral mixtures: Systematic combinations of pyroxenes, olivine, and iron oxides. Journal of Geophysical Research 86, No. B9, 7967-7982.

Storm, S., Bus, S.J., and Binzel, R.P., 2007. Olivine-pyroxene distribution of S-type asteroids in the main belt. Bulletin of the American Astronomical Society 39, 448.

Sunshine, J.M., Pieters, C.M., and S. F. Pratt, S.F., 1988. Gaussian Analysis of Pyroxene Reflectance Spectra. LPSC XIX, Abstract #1151.

van der Meer, F.D., 2004. Analysis of spectral absorption features in hyperspectral imagery. International Journal of Applied Earth Observation and Geoinformation 5, 55-6.

van Ruitenbeek, F.J.A., W.H., Bakker, H.M.A, van der Werff, T.E., Zegers, J.H.P., Oosthoek, Z.A., Omer, S.H., Marsh, and F.D., van der Meer, 2014. Mapping the wavelength position of deepest absorption features to explore mineral diversity in hyperspectral images. Planetary and Space Science 101, 108-117.

Williams, Q., and Jeanloz, R., 1988. Spectroscopic evidence for pressure-induced coordination changes in silicate glasses and melts. Science 239, No. 4842, 902-905.

Wyatt, M.B., Hamilton, V.E., McSween, H.Y. Jr., Christensen, P.R., and Taylor, L.A., 2001. Analysis of terrestrial and Martian volcanic compositions using thermal emission spectroscopy: 1. Determination of mineralogy, chemistry, and classification strategies. Journal of Geophysical Research 106, E7, 14711-14732.

Wyatt, M.B., and McSween, H.Y. Jr., 2002. Spectral evidence for weathered basalt as an alternative to andesite in the northern lowlands of Mars. Letters to Nature 417.

Appendices

6 Appendix 2B: Fitting the Curve, Workbook Instructions

(Note: The examples reference Excel® 2010, and while some of the formatting and keyboard shortcuts may be different for various versions of Excel® from 2007 through 2016, for both Mac and Windows, the mathematical functions have been tested and across all of the various Excel platforms and they operate identically)

The manuscript, workbook, and this set of instructions are not intended to be the definitive guide to curve fitting; rather it is intended, first, as a guide to what we believe are robust and reliable methods for empirical curve fitting, demonstrating functions in a manner that is accessible to those who are new to the field and having difficulty visualizing what is meant by continua, centres and the like, and secondly, as an illustration of the necessity for the dissemination of data to the community using a transparent and eminently repeatable framework. We use Excel, not to suggest those who are already curve fitting with other software switch to Excel, rather, it has been used because the students this work is aimed at are likely to both have and be somewhat familiar with Excel (99+% of the incoming undergraduates were using Microsoft Office in a recent survey of ~300 in an origins of the solar system class; this prior to Office 365 being offered for free to all Western students). This is aimed at those who are new to the field, new to, and perhaps unfamiliar with the mathematics, and may not be curve fitting now as they simply do not have access to software. Curve fitting in this manner can unfortunately be rather labour intensive, but it is intended as a learning tool first and foremost, where, in context, its laborious nature is appropriate.

When attempting to describe an object with spectra, we as a community need to be crystal clear about our curve fitting, the fitting parameters used, the parameters of the fits themselves that need to be supplied, and we need to ensure that we are disseminating data and derived metrics using math we can all comprehend and repeat.

There are a number of functions included in the Appendix A workbook that are fundamental to the curve fitting process and several that reference the more complex multi-step functions built into Excel which allow said curve fitting functions to operate. All of the recommended empirical curve fitting functions rely solely only on in-worksheet/in-workbook calculations and no macros are used.

6.1 Excel Short Cut Keys:

Shift+F10 = Right Click (Displays the Shortcut Menu)

F2 = in cell editing

Shift+Direction Arrows = Highlights cells (Particularly useful for copy/paste)

Ctrl+Up Arrow or **Ctrl+Down Arrow** = Jumps to the upper or lower most cell occupied by a value

Ctrl+Shift+Up Arrow or **Ctrl+Down Arrow** = Highlights the range from the current position to the highest or lowest most value in a column… same goes for right or left arrow keys

Ctrl+C = Copy (Copy cells)

Ctrl+V = Paste (Paste copied cells)

Ctrl+Z = Undo

Ctrl+Alt+V = Paste Special (Opens the Paste Special Dialog)

Ctrl+F3 = Opens the Name Manager

Ctrl+Page Up or **Ctrl+Page Down** = Jumps between worksheets in a workbook, either left-to-right or right-to-left

6.2 Keyboard Navigation (skip to page 11 if you are familiar with Excel)

Most of Excel can be navigated by keyboard shortcuts and one rarely needs to use a mouse (the same applies to all of Microsoft Office). The process of repeatedly cutting-and-pasting can be rather laborious so it can be useful to understand how to navigate about Excel and perform Excel functions without having to use a mouse, or bounce back and forth between the mouse and keyboard. There are several ways to go about keyboard based navigation using shortcut key and shortcut key combinations for navigation of the two ribbons at the top of the screen which direct most functions. The topmost ribbon is the *Quick Access Toolbar* which can be customized, as can the *Ribbon*. You can see an example of a customized *Quick Access Toolbar* in Figure 1… where several functions have been added, i.e., *Redo*, *Change Chart Type*, *Column Width*, *Row Height*, *All Borders*, *Outside Borders*, *No Borders*, *Name Manager*, *Paste Values* and *Paste Formulas*, which are an easy two-key press, or one click launch.

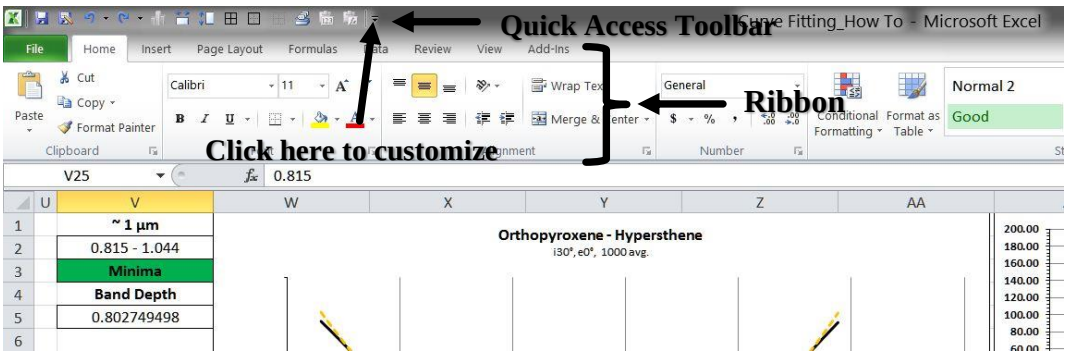

Figure 1: Quick Access Toolbar and Ribbon

Every function in the *Quick Access Toolbar* and the *Ribbon* can be launched using the keyboard alone; for keyboard access, simply hit the **Alt** key, which will bring up the Key

Tips, which are letters and numbers which highlight the function, then press the appropriate keys to call up the function/open the menu, etc.. For example, pressing **Alt** will bring up the Figure 2.

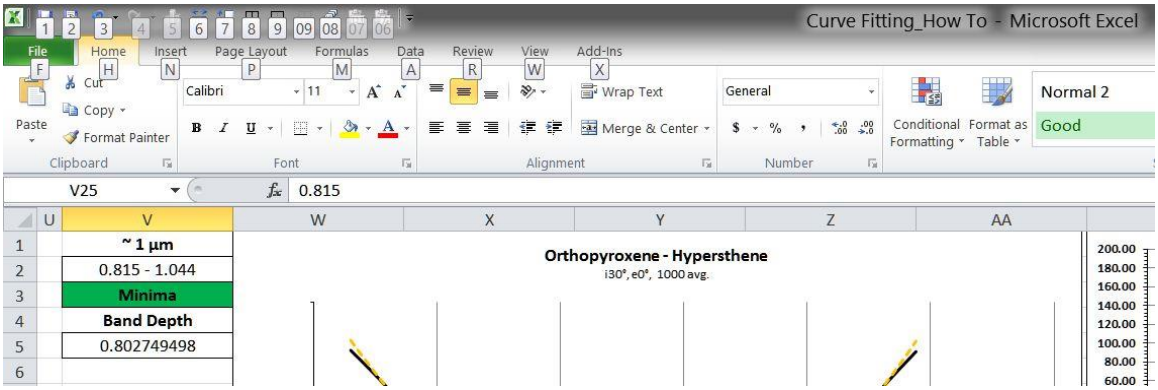

Figure 2: Alt Key Shortcut for the Quick Access Toolbar and Ribbon

Pressing any of the number keys, or number key combinations will launch the appropriate function in the *Quick Access Toolbar*, e.g., pressing **08** would launch the *Name Manager*, while pressing **1** would save the workbook (as would simple using the shortcut key combination, **Ctrl+S**). If the **H** key was pressed, it would bring up the following set of Key Tips for the *Home* tab of the *Ribbon* as depicted in Figure 3.

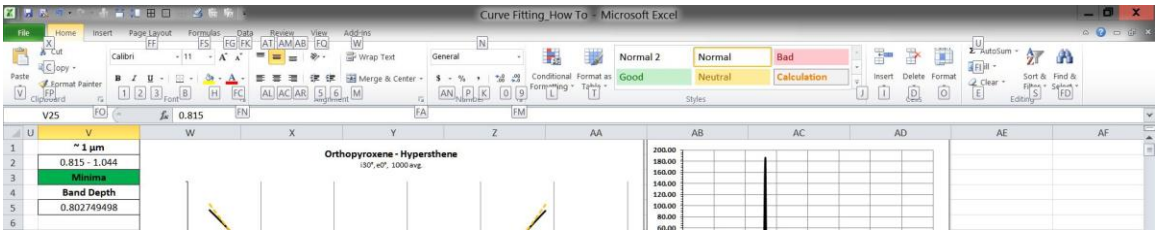

Figure 3: Alt+H

If one hits the letter **N** key now, it would bring them into the *Number* pane as shown in Figure 4, highlighting the choice of cell formatting, in this instance *General* and you

could navigate to through the available choices in the pop-up menu by using the **Up** and **Down Arrows**.

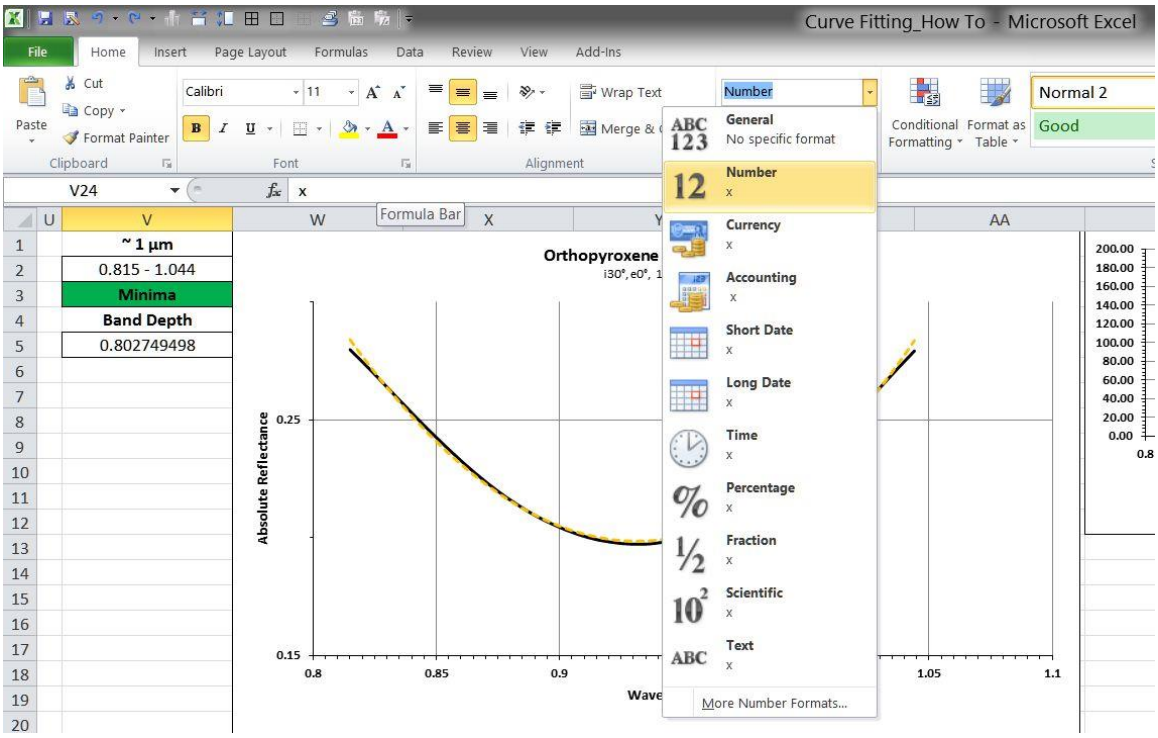

Figure 4: Alt+H, F, M... and Tab

With *Number* highlighted you would hit **Enter** to change the specific cells formatting from *General* to *Number*. If you then wanted to change the decimal places of the *Number* format, or the manner in which the number was displayed, e.g., commas demarcating thousands, starting anew, you would hit **Alt** to bring up the Key Tips for the *Quick Access Toolbar* and *Ribbon*, hit **H** for the *Home* tab, the **F** then **M** keys to bring up the *Formatting Cells* menu which can be navigated about internally using **Tab** and **Shift+Tab** while values can be changed using the **Arrow** keys.

Each menu is a little different, but the basics of **Tab**/**Shift+Tab** and using **Arrow** keys to navigate apply to all pop-up menus. For example, now in the inside the *Format Cell* pop-

up menu, of Figure 5, for a cell that is currently formatted to be *General* the menu will open thusly and the *Number* tab is highlighted by a dotted box.

Pressing the **Right** or **Left Arrow** keys will cycle through the tabs, while the **Up** and **Down Arrow** keys will do nothing. Pressing the **Tab** key will jump into Category where the **Up**/**Down** and **Right**/**Left Arrow** keys can be used to select a category as depicted in Figure 6.

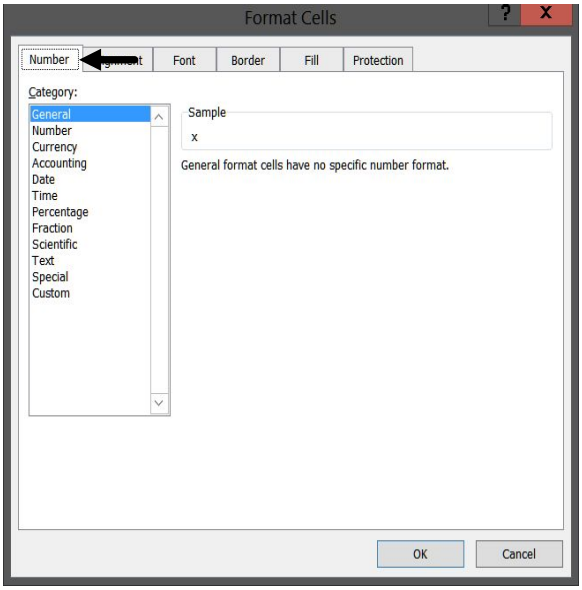

Figure 5: The Format Cells Pop-Up Menu

In the example in Figure 6, we have selected the *Number* category. If one wanted to apply the default two decimal place formatting to the currently highlighted cell, you would hit the **Enter** key to apply this formatting and exit the pop-up menu. If you wanted to change the number of Decimal places you could hit the **Tab** key once to highlight the number of decimal places and use the **Up**/**Down Arrow** keys to alter the number of decimal places shown, then hit the **Tab** key three

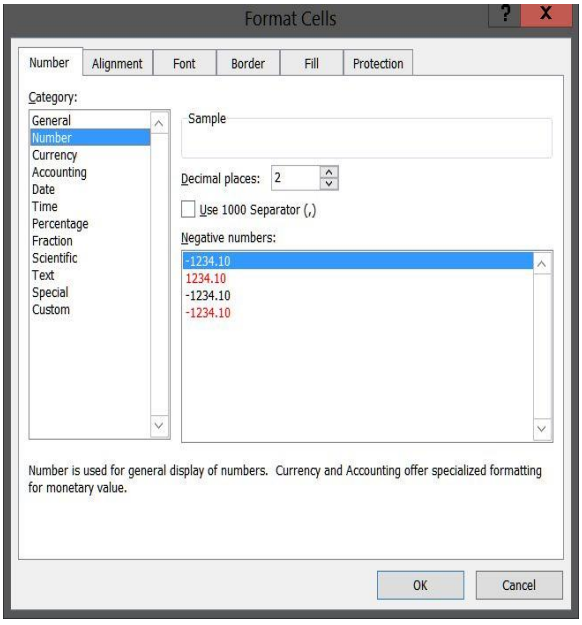

Figure 6: Navigating the Format Cells Pop-Up Menu

more times to move the ‘Ok’ button and hit the **Enter** key to leave the menu (or you could simply press the **Enter** key).

If you wanted to use the 1000 Separator, you could **Tab** key to it and use the **Spacebar** to toggle the checkmark in the check box on and off.

In the pop-up menu, one can also navigate partially with the **Arrow** keys, for example, from the Use 1000 Separator check box, pressing the **Down Arrow** key will highlight and allow you to choose one of the Negative Number display options, but you will not be able to then navigate out of the Negative Number display option window using the **Arrow** keys. Navigation using the keyboard works within all of the Excel shortcut and pop-up menus; it just requires a little experimentation to figure out how it works, and what combination of keys works best for you. Pressing the **Tab** key moves one down level, and **Shift+Tab** will move you back up.

6.2.1 Defined Name Ranges

The Polynomial Functions as well as several others require the use of defined 'Names.' Individual cells or a range of cells can be defined by a name. Names are defined using the *Shortcut Menu* which can be opened via a right click of the mouse or the **Shift+F10** keyboard shortcut.

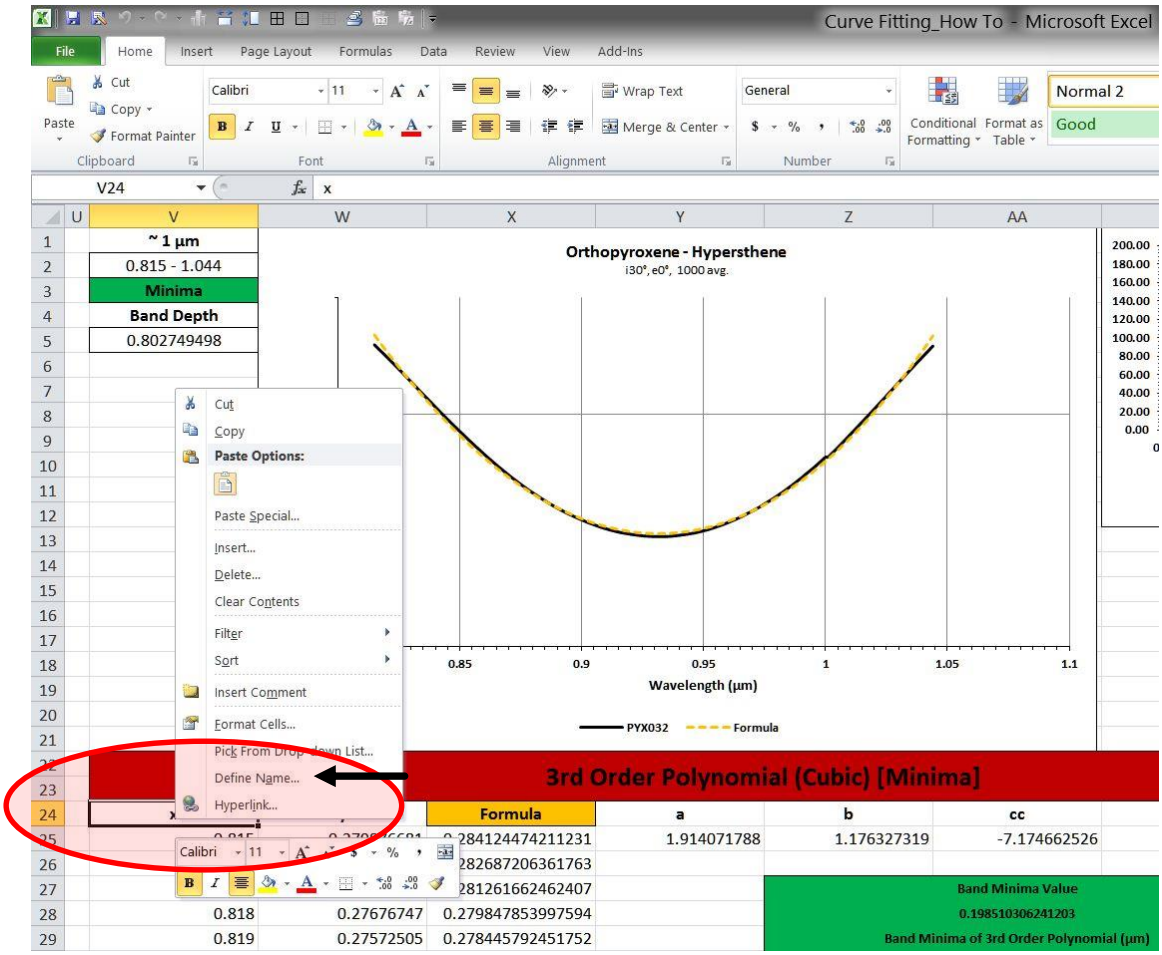

Figure 7: Using the Shortcut Menu and the keyboard to define a Name

When working with large numbers of spectra and creating a large workbook, each worksheet and the full workbook can end up containing a large number of defined names/name ranges and Excel has a *Name Manager* that can be added to the *Quick*

Access Toolbar and/or be opened with the **Ctrl+F3** keyboard shortcut. The polynomial functions and calculation of local slope rely on defined name ranges. Defined names allow these functions to operate without the use of Visual Basic based macros which we have found to be notoriously unreliable.

Names can be defined by bringing up the *Shortcut Menu* with a right-click of the mouse or hitting **Shift+F10** as depicted in Figure 7. It is easiest if this is done with the cell highlighted that contains the intended name, as in the example below, where 'x' is going to be name of the range named x which is column V, cell 25 through column V, cell 254 in the *Minima* worksheet.

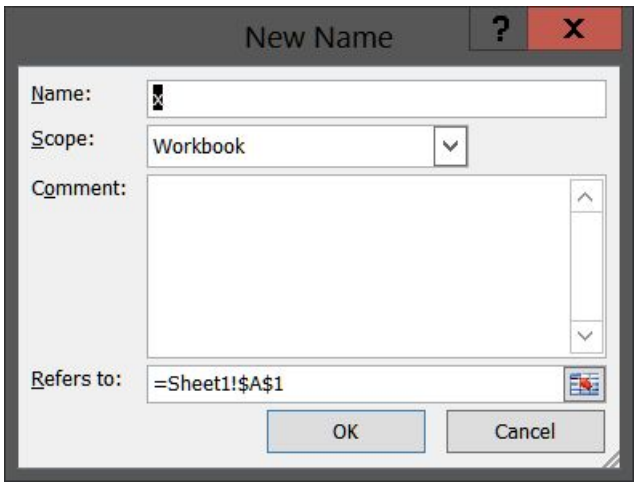

Figure 8: Defining a new Name

If 'x' (V24) is the highlighted cell, when you hit the **A** key or click on Define Name it will bring up the dialog box depicted in Figure 8.

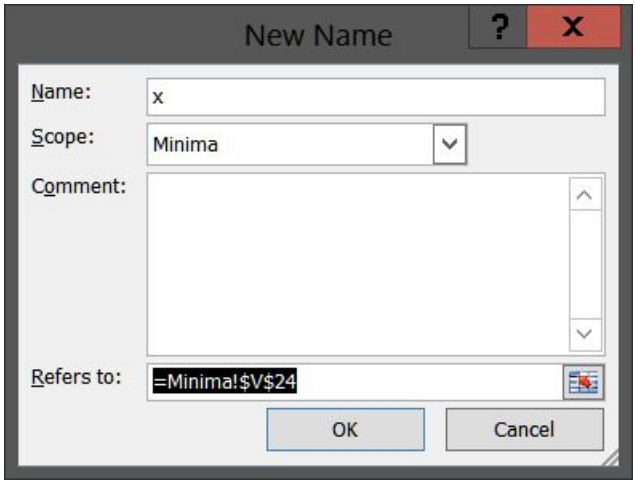

Figure 9: Continuing to define a new Name

As 'x' is the letter in cell V24, 'x' is the name, though you may choose something else. If, you open the *New Name* pop-up on a cell with a letter in it, and the *New Name* pop-up opens with a blank Name, it means you have already assigned something else the name 'x' in the worksheet or you have assigned it elsewhere, globally

to the entire workbook. It is exceedingly important you do not inadvertently assign names to be used throughout the entire workbook, as in doing so, you can mistakenly reassign all ranges or cells named ‘x’ to one range after the fact and change all of your previous work.

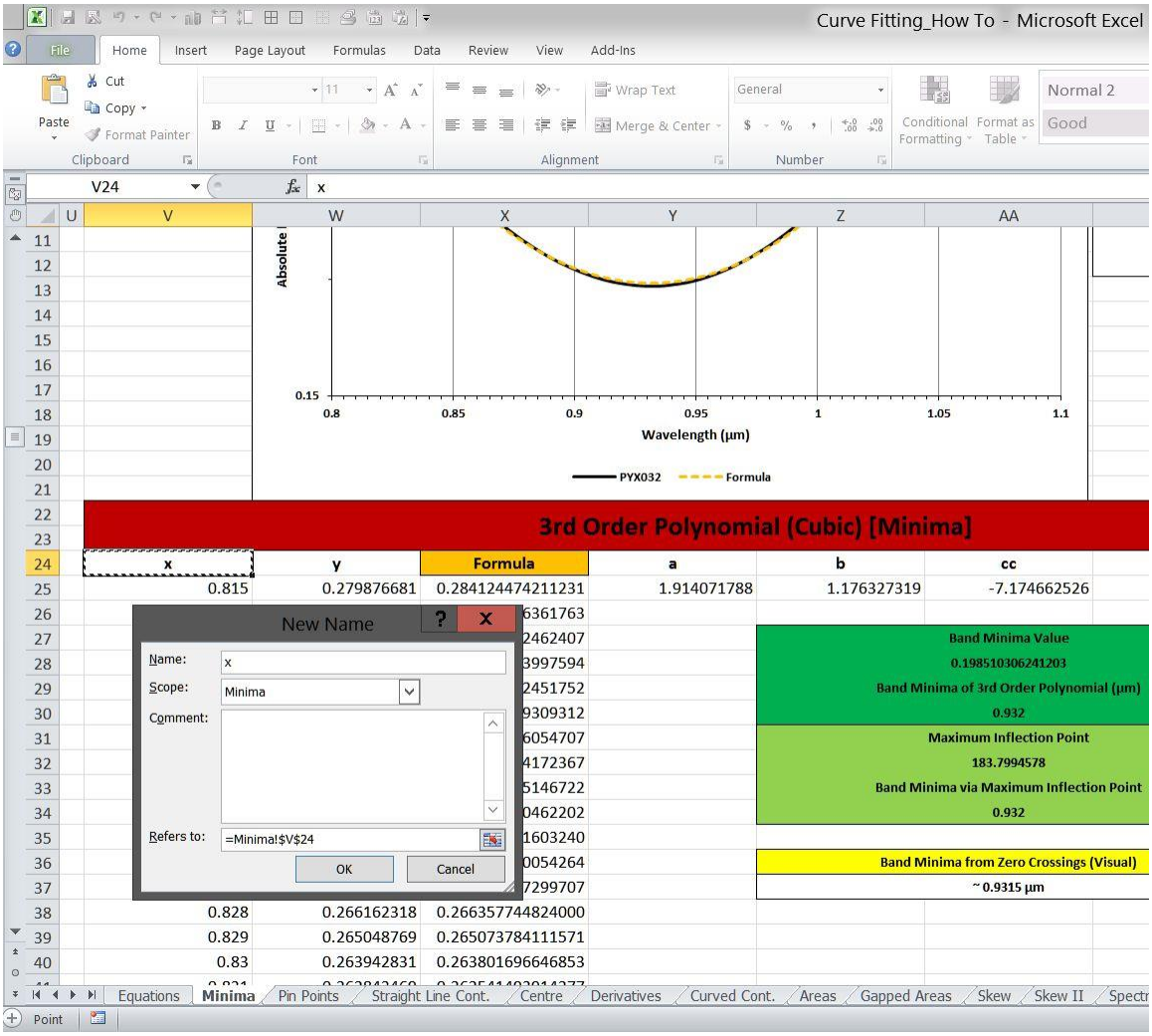

Figure 10: Define a new Name... Continued

As depicted in Figure 9, we want this range named ‘x’, so press the **Tab** key to navigate to Scope, then use the **Down Arrow** to highlight *Minima* and select it using **Enter**, then

Press **Tab** twice to navigate through Comment to Refers to, or press the **R** key. The *New Name* pop-up menu will look like Figure 10.

The screen like Figure 10, with the 'x', cell V24 highlighted with an animated moving dashed line around the cell.

You want the 'x' range to be cells V25 through V254 (in Excel ranges are denoted by colons, i.e., V25:V254), so you hit the **Down Arrow** key once to move the animated cell down to cell V25 then, while holding down the **Shift+Ctrl** keys, hit the **Down Arrow** key again. This will highlight all of the cells from your starting cell (V25) to the lowest

cell with a value in it in the column, V254. The screen would look like Figure 11.

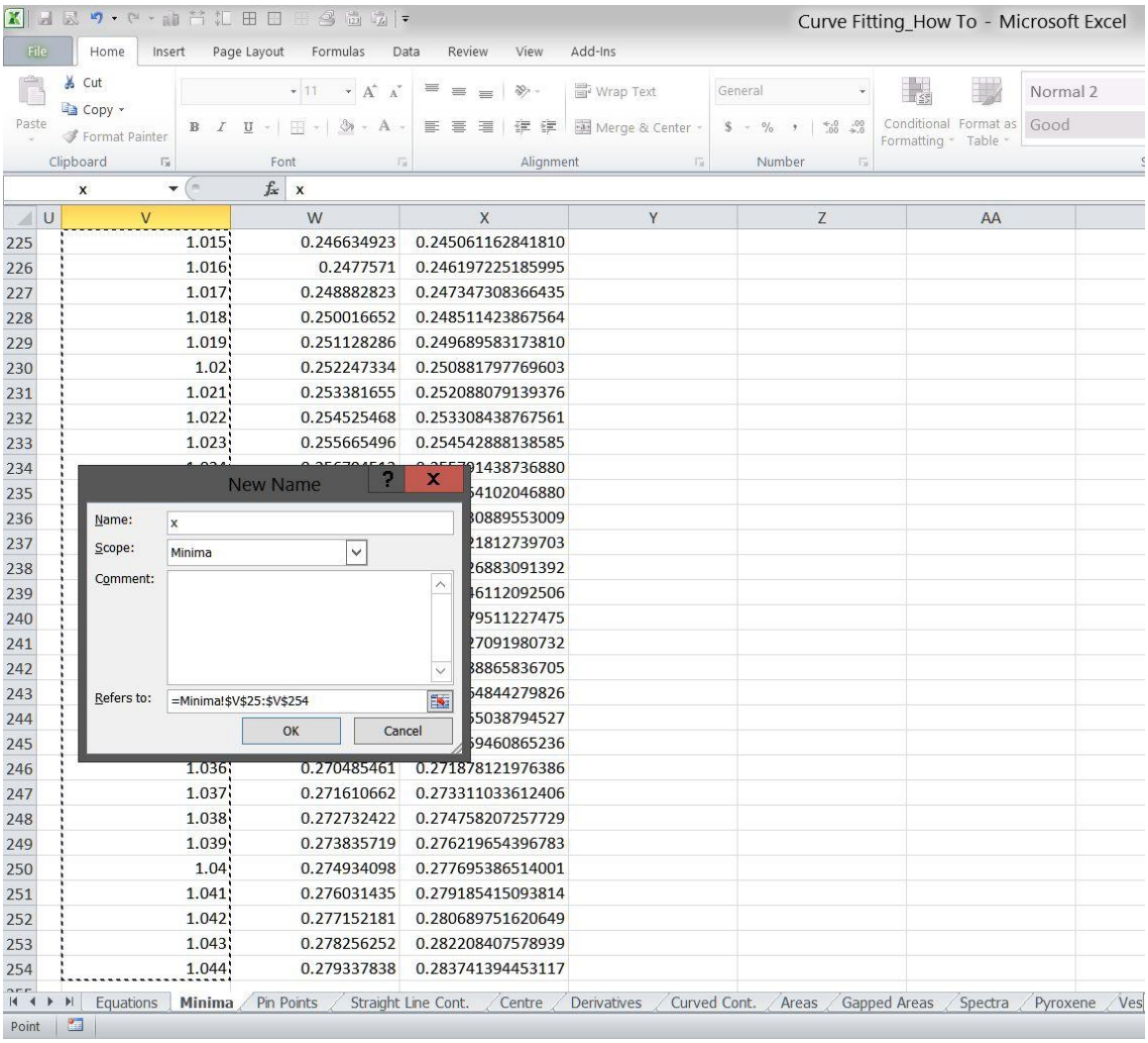

Figure 11: A new Name receives a Range

Where the Refers to: is =Minima!$V$25:$V$254 and the animated dashed highlight encompasses all of the cells in column V from cell 25 to cell 254. Now hit the **Enter** key and the range 'x' for the worksheet *Minima* is cells V25:V254, and it is locked to that range as denoted by the $ symbols preceding the V's and cell numbers above.

6.2.2 Name Manager

You can also define a name using the *Name Manger* which can be opened by pressing the **Ctrl+F3** key combination (or via the *Quick Access Toolbar* as we have shown above), but when a new name is to be assigned it is faster, and it involves fewer keystrokes to define new names by using the **Shift+F10** shortcut to open the *Shortcut Menu*, then pressing the **A** key to open the *New Name* pop-up to define a new name. The *Name Manager* is very useful to manage names, if you need to delete a set of names if you encounter a problem, to check to see if you have defined have the correct ranges for a set of names, if you want to see if full sets of names for a particular function are all there, or, if you may have mistakenly assigned a named range to the entire workbook. For example, the polynomial curve fitting functions, for a 3^{rd} order fit requires that x, y, Formula (for the polynomial itself), a, b, cc and Const are named ranges for the calculation of the polynomial coefficients, and derivation of the polynomial and the local slope. The *Name Manager* is depicted in Figure 12.

You can navigate about within the *Name Manager* just as you can with other pop-up menus, and it has a useful set of filters which you can use to troubleshoot problems you may be having with defined names within your worksheets.

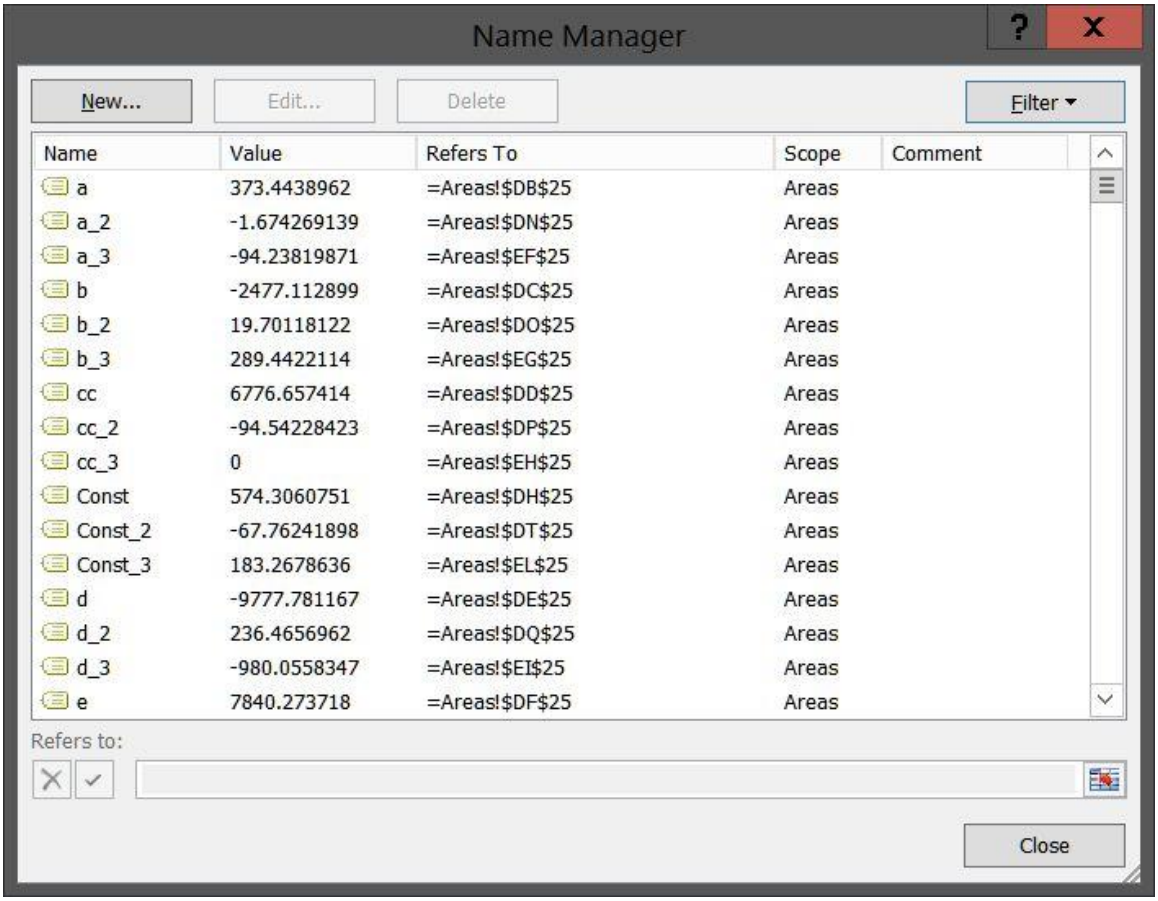

Figure 12: The Name Manager Pop-Up Menu

Based on the previous example, if you wanted to extend your named ranges for x, y and Formula further than V254 because you wanted to add another 30 data points beyond cell 254, you could paste that data in, then go to the *Name Manager* and change the cell limits from 254 to 284 for named ranges x, y and Formula, then go back to your worksheet and copy-and-paste the functions for Formula, Local Slope, Inflection Point and Delta Y/Delta X: Zero Crossing Proxy downward to encompass the new range to row 284.

6.3 Fitting the Curve: Example Walk-Through

We produced the workbook both for our own use, and to share it with the spectroscopic community. Our hope is that it can be a learning tool, especially for those who are new to the field and unsure what one might mean when discussing curve fitting, continua and the like, and that it might also be used as a framework for communicating what we have done to derive metrics from the spectra we are using in a completely transparent manner. By this, we mean to suggest that whenever you have curve fit a set of spectra you include both the spectra and all of the curve fitting maths/data in a manner akin to the *Pyroxene* and *Vesta* worksheets in the workbook. We do not mean to suggest the inclusion of absolutely everything is always necessary, but for example, if you performed the curve fitting one might for a sample like the pyroxene in the *Pyroxene* worksheet example, you could include the entire *Pyroxene* worksheet in a manuscript's supplementary material, or make it available in some other manner, e.g., via a website. Journals are beginning to require that everything necessary to make a figure be included in the supplementary materials and are starting to encourage the inclusion of more data. As an example, see the American Geophysical Union "AGU Publication Data Policy" at http://publications.agu.org/author-resource-center/publication-policies/data-policy/ that clearly encourages the inclusion of copious amounts of supplementary data.

If one did not want to include all of the data and fitting, then at a minimum, assuming fitting in a similar manner, one would have to include all of the derived metrics and the points in the spectrum that were used for the curve fits, e.g. the polynomial order, the fit statistics (see the *Minima* worksheet), and the nodes in the spectrum over which the

curves were applied. The same would be true for the straight or curved lines used for continuum removal and any and all other parameters that apply to any of the standard derived metrics or any other operations performed to smooth, and/or alter the spectra before the fitting was completed (see the *1* worksheet).

Ideally, one would always share all of their data and any manipulations/modifications/alterations thereof so you would not only have shared your spectra in an easy to access manner, but you would have also shared all of the curve fitting, the curves and the maths, so it is absolutely transparent what you did to derive your metrics. It is simply not good enough to provide band centres/minima/maxima, depths/heights, areas and FWHM metrics by "3rd order polynomial fits of centred bands" without a full description of all the parameters, and methods used to make the fits and produce the measurements as none of these methods are absolutes. For any derived set of metrics, if another researcher cannot repeat what you have provided and achieve identical results, your metrics may very well be useless.

The take home message: <u>a non-repeatable measurement is useless!</u>

The “Curve Fitting - How To” workbook is divided into three areas, a series of worksheets focusing on individual empirical methods, example worksheets for the samples used in the manuscript where each spectrum has gone through a full fitting routine (with more examples then are necessary; we would expect one only share those they favour, see the chart is worksheet *1*) and additional material that one might find useful that pertains to other methods of curve fitting and working with spectra in general.

We strongly suggest that a backup copy of the workbook be saved somewhere and that you always work with a new or a renamed working copy of the workbook. As written, there are no imbedded macros or linked data, so copying full worksheets to new worksheets will not break any formulae (you will have to change column assignments in the *Name Manager* if not pasting into the same lettered columns in a new worksheet and you will have to redo your figures data selections).

The first worksheet lists all the equations used in a format which highlights the variables used in a manner that is somewhat more user-friendly than listing cell column and row addresses. The *Equations* worksheet also contains a series of notes which pertain to the functions. **The *Equations* worksheet is locked using the password ‘curve.’** The worksheet can be locked and unlocked in the *Review* tab. To the right of each function header/title, you will find a listing of the worksheets which demonstrate the functions.

The formatting/layout of the workbook is a matter of personal taste, excepting the standard adopted by the many of the authors of the manuscript, and that of the Planetary Spectroscopy Facility (HOSERLab) at the University of Winnipeg, to keep the first 24 rows of any workbook reserved for notes about samples and spectra, where the first two

rows are for labels, 3 through 16 are assigned to various standard variable metrics of samples and their spectra, rows 17 through 24 are for notes and data begins at, and follows from row 25.

For this example we will walk through the first few steps of the fitting of the pyroxene sample named PYX032. All of the information of note regarding this sample is listed in rows 3 through 24 in each worksheet that contains any fitting of its spectra and further information regarding its chemistry can be found in the Sample Directory on the University of Winnipeg, Planetary Spectroscopy Facility (PSF) Website found at psf.uwinnipeg.ca.

6.4 The “Rules of the Road”

The following is a listing of instrument specifications/constraints, experimental set-up parameters, and derived metrics we would suggest should be reported in every publication that deals with spectroscopy. Those highlighted in **green** are absolutely required.

Instrument Specifications/Constraints:

- Instrument Manufacturer and Model #
- If a paper/manuscript exists which describes the instrument, it should be cited (e.g., Rayner et al., (2003) for the SpeX instrument, Korb et al., (1996) for the Designs & Prototypes Model 102 FTIR spectrometer, etc.)
- Instrument Type (i.e., FTIR, Fibre-Optic Dispersive Grating Reflectance UV-Vis-NIR, etc.)
- Instruments Full Wavelength Range
- Instruments Highest Spectral Resolution
- Spectral Wavelength Range measured
- Spectral Resolution
- Sampling Interval (If Available)
- Any modification of Data performed by the instrument/the instruments operating software or parameters that the user has set (i.e., a function that might convert spectral samples to so other resolution for data import, spectrum averaging, integration time, detector/ADC and/or Preamp gains, spectral resolution used for an experiment [where it is not fixed by the instrument], scan times, scan averaging, beam splitter type, detector type, aperture [slit width], phase correction mode, phase resolution, apodization function, zero filling, scanner velocity, etc.)

- Calibration Standard/Wavelength Standard Used
- Reflectance Standard
- Calibration Procedure (e.g., Wavelength Calibration maintained by measurement of a particular wavelength standard or maintained via measurement of a calibration light source/laser. Reflectance calibrated by measurement of an average of a number of spectra of a particular calibrated reflectance standard, with a number of spectra averaged for measurement of dark current, etc.)
- Anything else deemed of import (i.e., detector elements, a particular model of CCD, etc.)

Experimental Set-up:

- Any Instrument Accessory Used (e.g., Pike EasiDiff Diffuse Reflectance Accessory, a Goniometer, integrating sphere, external emissivity apparatus, etc.)
- If a paper/manuscript exists which describes a custom built experimental apparatus, it should be cited (e.g., Ruff et al., (1997), for the ASU emission apparatus/calibration/measurement procedure for emission spectra collected at the ASU Thermal Emission Laboratory)
- Light Source Bulb Type (e.g., Quartz Tungsten Halogen, Deuterium, Glo-bar, etc.)
- Light Source Power
- Light Source Type/Path (i.e., Collimated, Fibre-Optic, Diffuse, internal to the instrument, external, external but integrated with the instrument, etc.)
- Observation Phase Angles
- Instrument and Light Source Field-of-View (FOV)

- Sample Grain Size, Packing, Surface Roughness, etc.
- A Description of any sample container/holder used (Important: sample powder depth if powders are being investigated)
- Sample Temperature
- Anything else deemed of import

Metrics Derived from Curve Fitting:

- Band Minima (Interpolated or Nearest Value)
- Band Centres (If Applicable) (Interpolated or Nearest Value)
- Band Area
- As well as, but not so universally applicable: Skew, FWHM/RWHM and LWHM, etc.
- If a metric is something new, or a novel use of existing techniques; include a thorough description and ideally a graphic example
- Any modification of spectral data prior to fitting, e.g., smoothing (which may include data modification by the instrument)
- If a paper/manuscript, or series of papers exist which describe or introduce the techniques it/they should be cited (e.g., the series of papers and abstracts by J. M. Sunshine regarding MGM)
- Everything necessary to reproduce a reported metric:

For a fit polynomial minimum:

- Spectrum

- Beginning and end points of used for the fit (i.e., x values of the nodes)
- Polynomial Order
- Polynomial Coefficients (e.g., for a 3rd order polynomial a, b, c and the constant)
- Standard Errors for the Coefficients
- R-Squared value of the fit

For a fit centre:

- Spectrum
- Beginning and end points of used for the centre fit (i.e., x values of the nodes)
- Polynomial Order
- Polynomial Coefficients (e.g., for a 3rd order polynomial a, b, c and the constant)
- Standard Errors for the Coefficients
- R-Squared value of the fit
- Continuum Removal Method (And, for anything but a straight line, the functions/curves used)
- Pin Points used for the Continuum Removal
    - Nodes used when fitting the two polynomials to define the Pin Points for the Continuum Removal
    - Polynomial Order
    - Polynomial Coefficients (e.g., for a 3rd order polynomial a, b, c and the constant)

    - Standard Errors for the Coefficients
    - R-Squared value of the fit
- Anything else deemed of import

6.5 Adding Spectra to a Worksheet, and Inserting a Chart:

Pyroxene has two bands of note, referred to as Bands I and II with absorption maxima/reflectance minima at approximately 1 and 2 µm, respectively as depicted in Figure 13.

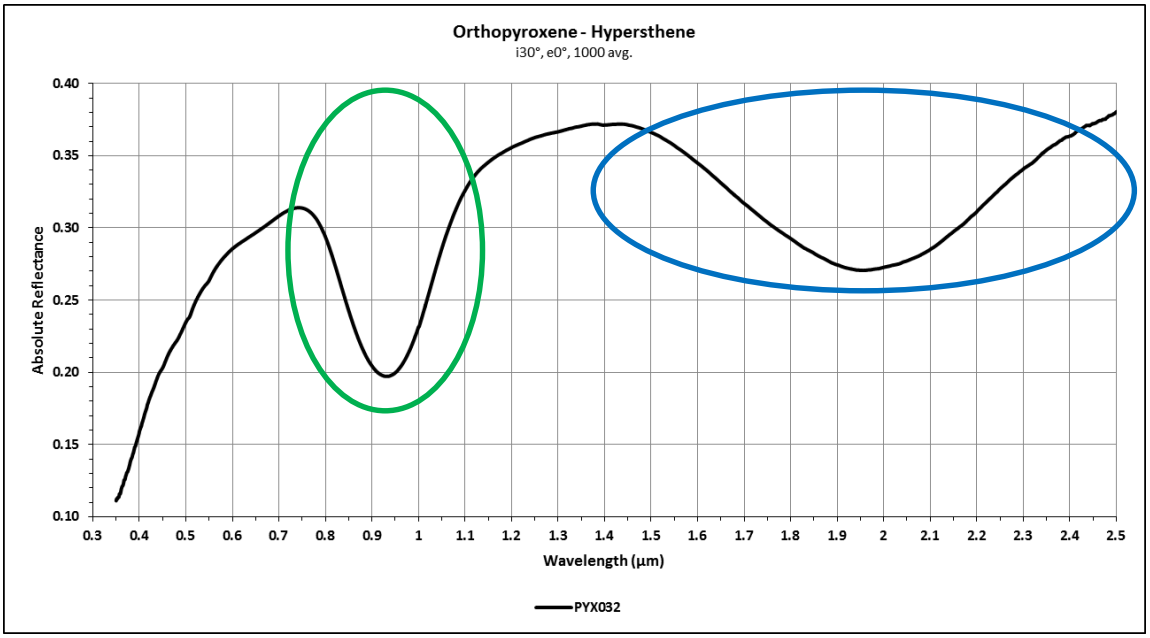

Figure 13: Bands I and II

The one metric that should always be calculated is the band minimum for each absorption in a spectrum. Band minima are the point of maximum absorption/minimum reflection (maximum absorbance, minimum transmission or minimum emission) expressed in wavelength. To be called a minima or maxima the fitting must be performed on otherwise unaltered spectra, as delivered by the spectrometer. So, for example, for reflectance spectra, a band minimum would be the wavelength value of an absorption derived from spectra where the continuum removal imposed by the process of reflectance

measurement was left intact, i.e., the imposed continuum has not been removed. For some instruments, some manipulation of the spectra must happen, as is the case with the spectra from the ASDI spectrometer we are using as an example, as the breaks in the spectra which occur at the instruments detector junctions must be removed. In cases such as these, the repair of these breaks and the method for such repair should be noted in any manuscripts experimental procedure, and for further discussion the spectra would be considered unaltered for the purposes of band minima derivation.

We have chosen a 3rd order polynomial as our standard curve fitting technique and to fit said simple curve, there are a number of caveats that are addressed in the *Minima* worksheet. We suggest a 3rd order polynomial as it is a simple curve that can define a minimum in both very high resolution and very low resolution, and exceedingly noisy, spectra. If one chooses to use higher order polynomials, more complex curves or techniques that employ data interpolation they run the risk of adding noise or data scatter into their calculation of the minimum position. Techniques that can add artificial resolution or increase the quality of a fit from a statistical perspective have their uses, as in the examples given in the *Area*, *Gapped Area*, *Vesta* and *Rossman* worksheets, where their use is entirely appropriate; however, for the purposes of curve fitting spectra to report band minima, centres and the pin points used for straight line continuum fitting, we recommend keeping it simple and using 3rd, and nothing but a 3rd order polynomials.

Band centres and areas are particularly useful for determining, to a first approximation, the mineral makeup of asteroids, specifically the S-type asteroids using the Cloutis plot as modified by Gaffey (Cloutis et al., 1986, Gaffey et al., 1993). As the calculation of Band

minima are a given, we would tend to start with having a look at the spectra for pin points, as we know we will be fitting straight line apparent continua to this samples spectrum.

The following example assumes you want to recreate the existing sheets by reproducing them, creating new worksheets from scratch, then cutting-and-pasting functions/formulae into newly created worksheets as necessary. If you so choose, you could simply copy entire worksheets and paste in new data to produce new curve fits. The *Pyroxene II* worksheet is an example of how one might go about setting up a worksheet to allow you to copy the entire worksheet and then simply replace only the column of spectral y data and have all of the fitting and calculations for the entire worksheet update based on the new spectrum. You could also though, paste in new data to a sheet you had copied then go about changing the named ranges and so on to reflect the fitting you want for your new data. While we prefer the method we espouse below, as it makes errors less likely, it is ultimately up to you how you want to go about making use of any of the functions we have provided.

The first step is to have a look at the spectra (see Figure 13). Bands I and II are centred at approximately 0.93 and 1.95 µm, there are a few spin forbidden bands between ~0.4 and 0.7 µm and a weak feature due to adsorbed water at ~1.4 µm (with another due to water having a miniscule influence at 1.9 µm). For fitting purposes, we are really only concerned with the minima, centres, areas, and secondarily, the skew of Bands I and II.

For minima fitting, we can leave the spectra, as is, but for fitting straight line apparent continua, such that we can remove the straight line apparent continua to isolate Bands I and II for derivation of further metrics we need to pick pin points to which we can pin the straight line apparent continuum. To do that, we, as a matter of course, unless one has another, specific reason to pick different pin points, will fit curves to the areas of band extinction (points of band extinction are the maxima in reflectance between two adjacent absorptions) on either side of Bands I and II to derive our points of band extinction using a transparent and repeatable process, such as fitting with the 3rd order polynomials that we recommend.

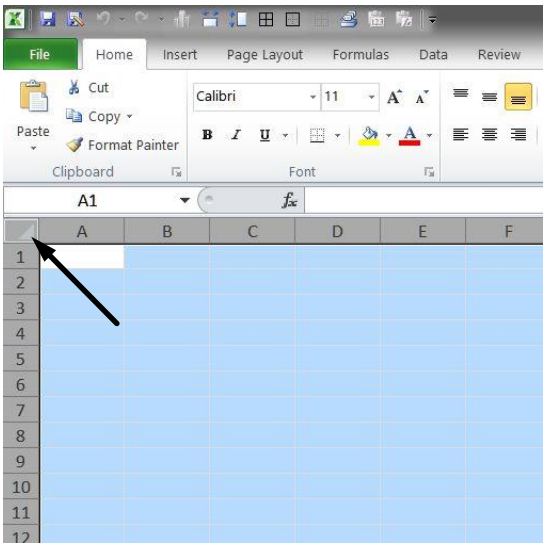

Figure 14: Setting up a new Worksheet

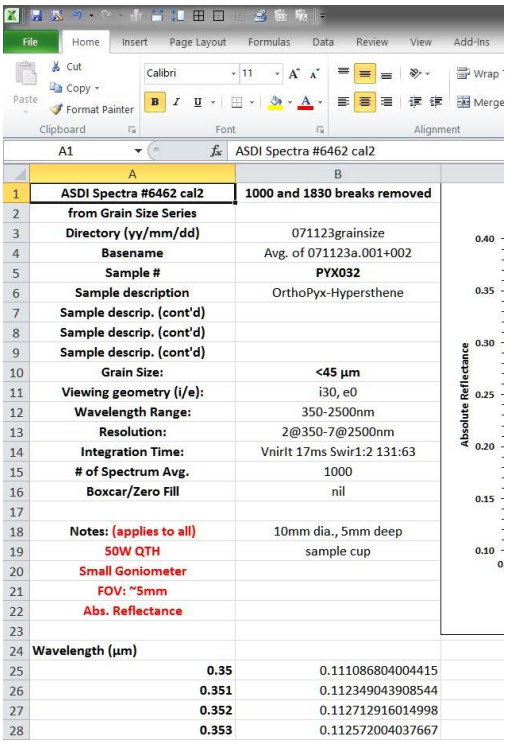

Figure 15: **Copying Spectra**

We begin by setting up our workbook. In the example depicted in Figure 14, when opening a new worksheet, if you **left-click** the square in the corner it will highlight every cell in the worksheet, and any changes you make to the layout will be applied to all of the rows and columns. These examples ware produced using 1080p monitors, so the entire worksheet is setup to have text centred horizontally in

the cells, the cells 23 points wide and rows 15 points high with the default text font being Calibri and the default size being 11 point. If you make those changes while the entire sheet is highlighted in blue, it will apply to every cell including those which are added anew as you add data to rows and columns beyond the default opening size. When finished adding formatting, **left-click** anywhere on the worksheet.

All of the spectra are already copy-and-paste ready, in the *Spectra* worksheet with all the pertinent information filled out in the first 23 rows. These spectra have already had their "1000 and 1800 breaks removed" as noted in Cell B1, so we are ready to copy it into our new worksheet. **Left-click** cell A1 as shown in Figure 15, hold the **Shift+Ctrl** keys down, and while doing so hit the **Left Arrow** once, then press the **Down Arrow** 5 times to highlight both columns A and B down to the bottom of the data in the two columns; with it all highlighted in blue, now press the **Ctrl+C** keys to copy the data.

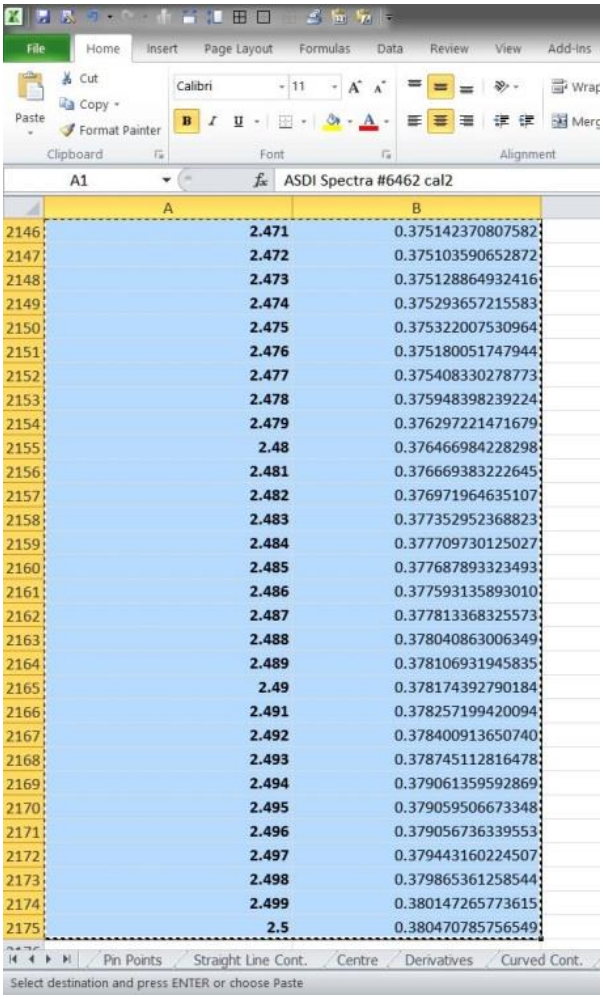

Figure 16: Copying Spectra Continued

With the data copied, since you are pasting it back into Excel in another worksheet, you can simply go to your new

worksheet, and with cell A1 selected hit the **Enter** key and your data will paste in (if you happened to have two separate instances of Excel open, for example to work on two different screens, you will need to paste using **Ctrl+V**). Since the data does not quite fit, we resize the widths of columns A and B to 28 point. Instead of starting a new chart, simply **Right-click** on the existing chart for spectra in the *Spectra* worksheet of sample PYX032 and paste it into your new worksheet using the **Ctrl+V** key shortcut (charts copied and pasted will paste down and left from their top left corner, so to paste in the chart, **Left-click** on Cell D1 and hit **Ctrl+V** or **Right-click** on cell D1 and select Paste (Keep Source Formatting)). Now you have a chart but, if you Right-click on the chart, and select Select Data and go to format the data for the Series name, Series X values and Series Y values you will see they point to the previous "Curve Fitting - How To" spreadsheet/workbook you copied the chart from as in Figure 17. You can fix each of the data links individually, but we find that rather time consuming, so we prefer to do it with the following method. **Right-click** on the chart and select **Select Data**. Rather than editing the data links, **Left-Click** on **PYX032** so it is highlighted in blue and click the **Remove** button.

That will turn the *Select Data Source* pop-up menu from the first into the second pop-up menu, i.e., Figure 17 turns into Figure 18.

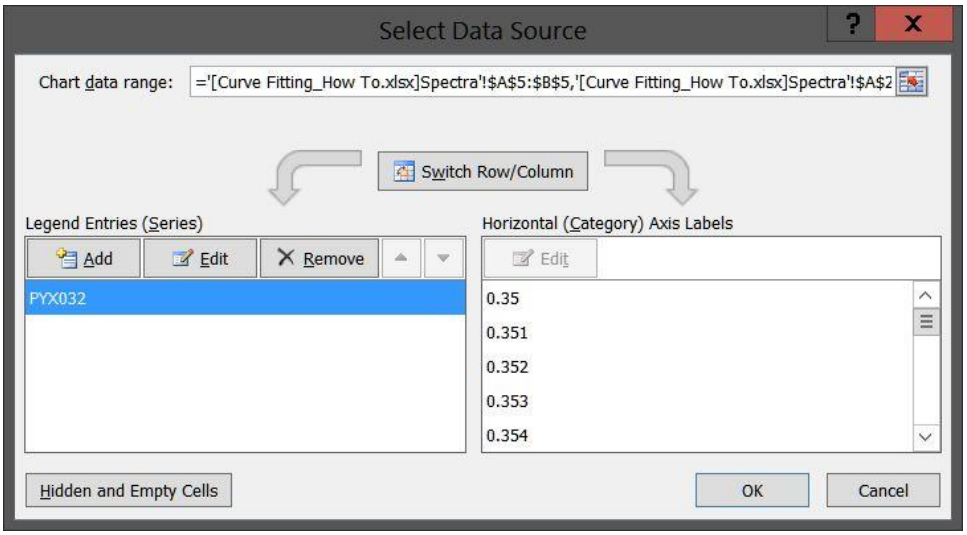

Figure 17: Changing the Chart Data Source

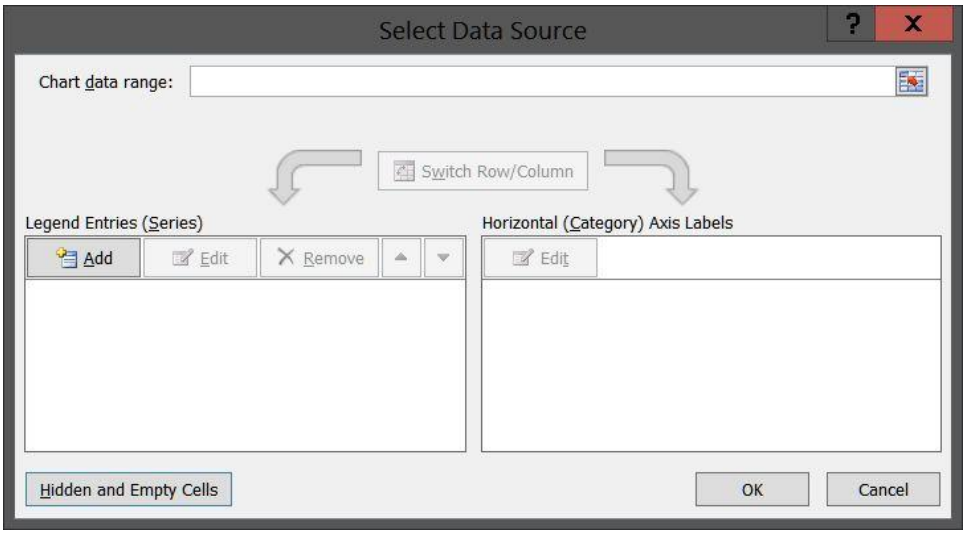

Figure 18: Changing the Chart Data Source Continued

Now, press the **A** key or click the **Add** button to bring up the *Edit Series* pop-up menu, or Figure 19, and without hitting any other keys, or clicking anything else, use the **Arrow**

keys to move around. The moving highlight box will start out around the last cell you had highlighted in the sheet (or the cell at the top left corner of the chart) and you can move it very quickly using the arrow keys to select the Series name. In this instance, navigate to cell B5 using the **Arrow** keys to pick the name "PYX032." To pick cell B5, hit the **Tab** key, which will select cell B5 as the Series name and navigate the cursor to Series X values. Now use the **Arrow** keys to navigate to cell A25, and with A25 actively highlighted, press **Shift+Ctrl+Down Arrow** to highlight the entire series of x values from A25 to A2175, now press the **Tab** key to set the x values and move to Series Y values and use the **Arrow** keys and **Shift+Ctrl+Down Arrow** to highlight B25:B2175.

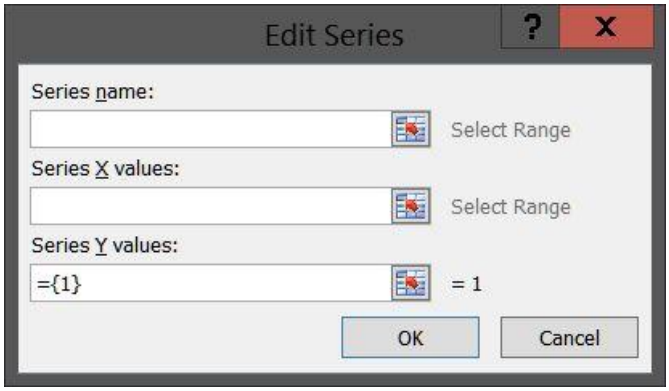

Figure 19: Picking new Source Data

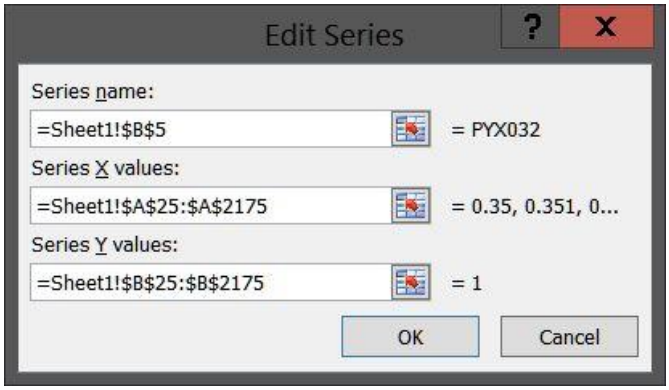

Figure 20: New Source Data Selected

The *Edit Series* pop-up menu will now look like Figure 20.

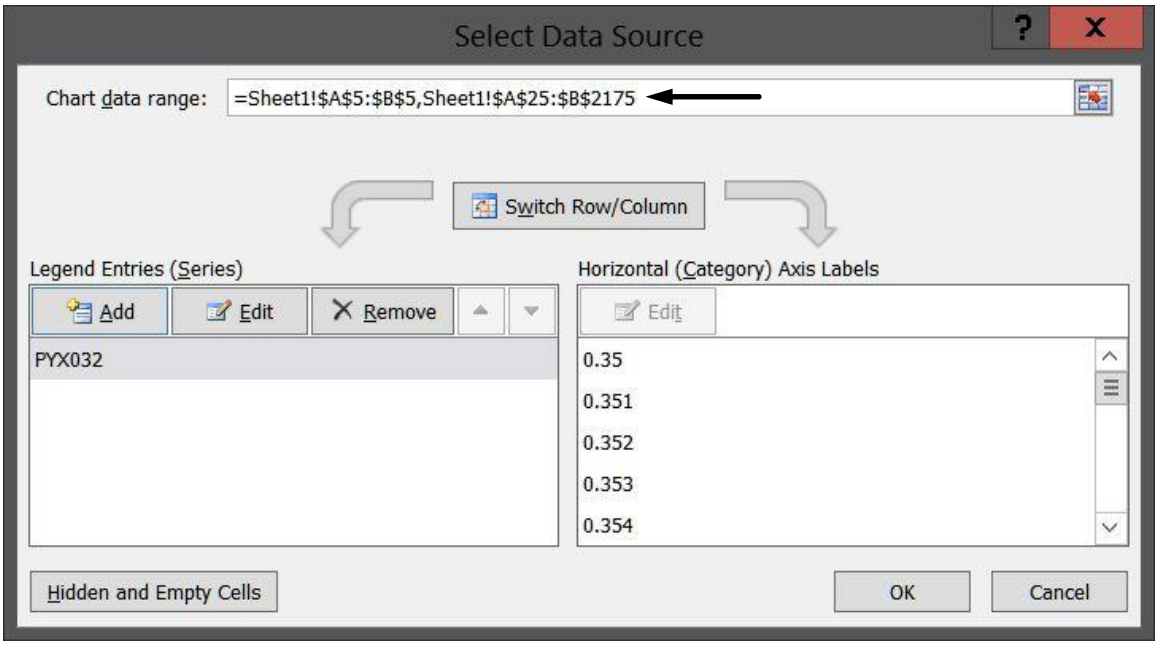

Figure 21: New Source Data Selected and applied

With all the series information entered, there will be a faint blue glow outlining the **OK** button, press the **Enter** key or click the **OK** button to apply the series data to your chart. The *Select Data Source* pop-up menu will now look like Figure 21, and you will note, the Chart data range will read "=Sheet1!$A$5:$B$5,Sheet1!$A$25:$B$2175" which encompasses the cells addressed in your new *Sheet1* as opposed to the earlier version

which addressed the same cells in another workbook.

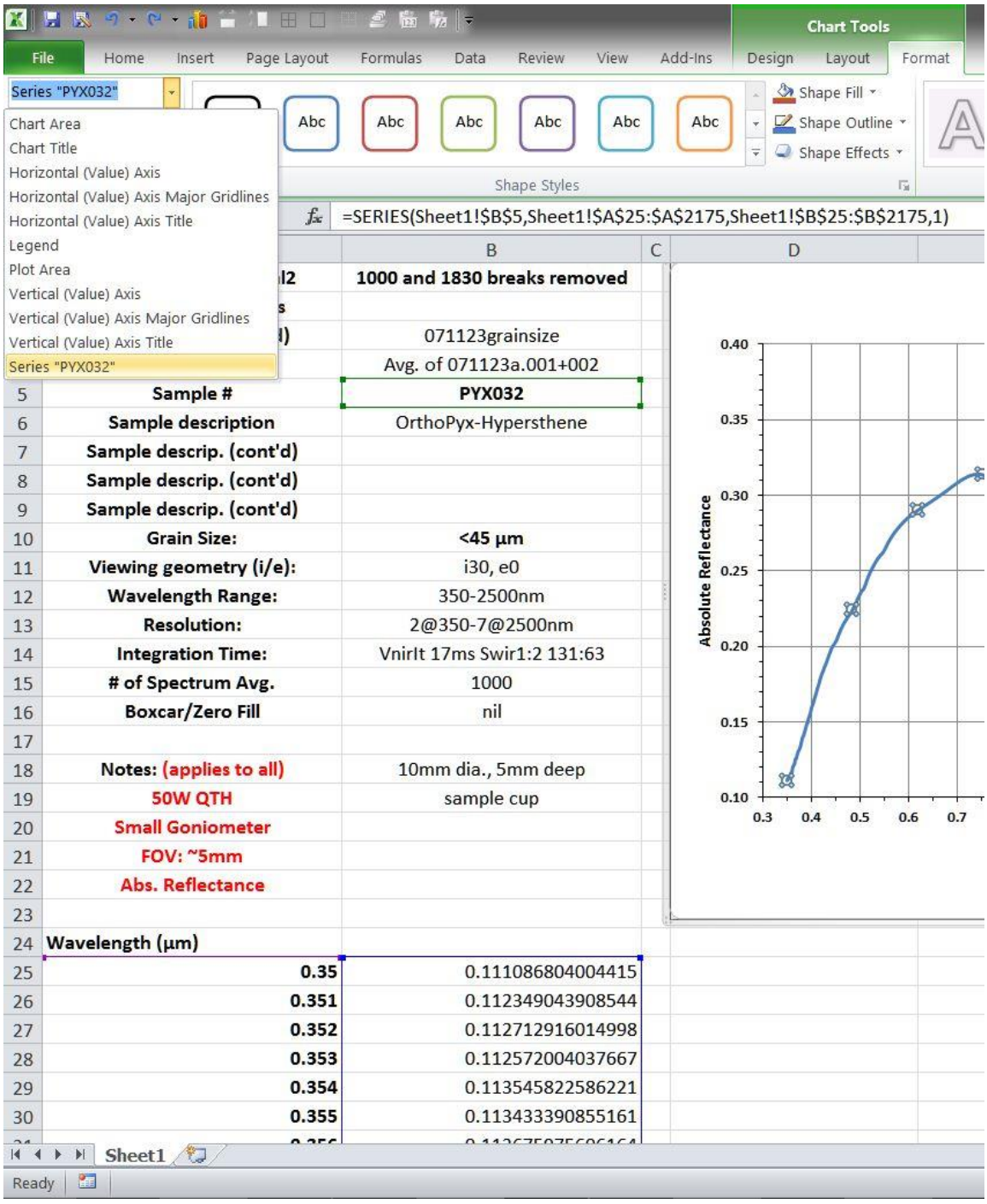

Figure 22: Using the Format Selection Menu

With the chart you have just inserted into your *Sheet1*, you have now redirected the source data so it is referencing the data in your worksheet, and the spectrum has now defaulted to the Excel default for the first smoothed line colour, blue. You can leave it, or change it to a colour of your choosing. To change the line colour, or other elements in a chart, there are a number of ways to get into a chart, or chart elements, e.g., the axes, title(s), axes labels, legend, and so on, and change the look, size, and background colours, etcetera.

Figure 22 illustrates the use of the *Format tab* to make changes to chart elements. You can **Double Left-click** on any element, **Right-click** to bring up the *Shortcut Menu* specific to charts, **Left-click** anywhere on a chart to bring up the *Chart Tools Ribbon*, select the *Format* tab and select any of the elements of the chart from the dropdown *Current Selection Menu* on the right and then click the **Format Selection** button under the dropdown *Current Selection Menu*. Each of the pop-up menus for the chart elements are a nested series of menus that deal with that particular element of the chart as depicted in Figure 23. For example, to change the colour of the line in the chart to black, one would need to use the *Line Color Menu* in the *Format Data Series* pop-up menu to change the line color from No line to Solid line and choose black as the colour. With a pop-up menu open one can navigate about it with the keyboard using **Tab**, specific **Letter** keys for functions and the **Arrow** keys just as an in the rest of Excel.

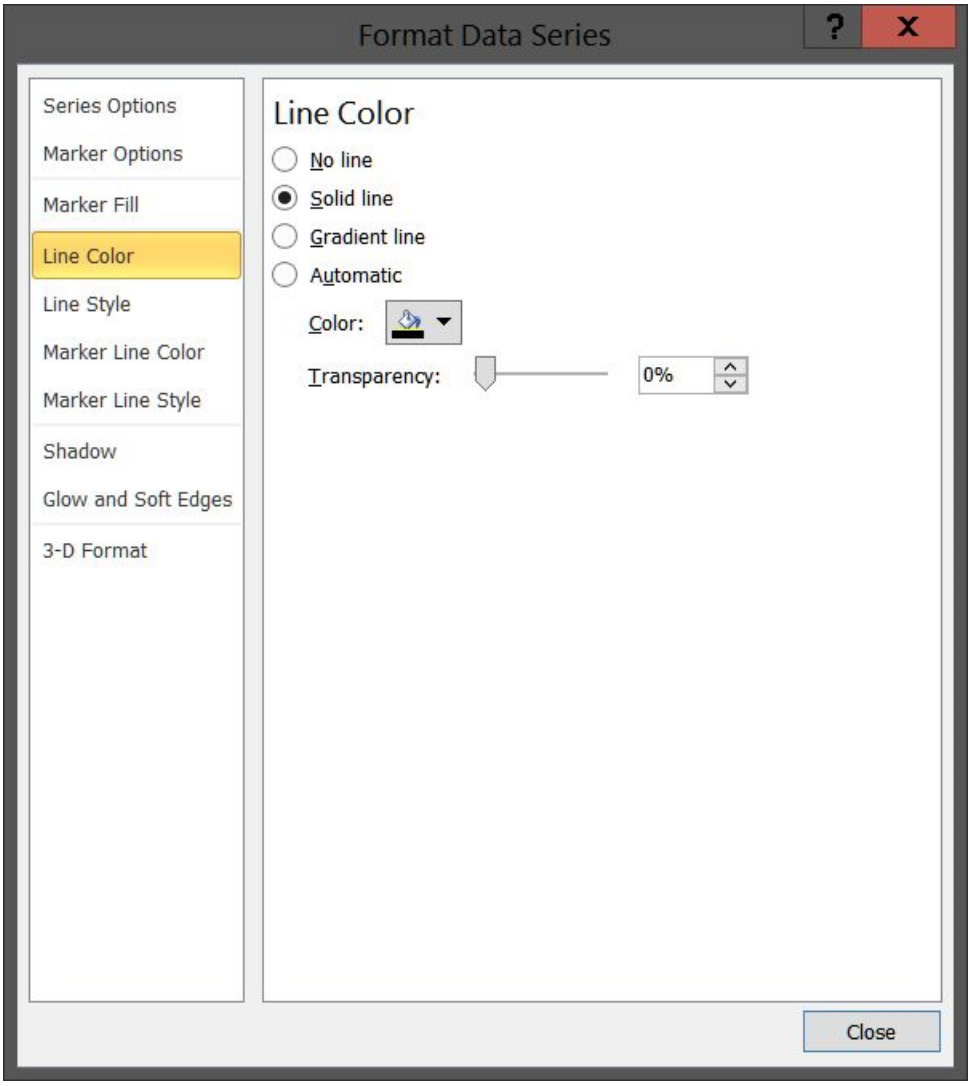

Figure 23: The Format Data Series nested Menu for Chart Objects

6.6 Picking portions of the spectrum to use for Pin Points:

For clarity, one may want to add thin empty, and/or colour filled columns to worksheets to highlight the move from one operation to another as one can see throughout the "Curve Fitting - How To" workbook. It is imperative you do so here, to maintain the cell-to-cell, column-to-column and column-to-cell relationships so you do not cause formula errors when cutting-and-pasting. To the right of the chart you have just inserted, change the column width for column I to 2 points, and infill it in black to show the break between charting up the spectrum that you are working with and the next function to be performed which will be picking portions of the spectrum which will be used to curve fit for pin point determination (see Figure 24).

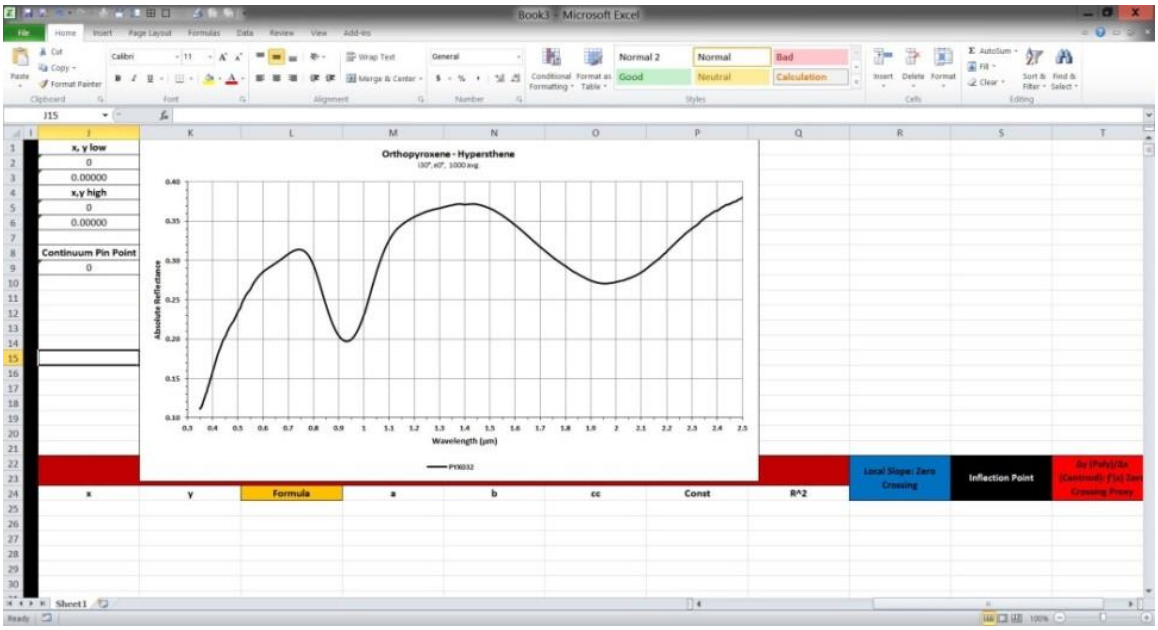

Figure 24: Pasting in a Chart

Now, copy and paste in the set of cells from J1:J9 and the set of cells from J22:T24, or the x, y locations and eventual continuum pin point cells and the title cell for the 3rd order polynomial fitting as in Figure 25.

Then, change all of the column widths for columns J through T to 18 points wide (this will resize them so all 11 columns will fit on a 1080p monitor at 100% zoom). Copy the chart you made of spectra and paste it into cell K1, then change the *Chart Type* to "X Y (Scatter), Scatter with only markers" and the ranges of the x and y scales to isolate the hump at approximately 0.74 µm.

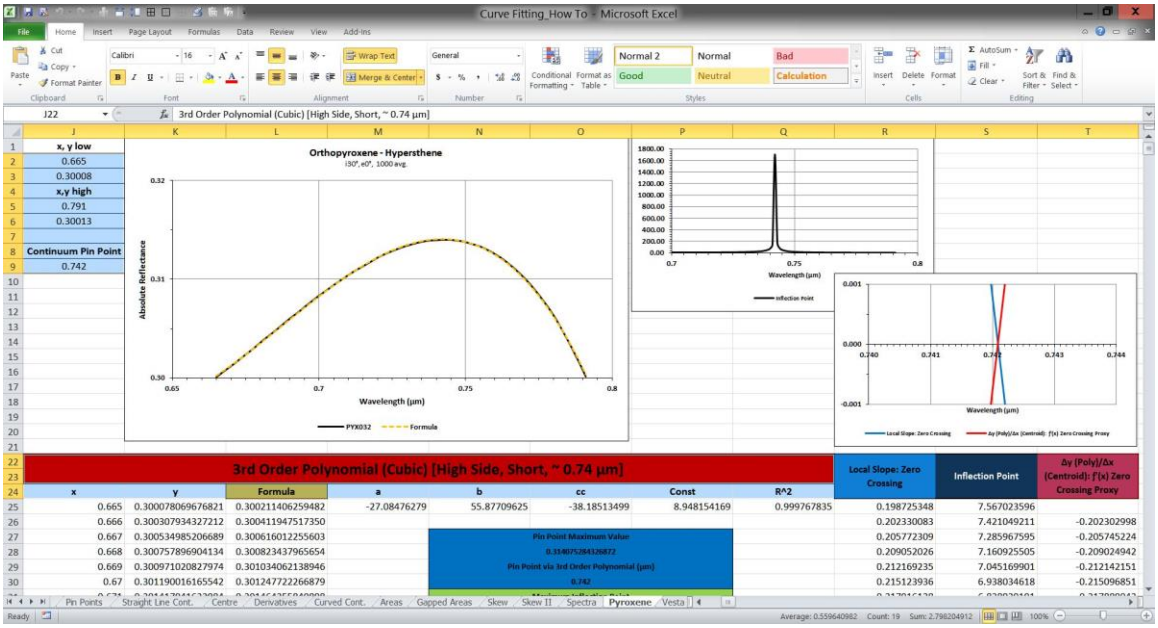

Figure 25: Pasting cell formatting into a worksheet

Ideally, the top of the hump would be symmetric about a maximum value, in this instance it is not, but, through a significant number of trials we have found that visual symmetry is not a significant issue when determining a band minima, centre or a pin point if you are considerate of the caveats one should use when picking the data ranges to use when trying to fit these features with simple polynomials. Pick data ranges where you have relative symmetry of height on both sides of the centre/minima/pin point in question and stay away from adding complexity to the curves, and you will generally be fine.

Examples of what <u>NOT</u> to do are shown in the *Minima* worksheet. We want to

isolate an area of the curve as shown in Figure 26, where we keep our data range large enough to ameliorate the spectral resolution of the data becoming an issue (for this data, collected by an ASDI FieldSpec Pro HR, the real spectral resolution is between 2 and 7 nm, but is output as 1 nm by the instrument using interpolation and you can see some of those interpolation artifacts near the peak where the data points form small straight line segments). The examples of data ranges in the green boxes in Figure 26 would be good, while red boxes would not, because you are isolating to small an area, selecting too large an area and introducing to much of the feature's inherent asymmetry into your calculation, or you are artificially tipping the wings of the feature by using the tipped red box, and adding asymmetry to your calculation by picking visual symmetry over data symmetry, i.e., count the number of data points on either side of the reflectance maximum encompassed by the tipped red box and you will find significantly more on the left side than the right.

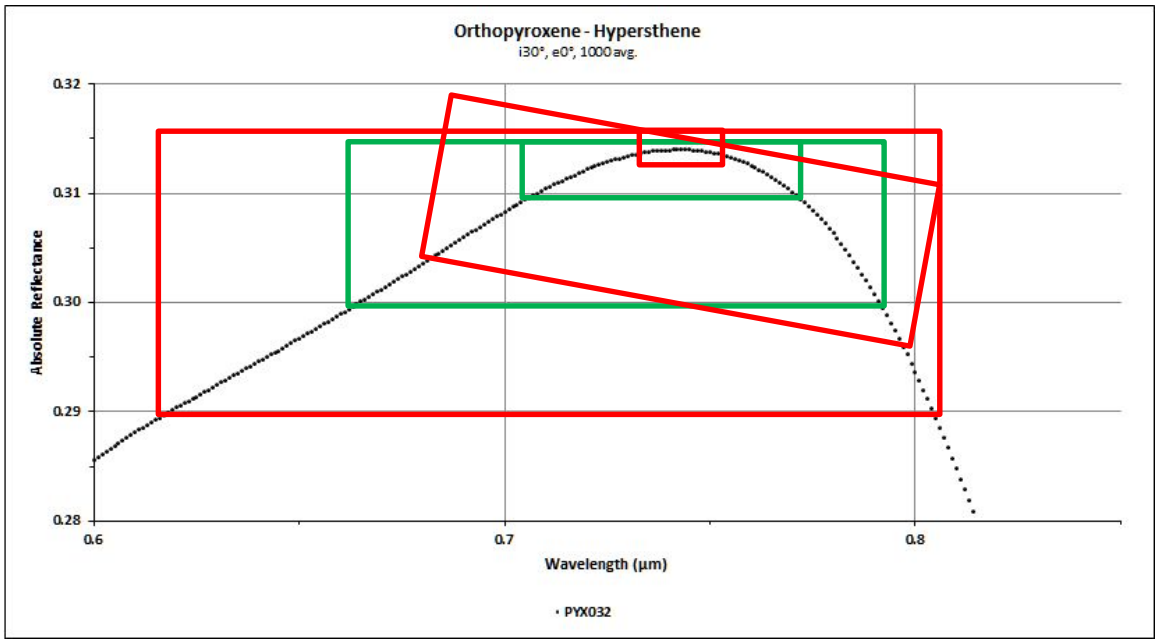

Figure26: Choosing an area of symmetry about the maximum

We have chosen to use the larger of the two green boxes and have picked all of the data points above 30% reflectance to use to calculate the pin point. You can hold your cursor over the data points to get the x and y coordinates of a particular data point to figure out the range you are going to copy out of your spectral data to use to calculate the pin point or simply scroll through the spectra to get your data range. Looking at the chart, our selected range will be from just over 0.6 to a little more than 0.8 µm, so we simply go to the spectra and scroll to the area to find the start and stop points for the data range to copy to the x and y columns for fitting the pin point. When finished with the chart used to pick the data range for fitting, simply delete it. For this example that will be A340:B466 (the nodes will be 0.665 and 0.791). Copy the range from A340:B466 from the spectra to the x and y columns for fitting (i.e., paste at cell J25). Because you have

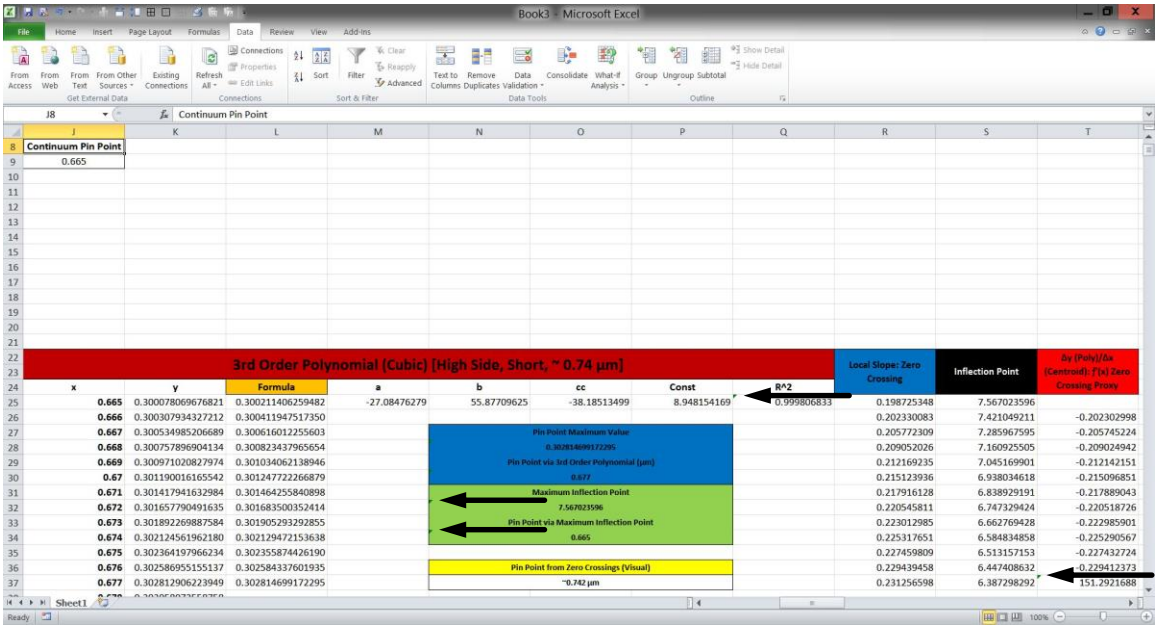

Figure 27: Creating formula errors while cutting-and-pasting

already copied cells J1:J9, and their extant formulae, they already reference cells J and

K25 and J and K151 for “x, y low” and x, y high” values so will they automatically infill (you would of course have to redo the addresses to reflect different “x, y high” cells if the data range were different). The “Continuum Pin Point” will still read ‘0’ as the cell it addresses is still blank.

Now go back to the *Pyroxene* worksheet and copy cells L25:T37 and paste them into the corresponding block of cells in your new worksheet. After you paste in the L25:T37 block from the *Pyroxene* worksheet it will look like the example in Figure 27, where all of the pasted cells still have numbers present, but if you look closely, cells N32, N34, Q25 and T37 have small green tabs in the left upper corner of each cell alerting you to an error in the formula for those cells.

In this instance, the errors arise because the formulas in them address cells that, in your new worksheet, are presently empty. We will fix that shortly. If you open the *Name Manager* now, you will see, as depicted in Figure 28, along with copying the formulas used to calculate the polynomial fit, pin point positions and so on, the copy-and-paste function also copied over the named

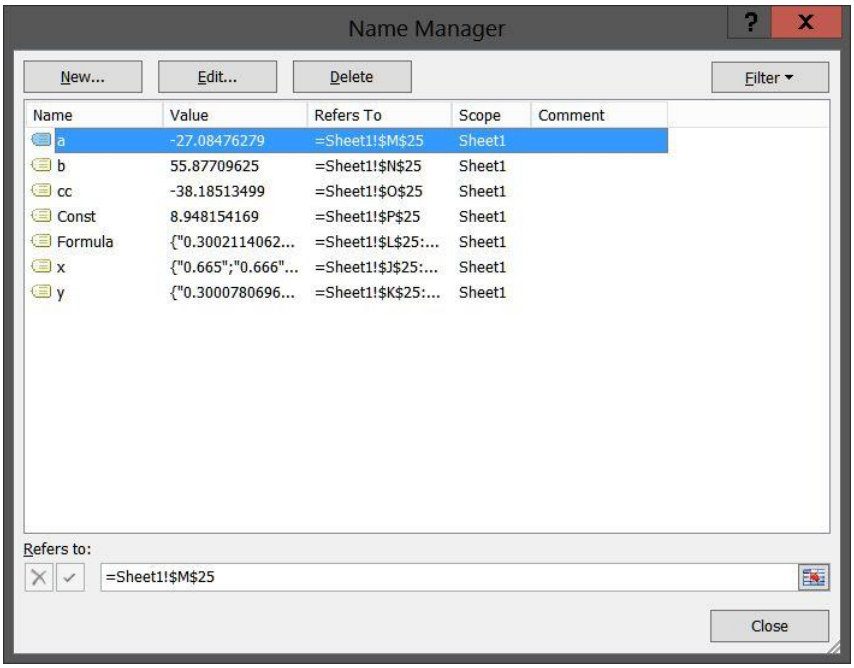

Figure 28: Automatic insertion of Named ranges

ranges and their cell assignments, but reassigned them all to the present *Sheet1* worksheet you are working in. Since we have set it up in exactly the same manner as the *Pyroxene* worksheet they were copied from. If you look inside the *Name Manger* you can see the named ranges and where they can be changed in the box beside Refers to. Working inside the *Name Manager* can be a quick and easy place to reassign the named ranges/cells when copying formulas from one worksheet to another, e.g., if we had preferred the worksheet be arranged a little differently and wanted to leave out the two spectra columns, the spectrum in the chart and the dividing column so that the fit data started in column A, you could paste in the L25:T37 block in the same manner, then go into the *Name Manager* and reassign all of the ranges by changing the column letter identifiers, moving them 9 columns leftward so J becomes A, K becomes B and so on. The same is true of the named ranges. If the data range were longer, or shorter you could reassign the data ranges for x, y and Formula, to reflect the new depth of the data in the column for all three affected columns. For the formulas that where copied in the L25:T37 block that do not use named ranges, should you need to edit them you can do so in cell by pressing **F2** or edit them in the *Formula Bar*.

As we are copying and reformatting our new worksheet to be an exact replica of the *Pyroxene* worksheet we could have copied the entire range of cells from L25:T151 but that is not what one would normally do as we would be copying from an existing worksheet to one where the data range depth differed (cell 25 is always the top) so we would not copy that entire set of cells. To fix those broken cells (i.e., N32, N34, Q25 and T37) and infill the columns simply copy the formulae used to create the polynomial (Formula), Local Slope: Zero Crossing, Inflection Point and the Δy (Poly)/Δx (Centroid):

f’(x) Zero Crossing Proxy down to the bottom of the data range and the broken formulae will be repaired as is depicted in Figure 29

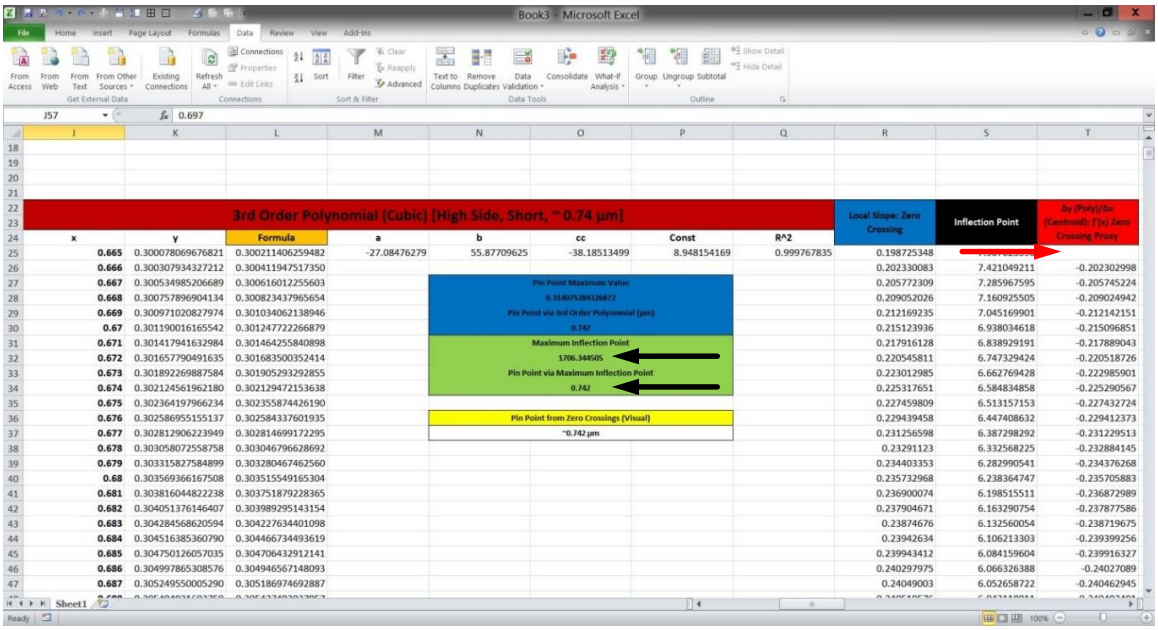

Figure 29: Formulae which broke with a cut-and-paste are now repaired

.

Note: The Δy (Poly)/Δx (Centroid): *f*’(x) Zero Crossing Proxy function calculates a local slope for one point, across three points of the polynomial, and as a simple function cannot calculate values for cells when values above and below the cell on the polynomial line are not present, i.e., it cannot calculate a value for the first or last point in the polynomial, so those cells are left blank. This is important both for the calculation of the values and must be remembered when charting the two zero crossings. Using this example, for the Local Slope: Zero Crossing, the data range for x and y would run from 25 to 151, e.g. J25:J151 and R25:R151 for x and y respectively, but for the Δy (Poly)/Δx (Centroid): *f*’(x) Zero Crossing Proxy, it would run from 26 to 150, e.g. J26:J150, T26:T150, for x

and y respectively. If one makes the error of not assigning the x and y ranges correctly when charting the Zero Crossings they will not cross at zero.

To copy the formulae, copy the formula in cell L25 and paste it into cells L25:L151, copy the formulae in cells R25 and S25 into cells R25:S151 and copy the formula in cell T26 to cells T26:T150. Doing so will automatically repair the formula errors which were present in cells N32, N34, Q25 and T37 that were errors resulting from the addressing of empty cells. As the formulae were written for the same data ranges the formulae that are using named ranges and those that address cell ranges are all correct as in the figure below. When using different data ranges (e.g., data that runs from cell 25 down to a different number) fixing the named range is completed in the name manager, and those functions that address cells can be fixed in the worksheet or the *Formula Bar*. **The maximum inflection point and x matching functions could be changed to use names, but we prefer to leave them as is and use them as a check of our work by confirming we have them adressed to the correct data ranges each time.**

Do not forget that the data range for Δy (Poly)/Δx (Centroid): $f'(x)$ Zero Crossing Proxy function (and the corresponding x values when charting it) should stop one short of the

bottom of the range and start one short of the top (red arrows in Figure 29 and 30).

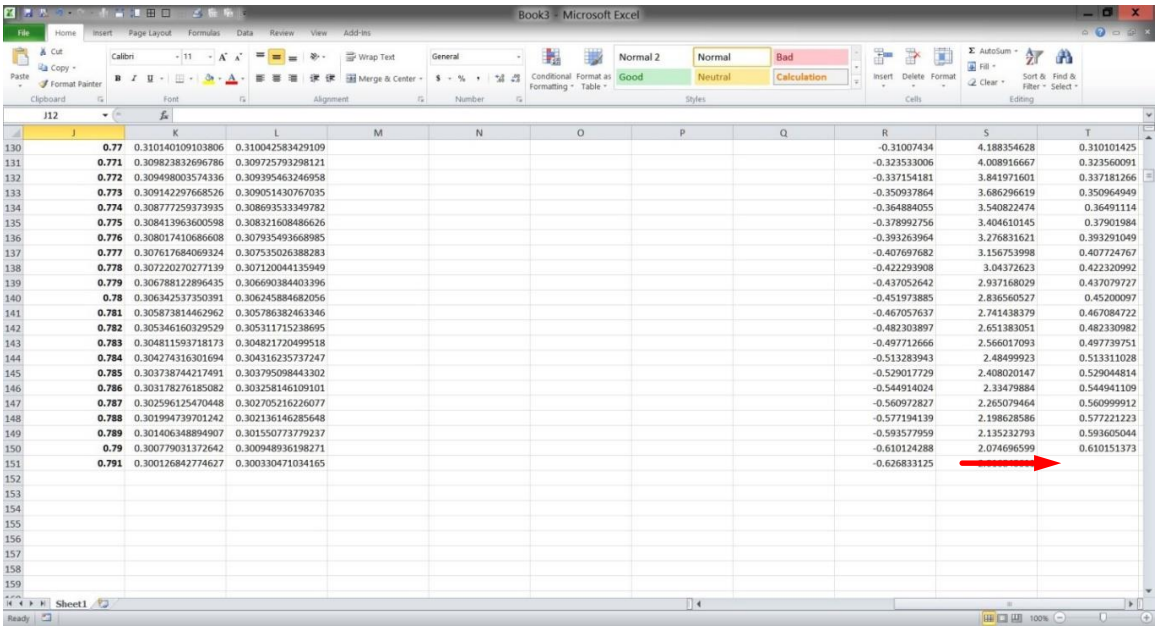

	J	K	L	R	S	T
130	0.77	0.310140109103806	0.310042583429109	-0.31007434	4.188354628	0.310101425
131	0.771	0.309823832696786	0.309725793298121	-0.323533006	4.008916667	0.323560091
132	0.772	0.309498003574336	0.309395463246958	-0.337154181	3.841971601	0.337181266
133	0.773	0.309142297668526	0.309051430767035	-0.350937864	3.686296619	0.350964949
134	0.774	0.308777259379935	0.308693533349782	-0.364884055	3.540822474	0.36491114
135	0.775	0.308413963600598	0.308321608486626	-0.378992756	3.404610145	0.37901984
136	0.776	0.308017410686608	0.307935493668985	-0.393263964	3.276831621	0.393291049
137	0.777	0.307617684069324	0.307535026388283	-0.407697682	3.156753998	0.407724767
138	0.778	0.307220270277139	0.307120044135949	-0.422293908	3.04372623	0.422320992
139	0.779	0.306788122896435	0.306690384403396	-0.437052642	2.937168029	0.437079727
140	0.78	0.306342537350391	0.306245884682056	-0.451973885	2.836560527	0.45200097
141	0.781	0.305873814462962	0.305786382463346	-0.467057637	2.741438379	0.467084722
142	0.782	0.305346160329529	0.305311715238695	-0.482303897	2.651383051	0.482330982
143	0.783	0.304811593718173	0.304821720499518	-0.497712666	2.566017093	0.497739751
144	0.784	0.304274316301694	0.304316235737247	-0.513283943	2.48499923	0.513311028
145	0.785	0.303738744217491	0.303795098443302	-0.529017729	2.408020147	0.529044814
146	0.786	0.303178276185082	0.303258146109101	-0.544914024	2.33479884	0.544941109
147	0.787	0.302596125470448	0.302705216226077	-0.560972827	2.265079464	0.560999912
148	0.788	0.301994739701242	0.302136146285648	-0.577194139	2.198628586	0.577221223
149	0.789	0.301406348894907	0.301550773779237	-0.593577959	2.135232793	0.593605044
150	0.79	0.300779031372642	0.300948936198271	-0.610124288	2.074696599	0.610151373
151	0.791	0.300126842774627	0.300330471034165	-0.626833125	[illegible]	
152						
153						
154						
155						
156						
157						
158						
159						

Figure 30: The bottom of the Δy *(Poly)/Δx (Centroid): f '(x) Zero Crossing Proxy* column

At this point, after confirming all of the named ranges and cell ranges for all of the functions are correct, one could move on if they did not want to add charts, which are largely responsible for the on-disk size of the workbooks. For security, one may tend to add charts for everything as a second check to be sure all of the functions are correct and to check the zero crossings visually to look for problems.

A group of charts can be copied together (or they could have been copied over with the headings and titles, which was step one) by moving the highlighted cell to K1 with the

Arrow keys, holding down the **Shift** key and picking cells K1:T21 as in Figure 31.

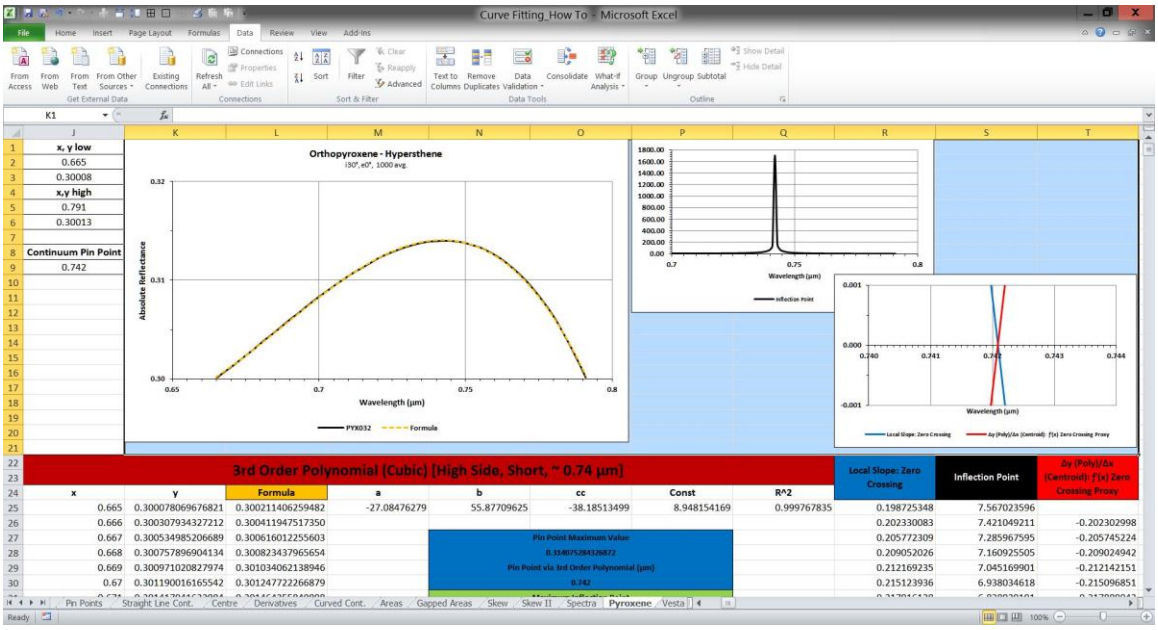

Figure 31: Copying a grouping of charts

Pressing **Ctrl+C** will copy the cells and the charts within, in front of the cells, and pressing the **Enter** key or **Ctrl+V** keys with cell K1 highlighted in your new worksheet will paste all three charts in. Unfortunately, there is no way, outside of a macro, to paste charts into a new worksheet/workbook and have the data addresses reassigned to the new worksheet/book. Instead of Edit-ing the data selections in the charts it is faster to simply Remove and redo the data selections so they address data ranges in the new worksheet.

Picking the next pin point follows the same procedure, copying the chart with the spectra and choosing the area either side of the reflectance maximum at ~1.4 µm to fit to calculate the pin point. Instead of copying individual pieces, i.e., the titles, headings, formulae and charts, you can copy the whole set at once by selecting cells V1:AF37 (we will continue to pretend the data range would be different) and paste the whole lot at cell

V1 in the our new worksheet and resize column U to 2, and columns V through AF to 18. You will notice the charts will resize themselves wider when pasted in and will lose width to resize appropriately when changing column widths to 18. But there is now a problem, as cutting and pasting in this fashion will break all of the formulae causing everything that involved any sort of formula to report "#VALUE!" in the cells, as depicted in Figure 32.

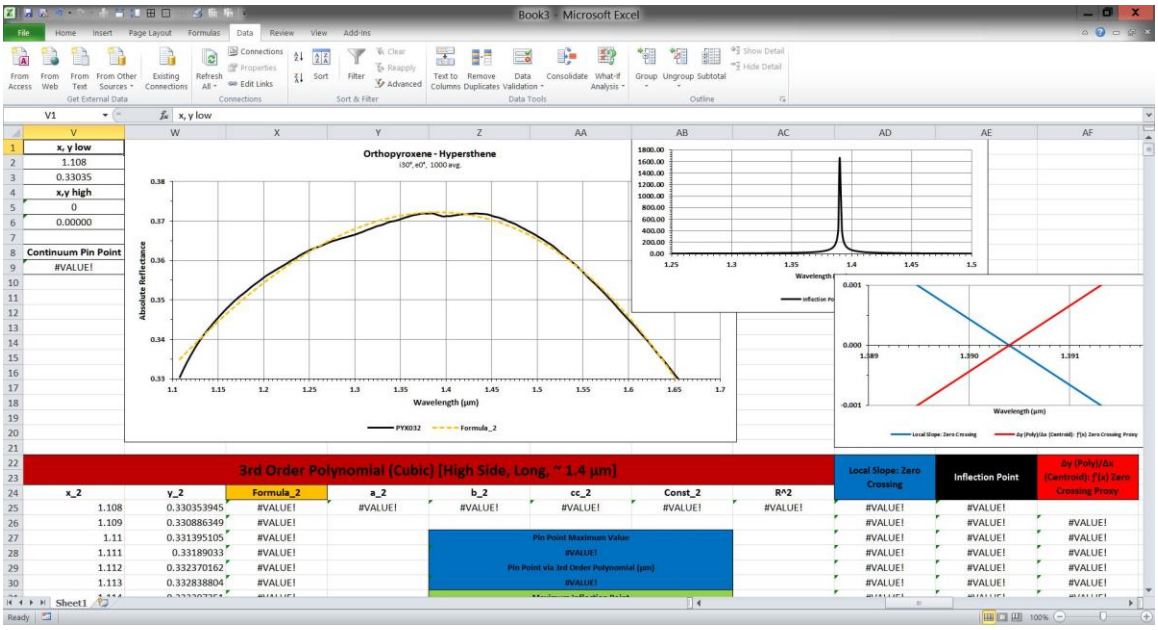

Figure 32: #VALUE!

Fortunately, the problem can be fixed by pasting in the rest of the x and y data ranges. The issue arose because the named ranges, x_2 and y_2 were pasted into the new worksheet and expected data running from cell 25 down to cells 571 and cells 38 through 571 were empty. Pasting in the x_2 and y_2 data will fix all but the R^2 value which will no longer report an error when the polynomial formula is pasted into the full range of cells and the Maximum Inflection Point and Pin Point via Maximum Inflection Point

Values which will be repaired when the formulae for the two zero crossings and the inflection point are pasted into the appropriate data ranges.

6.7 Straight Line Apparent Continuum Calculation and Removal

Straight line apparent continuum removal is preformed to isolate a section of the spectrum for area calculation (it also seems it is often done simply in deference to tradition). It has no real purpose beyond isolating a portion of the spectrum to define that portion's area. It is important to remember that our application of a straight line above an absorption and using the line to isolate and/or centre the absorption in no way approximates some sort of absorption isolation that allows one to model the absorptions in their natural state, nor does leaving the spectrum unadulterated. Everything above, in this case, a reflectance spectrum, is the continuum and placing a straight line atop an absorption, then removing a portion of the existing continuum above that line does not mimic any natural process of spectral alteration due to real effects such as grain size or phase angle variation. No matter the method, removing a straight line continuum always alters the spectrum. The reflectance spectrum is output by the reflectance spectrometer, via division and referencing a white reference for reflectance values, which means the spectrum already has its real continuum removed, further alteration of that spectrum is not necessarily advisable, and should you be not looking to calculate areas, an unnecessary practice (see the *Straight Line Cont.* and *Blackbody* worksheets).

Unlike the fitting of polynomials, the functions used do not use named ranges so the cut-and-paste operations are a little simpler. The fit straight lines run from calculated Pin

Point-to-Pin Point or some other point in the spectrum, e.g., in the pyroxene example, Band II runs from 1.39 to the last data point at 2.5 µm. While this is not the point of band extinction between Band II and the absorptions that you cannot see that occur between 2.8 and ~4 µm, it is a point that can be used consistently. Indeed, any choice of pin point is arbitrary, but as long as the reader is aware of those points, they can compare across data sets. Like every other metric, the key here is to be transparent and tell/show your reader what you have done so they can either compare directly or identical results can be reproduced.

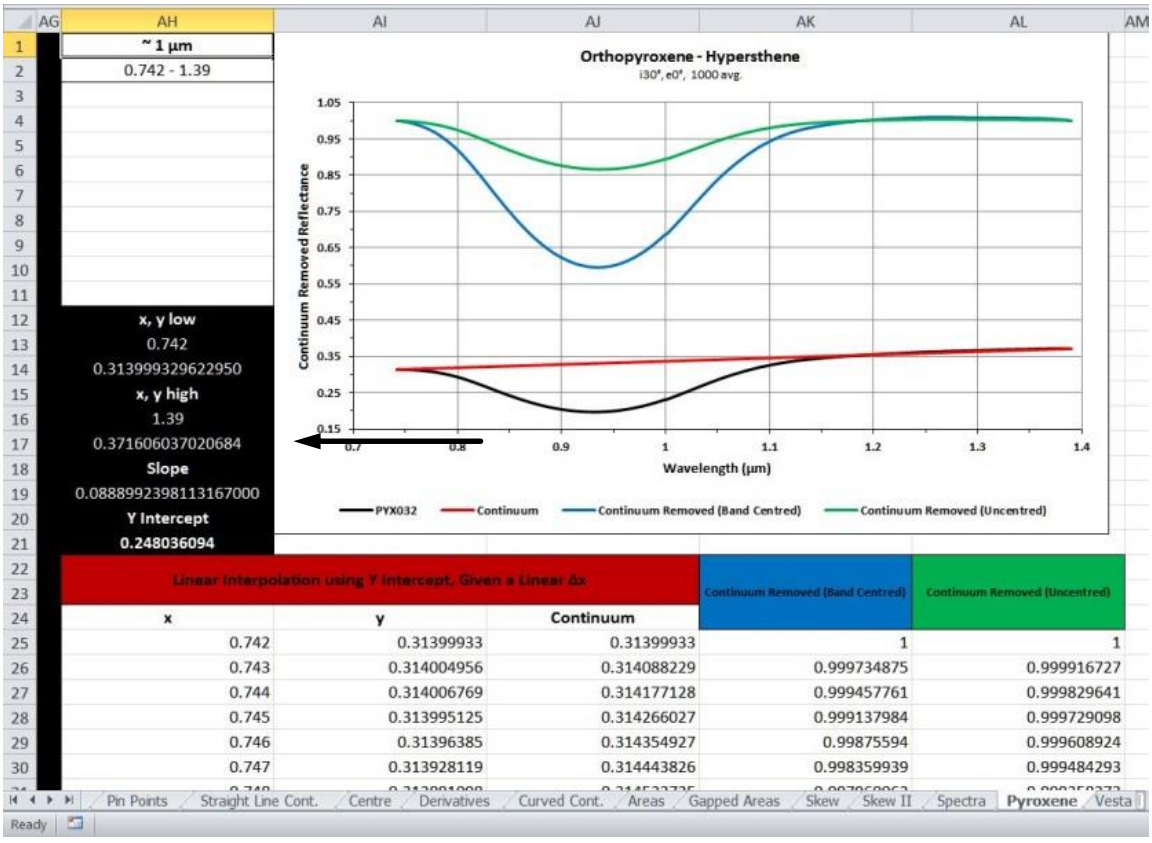

x	y	Continuum	Continuum Removed (Band Centred)	Continuum Removed (Uncentred)
0.742	0.31399933	0.31399933	1	1
0.743	0.314004956	0.314088229	0.999734875	0.999916727
0.744	0.314006769	0.314177128	0.999457761	0.999829641
0.745	0.313995125	0.314266027	0.999137984	0.999729098
0.746	0.31396385	0.314354927	0.99875594	0.999608924
0.747	0.313928119	0.314443826	0.998359939	0.999484293

Figure 33: Y Intercept

The function relies on the calculation of the Y Intercept and as such, the number of data steps and their linearity or lack thereof has no bearing on the function. It simply uses the Y Intercept to calculate the y values of a straight line between two points for equivalent x values as given by the data. If for some reason you wanted to have higher resolution in the line than in the data, use the Piecewise Linear Interpolation function included in the workbook to add extra resolution to the derived straight line apparent continuum after deriving the straight line using Y Intercept method.

The calculation of the straight line relies on the set of functions contained in cells AH12:AH21 and the Continuum function used in column AK that can be copied and pasted as a set as long as the cell-to-cell and column relationships are kept the same, as depicted in Figure 33. The only cells which require any change are AH16 and AH17 which are the x, y high (high and low here refer to high and low in terms of x values… 1.39 μm being "higher" than 0.742 μm) values which must be readdressed to reference the bottommost cells in the x and y columns respectively. The function for Continuum references both the Slope and the Y Intercept cells that are fixed in the Continuum function. The straight line continuum removal via division, i.e., Band Centred, and the straight line continuum removal via linear translation, i.e., Uncentred, functions only reference the y and Continuum columns. **Most important for simple cut-and-paste operation (and with all of the other functions in the workbook), is to keep the cell-to-cell relationships exactly as you see them so you will not have to rewrite any formulae, e.g., the functions in cells AH12:AH21 should always be in the x data column, in those numbered cells, above the x data, the columns should be x, y, Continuum, Band Centred and Uncentred. Keeping the cell-to-cell relationship**

constant will allow you to copy and paste the functions into any columns and still have the formulae work correctly. One can move things about to some extent by using Cut or **Ctrl-X**, e.g., if you used **Ctrl-X** to move cells AH12:AH21 up one so they fell in AH11:AH20 all of the functions which addressed those cells would change accordingly so all formulae remain functional in the unmoved Continuum column. If you move some portion of the cells using copy-and-paste, but not others, you will break the formulae and it will result in something which looks like the example in Figure 34.

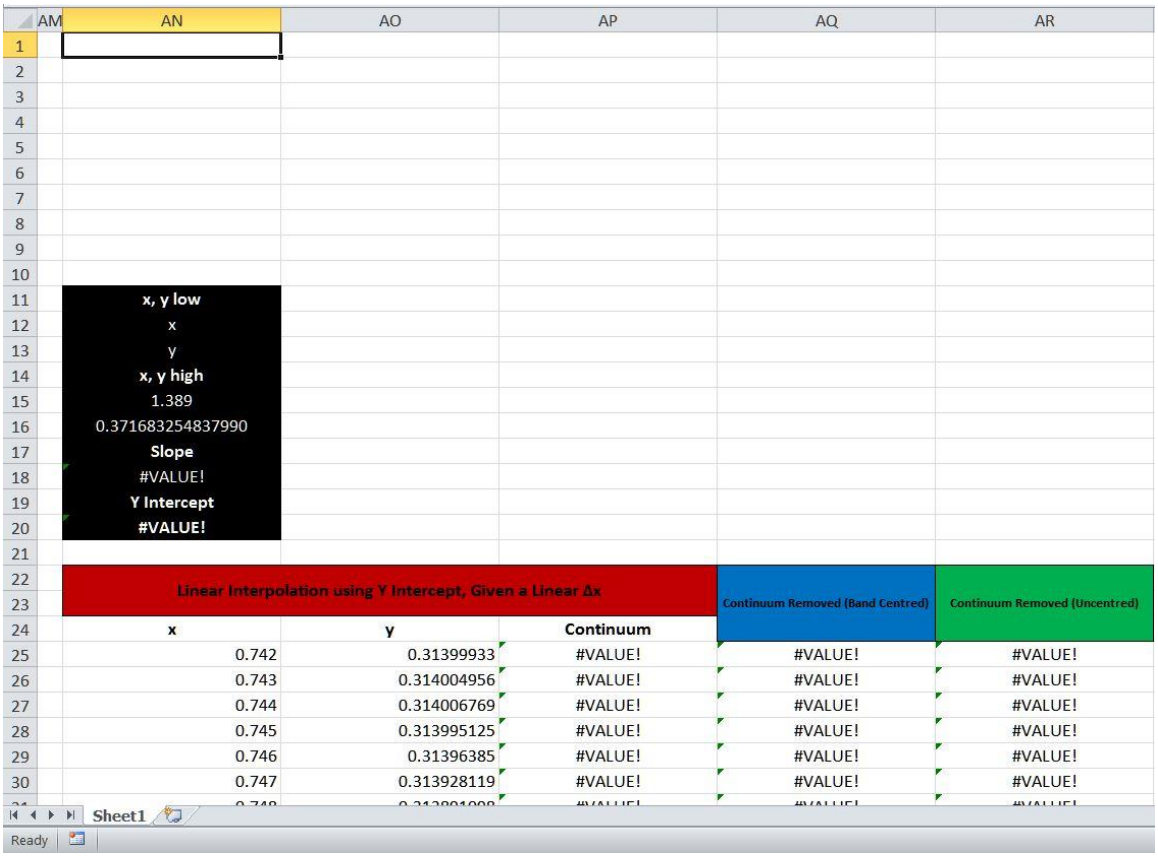

Figure 34: Formulae errors as a result of a loss of cell-to-cell relationship as a result as a result of a pasting error

The functions for Slope and Y Intercept have been moved up one cell and readdressed accordingly, but the cells they original addressed have not been moved in a

corresponding fashion which has broken the functions in the columns below and to the right. If you run into situations where this happens double check that you have not inadvertently copied and pasted sections into new columns/workbooks or worksheets in different positions. To fix this, now moving the AN11:AN20 section back down via cut-and-paste will not repair the problem, instead go back using **Ctrl-Z** and re-paste the block of cells in the appropriate spot. A suggested procedure would be to highlight and copy cells AH1:AL25 as per the example to the left and then paste in the appropriate x and y data and copy-and-paste the Continuum, Centred and Uncentred formulae from their respective starting cells in row 25 downward to fall in line with the x and y data as

is depicted in Figure 35.

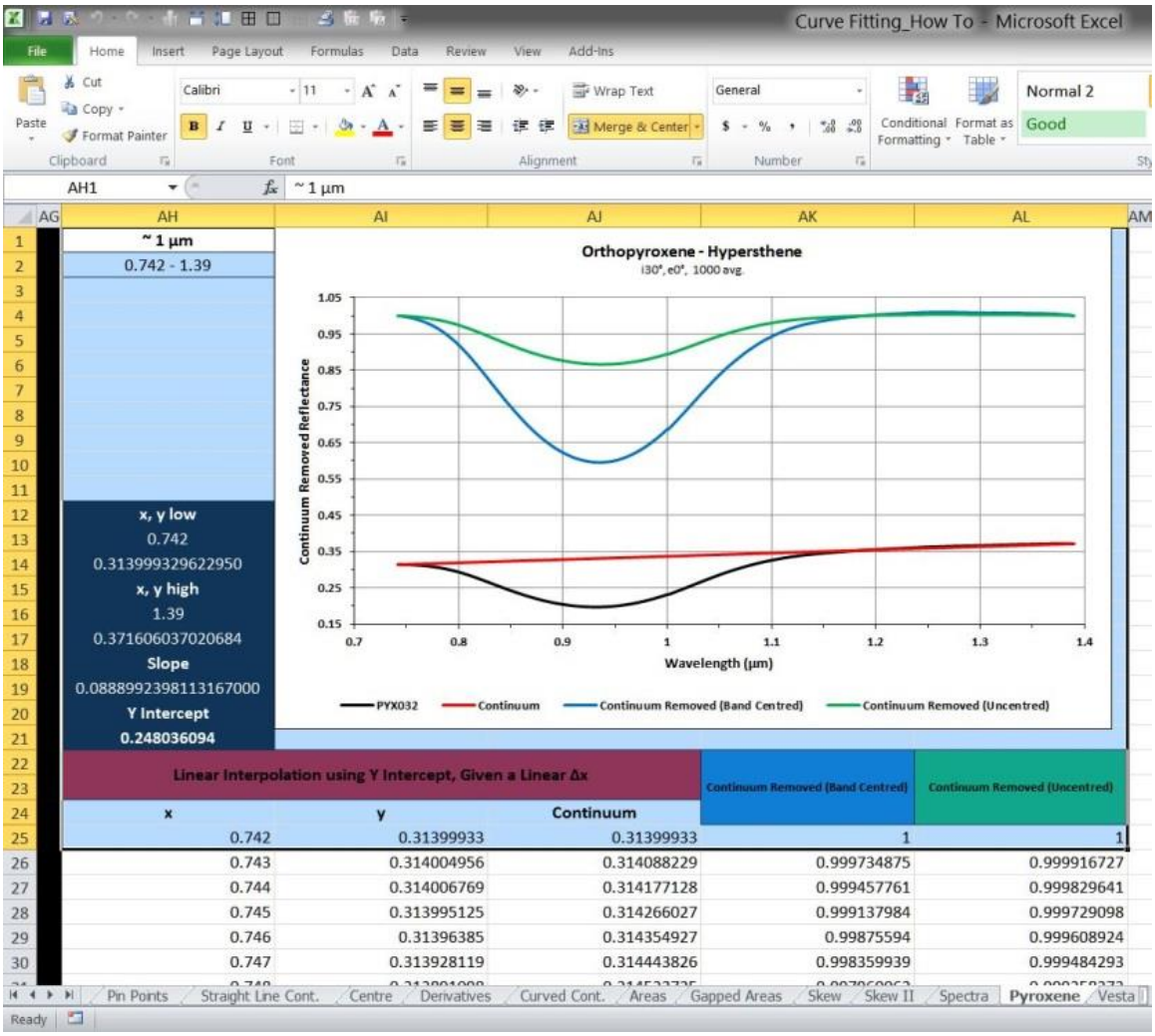

Figure 35: Suggest copy-and-paste procedure

These examples all use data that is pasted in to the x and y columns so it is a static set of cells filled with numbers in each and every instance. This is the method recommended for use when working with individual spectra, if one happens to be working with a set of spectra, such as a grain size or a mixture set series, and the pin points will be the same throughout the full set, as well as portions used for area calculation, portions the same for centre calculation and so on, one could set up a full worksheet so x and y columns for

various functions addressed x and y data from other portions of a worksheet such that one could copy an entire worksheet and do nothing but change the first column where y data appears (column B) and have all other functions in the worksheet key off that one column. The *Pyroxene II* worksheet is setup in this manner and if you paste another set of y data into B25:B2175 all of the functions in the worksheet which follow to the right will use the new y data you have pasted into column B.

6.8 Minima and Centre Fitting

The fitting of minima and centres follows the same procedures, with the same caveats, as shown in the fitting of pin points. The only difference of significance are the functions used to calculate the minima/center values and the functions that match the corresponding x values with the calculated y values for minim or centre. Given one is working with reflectance spectra, the minima and centre values and their matching function use "MIN" (for minimum) operators to find the minimum value of the fit polynomial and then match that calculated minimum with a corresponding x value, while the pin point function uses "MAX." We always recommend one use a 3rd order polynomial for fitting, no matter the data resolution but 2nd through 8th order are provided and may have specific uses. Like the pin point fitting, these functions only return fit y values that correspond with existing x values and will only return wavelength positions for existing x values in the data. Should one want to interpolate data in between existing x data values we have provided the means to do so, but would caution against ever using any method of interpolation to return calculated minima or centre values to an accuracy beyond that of the existing spectral resolution of a given dataset. We have included methods for polynomial,

Lagrange-polynomial, piecewise linear, and simple linear interpolation, and each can be quite useful but we would argue that one should only produce and report an interpolated minima or centre if his or her intention is to scream loudly, and repeatedly that the minima and/or centre is interpolated.

The *Minima* worksheet contains a number of examples of what specifically, NOT, to do when calculating a band centre or minima. It is important that one not add asymmetry to bands by picking areas where visual symmetry will result in data asymmetry or areas with different heights about the band centre or minima (see "Picking portions of the spectrum to use for Pin Points"). The important part, as always, is not that you necessarily do things "correctly," rather, that you share what you have done in a transparent manner so it can either be used with full knowledge of your methods, or it can be repeated. If one did not want to or could not share an entire workbook of fitting data, one should at a minimum provide the derived centres and/or minima, node values for the polynomial fits for the fitting of pin points, centres and minima, the pin point values used for centring, and a full set of fit statistics if the fit repeatability may be an issue (see the example in the *Minima* worksheet) as well as the spectra in the format in which it was fit ("the format in which it was fit" means one should be providing spectra that, for example, in the case of the pyroxene spectra used herein, is provided with the spectral breaks corrected as per the current standardized method used by the PSF and other facilities using ASDI spectrometers). Without all of these requisites met, the minima, centres and so on provided, are essentially useless.

6.9 Area Calculation and BAR

The calculation of area and Band Area Ratios (BAR) can be rather complex and is fraught with the possibility for inaccuracy. Area can be calculated in a number of ways, all which can introduce uncertainty in the eventual BAR versus band centre positions on a plot of S asteroid subtypes. Beyond BAR, area can have other uses as a metric on its own, as a metric to use to compare change in area of one band versus another or be used to calculate the skew of a band. If one looks at the examples in the *Areas* worksheet, which use the PYX032 samples spectra, it would appear all three methods, while giving different unitless values of area for each method, result in identical BAR results. Scroll to the right of the area fit examples and you can see the differences between each when BAR is not expressed with only two decimal places. With rounding to 2 decimal places, the BAR values appear to be the same for all three methods, but they are not when rounding is removed and the full 15 decimal place precision is shown. Equivalency is lost at the third decimal place. It is up to the user to decide if this is acceptable or not, but one must be aware that there simply is not one "correct" method you can use to derive an area of some bound space when a portion of that space is bound by a curve. One could use a method like that shown in the *Skew II* worksheet and use something representative of the area such as the simple triangle for which, an area can be definitively defined, but the problem lies both with the method you choose and the one used by the author whose previous work you might like to use for comparison (where, unfortunately, the methodology used for defining area is rarely revealed or discussed). What is important is that we acknowledge that the calculation of area when a portion of that area is bound by a curve is always going to be troublesome, and should the methods not be transparent,

anything derived from a comparison of areas or a ratio of areas versus a centre position should be treated as approximate.

The problems of area calculation become compounded when the data gets quite noisy, is of low spectral resolution or has data gaps. The *Gapped Areas* worksheet has several different methods for dealing with calculating areas with data gaps where they can be ignored or one can use various methods to fill-in the gaps, e.g., using the data from the function which fills gaps in with '1' values for straight line continuum removal of gapped data, infilling using polynomial interpolation and infilling using piecewise linear interpolation (simple linear interpolation as shown in the *Skew* worksheet could also be used). Specific functions are included for ignoring gaps using Integration of Regression, the Trapezoid Rule and Chords where data with inserted '1' values are removed, or original gapped data is used, but again, as in any calculation of area when a curve is involved, there is no "right" answer. Also included in the *Gapped Areas* and *Vesta* worksheets are examples of adding spectral resolution to the spectra of Vesta where data gaps were filled via interpolation, as well as, simply adding extra spectral resolution via interpolation to demonstrate the effect data resolution has on the area calculation functions. Again, there is no "correct" method, and while for fitting using a low order polynomial we can ignore the "quality" of the fit, and instead stay inside a set of bounds that means we should be able to compare one fit to another fit among researchers and across data sets, the same can never be said of area.

6.10 Derivatives, Curved Continua, Skew, Imposed and Real Continua, Gaussian Fit Optimization, Gaussian Modelling, Line Shapes, Smoothing and I/F

Several worksheets and functions are included because they illustrate various methods and processes which, while not a part of what one would consider the normal curve fitting process, illustrate important concepts. A couple of worksheets are included which are examples of different operations so one can see for themselves why it may not be a good idea to actually perform these oft overused functions. Additionally, there are several functions that are included simply because they come in handy, such as the function for flipping data, which is quite useful when data was collected in wavenumber but you would like to display it in wavelength.

6.10.1 Derivatives

The calculation of first (f'(x)) and second (f"(x)) derivatives of a spectrum is not useful for curve fitting to define minima of maxima, and should **NEVER** be used to do so. We have included them, as, after using the Inflection Point delta function to calculate the inflection point values for the first and second derivatives of the spectrum, the inflection point maxima can be used as guides for polynomial fitting as they can provide the limits for the data range over which the polynomial should be fit as depicted in Figure 36.

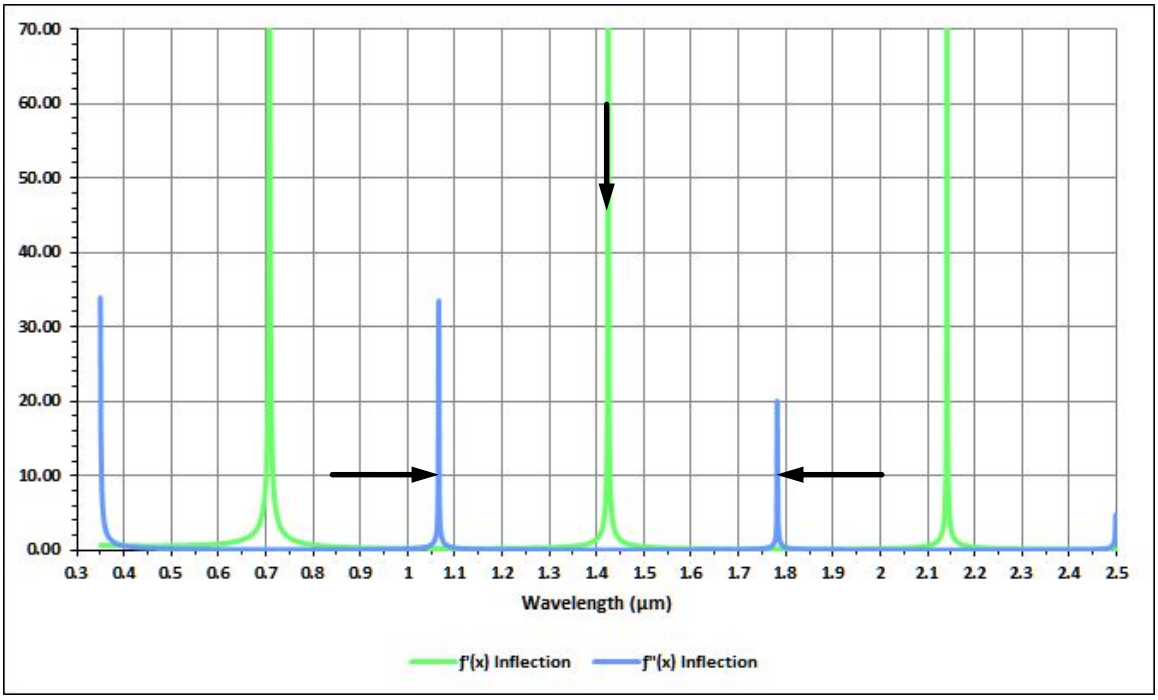

Figure 36: Inflection Points derived from the 1st and 2nd derivatives of a sign wave function

For example, using the inflection points for the first and second derivative of the of the approximately 1.4 µm absorption of the sine wave function in the *Derivatives* worksheet one could look at the chart below and see that to fit the ~1.4 µm band, one should keep the polynomial used to do so inside of the maxima of the inflection points of the second derivative immediately to the right and left of the approximate minima of the absorption in question. Doing so will ensure that one never uses a portion of the non-simple part of the curve surrounding an absorption and does not end up adding too much data to the polynomial fit to derive the minima.

If one looks over the examples of 1st and 2nd derivatives and the inflection points thereof, for actual spectra provided, it is not quite as easy as the pristine sine wave example in Figure 36 makes it appear, but it could be of use if one is struggling to pick areas to isolate for minima/centre and pin point fitting. One could also, instead of relying on

discretion or the use of derivatives, simply pick a fixed number of points each side of the present numerical minima/maxima. Using a logical approach, an absorption could be fit using a polynomial over a fixed data range, e.g., for the ASDI spectrometer, its fixed resolution is between 2 and 7 nm. With its worst case resolution being 7 nanometres, one could say, we will always take 28 points (or 4 times the worst possible spectral resolution) either side of the extant absorption minima for fitting (except where that value forced one to use a portion of the curve that passed over the nearest inflection point of the 2nd derivative). This would be a perfectly acceptable methodology as long as it was shared with your readers.

6.10.2 Curved Continua

Curved continua are presented both as examples of how it may be performed, and to suggest it is unnecessary and unwise to add the extra level of complexity by using a curve to isolate an absorption feature for what amounts to an arbitrary demarcation to define an area. The fitting of a curve that has no resemblance to any measure of reality simply adds complexity and complicates repeatability. In the examples provided we have explored the use of simple and complex curves in various spaces and find that straight lines fit to reflectance spectra with their inherent imposed continuum still intact (i.e. standard reflectance spectra) is the simplest method mathematically and it is also eminently repeatable across platforms as any methods one uses to derive a straight line between two points should always result in a straight line. Curved lines will in many cases be very nearly straight lines, they, require more effort as someone will often have to be checking to see if the convex hull desired is achieved, they are no more likely to resemble the real continuum (the blackbody reflectance or emission continuum) of a sample than straight

line apparent continua, and the repeatability of curved continua is likely to always be an issue unless the curved apparent continua themselves are shared.

6.10.3 Skew/Asymmetry

Skew may be a useful metric, which one may want to included when parameterizing spectra, but it has not been widely used and there exists little published data for comparison. We have included three methods for its derivation, but would suggest only one actually be used, Right and Left Width at Half Maximum (RWHM and LWHM). Full Width at Half Maximum (FWHM) is a widely used metric in several other fields and has an established methodology for simply measuring the height of a feature from some defined point (generally an applied baseline), and reporting the width of the feature at half of the height. We have included both a method using representative triangles and one using area either side of the centre/maxima/minima, but as stated, using a measure of area will always be troublesome, and the use of a representative triangle may be an oversimplification (though less labour intensive should one want to have a look through data quickly and see if a measure of skew could be useful). We do caution though, that while a measure of skew may be useful in distinguishing between simple two component mixtures, when dealing with multiple-component assemblages, such as basalt, the overlapping absorptions about Band I from more absorbing species would mean a measure of skew would be unlikely to be of use.

No matter the method used to calculate skew, we will almost always have an issue using the calculated position of the point from which to measure FWHM/RWHM and LWHM. The issue can be ameliorated by using a Gaussian fit which includes a measure of skew

as in the EGO Algorithm (see. Pompilio et al., 2009, Pompilio et al., 2010), or by treating it in one of the two following ways. The value at which we measure the width is exactly one half the height, which is very unlikely to ever fall at an existing set of y values that are equivalent y values on both sides of the half height point, or, will be parallel to the baseline/unity/applied straight line continuum, as we are always dealing with data sets that are x and y point values and not actual curves. The problem can be addressed by two different means, by using the nearest existing y values and their corresponding x values or interpolating a new x value for the calculated FWHM measurement point. We have included an example of simple linear interpolation to derive new x values, but would suggest that this is not the method one should choose, rather, we would argue for the use of the immediately adjacent points which already exist. A series of functions are included to check to see if equivalent y values for the FWHM measurement point exist as well as functions to find the closest existing y values and match those to their corresponding x values. Inserting the function set is a cut-and-paste operation but the choice of which values to use for FWHM, RWHM and LWHM require the user to actively change the calculations for each of these values based on closest values as do the cell references for Band Depth, and the cell ranges for HBDR matching and HDBR corresponding functions.

Referencing the example to the shown in Figure 37, the Centre is simply a cell to be filled in (for continuum removed but uncentred data, it would be minima as per other examples in the *Skew* worksheet) while the FWHM, RWHM and LWHM functions require user intervention to point them to the correct cells, and change the centre or minima value used for calculation. The highlighting in cells AC and AF16 and AC and AF20 are user-inserted to highlight the values closest to the calculated FWHM measurement point. The x and y columns are set up such that the centre (or minima) x and y values are in the bottommost cells of the range for the data left of the centre and repeated in the topmost cells for the data to the right of the centre.

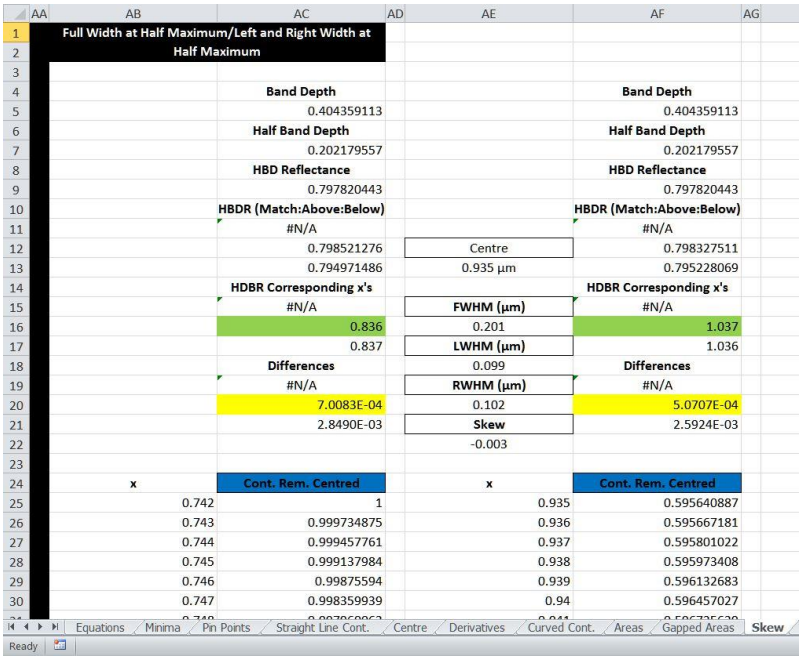

	AB	AC	AE	AF
1	Full Width at Half Maximum/Left and Right Width at Half Maximum			
4		Band Depth		Band Depth
5		0.404359113		0.404359113
6		Half Band Depth		Half Band Depth
7		0.202179557		0.202179557
8		HBD Reflectance		HBD Reflectance
9		0.797820443		0.797820443
10		HBDR (Match:Above:Below)		HBDR (Match:Above:Below)
11		#N/A		#N/A
12		0.798521276	Centre	0.798327511
13		0.794971486	0.935 µm	0.795228069
14		HDBR Corresponding x's		HDBR Corresponding x's
15		#N/A	FWHM (µm)	#N/A
16		0.836	0.201	1.037
17		0.837	LWHM (µm)	1.036
18		Differences	0.099	Differences
19		#N/A	RWHM (µm)	#N/A
20		7.0083E-04	0.102	5.0707E-04
21		2.8490E-03	Skew	2.5924E-03
22			-0.003	
24	x	Cont. Rem. Centred	x	Cont. Rem. Centred
25	0.742	1	0.935	0.595640887
26	0.743	0.999734875	0.936	0.595667181
27	0.744	0.999457761	0.937	0.595801022
28	0.745	0.999137984	0.938	0.595973408
29	0.746	0.99875594	0.939	0.596132683
30	0.747	0.998359939	0.94	0.596457027

Equations | Minima | Pin Points | Straight Line Cont. | Centre | Derivatives | Curved Cont. | Areas | Gapped Areas | Skew

Ready

Figure 37: Measuring Skew and/or Asymmetry

6.10.4 Blackbody Curves: Imposed and Real Continua

The concept of a continuum can be difficult to grasp, but it gets even more complicated when one is using data where some alteration of the real continuum has already been performed through the process of dividing out the real continuum, as is common practice in reflectance spectroscopy, or when one is wanting to model spectra in a manner that has some connection to the actual shape of a real absorption. When dealing with infrared

emission spectra, the continuum is a function of the temperature of the planetary or sample surface. Emission spectra are normally displayed continuum removed where a blackbody curve for the equivalent temperature is removed via division. An example of an emission spectrum is provided in the *Blackbody* worksheet with the 'Continuum/Black n' Greybody Curve Generator.' The majority of research regarding emission spectra references continuum removed spectra and one should always be aware that if any modelling, as we choose to define it, of the spectra is to be performed, the spectra must still have their real continuum intact (or have it reapplied) and the modelling must be performed in energy space.

For reflectance spectra, the real continuum is more complicated as it is a combination of two blackbody curves, that are in reality greybody curves, one representing the thermal IR emission of the sample or planetary surface at that surface's given temperature, and another representing the emission of the light source used for sample measurement (for asteroids and other "warm" planetary surfaces one will also have to take into account thermal excess, which is ameliorated during reflectance instrument calibration/reflectance measurement in the lab, assuming reflectance standard and sample are the same temperature; see Abell, 2003, and Reddy et al., 2013, and references therein). These two have to be combined to produce one continuum which can then be applied to remove the continuum imposed on the spectrum by the process of reflectance measurement/instrument calibration, which involves the referencing of a reflectance standard. The process involves referencing a very nearly 100% reflectance standard across the UV thru NIR wavelength range (often Halon or Spectralon®) to correct the instrument response and the emission of the light source, such that, in combination,

spectra thereafter collected of the reflectance standard will be a flat line at unity. Removing the imposed continuum so that the spectra can be modeled in eV space is further complicated as the curve of the light source may not be known (this is problematic if one wants to model spectra from data sets where the spectrometers and their light sources no longer exist, and is another reason to favour using straight line continuum removal in wavelength space for band isolation) and a black body is a theoretical construct that does not exist. Rather, the Sun and our light sources for laboratory work emit greybody radiation. For the examples in the workbook we have used the emission curve of the sun which is not entirely accurate, though it is a reasonably accurate representation of the Sun/the light source used. As presented, all the functions accepting the 'Scale Factor' reference the temperature cell in the *Blackbody* worksheet so one can experiment with different blackbody curves by simply changing the temperature in the light green and light blue highlighted temperature cells for the two curves and see the resulting changes in the greybody curve and imposed continuum removed spectrum. Without knowing the grey body value absolutely, some significant experimentation would be required to alter the value such that the combined Reflectance and Emission Continuum would reflect reality. Rather than significantly complicate the production of Imposed Continuum Removed spectra, and taking a page from those who work with emission spectra, we have chosen to simply use a blackbody curve. The Scale Factor can be used to 'grey' the Normalized Reflectance Continuum before it is combined additively with the Emission Continuum. Scale factor (1 = for a black body, <1 for a grey body) can be adjusted in cell D12 in the *Blackbody* worksheet example but it will not alter the combined Reflectance and Emission Continuum and the Imposed

Continuum Removed spectrum (it could if one chose to rewrite the additive 'Ref. Emiss. Continuum' function). We have shown the Reflectance Continuum for wavelengths shorter than those used in the spectrum to illustrate the blackbody curve approaching 0 but in practice this is not necessary (see the demonstration of 'Thermal Excess' in the same worksheet).

6.10.5 Gaussian Fitting and Gaussian Modelling (Fit Optimization and Curve Deconvolution)

Gaussian fitting, and Gaussian modelling are included for purposes of illustration and we do not intend to suggest that Gaussian fitting/modelling become standard practice. Performing fully manual fitting/modelling can be quite instructive, and the manual + automation methods we have demonstrated can be exceedingly tedious so a broad application is not expected. We have included examples of automated fit optimization/curve deconvolution (which could equally apply to modelling) that we expect one will be more likely to employ if one had both an automated optimization routine and Automatic Parameter Initialization function seamlessly together (see Makarewicz et al., 2009). One should note, that when fitting or modelling, an amount of inaccuracy must be accepted, as the discrete absorptions we are attempting to model do not account for the full continuum of features that make up the spectrum. The continuum of features that create the spectrum are a combination of discrete absorptions, overtones of infrared absorptions, optical effects and so on that will not always be Gaussian in nature. As such, any model based solely on discrete Gaussian absorptions leaves the problem severely under-constrained. One also has to accept a certain amount of inaccuracy when fitting Gaussians or any other curves to spectra that have an imposed

continuum as a result of the reflectance measurement process or have been straight line apparent continuum removed as has been done for the examples we show in the *Gauss. Fit & Fit Optimization* worksheet.

There are instances where manually or automatically fitting and/or modelling of absorptions can be quite useful, such as approaching the fitting and/or modelling of a particular absorption in a completely unknown sample and attempting to fit it with the bare minimum number of Gaussians to lead one in a direction for describing said sample. It can also be, and may be, the only reasonably useful means of fitting shoulders on absorption bands. Gaussian fitting, as shown, we would suggest not be normally used to describe absorption band minima or centres as the Gaussian fits will always be under-constrained approximations which are difficult to repeat. As shown by Gallie et al., 2008, Gaussians fit in wavelength space and energy space are essentially equivalent, and while we believe this to be true and have shown our examples of Gaussian fit optimization/curve deconvolution in wavelength space, we hesitate to advocate for the use of automated Gaussian fit optimization as a curve fitting method to be applied in place of empirical curve fitting. Rather, Gaussian fit optimization/curve deconvolution is an exceedingly useful part of a large tool kit spectroscopists can use to define spectra, which we would suggest follows empirical curve fitting in efficacy.

We have included a second worksheet, *Gaussian Modelling*, as individual absorptions are generally symmetric in energy space about the maximum of the absorption for many absorption processes such that any asymmetry is the result of another adjacent symmetric absorption exerting its influence to create an apparent asymmetry. Given the inherent

lack of absorption symmetry in wavelength space, coupled with the fact that most fitting of reflectance spectra is performed on spectra which have already had a reflectance measurement continuum imposed upon them, we should recognize that without both removing the imposed continuum in wavelength space and then converting the imposed continuum removed spectrum to energy space, we cannot be actually modelling anything "real" using symmetric curves so we should always be making the distinction between Gaussian Fitting and Gaussian Modelling. To model a spectrum with a Gaussian or any other curve symmetric about its centre, the spectrum must be in a format where no continuum has been imposed or removed (excepting removal of the imposed continuum), it must in energy space, and any fitting of Gaussians, Lorentzians, Pseudo-Voigts or other symmetric curves, to a reflectance spectrum in any other state is simply fitting.

6.10.6 Gaussian Fit Optimization using Solver and/or OpenSolver

In the *Gauss. Fit & Fit Optimization* worksheet we have included examples which detail the use of the Excel Solver Add-In (built into Excel 2010 and newer versions) and the OpenSolver Add-In to optimize the Gaussian fits of the continuum removed spectra of the pyroxene sample we use throughout as an example (see Walsh and Diamond, 1985 and Mason, 2012). This methodology is for all intents and purposes identical to the processes of non-linear curve fitting used by the Modified Gaussian Model excepting the specific non-linear optimization algorithm. Given our extensive experience we would suggest Gaussian fit optimization/curve deconvolution in this manner be applied sparingly and following a set of empirical curve fits that should be performed as a first step. The Gaussian fitting/modelling techniques can be exceedingly useful, especially when attempting to define the position of shoulders on absorptions, but they require a set

of constraints be placed on the fit optimization of each absorption, or set of absorptions based on *a priori* knowledge of sample composition that can make it quite tedious to perform. Alternatively, one can employ an iterative optimizing technique that requires the operator have significant spectroscopy experience so mistakes such as using too many absorption bands do not become commonplace. If one chooses to perform fits or modelling using Gaussians, ideally, the full set of constraints would be shared just as we suggest is a requisite for empirically fit data. If one did want to perform Gaussian fit optimization or modelling on a regular basis and share the fits in publications we would suggest they favour the open source and more feature rich OpenSolver or MGM.

Both Solver and OpenSolver operate in a similar manner. They both attempt to minimize (or maximize/seek a specific value) for a single cell by altering a number of others. In our case, we are using a non-linear optimization algorithm to attempt to seek the lowest possible Root-Mean-Square (RMS) value by setting the solver to alter a specific set of values within specific windows, i.e., constraining the fits (Note: Gaussian fit optimization in this manner is a non-linear problem, linear optimization will not work). This has to be done or the solvers/MGM will fit Gaussians in a manner which satisfies the algorithms goal to produce a minimum RMS value. If left unconstrained (beyond the number of Gaussians to fit which is a given ever present constraint in the demonstrated method) the solver will find the minimum RMS value and produce a fit optimization that looks something like the example in Figure 38 (Example #3 from the *Gauss. Fit & Optimization* worksheet), where to achieve the lowest possible RMS value the Solver has placed 4 Gaussians in the second absorption feature. This is a “better” fit, but it is in no way a reflection of reality.

To produce a fit that is in some manner consistent with reality we have to approach Gaussian fit optimization using our *a priori* knowledge of the absorptions we are attempting to fit and constrain the fitting algorithm by either writing constraints or beginning with a nearly optimized fit, so it is attempting to optimize the fit of Gaussians that are constrained to their assigned wavelength spaces. (Therein lays the rub – if we do not know beforehand how many Gaussians should be fit, how does one constrain the fit so it reflects reality?) For example, below are screen captures of the popup meus for both Solver and OpenSolver which show the constraints placed on the GRG nonlinear and NOMAD nonlinear optimization algorithms applied by each respectively. If one does not provide a set of constraints the optimized fit will end up looking much like the optimized fit in Figure 38. We know we are dealing with a pyroxene, and that Band I is comprised

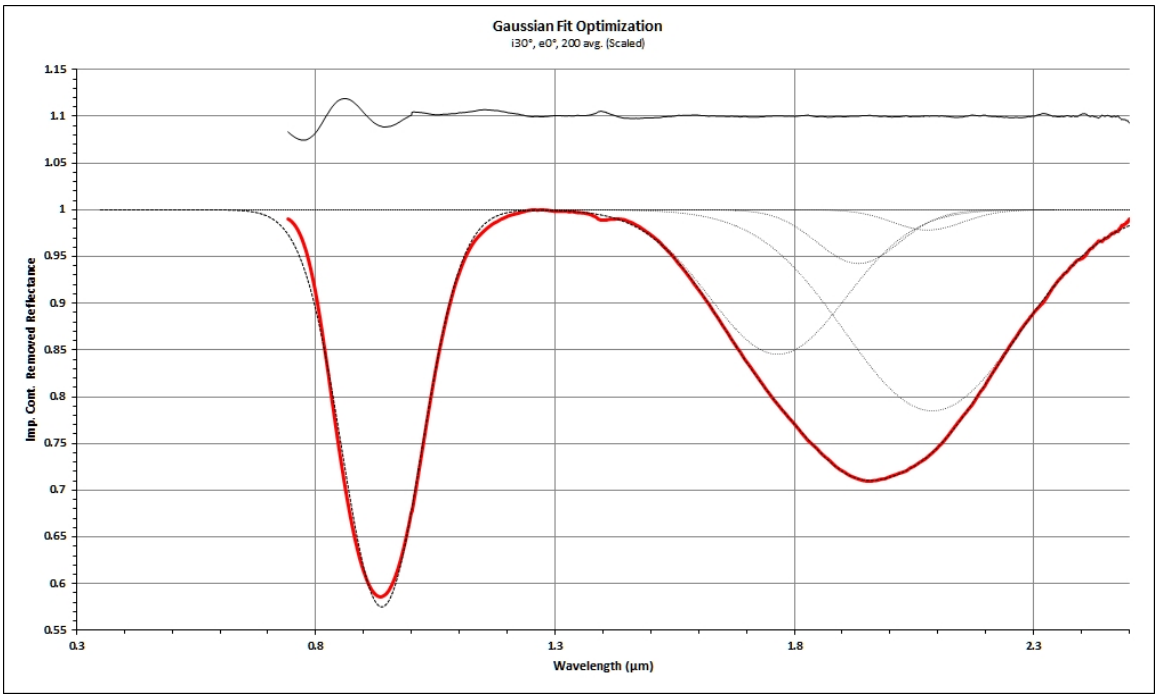

Figure 38: Unconstrained Gaussian Fit Optimization

of two discrete absorptions, Band II is produced by one absorption mechanism and there

are two small contributions from a miniscule amount of adsorbed water present in the powdered sample. To constrain the Gaussian optimization we bound each of the five Gaussians within a small wavelength window.

The constraints placed on the Solver based fit optimization used in example #4 are shown in Figure 39, along with the resulting fit which is now firmly rooted in reality.

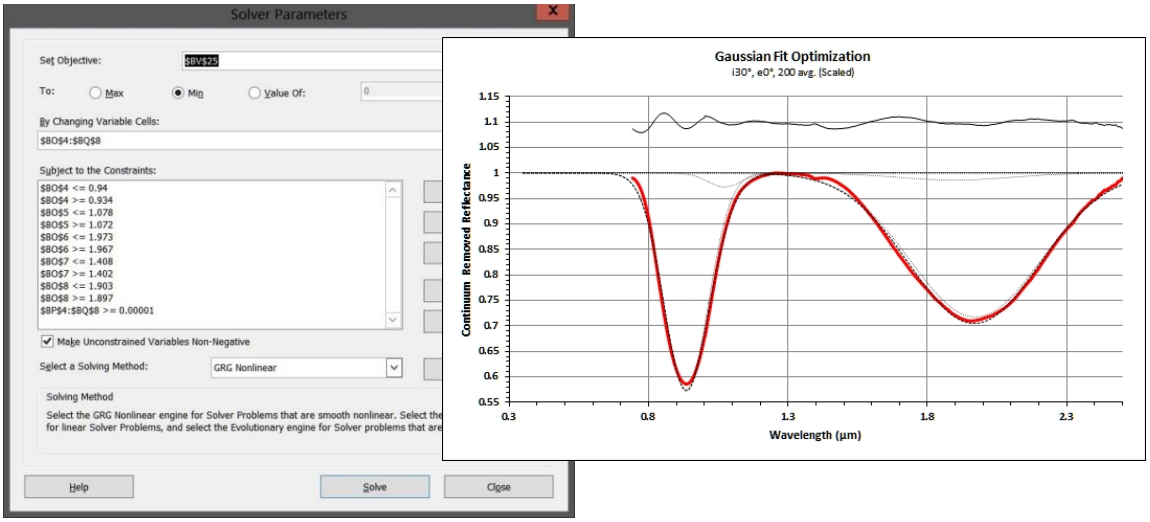

Figure 39: Gaussian Fit Optimization with Solver

The next example is a similar fit performed using OpenSolver (Example #5) and a similar set of constraints that for all intents and purposes produces an equivalent result. The RMS values are nearly identical but the fits are ever so slightly different (Figure 40).

Both of these fit optimizations depicted in Figures 39 and 40, can be improved by further constraint, more iteration, and so on. If we separated the two sections so the fit optimization did not have to bridge the connection between Bands I and II (which we have created), constrained the depth of the 1.4 µm water feature and constrained the width of the 1.9 µm water feature we could definitely improve the fit, but where would one stop tweaking constraints? Gaussian fit optimization/curve deconvolution certainly

has its uses, but when we do not reasonably know the mineralogy of the samples so we can adequately constrain the fit optimization, and we want whatever process we have used to derive fit metrics to be repeatable, fit optimization performed in this manner is simply inappropriate. That said, Gaussian fit optimization/curve deconvolution does have merit and can be especially useful when trying to discern the wavelength position of a shoulder or when mineralogy/number of absorptions are unknown and one begins optimizing with just one Gaussian and continues to add more Gaussians until a fit deemed adequate using a minimum number of Gaussians is achieved.

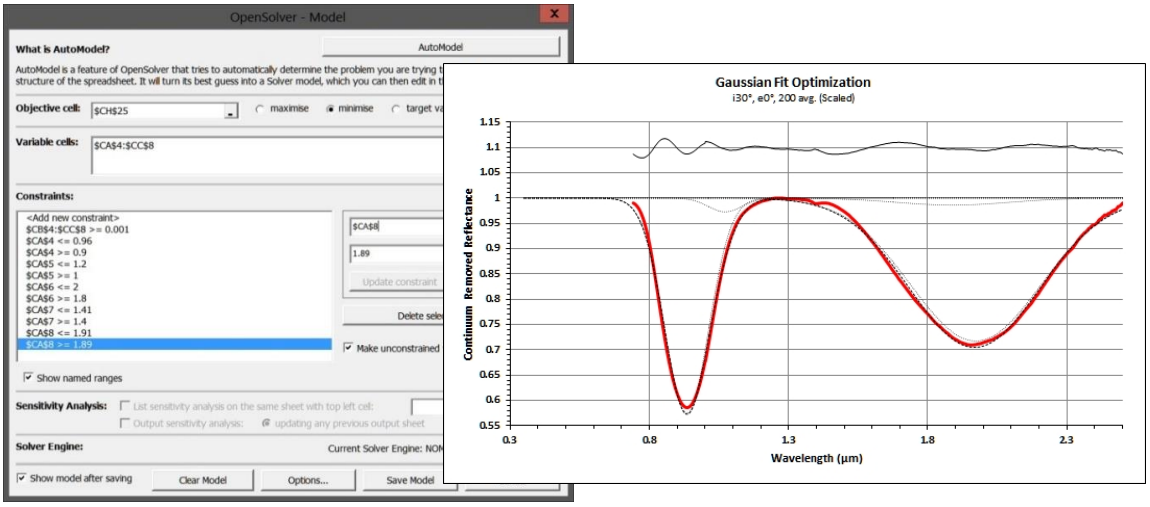

Figure 40: Gaussian Fit Optimization with OpenSolver

If one is using OpenSolver employing NOMAD there is also a rather speedy method to optimize fits if one begins with a fit produced by hand that if reasonably good. Producing good fits by hand is quite easy when working with isolated, straight line apparent continuum removed bands as in examples two through five where you can begin with the three bands, 1, 2 and 3 in each example. Begin with very narrow Gaussians with approximate centres, set the scalar to a value so the 'fit' from the fit column is close and

then expand the Gaussian FWHM to a value that is close. With a set of three Gaussians that are somewhat close, you can use OpenSolver to optimize the fit without adding constraints by setting up OpenSolver to minimize the 'RMS: Residual cell' and restricting the 'Variable Cells' to only a single scalar, then single FWHM for one absorption, then both FWHM and scalar for a single absorption, stepping through each absorption, then FWHM and scalars for all three absorptions, centre, FWHM and scalar for each absorption individually, and finally all nine variables concurrently. We have had great success following this procedure when optimizing summed Gaussian fits without constraints using OpenSolver employing NOMAD with a maximum solution time of 3,600 seconds, maximum number of iterations of 20,000 and precision of 0.000001 in isolated worksheets (i.e., not inside Appendix A) where the isolated workbook is the only item open in Windows XP, 7, 8, 8.1 and 10. Optimized fits such as those in examples 2 through 5 can be produced in a manner of minutes in this fashion.

6.10.7 Line Shapes

Line shapes for other curve profiles in addition to Gaussians have been included to illustrate the differences and allow one to play with the curves and see how each change in parameter will affect the lines shapes. In general, Gaussians best model absorptions in solids, Lorentzians best model absorptions in gasses and Pseudo-Voigts best model absorptions in liquids. Included are standard formulations for Gaussian and Lorentzian line shapes and the same line shapes modified to use depths/heights and FWHM values that relate to the percent absorbance/reflectance and wavelength/eV scales. The Pseudo-Voigt function is a combination of Gaussian and Lorentzian lines shapes where the Gaussian and Lorentzian functions use the same FWHM and scale heights, but the degree

of each in the Pseudo-Voigt curve can be altered by changing the degree of Lorentzian participation where Lorentzian ° = 0 is purely Gaussian and Lorentzian ° = 1 is purely Lorentzian. See the examples in the *Line Shapes* worksheet.

6.10.8 Smoothing

Smoothing functions have been included to illustrate the issues that arise when one attempts to smooth data. We would advise one not to smooth data as it tends to cause more harm than good. Common practice with modern spectrometers is to average a number of spectra to improve the signal-to-noise ratio and given this, combined with the high spectral resolution of most modern spectrometers, the data is in effect, already smooth. If one looks at the examples in the *Smoothing* worksheet, for high spectral resolution data the smoothing does essentially nothing to the large absorptions and will mute sharp absorptions, which makes them more difficult to identify/fit. With lower resolution and/or marginally noisy data, smoothing tends to affect the large absorptions by altering their depth and slopes while also creating spurious features where the smoothing function follows the noise in the spectrum. Given that smoothing is almost always adding complexity where its addition is unnecessary, we suggest it not be used and have included the *Smoothing* worksheet as an illustration of, and reasons for, what one ought not do.

6.10.9 Imposed Continuum Removal, I/F (Intensity/Flux) and Thermal Excess

Figure 2D in the manuscript illustrates imposed continuum removal on the reflectance spectrum by standard reflectance measurement procedure where the spectrum is presented as I/F, or Intensity/Flux (see Figure 41). Procedurally this involves several steps in the calibration of a reflectance spectrometer where firstly, the combined response curve of the detector(s) (normally a single defined function that is not dynamically updated), the emission curve of the light source and the emission curve of the white reference reflectance standard, at what should be the same temperature for both white reference reflectance standard and ensuing samples, are all removed from the final, as delivered spectrum, by division such that intensity, or the signal returned is divided by the combined emission curves of the light source and emitting sample. The value is unity, or 100% reflectance, is defined by the "whiteness" of the white reference sample, normally Halon or Spectralon® for NIR reflectance spectroscopy. Inherent in this procedure is the contrast stretch of the I/F spectrum and of particular note, the source of the thermal excess oft seen in asteroid, and other spectra,

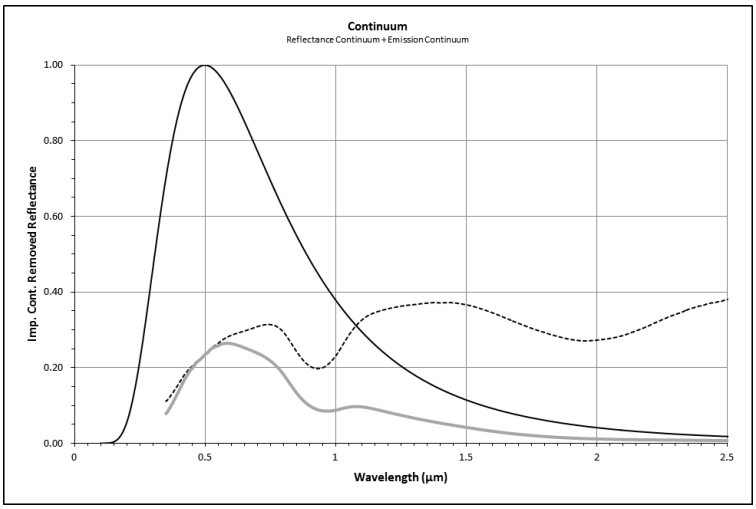

Figure 41: Imposed Continuum Removal

when the temperature of the emitting sample/body is not factored into the I/F calculations.

Firstly, thermal excess is not actual excess, as in the object being observed is warmer than we had anticipated. Rather, thermal excess is excess upward swing in the spectrum long ward of approximately 2 microns (though where the effect would be defined as significant is open to interpretation) where the I/F spectrum has an excess upward climb of reflectance values because when computing the I/F spectrum we have not accounted for the emissive portion of the combined reflectance and emission continuum. We have demonstrated this effect in the *Blackbody* worksheet. Inset is a copy of Figure 2-2D (Figure 41). In this example, we have used a reasonably accurate representation of the combined light source/solar emission blackbody curve and the blackbody emission curve for the sample given the sample temperature when its spectrum was collected. If one looks at the reflectance spectrum in figure 2-2D (black dashed line) there is no thermal excess because the thermal emission of the sample was accounted for during reflectance instrument calibration.

To produce an example of thermal excess, shown in Figure 42, we have taken the same samples spectrum (light blue), removed its imposed continuum using the combined solar and emission blackbody curves/continua (dark blue), then added thermal excess to the samples imposed continuum removed spectrum (black dash – dot) and redone the I/F

division to remove just the reflectance continuum (red).

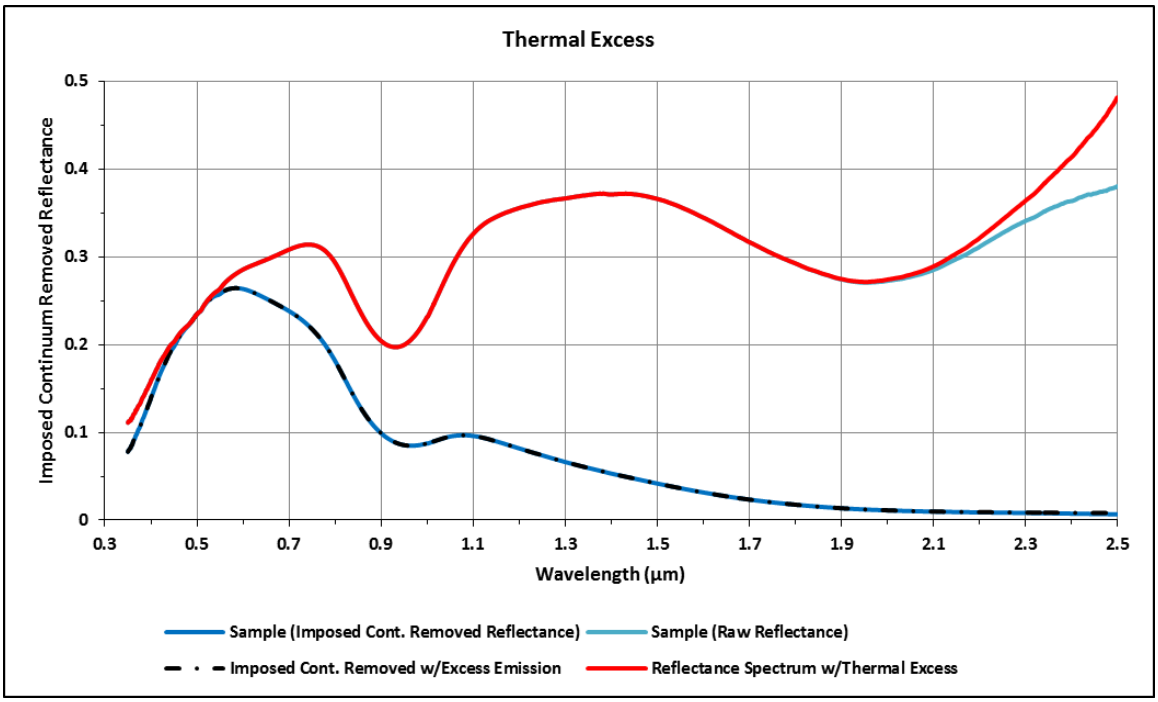

Figure 42: Thermal Excess

This is an accurate recreation of thermal excess as seen in asteroid spectra and also is an example of how we could go about correcting it as several factors are given. For example, for both emission and reflectance spectra, standard formulation would seem to be the use of blackbody curves with peak emissions of 1, and they are removed by division to produce reflectance or emission spectra where in each, one x/y point directly below the emission peak remains fixed such that we can always return to absolute emission and reflection values and thermal excess is a function of incomplete maths which we can repair as the combination of reflectance and emission blackbody curves/continua are purely additive.

6.11 References

Abell, P.A., 2003. Near-IR spectroscopy of main belt and near-Earth objects: A study of their composition, meteorite affinities and source regions. Ph.D. Dissertation, Rensselaer Polytechnic Institute, Troy, New York.

Cloutis, E.A., Gaffey, M.J., Jackowski, T.L., Reed, K.L., 1986. Calibrations of phase abundance, composition, and particle size distribution for olivine–orthopyroxene mixtures from reflectance spectra. J. Geophys. Res. 91 (B11), 11641–11653.

Gallie, E. A., Lyder, D. A., Rivard, B., and Cloutis, E. A., 2008. Equivalence of Modified Gaussian Model (MGM) in Wavenumber and Gaussian in Wavelength for Deconvolution of Hyperspectral Reflectance Spectra. International Journal of Remote Sensing 29, No.14, 4089-4096.

Gaffey, M. J., Bell, J. F., Hamilton Brown, R., Burbine, T. H., Piatek, J. L., Reed, K. L., Chaky, D. A., 1993. Mineralogical variations within the S-type asteroid class. Icarus 106, 573-602.

Makarewicz, H.D., Parente, M., Bishop, J.L. 2009. Deconvolution of VNIR spectra using Modified Gaussian Modeling (MGM) with automatic parameter initialization (API) applied to CRISM. IEEE Whispers, Article 5289046.

Mason, A. J., 2012. OpenSolver - An Open Source Add-in to Solve Linear and Integer Problems in Excel. Operations Research Proceedings 2011: Selected Papers of the International Conference on Operations Research, eds. Diethard Klatte, Hans-Jakob Luthi, Karl Schmedders, Springer Berlin Heidelberg, 401-406.

Pompilio, L., Pegrazzi, G., Sgavetti M., Cloutis, E.A., Craig, M.A., Roush, T.L., 2009. Exponential Gaussian approach for spectral modeling: The EGO algorithm I. Band saturation. Icarus 201, 781-794.

Pompilio, L., Pegrazzi, G., Cloutis, E.A., Craig, M.A., Roush, T.L., 2010. Exponential Gaussian approach for spectral modeling: The EGO algorithm II. Band asymmetry. Icarus 208, 811-823.

Reddy, V., Gaffey, M. J., Abell, P. A., Hadersen, P. A., 2012. Constraining albedo, diameter and composition of near-Earth asteroids via near-infrared spectroscopy. Icarus 219, 382-392.

Walsh, S., and Diamond, D., 1985. Non-Linear Curve Fitting using Microsoft Excel Solver. Talanta 42, No. 4, 561-572.

Curriculum Vitae

Michael A. Craig

EDUCATION:

09/2010 – present Ph.D. Geology/Planetary Science, Department of Earth Sciences, University of Western Ontario, London, Ontario, Canada. Supervisors: Dr. Edward Cloutis (University of Winnipeg), Dr. Roberta Flemming (UWO) and Dr. Gordon Osinski (UWO).

08/2010 M.Sc. Geology/Planetary Science, Department of Earth Sciences, University of Western Ontario, London, Ontario, Canada. Supervisors: Dr. Roberta Flemming and Dr. Gordon Osinski.

10/2005 B.Sc. Geography, University of Winnipeg, Winnipeg, Manitoba, Canada.

10/2005 B.A. Environmental Studies, University of Winnipeg, Winnipeg, Manitoba, Canada.

PROFESSIONAL WORK EXPERIENCE:

09/2008 – present Graduate Teaching Assistant, Department of Earth Sciences, University of Western Ontario, London, Ontario, Canada.

05/2009 – present Graduate Research Assistant, Department of Earth Sciences, University of Western Ontario, London, Ontario, Canada.

01/2008 – 04/2008 Graduate Research Assistant, Department of Space Studies, University of North Dakota, Grand Forks, North Dakota, USA.

10/2006 – 12/2007 Technician, Tech Level 3, Department of Geography, Planetary Spectroscopy Facility (PSF), University of Winnipeg, Winnipeg, Manitoba, Canada.

09/2003 – 12/2003 Teaching Assistant, Department of Geography, University of Winnipeg, Winnipeg, Manitoba, Canada.

04/2000 – 10/2006 Student Research Assistant, Department of Geography, University of Winnipeg, Winnipeg, Manitoba, Canada.

AWARDS AND SCHOLARSHIPS:

09/2013 – 08/2014 Ontario Graduate Scholarship: $15,000.

04/2013 – 03/2015 National Sciences and Engineering Research Council of Canada (NSERC) CREATE Fellowship Travel/Rotation Funding: $4,000.

04/2013 – 03/2015 National Sciences and Engineering Research Council of Canada (NSERC) CREATE Fellowship: $21,000. Funding declined, fellowship accepted.

03/2013 Astromaterials Teaching and Research Opportunities/Centre for Planetary Science and Exploration (ASTRO-CPSX) Travel Award: $1,000.

09/2010 – 08/2013 National Sciences and Engineering Research Council of Canada (NSERC) Postgraduate Scholarship, Doctorate (PGSD): $63,000.

09/2010 – 08/2012 Ontario Graduate Scholarship: $30,000. Declined.

04/2009 – 03/2010 National Sciences and Engineering Research Council of Canada (NSERC) CREATE M.Sc. student award in the Canadian Astrobiology Training Program (CATP), single award: $6,426.

01/2001 – 12/2004 Canada Millennium Scholarship and Manitoba Millennium Bursary, awarded once each year: ~$25,600.

COURSES TAUGHT – TEACHING ASSISTANT:

09/2013 – 12/2013 ES1086F, Origin and Geology of the Solar System, Department of Earth Sciences, University of Western Ontario, London, Ontario, Canada.

09/2012 – 12/2012 ES9580a/9680a, Geology & Geophysics Graduate Seminar, Department of Earth sciences, University of Western Ontario, London, Ontario, Canada.

01/2012 – 04/2012 ES2212b, Genesis of Meteorites and Planetary Materials, Department of Earth Sciences, University of Western Ontario, London, Ontario, Canada.

01/2011 – 04/2011 ES3310b, Advanced Mineralogy, Department of Earth Sciences, University of Western Ontario, London, Ontario, Canada.

01/2010 – 04/2010 Centre for Planetary Science and Exploration, Public Outreach, University of Western Ontario, London, Ontario, Canada.

09/2009 – 12/2009 ES1023a-2123a, Planet Earth: Shaken and Stirred, Department of Earth Sciences, University of Western Ontario, London, Ontario, Canada.

01/2009 – 04/2009 ES3310b, Advanced Mineralogy, Department of Earth Sciences, University of Western Ontario, London, Ontario, Canada.

09/2008 – 12/2008 ES1023a, Planet Earth: Shaken and Stirred, Department of Earth Sciences, University of Western Ontario, London, Ontario, Canada.

09/2003 – 12/2003 GEOG 23.1202/3, Introductory Earth Science, Department of Geography, University of Winnipeg, Winnipeg, Manitoba, Canada.

MEDIA INTERACTIONS AND MENTIONS:

09/2007 Undergraduate research featured in article: "U of W prof. part of Mars mission: building equipment for data analysis" Winnipeg Free Press.

08/2006 Undergraduate research featured in Research 2006, University of Winnipeg.

04/2006 Interviewed by Canadian Foundation for Innovation (CFI) writer, Melanie Chambers, in connection with CFI Innovation Canada magazine for article "Life on Mars."

04/2003 Featured in Undergraduate Edge, Highlighting undergraduate student research, Think Link, University of Winnipeg.

10/2002 Undergraduate research featured in Vie Junior magazine article: "Mars en laboratoire."

08/2002 Undergraduate research featured in article "NASA eyes U of W's Mars Simulator" Winnipeg Free Press.

PUBLICATIONS:

Articles Published in Refereed Journals:

Cloutis, E. A., F. C. Hawthorne, S. A. Mertzman, K. Krenn, M. A. Craig, D. Marcino, M. Methot, J. Strong, J. F. Mustard, D. L. Blaney, J. F. Bell, and F. Vilas (2006) "Detection and discrimination of sulfate minerals using reflectance spectroscopy"; Icarus, 184, 121-157.

Cloutis, E. A., M. A. Craig, J. F. Mustard, R. V. Kruzelecky, W. R. Jamroz, A. Scott, D. L. Bish, F. Poulet, J-P. Bibring, P. L. King (2007) "Stability of hydrated minerals on Mars"; Geophysical Research Letters, 34, L20202, 5 pgs.

Cloutis, E. A., K. McCormack, D. T. Bailey, M. A. Craig, S. K. Mertzman, M. A. Robinson, M. Riner, J. F. Bell III (2007) "Ultraviolet spectral reflectance properties of common planetary minerals"; Icarus, 197, 321-347.

Cloutis, E. A., M. A. Craig, R. V. Kruzelecky, W. R. Jamroz, A. Scott, F. C. Hawthorne, S. A. Mertzman (2008) "Spectral reflectance properties of minerals exposed to simulated Mars surface conditions"; ICARUS, 195, 140-168.

Horgan, B. H., J. F. Bell III, E. Z. Noe Dobrea, E. A. Cloutis, D. T. bailey, M. A. Craig, L. H. Roach and J. F. Mustard (2009) "Distribution of hydrated minerals in the north polar region of Mars"; Journal of Geophysical Research, 114, E01005, 27 pgs.

Pompilio, L., G. Pedrazzi, M. Sgavetti, E. A., Cloutis, M. A. Craig and T. L. Roush (2009) "Exponential Gaussian approach for spectral modeling: The EGO algorithm"; Icarus, 201, 781-794.

Rice, M. S., J. F. Bell III, E. A. Cloutis, A. Wang, S. W. Ruff, M. A. Craig, D. T. Bailey, J. R. Johnson, P. A. de Souza, Jr. and W. H. Farrand (2010) "Silica-rich deposits and hydrated minerals at Gusev Crater: Vis-NIR spectral characterization and regional mapping"; Icarus, 205, 375-395.

Cloutis, E. A., P. S. Hardersen, D. L. Bish, D. T. Bailey and M. A. Craig (2010) "Reflectance spectra of iron meteorites: Implications for spectral identification of their parent bodies"; Meteoritics and Planetary Science, 45, Nr 2, 304-332.

Pompilio L., G. Pedrazzi, A. Lisotti, E. A. Cloutis, M. A. Craig, T. L. Roush (2010) "Exponential Gaussian approach for spectral modelling: the EGO algorithm II. Band Asymmetry"; Icarus, 208, 811-823.

Rice, M. S., E. A. Cloutis, J. F. Bell III, D. L. Bish, B. H. Horgan, S. A. Mertzmann, M. A. Craig, R. W. Renaut, B. Gautason, and B. Mountain (2013) "Reflectance Spectra Diversity of Silica-Rich Materials: Sensitivity to Environment and Implications for Detection on Mars"; Icarus, 223, 1, 499-533.

Battler, M. M., G.R. Osinski, D. S. S. Lim, A. F. Davila, F. A. Michel, M. A. Craig, M. R. M. Izawa, L. Leoni, G. F. Slater, A. G. Fairen, N. R. Banerjee and L. J. Preston (2013) "Characterization of the acidic cold seep emplaced jarositic Golden Deposit,

NWT, Canada, as an analogue for jarosite deposition on Mars"; Icarus, 224, 2, 382-398.

Tornabene, L. L., G. R. Osinski, A. S. McEwen, J. J. Wray, M. A. Craig, H. M. Sapers, and P. R. Christensen, (2013) "Impacts and hydrated Silicates on Mars: A Synthesis"; Journal of Geophysical Research, 118, 994-1012.

Izawa, M. R. M., D. M. Applin, P. Mann, M. A. Craig, E. A. Cloutis, J. Helbert and A. Maturilli, (2013) "Reflectance Spectroscopy (200-2500nm) of highly-reduced phases under oxygen- and water-free conditions"; Icarus, 226, 2, 1612-1617.

Izawa, M. R. M., E. A. Cloutis, D. M. Applin, M. A. Craig, P. Mann and M. Cuddy, (2014) "Laboratory Spectroscopic Detection of Hydration in Pristine Lunar Regolith"; Earth and Planetary Science Letters, 390, 157-164.

Izawa, M. R. M., M. A. Craig, D. M. Applin, J. A. Sanchez, V. Reddy, L. LeCorre, P. Mann and E. A. Cloutis, (2015) "Variability, Absorption Features, and Parent Body Searches in "Spectrally Featureless" Meteorite Reflectance Spectra: Case Study – Tagish Lake"; Icarus, 254, 324-332.

Berger, J. A., P. L. King, A. Green, M. A. Craig, M. N. Spilde, S. P. Wright, T. S. Kunkle and R. J. Lee, (2015) "Effect of Halite Coatings on Thermal Infrared Spectra"; Accepted, Journal of Geophysical Research: Solid Earth, 120, No., 4, 2162-2178.

Articles Submitted/In Review/Accepted in Refereed Journals:

Izawa, M. R. M., E. A. Cloutis, D. M. Applin, M. A. Craig, P. Mann and M. Cuddy, (2014) "Spectral-Compositional Relationships for Pristine Lunar Regolith Samples"; In Review: Icarus.

Craig, M. A., G. R., Osinski, E. A., Cloutis, R. L., Flemming, M. R. M. Izawa, V. Reddy, S. K. Fieber-Beyer, L. Pompilio, F. van der Meer, J. A. Berger, M. S. Bramble, and D. M. Applin, (2015) "Fitting the Curve in Excel®: Systematic Curve Fitting of Laboratory and Remotely Sensed Planetary Spectra"; In Review: Computers and Geosciences.

Theses:

Craig, M. A. (2010) "The Effects of Impact on the NIR Spectra of Carbonates and Calibration for use in Planetary Remote Sensing"; M.Sc. Thesis, University of Western Ontario.

Conference Abstracts:

Cloutis, E. A., D. Goltz, M. Craig, D. Marcino, K. M. Krenn, and J. Strong (2000) "Identification of specific water-bearing minerals on Mars: The role of reflectance spectroscopy"; 46th International Conference on Analytical Sciences and Spectroscopy.

Craig, M., E. A. Cloutis, and T. Mueller (2001) "ME and mini-ME: Two Mars environmental simulation chambers for reflectance spectroscopy"; Lunar and Planetary Science Conference, 32, abstract #1368.

Craig, M. A., E. A. Cloutis (2006) "Sulfate stability under simulated Martian conditions"; Lunar and Planetary Institute, Martian Sulfates as Recorders of Atmospheric-Fluid-Rock Interactions, abstract #7013.

Craig, M., E. A. Cloutis, L. Kaletzke, K. McCormack, and L. Stewart (2006) "Alteration of hydration absorption features in reflectance spectra of selected sulfates in a low pressure environment: 0-45-4.3 μm"; Lunar and Planetary Science Conference, 37, abstract #2112.

Cloutis, E. A., M. Craig, L. Kaletzke, K McCormack and L. Stewart (2006) "Hoserlab: A new planetary spectrophotometer facility"; Lunar and Planetary Science Conference, 37, abstract #2121.

McCormack, K., E. Cloutis, J. F. Bell, L. Stewart, L. Kaletzke and M. Craig (2006) "Determining mineral composition in the ultraviolet spectral region from 200 to 400 nanometres"; Lunar and Planetary Science Conference, 37, abstract #2158.

Kaletzke, L., E. Cloutis, M. Craig, K. McCormack and L. Stewart (2006) "Possible explanations for the 506nm feature in telescopic spectra of Vesta"; Lunar and Planetary Science Conference, 37, abstract #2174.

Stewart, L., E. Cloutis, J. Bishop, M. Craig, L. Kaletzke and K. McCormack (2006) "Classification of iron-bearing phyllosilicates based on ferric and ferrous iron absorption bands in the 400-1300 nm region"; Lunar and Planetary Science Conference, 37, abstract #2185

Craig, M. A., E. A. Cloutis, D. T. Bailey (2007) "The effects of grain size, <45-1000 μm, on the reflectance spectrum of planetary analogs from 0.35-2.5 μm"; Lunar and Planetary Science Conference, 38, abstract #1356.

Cloutis, E. A., M. A. Craig, D. T. Bailey (2007) "Bidirectional reflectance properties of orthopyroxene"; Lunar and Planetary Science Conference, 38, abstract #1300.

Reddy V., E. A. Cloutis, M. A. Craig, M. J. Gaffey (2007) "Spectral calibration of orthopyroxene – clinopyroxene mixtures: implications for interpreting asteroid spectra"; 70th Annual Meteoritical Society Meeting, 42, abstract #5077.

Craig, M. A., E. A. Cloutis, V. Reddy, D. T. Bailey, M. J. Gaffey (2008) "The effects of grain size, <10μm – 4.75mm, on the reflectance spectrum of planetary analogs from 0.35-2.5μm"; Lunar and Planetary Science Conference, 39, abstract #2082.

Cloutis, E. A., D. T. Bailey, M. A. Craig, P. S. Hardersen (2008) "Reflectance Spectra of Iron Meteorite Powders"; Lunar and Planetary Science Conference, 39, abstract #1082.

Pompilio, L., G. Pedrazzi, M. A. Craig, M. Sgavetti, E. A. Cloutis (2008) "Spectral modeling of planetary analogues, preliminary results"; Lunar and Planetary Science Conference, 39, abstract #1550.

Hogan B. H. N., J. F. Bell III, E. Z. Noe Dobrea, E. A. Cloutis, D. T. Bailey, M. A. Craig, L. Stewart (2008) "Hydrated units in the Martian north polar region"; Lunar and Planetary Science Conference, 39, abstract #2122.

Reddy V., E. A. Cloutis, M. A. Craig and M. J. Gaffey (2008) "Spectral calibration of orthopyroxene - type A clinopyroxene mixtures: implications for interpreting asteroid spectra"; Lunar and Planetary Science Conference, 39, abstract #2007.

Cloutis E. A., R. J. Leveille, D. T. Bailey, L. Stewart, M. A. Craig, K. McCormack, and L. Kaletzke (2008) "Mineral suites in carbonate- and sulfate-rich environments: Implications for remote sensing of Mars", proceedings of: GAC/MAC Annual Meeting, May26-28, 2008.

Craig, M. A., G. R. Osinski and R. L. Flemming (2009) "UV-Vis-NIR Reflectance spectra of shocked carbonates from the Haughton Impact Structure, Devon Island, Canada: 0.35-2.5 μm; Implications for carbonate identification on Mars"; Lunar and Planetary Science conference, 40, abstract #1643.

Cloutis E. A., P. S. Hardersen, V. Reddy, M. J. Gaffey, D. T. Bailey and M. A. Craig (2009) "Metal-Orthopyroxene and Metal-Olivine Mixtures: Spectral reflectance properties and implications for asteroid spectroscopy"; Lunar and Planetary Science conference, 40, abstract #1332.

Rice, M. S., J. F. Bell III, E. A. Cloutis, A. Wang, S. W. Ruff, M. A. Craig, D. T. Bailey, J. R. Johnson, P. A. de Souza Jr. and W. H. Farrand (2009) "Silica-rich deposits and hydrated minerals at Gusev Crater, Mars"; Lunar and Planetary Science conference, 40, abstract #2143.

Craig, M. A., R. L. Flemming, G. R. Osinski and E. A. Cloutis (2010) "UV-Vis-NIR spectra of intimate mixtures of synthetic CaCO3 and amorphous SiO2: 0.35-2.5 μm; Implications for the spectral identification of shocked assemblages on Mars"; Lunar and Planetary Science Conference, 41, abstract #2110.

Izawa, M. R. M., R. L. Flemming, N. R. Banerjee, P. J. A. McCausland, L. J. Preston, D. E. Moser, I. R. Baker, M. A. Craig, E. A. Cloutis and S. Matreev (2010)

"Multimethod study of E chondrite shock"; 73rd Annual Meteoritical Society Meeting, 42, abstract #5345.

Craig, M. A., G. R. Osinski, R. L. Flemming, and E. A. Cloutis (2011) "Spectral identification of impact glasses via NIR reflectance spectroscopy"; Lunar and Planetary Science Conference, 42, abstract #2411.

Battler, M. M., G. R. Osinski, D.S. S. Lim, A. F. Davila, F. A. Michel, M. A. Craig, M. R. M. Izawa, L. Leoni, G. F. Slater, A. G. Fairen and S. W. Starratt (2011) "The Golden deposit in the Canadian Arctic as an analogue for jarosite deposition at Meridiani Planum and Mawrth Vallis, Mars"; Lunar and Planetary Science Conference, 42, abstract #2759.

Cloutis, E., P. Badiou, D. Bailey, G. Berard, M. Craig, G. Goldsborough, S. Grasby, W. Last, K. Londry, P. Mann, and J. Stromberg (2011) "The East German Creek, Manitoba Hypersaline Springs: Analogue for 'Last Refuge' on Mars"; Analogue Sites for Mars Missions Conference, abstract #6008.

Mann, J. P., E. A. Cloutis, M. S. Rice, M. A. Craig, and G. M. Berard (2012), "Variations in Reflectance Spectra Associated with Exposure of Hydrated Minerals to Simulated Mars Surface Conditions;" Lunar and Planetary Science Conference, 43, abstract #2351.

Loiselle, L., E. A. Cloutis, M. Craig, A. Koujelev, S. Lui, S. Sheih, G. Southam, R. Leveille, M. Dyar, and P. King (2012) "Structural and Chemical Characterization of 'Biogenic' and Abiotic Jarosite: Implications for the Search for Life on Mars"; NASA Astrobiology Science Conference, 2012.

Craig, M. A., R. L. Flemming, G. R. Osinski, E. A., Cloutis, M. R. M. Izawa, H. M. Sapers, and C. L. Marion (2013) "XRD Patterns of Glassy Impactites: Amorphous Curve Fitting and Composition Determination with Implications for Mars"; Lunar and Planetary Science Conference, 44, abstract #2319.

Izawa, M. R. M., D. Applin, P. Mann, M. A. Craig, and E. A. Cloutis (2013) "Ultraviolet, Visible and Near-Infrared Reflectance Spectroscopy of Highly-Reduced Phases under Oxygen- and Water-Free Conditions"; Lunar and Planetary Science Conference, 44, abstract #1788.

Izawa, M. R. M., M. A. Craig and E. A. Cloutis (2013) "Spectral Variations in the Tagish Lake Carbonaceous Chondrite in the Ultraviolet, Visible and Near-Infrared"; Lunar and Planetary Science Conference, 44, abstract #3019.

Craig, M. A., R. L. Flemming, G. R. Osinski, E. A., Cloutis, J. Anderson, M. R. M. Izawa, H. M. Sapers, and C. L. Marion (2013) "XRD Patterns of Glassy Impactites: Correlating Composition and Origin via Cluster Variation Analysis and Implications for Mars"; proceedings of the GAC/MAC annual Meeting, abstract #252.

Craig, M. A., G. R. Osinski, R. L. Flemming, E. A. Cloutis, B. Horgan, L. L. Tornebene, M. R. M. Izawa, H. M. Sapers, C. L. Marion, D. M. Applin, P. Mann and J. Stromberg, (2014) “Near-Infrared Spectra of Glassy Impactites from Terrestrial Impact Structures”; Lunar and Planetary Science Conference, 45, abstract #2417.

Cole, S. B., E. Cloutis, M. Cuddy, M. R. M. Izawa, P. Mann, M. A. Craig, V. Pietrasz and S. W. Sqyures, (2014) “The Large Mars Atmosphere Simulation Chamber at the University of Winnipeg”; The American Geophysical Union Fall Meeting, abstract #P11A-3740.